

Application of an inverse analysis using the Ensemble Kalman Filter method to a deep excavation case

with validation of constitutive soil models

by

Konrad Bartczak

to obtain the degree of Master of Science
at the Delft University of Technology,
to be defended publicly on Tuesday January 14, 2020 at 03:30 PM.

Student number: 4735951
Project duration: February 1, 2019 – January 14, 2020
Thesis committee: Prof. Dr. Michael A. Hicks, TU Delft, Geo-engineering
Dr. Ronald B.J. Brinkgreve, TU Delft, Geo-engineering
Dr. Ir. Femke C. Vossepoel, TU Delft, Petroleum Engineering
Dr. Shuhong Tan, Royal HaskoningDHV
MSc. Antonios Mavritsakos, Royal HaskoningDHV

An electronic version of this thesis is available at <http://repository.tudelft.nl/>.



Executive Summary

Displacement control is of utmost importance in deep excavation design and is usually based on numerical modelling, e.g. Finite Element Method (FEM). Numerical methods tend to be more conservative when analysing soil behaviour during deep excavation, whereas for practical and economic reasons this is not favoured. The inverse analysis allows for the identification of the soil parameter set that can provide the measurements observed in the monitoring when it is applied in the model. When performed in a probabilistic concept, it reduces parameter uncertainty and enables the stochastic prediction of future soil behaviour.

In this thesis, capabilities and limitations of difference advanced constitutive models are investigated. The Generalized Hardening Soil Small strain model (GHS) presented a positive aspect in modelling soil behaviour during deep excavation with its various stress/strain dependency settings. Its configuration GHS1120 captured the stiffness in the small-strain range best from all four material models considered for the presented soil data.

Because of the uncertainties originating from the size of the domain and limitations of site investigation, the soil parameters can only be shown as probability distributions. To make that distribution more accurate, comparative selection together with a simple physical model governed by coupled spring equation is used to choose the best-fit inverse analysis optimisation algorithm. Due to its robustness, efficiency, no need for of a gradient vector of multiple outputs and insight into well-propagated sample variance the chosen algorithm was the Ensemble Kalman Filter

Thereafter, the choice of the relevant parameters is done based on the conducted sensitivity analysis and engineering judgement. Having the most competitive optimization approach selected, remote scripting with Python is used to utilise Finite Element (FE) modelling in the 2D Plaxis software.

The script developed in Python environment is used to perform automatic runs, which iteratively updated the input parameters with response observation (diaphragm wall deflections) using the Ensemble Kalman filter optimisation algorithm based on a chosen excavation stage. The re-calibrated parameters are checked with the data, which was used to create synthetic measurements made using the same FE, to perform reliability assessment of the developed Python-based algorithm and investigate its capabilities and limitations.

The sensitivity studies based on multiple runs of the algorithm with different targets, observation types and configurations of the script allowed to draw solid conclusions regarding the application of the algorithm in feedback-loop oriented design. This touched upon the issues of the type and volume of required observations to be gathered from the field monitoring system, the influence of the soil conditions on the efficiency of the estimations and the connection between the optimisation process and the required site investigation program.

The further development of the presented optimisation method is expected to increase certainty in setting alarm thresholds in the applications of the Observational Method.

Table of Contents

List of Figures	vii
List of Tables	xiii
List of Units	xiv
List of Abbreviations	xvii
1 Introduction	1
1.1 Motivation and case background	1
1.2 Research objectives	2
1.3 Methodology and the thesis layout	2
2 Problem definition and the literature review	5
2.1 Physical phenomenon of heave	5
2.2 Numerical modelling of a deep excavation case.	6
2.3 Constitutive models in the deep excavation applications	8
2.4 Inverse finite-element modelling	11
3 Investigation of material models and calibration of soil parameters	15
3.1 Introduction	16
3.2 Sub-soil parameters assessment	18
3.3 Studies on the material model parameters	26
3.4 Conclusions.	42
4 Target measurements in the 2D finite-element model	43
4.1 Introduction	43
4.2 Material models' performance comparison	45
4.3 Sensitivity analysis of the input parameters	48
4.4 Summary and the model selection	52
5 Set-up of the inverse analysis method	53
5.1 Introduction	53
5.2 Kalman Filter	53
5.3 Optimisation process experiment.	58
5.4 Calibration of the method.	65
5.5 Conclusions.	69
6 Application of the inverse analysis in the FEM	71
6.1 Introduction	71
6.2 Setting up the problem	72
6.3 Post-processing of the algorithm performance	76
6.4 Conclusions.	89
7 Conclusions and recommendations	91
7.1 Conclusions.	91
7.2 Limitations of the research	92
7.3 Recommendations for further studies.	93
Bibliography	95
Appendices	101
A Calibration of the material models parameters	103
A.1 Subsoil parameters assessment	103
A.2 Studies on the material model parameters	107

B	Target measurements in the two-dimensional finite-element model	113
B.1	Sensitivity analysis of the input parameters	113
C	Estimation method in the inverse analysis	127
C.1	Extended Kalman Filter	127
C.2	Configuration of the script's functions	129
D	Application of the inverse analysis in the FEM	143
D.1	Performance depending on the observation vector	143

List of Figures

1.1	Workflow of the problem modelling.	3
2.1	PSR chart - comparison of PSR values in clay and in sand according to Hsiung et al. (2016) [45] (denoted as <i>This study</i>) and Ou et al. [17] (denoted as <i>Ou [2]</i>).	8
2.2	The workflow of the GHS model.	10
2.3	The extensions of the Kalman Filter optimization algorithm.	14
3.1	Top view of the project location with marked boreholes locations (marked as blue and red circles).	15
3.2	Longitudinal cross-section of building pit.	16
3.3	The method of calibration of soil parameters (in here, the s_u in the NGI-ADP model based on triaxial UU1 test).	17
3.4	Workflow of calibration of the HSS model input parameters.	17
3.5	The confining pressure as a function of depth for the considered cross-section ($K_0 = 0.645$).	18
3.6	In-depth distribution of the undrained shear strength obtained from the UU and UC triaxial tests.	19
3.7	Distribution of the secant undrained stiffness obtained in the triaxial CU tests as a function of test confining pressure.	19
3.8	Distribution of the secant undrained stiffness obtained in the triaxial UU tests as a function of test confining pressure.	20
3.9	The vertical effective and total stresses as a function of depth for the considered cross-section ($OCR = 1.0$).	22
3.10	Reference tangent oedometer stiffness E_{oed}^{ref} as a function of depth.	23
3.11	Reference un/re-loading stiffness E_{ur}^{ref} as a function of depth.	23
3.12	Stress paths computed for the calibrated HSS model parameters compared to the paths from the laboratory tests - triaxial CU1 test.	29
3.13	Stress paths computed for the calibrated HSS model parameters compared to the paths from the laboratory tests - triaxial CU2 test.	29
3.14	Stress paths computed for the calibrated HSS model parameters compared to the paths from the laboratory tests - triaxial UU1 test.	30
3.15	Stress paths computed for the calibrated HSS model parameters compared to the paths from the laboratory tests - triaxial UU2 test.	30
3.16	Stress paths computed for the calibrated HSS model parameters compared to the paths from the laboratory tests - oedometer tests.	31
3.17	Stress paths computed for the calibrated NGI-ADP model parameters compared to the paths from the laboratory tests - triaxial UU1 test.	32
3.18	Stress paths computed for the calibrated NGI-ADP model parameters compared to the paths from the laboratory tests - triaxial UU2 test.	33
3.19	Stress paths computed for the calibrated SHANSEP MC model parameters compared to the paths from the laboratory tests - triaxial UU1 test.	34
3.20	Stress paths computed for the calibrated SHANSEP MC model parameters compared to the paths from the laboratory tests - triaxial UU2 test.	35
3.21	Stress paths for the calibrated parameters of the HSS model and the selected GHS model variations - triaxial CU2 test at $\sigma_3 = 450$ kPa.	36
3.22	Stress paths computed for the calibrated parameters of the HSS model and the selected GHS model variations - triaxial UU1 at $\sigma_3 = 550$ kPa.	36
3.23	Stress paths computed for the calibrated GHS1120 model parameters compared to the paths from the laboratory tests - triaxial CU1 test.	37
3.24	Stress paths computed for the calibrated GHS1120 model parameters compared to the paths from the laboratory tests - triaxial CU2 test.	37

3.25	Stress paths computed for the calibrated GHS1120 model parameters compared to the paths from the laboratory tests - triaxial UU1 test.	38
3.26	Stress paths computed for the calibrated GHS1120 model parameters compared to the paths from the laboratory tests - triaxial UU2 test.	38
3.27	Stress paths for the small strain range for the calibrated GHS2021 and GHS2121 models' parameters compared to the stress path from the laboratory test - triaxial CU2 test.	39
3.28	Stress paths for the small strain range for the calibrated GHS1120 and GHS1121 models' parameters compared to the stress path from the laboratory test - triaxial UU1 test.	39
3.29	Comparison of the performance of the calibrated HSS and GHS models parameters - triaxial CU2 test at $\sigma_3 = 450$ kPa.	40
3.30	Comparison of the performance of the calibrated HSS, NGI-ADP, Shansep MC and GHS1120 models' parameters - the triaxial UU1 test at $\sigma_3 = 550$ kPa.	41
4.1	The effective stress distribution in the two-dimensional Plaxis model.	43
4.2	The evolution of the building displacements throughout the excavation steps for the SHANSEP MC Undrained A model.	44
4.3	Comparison of the computed settlements of the building for different material models - phase 12.	45
4.4	Comparison of the computed settlements of the building for different material models - phase 15.	45
4.5	Comparison of the computed d-wall deflections for different material models - phase 12.	46
4.6	Comparison of the computed d-wall deflections for different material models - phase 15.	46
4.7	The evolution of the displacements of the building (middle node) throughout the excavation steps for different material models.	46
4.8	Comparison of the computed settlements of the building for different settings of the GHS model - phase 12.	47
4.9	Comparison of the computed settlements of the building for different settings of the GHS model - phase 15.	47
4.10	Comparison of the computed d-wall deflections for different settings of the GHS model - phase 12.	47
4.11	Comparison of the computed d-wall deflections for different settings of the GHS model - phase 15.	47
4.12	Comparison of the computed settlements of the building for different settings of the GHS model - phase 12.	48
4.13	Comparison of the computed settlements of the building for different settings of the GHS model - phase 15.	48
4.14	Comparison of the computed d-wall deflections for different settings of the GHS model - phase 12.	48
4.15	Comparison of the computed d-wall deflections for different settings of the GHS model - phase 15.	48
5.1	The workflow of Extended Kalman Filter algorithm.	54
5.2	The workflow of Ensemble Kalman Filter algorithm.	56
5.3	Scheme of coupled springs problem.	58
5.4	The probability distribution plotted for the initial mean and covariance of the two springs stiffness values.	58
5.5	Definition of an error function [99]	59
5.6	The optimisation of the spring problem using the EKF algorithm - the evolution of the estimated variables and measurements throughout the iterations.	59
5.7	The optimisation of the spring problem using the EKF algorithm - the evolution of RMSE throughout the iterations.	60
5.8	The optimisation of the spring problem using the EKF algorithm - the evolution of RMSE throughout the calculation model runs.	60
5.9	The variables evolution throughout the iterations in the two-spring problem optimisation using the EKF algorithm.	60

5.10	The optimisation of the spring problem using the EKF algorithm - the Pearson's coefficient evolution throughout the iterations.	60
5.11	The optimisation of the spring problem using the EKF algorithm - the evolution of the variables' variances and covariance.	60
5.12	The optimisation of the spring problem using the EnKF algorithm - the evolution of the estimated variables and measurements throughout the iterations.	61
5.13	The optimisation of the spring problem using the EnKF algorithm - the evolution of RMSE throughout the iterations.	62
5.14	The optimisation of the spring problem using the EnKF algorithm - the evolution of RMSE throughout the calculation model runs.	62
5.15	The variables evolution throughout the iterations in the two-spring problem optimisation using the EnKF algorithm.	62
5.16	The optimisation of the spring problem using the EnKF algorithm - the ensemble evolution throughout the iterations.	63
5.17	The optimisation of the spring problem using the EnKF algorithm - ensemble evolution in parameters space (focus on the initial ensemble).	63
5.18	The optimisation of the spring problem using the EnKF algorithm - ensemble evolution in parameters space (focus on the last ensembles).	64
5.19	The optimisation of the spring problem using the EnKF algorithm - the Pearson's coefficient evolution throughout the iterations.	64
5.20	The optimisation of the spring problem using the EnKF algorithm - the evolution of the variables' variances and covariance.	64
5.21	Variation of RMSE and SPREAD for cases with accurate and inaccurate initial conditions [48].	66
5.22	Measurement and process variances sensitivity studies - total number of <i>Runs</i> (calculated ensemble members in all iterations summed) needed to reach tolerance of 0.01.	67
5.23	Measurement and process variances sensitivity studies - the lowest RMSE reached for a total of 7500 members calculated.	67
5.24	The total number of iterations needed to reach particular tolerance levels.	68
5.25	The total number of calculated ensemble members (<i>Runs</i>) needed to reach particular tolerance levels.	68
6.1	The diaphragm wall deflections computed for the established targets.	73
6.2	Histogram and PDF of log-normally distributed E_{50}^{ref} parameter and the input variable based on it.	74
6.3	Workflow of the lognormal - normal - lognormal transformation in the EnKF script.	74
6.4	Derivation of the degrees of freedom of the diaphragm wall deflections curve for the initial variable value.	75
6.5	The ensembles created in each iteration for the run with targets set to $X_E = 10.0$ MPa and $X_\gamma = 0.00004$	76
6.6	The members with the mean throughout the iterations for the run with targets set to $X_E = 10.0$ MPa and $X_\gamma = 0.00004$	77
6.7	The RMSE computed for the mean output of each iteration for the run with targets set to $X_E = 10.0$ MPa and $X_\gamma = 0.00004$	77
6.8	The d-wall deflections computed for the means of the ensemble of each iteration for the run with targets set to $X_E = 10.0$ MPa and $X_\gamma = 0.00004$	77
6.9	The d-wall deflections computed for the members of the first iteration for the run with the targets set to $X_E = 10.0$ MPa and $X_\gamma = 0.00004$	78
6.10	The comparison of the RMSE computed for the mean output of each iteration for different ensemble sizes - case of one variable X_E	78
6.11	The comparison of the estimated mean of the ensemble of each iteration for different ensemble sizes - case of one variable X_E).	79
6.12	The comparison of the RMSE computed for the mean output of each iteration for different targets - one variable case.	79
6.13	The evolution of the estimated mean of the ensembles throughout the iterations for a different targets - one variable case.	80

6.14	The comparison of the RMSE computed for the mean output of each iteration for different targets - two variables case.	80
6.15	The evolution of the estimated mean of the ensembles (for X_E variable) throughout the iterations for a different targets - two variables case.	81
6.16	The evolution of the estimated mean of the ensembles (for X_γ variable) throughout the iterations for a different targets - two variables case.	81
6.17	The comparison of the RMSE computed for the mean output of each iteration for different observation vectors - one variable case.	82
6.18	The evolution of the estimated mean of the ensembles throughout the iterations for a different observation types - one variable case.	82
6.19	The computed diaphragm wall deflection for the runs with different observation vectors and the deflections imitating a true case.	83
6.20	The comparison of the RMSE computed for the mean output of each iteration for different correlation coefficients - two variables case.	84
6.21	Pearson's correlation coefficient evolution throughout the iterations for different initial correlation values.	84
6.22	The evolution of the estimated mean (the X_E variable) of the ensembles throughout the iterations for different correlation coefficients - two variables case.	85
6.23	The evolution of the estimated mean (the X_γ variable) of the ensembles throughout the iterations for different correlation coefficients - two variables case.	85
6.24	The evolution of the estimated variance of the X_E variable throughout the iterations for different initial correlation values.	86
6.25	The evolution of the estimated variance of the X_γ variable throughout the iterations for different initial correlation values.	86
6.26	The ensemble created in each iteration for the initial value of $\rho = 0.0$	86
6.27	The ensemble created in each iteration for the initial value of $\rho = -0.50$	86
6.28	The ensemble created in each iteration for the initial value of $\rho = 0.0$ - focus on the last iterations.	87
6.29	The ensemble created in each iteration for the initial value of $\rho = -0.50$ - focus on the last iterations.	87
6.30	The ensemble created in each iteration for the initial value of $\rho = -0.70$	87
6.31	The ensemble created in each iteration for the initial value of $\rho = -0.90$	87
6.32	The ensemble created in each iteration for the initial value of $\rho = -0.70$ - focus on the last iterations.	88
6.33	The ensemble created in each iteration for the initial value of $\rho = -0.90$ - focus on the last iterations.	88
A.1	Distribution of the effective internal friction angle obtained in the CU triaxial tests as a function of depth.	103
A.2	Distribution of the effective cohesion value obtained in the CU triaxial tests as a function of depth.	103
A.3	Distribution of the secant stiffness as a function of depth obtained in triaxial CU tests.	103
A.4	Distribution of the secant stiffness as a function of depth obtained in triaxial UU tests.	103
A.5	Pressuremeter limit pressure p_L as a function of depth.	104
A.6	The undrained shear strength s_u obtained in the PMT testing.	104
A.7	Pressuremeter stiffness modulus E_M as a function of depth.	104
A.8	Pressuremeter rebound modulus E_{ur} as a function of depth.	104
A.9	The one-dimensional consolidation test pre-consolidation pressure σ'_p as a function of depth.	104
A.10	The consolidation test swelling index C_e as a function of depth.	105
A.11	The consolidation test compression index C_c as a function of depth.	105
A.12	Atterberg test Plasticity Index $P.I.$ as a function of depth.	105
A.13	The consolidation test initial void ratio e_0 as a function of depth.	105
A.14	Natural water content w as a function of depth.	105
A.15	Atterberg test Plasticity Limit $P.L.$ as a function of depth.	105
A.16	Atterberg test Liquid Limit $L.L.$ as a function of depth.	106
A.17	Dry unit weight γ_d as a function of depth.	106
A.18	Test water content w_{test} as a function of depth.	106

A.19	Total unit weight γ_{sat} as a function of depth.	106
A.20	The undrained shear strength s_u obtained in the PMT, UC and UU tests as a function of confining pressure (with corresponding averaged depth).	106
A.21	Test results from the consolidation test: borehole CR-19, depth 37.90 m, <i>CH</i> clay type.	107
A.22	Test results from the consolidation test: borehole CR-A6, depth 54.10 m, <i>CH</i> clay type.	107
A.23	Test results from the consolidation test: borehole CR-A19, depth 55.45 m, <i>CH</i> clay type.	107
A.24	Test results from the triaxial UU1 test: borehole CR-A-4 and depth of around 60.60 m.	108
A.25	Test results from the triaxial UU2 test: borehole CR-A-1 and depth of around 67.35 m.	108
A.26	Test results from the extension triaxial: borehole CR-A-19-51 and depth of around 51.65 m.	108
A.27	Test results from the triaxial CU test: borehole CR-A-15 and depth of around 46.15 m.	109
A.28	Test results from the triaxial CU test: borehole CR-A-15 and depth of around 52.15 m.	109
C.1	The optimisation of the spring problem using the EKF algorithm - the evolution of the estimated variables and measurements throughout the iterations for tough initial conditions.	127
C.2	The optimisation of the spring problem using the EKF algorithm - the evolution of RMSE throughout the iterations for tough initial conditions.	128
C.3	The variables evolution throughout the iterations in the two-spring problem optimisation using the EKF algorithm for tough initial conditions.	128
C.4	The optimisation of the spring problem using the EKF algorithm - the Pearson's coefficient evolution throughout the iterations for tough initial conditions.	128
C.5	The optimisation of the spring problem using the EKF algorithm - the evolution of the variables' variances for tough initial conditions.	128
C.6	The error evolution throughout the iterations for the ensemble size of $N = 10$	129
C.7	The error evolution throughout the iterations for the ensemble size of $N = 10$	129
C.8	The error evolution throughout the iterations for the ensemble size of $N = 15$	130
C.9	The error evolution throughout the iterations for the ensemble size of $N = 15$	130
C.10	The error evolution throughout the iterations for the ensemble size of $N = 20$	131
C.11	The error evolution throughout the iterations for the ensemble size of $N = 20$	131
C.12	The error evolution throughout the iterations for the ensemble size of $N = 25$	132
C.13	The error evolution throughout the iterations for the ensemble size of $N = 25$	132
C.14	The error evolution throughout the iterations for the ensemble size of $N = 40$	133
C.15	The error evolution throughout the iterations for the ensemble size of $N = 40$	133
C.16	The error evolution throughout the iterations for the ensemble size of $N = 50$	134
C.17	The error evolution throughout the iterations for the ensemble size of $N = 50$	134
C.18	The error evolution throughout the iterations for the ensemble size of $N = 75$	135
C.19	The error evolution throughout the iterations for the ensemble size of $N = 75$	135
C.20	The error evolution throughout the iterations for the ensemble size of $N = 100$	136
C.21	The error evolution throughout the iterations for the ensemble size of $N = 100$	136
C.22	The error evolution with a corresponding bandwidth of 2σ , averaged from 25 simulations, throughout the iterations for the ensemble size of $N = 10$	137
C.23	The error evolution with a corresponding bandwidth of 2σ , averaged from 25 simulations, throughout the iterations for the ensemble size of $N = 15$	137
C.24	The error evolution with a corresponding bandwidth of 2σ , averaged from 25 simulations, throughout the iterations for the ensemble size of $N = 20$	138
C.25	The error evolution with a corresponding bandwidth of 2σ , averaged from 25 simulations, throughout the iterations for the ensemble size of $N = 25$	138
C.26	The error evolution with a corresponding bandwidth of 2σ , averaged from 25 simulations, throughout the iterations for the ensemble size of $N = 40$	139
C.27	The error evolution with a corresponding bandwidth of 2σ , averaged from 25 simulations, throughout the iterations for the ensemble size of $N = 50$	139
C.28	The error evolution with a corresponding bandwidth of 2σ , averaged from 25 simulations, throughout the iterations for the ensemble size of $N = 75$	140
C.29	The error evolution with a corresponding bandwidth of 2σ , averaged from 25 simulations, throughout the iterations for the ensemble size of $N = 100$	140
C.30	The percentage value of script runs in which the computed error is below tolerance of 0.01 in a function of iterations for 8 ensemble sizes.	141

C.31	The percentage value of script runs in which the computed error is below tolerance of 0.01 in a function of R value for 8 ensemble sizes.	141
D.1	The computed RMSE throughout the iterations for different observation types - manually created measurements case.	143
D.2	The evolution of the estimated mean (the X_E variable) of the ensembles throughout the iterations for a different observation types - manually created measurements case with two variables.	144
D.3	The evolution of the estimated mean (the X_γ variable) of the ensembles throughout the iterations for a different observation types - manually created measurements case with two variables.	144

List of Tables

2.1	Switches of the GHS material model with respect to the stress-dependency of stiffness and the stress-dependency formulas	11
3.1	Parameters obtained in the triaxial tests.	20
3.2	Clay parameters obtained in Pressuremeter tests.	21
3.3	Clay parameters obtained from one-dimensional consolidation tests.	22
3.4	The stiffness parameters obtained from one-dimensional consolidation tests.	23
3.5	Parameters obtained from Atterberg Limits tests.	24
3.6	State parameters obtained from the index tests.	24
3.7	Summary of the input parameters.	25
3.8	Parameters obtained in the representative triaxial CU tests.	27
3.9	Parameters obtained in the representative triaxial UU tests.	27
3.10	Parameters obtained in the representative one-dimensional consolidation tests.	28
3.11	The initial and the calibrated parameters of the HSS model.	31
3.12	The initial and the calibrated parameters of the NGI-ADP model.	33
3.13	The initial and the calibrated parameters of the SHANSEP MC model.	35
3.14	Differences between the material models.	42
4.1	Construction phases as in the Plaxis 2D model.	44
4.2	Configurations of material model parameters and drainage approach depending on construction phases.	45
4.3	Sensitivity of the HSS model parameters for construction phases 12 and 15.	50
4.4	Sensitivity of the NGI-ADP model parameters for construction phases 12 and 15.	51
4.5	Sensitivity of the SHANSEP MC model parameters for construction phases 12 and 15.	51
4.6	Sensitivity of the GHS2142 model parameters for construction phases 12 and 15.	52
4.7	Comparison of the time-expensiveness of calculation with different material models.	52
5.1	Studies of the 'success rate', i.e. the number of runs where error fell below the tolerance specified as $RMSE = 0.01$, for ensemble sizes $N = [10, 15, 20, 25, 40, 50, 75, 100]$	68
6.1	The sets of HSS model parameters used to compute the target diaphragm wall displacements.	73
A.1	HSS and GHS material models' initial input parameters for the representative tests.	110
A.2	NGI-ADP material model initial input parameters for the representative tests.	111
A.3	Shansep MC material model initial input parameters for the representative tests.	111
B.1	The d-wall deflection errors and the building settlements differences computed for the lower-bound values of the HSS model parameters sensitivity studies (phase 12).	114
B.2	The d-wall deflection errors and the building settlements differences computed for the higher-bound values of the HSS model parameters sensitivity studies (phase 12).	115
B.3	The d-wall deflection errors and the building settlements differences computed for the lower-bound values of the HSS model parameters sensitivity studies (phase 15).	116
B.4	The d-wall deflection errors and the building settlements differences computed for the higher-bound values of the HSS model parameters sensitivity studies (phase 15).	117
B.5	The d-wall deflection errors and the building settlements differences computed for the NGI-ADP model parameters sensitivity studies (phase 12).	119
B.6	The d-wall deflection errors and the building settlements differences computed for the NGI-ADP model parameters sensitivity studies (phase 15).	120
B.7	The d-wall deflection errors and the building settlements differences computed for the SHANSEP MC model parameters sensitivity studies (phase 12).	122

B.8	The d-wall deflection errors and the building settlements differences computed for the SHANSEP MC model parameters sensitivity studies (phase 15).	122
B.9	The d-wall deflection errors and the building settlements differences computed for the GHS model parameters sensitivity studies (phase 12).	124
B.10	The d-wall deflection errors and the building settlements differences computed for the GHS model parameters sensitivity studies (phase 15).	125

List of Units

Units		
α	[-]	SHANSEP coefficient
α	[-]	Correction coefficient in pressuremeter stiffness modulus formula
$\varphi(\varphi')$	[°]	(Effective) Internal friction angle
$\gamma_{0.7}$	[-]	Threshold shear strain at $G_s = 0.722G_0$
γ_d	[kN/m^3]	Dry unit weight
γ_f^C	[%]	Shear strain at failure in triaxial compression
γ_f^E	[%]	Shear strain at failure in triaxial extension
γ_f^{DSS}	[%]	Shear strain at failure in direct simple shear
γ_{sat}	[kN/m^3]	Saturated unit weight
ε	[-]	Error computed in RMSE function
ε_{50}	[-]	Strain at 50% of maximum deviator stress in triaxial tests
ε_f	[-]	Strain at failure in triaxial tests
$\nu(\nu')$	[-]	(Effective) Poisson's ratio
ν_{ur}	[-]	Un/re-loading Poisson's ratio
$\phi(\phi')$	[°]	(Effective) Internal friction angle
ψ	[°]	Angle of dilatancy
σ	[m]	Standard deviation in the inverse analysis
σ'_1	[kPa]	Major effective principal stress
σ'_3	[kPa]	Minor effective principal stress
σ'_p	[kPa]	Pre-consolidation pressure
σ_t	[-]	Tension cut-off and tensile strength
σ'_v	[kPa]	Effective vertical stress
$\sigma_{tension}$	[kPa]	Tensile strength
$\sigma_{measurement}^2$	[-]	Measurement noise in Kalman Filter
$\sigma_{process}^2$	[-]	Process noise in Kalman Filter
τ^0/s_u^A	[-]	Initial mobilization
c	[kPa]	Cohesion of soil
c'	[kPa]	Effective Cohesion of soil
C_c	[-]	the compression index
$C_e = C_s$	[-]	Swelling/reloading index
c_{inc}	[kPa]	the increase of the cohesion with depth
$e_{init} = e_0$	[-]	Initial void ratio
E	[MPa]	Young's modulus
E_0	[MPa]	Initial stiffness
E_{50}	[MPa]	Secant stiffness from triaxial test
E_{50}^{ref}	[MPa]	Secant stiffness from triaxial test at reference pressure
$E_{50undrained}$	[MPa]	Secant undrained stiffness from triaxial test
E_M	[MPa]	Pressuremeter stiffness modulus
E_{oed}	[MPa]	Tangent stiffness from primary oedometer loading
E_{oed}^{ref}	[MPa]	Tangent stiffness from primary oedometer loading at p^{ref}
E_{ur}	[MPa]	Reference un/reloading stiffness
E_{ur}^{ref}	[MPa]	Reference un/reloading stiffness (at strains $\varepsilon \approx 10^{-3} \div 10^{-2}$)
G_0^{ref}	[MPa]	Reference shear stiffness at small strains ($\varepsilon < 10^{-6}$)
G_{50}^{ref}	[MPa]	Secant shear modulus
G_{ur}	[-]	Unloading/reloading shear modulus

Units		
G_{ur}/s_u^A	[-]	Ratio unloading/reloading shear modulus over active shear strength
G/S_u	[-]	G over S_u ratio
K_0	[-]	Lateral earth pressure at rest
K_0^{nc}	[-]	K_0 value for normal consolidation
$L.L.$	[-]	Liquid Limit in Atterberg limits test
m	[-]	Power for stress-level dependency of stiffness
m	[-]	Power to which OCR is raised in formula for the undrained shear strength in SHANSEP MC model
n	[-]	Number of degrees of freedom of system
N	[-]	The ensemble size in Ensemble Kalman Filter
μ	[m]	Mean of the estimates in the inverse analysis
ν	[-]	Poisson's ratio
ν'	[-]	Effective Poisson's ratio
ν_{ur}	[-]	Poisson's ratio for unloading/reloading
$\rho = \rho_{xy}$	[-]	Pearson's correlation coefficient
OCR_{min}	[-]	Minimum OCR
p'	[kPa]	Mean effective stress
p_c	[kPa]	Pre-consolidation pressure
$P.I.$	[-]	Plasticity Index
$P.L.$	[-]	Plastic Limit in Atterberg limits test
p_L	[MPa]	Plastic limit in Pressuremeter test
p^{ref}	[-]	Reference pressure for stiffness (100 kPa)
R_f	[-]	q_f/q_a failure ratio as in Duncan-Chang model R_f
s_u	[kPa]	Undrained shear strength
$s_{u,inc}^A$	[kN/m ² /m]	Increase of shear strength with depth
$s_{u,min}$	[kPa]	minimum value of the undrained shear strength taken in the calculations in order to avoid almost-zero shear strengths at low values of vertical stress
$s_{u,ref}^A$	[kPa]	Reference (plane strain) active shear strength
s_u^{DSS}/s_u^A	[%]	Ratio of direct simple shear strength over active shear strength
s_u^P/s_u^A	[-]	Ratio of passive shear strength over active shear strength
$s_u^{C,TX}/s_u^A$	[-]	Ratio triaxial compressive strength over active shear strength
$WC = w$	[%]	Water Content
x, x_1, x_2	[m]	Variables in inverse analysis set up
X_γ	[MPa]	Variable equal to $\gamma_{0.7}$ in the inverse analysis
X_E	[MPa]	Variable equal to E_{50}^{ref} in the inverse analysis
y	[m]	Displacements (measurements) in the inverse analysis
y_{ref}	[m]	Reference depth
z	[m]	Displacements (observations) in the inverse analysis

List of Abbreviations

Abbreviations	
1D	One-dimensional consolidation (Oedometer)
2D	Two-dimensional
3D	Three-dimensional
ADP	Acronym for undrained analysis based on active (A), direct simple shear (D) and passive (P) types of loading
CH	High-plasticity clay
CL	Low-plasticity Clay
CPT	Cone Penetration Test
CU	Consolidated Undrained triaxial test
DF	Discrete Fréchet distance
DH	The Hausdorff distance
DPSH	Dynamic Probing Super Heavy
DS	Direct Shear Test
DTW	Dynamic Time Warping
EC7	Eurocode 7
EKF	Extended Kalman Filter
EnKF	Ensemble Kalman Filter
FE	Finite Element
FoS	Factor of Safety
GA	Genetic Algorithms
GHS	Generalized Hardening Soil
HS	Hardening Soil material model
HSS	Hardening Soil with small-strain stiffness material model
IEKF	Iterated Extended Kalman Filter
KF	Kalman Filter
KG	Kalman Gain
LEPP	Linear-Elastic Perfectly-Plastic
MC	Mohr-Coulomb
NGI	Norwegian Geotechnical Institute
NGI-ADP	Norwegian Geotechnical Institute ADP material model
OCR	Over-Consolidation Ratio
OM	Observational Method
PCM	Partial Curve Mapping
PDF	Probability Density Function
POP	Pre-Overburden Pressure
PMT	The Ménard pressuremeter test
RMSE	Root Mean Square Error
SC-CL	Clayey Sand
SP	Poorly-graded Sand
SHANSEP	Stress History and Normalized Soil Engineering Properties
SHANSEP MC	Stress History and Normalized Soil Engineering Properties Mohr-Coulomb
SPT	Standard Penetration Test
UCS	Unconfined Compressive Strength test
UKF	Unscented Kalman Filter
ULS	Ultimate Limit State
UU	Unconsolidated Undrained triaxial test



Introduction

1.1. Motivation and case background

Nowadays, due to congested urban environments, the construction of deep building pits is more and more demanding for engineers. Factors such as ground movements induced by the excavation, heterogeneity of soil conditions and many others need to be taken into account and reliably assessed. To satisfy the requirements of the growing number and importance of involved stakeholders and to avoid risks of growing value such as potential damage to surrounding high-rise buildings, the design procedure requires careful consideration of the strength and stability of the structural elements concerning all of the stages during the construction process [23]. In the geotechnical design of such constructions, usually theoretical and empirical methods and advanced numerical analyses are used, where laboratory tests, field measurements are utilized.

During the excavation process, the induced ground displacements by the construction works of the station should remain within strict limits to avoid damages to the adjacent buildings. In order to limit the displacements, excavation occurs within the protection of diaphragm walls, supported by struts placed at different levels. The project is characterised by a very high cost of risks connected with the uncertainties in soil parameters prediction, soil variability and design solutions that are not fully optimal.

The numerical modelling is an effective way to investigate the soil-structure interaction mechanisms in deep excavations, and it can provide all the required information for design purposes [23]. Since the excavation geometry is not always typical two-dimensional (2D) problem, in most cases, a detailed three-dimensional (3D) model is required to attain a satisfactory numerical model of the performance of deep excavation [38, 56, 100]. Another critical issue in the modelling process, is the material model for the soil, structures, and the soil-structure interface, which allows taking the initial stress state in the ground [75], and small strain non-linearity of soils into account [76, 84]. The numerical modelling, when combined with the installation of a field monitoring system, can allow monitoring the performance of deep excavations during the construction process, and can provide immediate feedback to engineers to ensure the safety of the project [23]. However, the shape functions used in the 3D models to create the triangular finite element cause a need to use very fine mesh refinement hence is very time-consuming. Therefore, in this report, only 2D modelling is used.

The main issue to be addressed is how to deal with the uncertainties and what could be done in order to improve the certainty in foreseeing the deformations. To investigate which model aspects are the most critical, several elements need to be taken into account such as approach, reliability, observational method and accuracy of the model performance. For the assessment on how safe and well cost-optimised the employed construction design is, Observational Method (OM) was applied, so to learn from experiences gained in the less critical sections, and to allow to optimise the pit design at adjacent more critical sections. It requires some confidence in model performance, including the extrapolation from one section to the other.

Another aspect is that the actual soil behaviour is a point of discussion, i.e. whether should it be fully drained, undrained and how to decide on safe, but not over-conservative, upper and lower boundaries in OM approach. A special point of attention is the reliability of the predictions since the vertical displacements of the

surrounding terrain appeared to be much larger than adopted in the building damage predictions.

1.2. Research objectives

1.2.1. Analysis of the geomechanical factors related to heave phenomenon

Considering that the heave appears to be much larger than in the Finite-Element (FE) computations, the research on what could be the potential reason for it is performed. The focus is on the clay layer of low and high plasticity, and the main goal is to understand what might be the potential aspects influencing the expansiveness of the sub-soil. An important question is if the swelling behavior can be treated as coupled, and how should it be included in the computations of the geomechanical soil parameters.

1.2.2. Validation of the material models

The focus of this part is to investigate the advantages, disadvantages, capabilities and limitations of different material models and find answers to the following questions:

- To what extent is it possible to reproduce the stress-strain relationship obtained in the laboratory tests with the usage of the aforementioned constitutive soil models;
- Which of the material models' configurations of different plastic yield functions and capabilities to model the undrained behavior and stress dependency of stiffness gives the results closest to the reality.
- What is the best constitutive model to represent the soil behaviour for the local soils in this specific, deep excavation application.

1.2.3. Reliability updating of consecutive construction phases

The main question raised is how an available field monitoring data from the site can help to predict soil parameters better and to optimise a construction design by increase certainty in optimise a construction design related to the further construction phases by increasing confidence in switching between different scenarios of consecutive construction phases in the Observational Method. The usage of reliability updating and data assimilation is based on studies of different inverse analysis approaches and finding addressing the following side-questions related to the chosen optimisation method:

- How the algorithm seeks for the solution and how to judge if the final estimate is a desired one?
- How to create a random parameters space and what limitations should be considered?
- How the formulation of the chosen material model influences the efficiency of the algorithm?
- What is the time-expensiveness of the inverse analysis process?
- How reliable are the results obtained via the inverse analysis?

1.3. Methodology and the thesis layout

This report endeavours to give an answer on how to reduce the uncertainty in the deep excavation design by the means of an inverse analysis. It shows the steps performed in creating a tool for the optimization of the deep excavation design using the Ensemble Kalman Filter optimisation algorithm including the activities required beforehand, i.e. analysis of a site investigation data, setting the finite-element model and calibration of parameters of the chosen material model.

The simplified workflow of the thesis is shown in Figure 1.1.

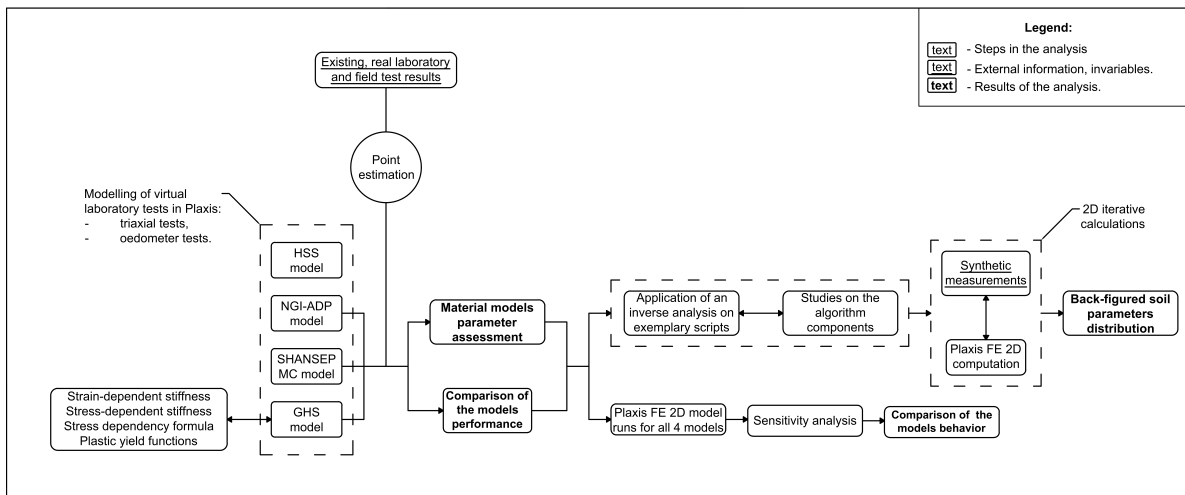


Figure 1.1: Workflow of the problem modelling.

Specifically, the present thesis consists of seven chapters organized as follows:

1. The *Introduction*, provides general background information of the project, highlights the key objective of this report and shows how these are addressed in the latter sections.
2. The *Problem statement and the literature review*, provides a current state-of-the-art review on deep excavation design. The focus of this chapter is to summarize the actual knowledge on the reasons for the ground heave including the nature of expansive soils, the constitutive models commonly used in this kind of constructions and available methods of inverse analysis regarding geotechnical applications.
3. The *Investigation of material models and calibration of soil parameters* delivers the point-estimation for each significant soil quantity based on the existing soil investigation data. Then, using the Plaxis Soil-Test facility it describes the responses of different material models, investigates capabilities and limitations which together with a sensitivity analysis of a customizable parameters give insight on which one is most suitable for the analyzed soil domain. Furthermore, it provides the initial parameters distribution for the inverse analysis.
4. The *Target measurements in the 2D finite-element model*, this chapter utilizes the knowledge gained in the previous chapter, i.e. the chosen material models are being used in the full two-dimensional (2D) finite-element model of the deep excavation. Additional assessment on the performance of different material models and different drainage settings is given and assumptions on the material model to be used in the inverse analysis part are made.
5. The *Set-up of the inverse analysis method*, compares and explains the extensions of the chosen inverse analysis method. The developed EnKF script is tested on a simple, stiffness-related application to draw conclusions and show the performance of this optimisation algorithm.
6. The *Application of the inverse analysis in the FEM*, incorporates the Plaxis 2D remote scripting tool to connect the FE software with the optimization to run an iterative optimisation process. The results of the 2D FEM computations of the given parameters distribution are compared with the site measurement results and are used in the machine learning iterative algorithm to back-figure the soil parameters distribution with a experimentally proven certainty. The conclusions based on the loop of calibration of the model according to synthetic monitoring measurements are drawn.
7. The *Conclusions and recommendations*, summarizes the research undertaken through this report highlighting the most important results and conclusions. Moreover, some suggestions considering for future studies of this thesis' topic are provided.

2

Problem definition and the literature review

In this project, the initially applied approach depended on the prediction of effective stress state after the critical excavation depth was reached. From thereon, an undrained behaviour was simulated using the Hardening Soil Small-strain (HSS) model with quantities obtained from the advanced laboratory, i.e. effective stress path tests. To better understand the realistic effective stress state, it was decided to investigate the characteristic of different material models and find out their capabilities and limitations. Also, possible causes for the heave phenomenon are investigated, and analysis on how the numerical computations do treat swelling of cohesive layers is performed. Last, but not least, having the measurement system installed as apart of OM, the inverse analysis procedure can be incorporated in this project as a tool to increase the certainty in the decision-making process. Literature concerning the inverse analysis methods and their applications in geotechnical-related problems is studied, and the choice of the approach is made.

2.1. Physical phenomenon of heave

The ground heave phenomenon can be caused by several reasons. The swelling processes were sub-divided into (i) mechanical and (ii) physicochemical [9]. The mechanical swelling takes place in response to elastic and time-dependent stress unloading, i.e. overburden recovery, for example, erosion, tectonic uplift or excavation procedure. Whereas, the physicochemical swelling can be divided into crystalline swelling driven by the hydration energy, and osmotic swelling connected with the electrical double layer effects [42]. It can also be divided into short- and long-term swelling of the sub-soils (especially crucial for a highly expansive soil), changes in the water table level and freezing of the soil. In this case, for physical modelling of the ground heave, two main heave reasons should be thoroughly analyzed, i.e. due to the swelling potential, and the reduction of the pre-overburden pressure.

There are several factors that influence the swelling potential, such as:

- climate - the depth and degree of desiccation affects the amount of swell;
- soil profile - the thickness affects the magnitude of total heave;
- groundwater - even an expansive soil may never swell if its moisture content stays constant at all times [90];
- drainage - drainage around the structure reduces the swelling problem [19].

Tel Aviv is located in semi-arid/Mediterranean climate zone [46], where potentially expansive soils are widely spotted due to evapotranspiration rate exceeding the precipitation. Formation of montmorillonite, which in Israel's clay soil areas is present in quantities ranging from 40 to 80 per cent, is aided by an alkaline environment, presence of magnesium ions and lack of leaching, i.e. conditions favourable in semi-arid regions [19]. The clay layer is considerably thick and ranges from 15 to 20 meters; the whole layer is around 10 meters below the groundwater level, so many moisture content changes are unlikely to happen. Even though the

dewatering is planned, the clay domain will remain fully saturated. Hence the heave origin is related only to the overburden recovery.

The depth below the ground surface of the bottom of the excavation in this project is 30.0 meters. As the excavation proceeds, the sub-soil is subjected to unloading, and thus reduction of total stress. Initially, it causes a decrease of the pore water pressure and evolution of the negative excess pore pressure, however, later it causes a regular intake of water till pore pressure reaches the equilibrium (static pressure) during which, heave will steadily develop. To estimate the magnitude of the potential heave associated with changes in effective stress, the reversed oedometer test-based methods can be used [42]. Most of the oedometer test-based methods point swelling pressure as initial and overburden pressure as final stress condition. In contrast to these methods, the suction-based methods can be used to predict the ground heave of expansive unsaturated soils during the wetting process, where the final condition can be quantified by the suction value corresponding to specific void ratio [42].

For this case, where soil remains fully saturated during the whole excavation process, the potential heave of expansive soil can be described by several methods. The most popular ones, which follow the oedometer test-based heave prediction methods are:

- Fredlund (1983) method,
in which the heave of the soil layer ΔH is given by:

$$\Delta H = C_s \frac{H}{1 + e_0} \log \left(\frac{P_f}{P'_s} \right) \quad (2.1)$$

where: H is the thickness of soil layer, C_s is the swelling index, e_0 is the initial void ratio, P'_s is the corrected swelling pressure, P_f is the final stress state and is equal to $P_f = \sigma_y + \Delta\sigma_y - u_{wf}$.

- Hamber Nelson (1984) method,
in which the heave of the soil layer ΔH is given by:

$$\Delta H = C_s \frac{H_i}{1 + e_0} \log \frac{K P_f}{10 \left(\frac{C_w}{C_s} \Delta w \right)} \quad (2.2)$$

where: H_i is the thickness of the i^{th} layer, i is the number of the soil layers, C_s is the swelling index, C_w is the suction modulus ratio, K is the correction parameter, Δw is the water content change and P_f is the final stress state.

For the Fredlund method, the elastic modulus needs to be evaluated, where instead of *in situ* suction, the matric suction equivalent is used. Hence, instead of the swelling index with respect to matric suction, C_{ms} , the measured swelling index on the net normal plane C_{ts} is calculated [21]. In this method, the maximum potential heave is calculated by dividing the soil domain into many sub-layers, after that the maximum heave for each layer ΔH_i is calculated by multiplying the vertical strain of a soil layer ϵ_y by the layer thickness h_i . The heave of each sub-layer is then summed. The calculation of the total heave using the Nelson method is analogous, however it uses the C_w and C_s parameters to calculate the heave of each layer.

The governing equations of both methods can be solved using the FE analysis [1, 64]. The biggest disadvantage of the Fredlund (1983) method is that it is time-consuming. In contrast, the biggest pitfall of the Hamber Nelson (1984) method is that it does not take into account the effect of overburden pressure and hence may overestimate the heave. However, it is relatively faster. No information about the usage of any of both method in numerical modelling is available in the existing literature.

2.2. Numerical modelling of a deep excavation case

2.2.1. Assumptions of plain-strain models

Excavations are generally analysed as plain-strain problems, because usually, a soil responds more closely to the plane strain conditions than the triaxial conditions in such cases [66]. The assumptions of plain-strain models are:

- The calculated are the major and minor in-plane principal stresses (σ_1 and σ_3) and the out-of-plane principal stress (σ_z). Also, in-plane displacements and strains are calculated.
- The out-of-plane strain is zero by definition ($\varepsilon_z = 0$) and the length of the excavation (along the out-of-plane longitudinal axis) needs to be much larger (infinity length) than the width of the excavation [39].

However, the out-of-plane dimensions of deep excavations rarely happen to be many times larger than the cross-sectional dimensions. Therefore, neglecting the stress flow around the corners of the building pit leads to incorrect calculation (overestimation) of the stress changes for plain-strain conditions. The stress changes are greater for the case where the out-of-plane dimension approaches the in-plane dimensions. Therefore, the usage plain-strain models for deep excavations is not always the most accurate way of modelling such problems and creating a 3D finite-element models may help to avoid the over-conservative design.

2.2.2. Three-dimensional factor

Since the construction considered is not two-dimensional, the question is whether the result from the 2D FE analysis is the same as from the 3D one. The critical question is if the factor, which incorporates the 3D effects by adjusting the 2D results, so they fit the 3D results, is needed in that kind of analysis or not.

One of the most prevalent factors for describing the phenomenon of the 3D effects is Plane Strain Ratio (PSR) introduced by Ou et al. [17] and is calculated as in Formula 2.3 below.

$$PSR = \frac{\delta_{hm,d}}{\delta_{hm,ps}} \quad (2.3)$$

where $\delta_{hm,d}$ is the maximum wall deflection at a specific section along the wall, and $\delta_{hm,ps}$ is the maximum wall deflection of the section under plane strain conditions.

Another way, which can be used to assess how to factor in for the three-dimensional effects, would be to compare the maximum settlements in the specific points under the building in 3D and 2D model in the 3D model to these settlements calculated under plane strain condition.

To answer the question of how the 2D and 3D results are bounded with each other, several finite element analyses are available in the literature [16, 17, 20, 31, 57]. From these studies, the following conclusions have been drawn [29]:

- Smaller movements develop at the corners of the excavation box. Moreover, the centre of the excavation wall deflections tends to differ between 2D and 3D approaches.
- 2D calculations of movements near the centre of the excavation wall generally over-predict the measured displacements.
- For smaller ratios of the length of the wall to the height of excavation (L/H_e), the 2D analysis overestimated the amount of movement which would occur near the centre of the excavation wall, while the results of the 3D analysis better agreed with the measured movements.
- For rigid walls and lower factors of safety against basal heave and L/H_e larger than 6, plane strain and 3D analyses are characterized by same maximum movements in the centre of the excavation.
- Also, smaller values of L/B yield lower values of PSR than higher ones.
- Stiff wall systems produce lower PSR than flexible wall systems.
- Excavations with lower FoS against basal heave produce lower PSR.

The PSR factor shows different results for different depths. It tends to increase with a distance from the corner of the excavation and then reaches a constant number at large values of that distance. The influence of the distance from the corner d_{corner} to the analyzed profile disappears for values of 30 meters and more from the corner. When this phenomenon, so-called the corner effect, does not apply, the maximum wall displacement at a certain d_{corner} is not significantly smaller than the maximum displacement under plane

strain conditions, what suggests the decreasing influence of the 3D effect on the wall displacement [45].

In Figure 2.1, one can see an alternative to transferring wall displacements accounting for 3D effects of excavation on wall deformation in terms of width-to-length (B/L) ratio of the excavation box. The chart compares the PSR values between two studies: in the sand by Hsiung et al. (2016) [45] and in clay by Ou et al. [17].

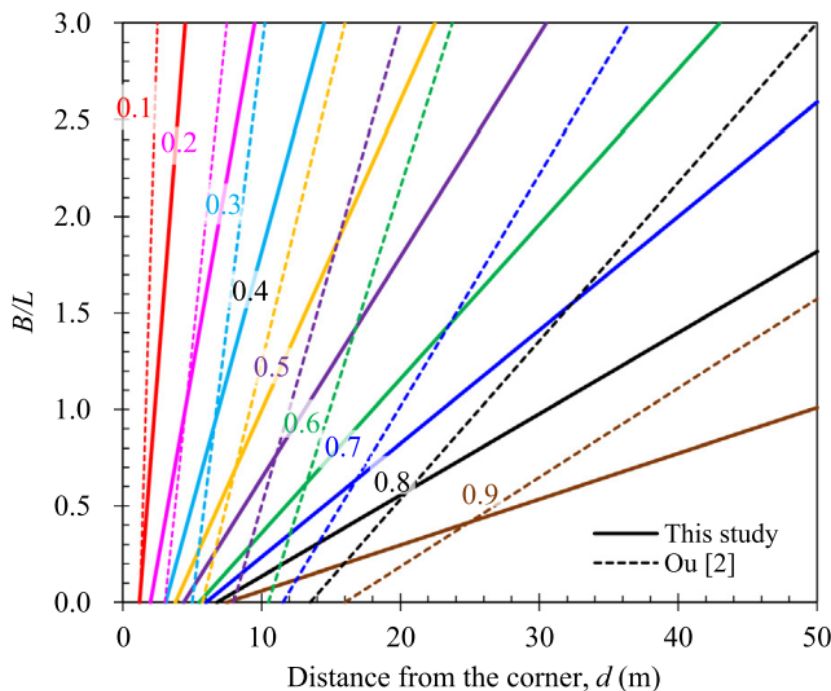


Figure 2.1: PSR chart - comparison of PSR values in clay and in sand according to Hsiung et al. (2016) [45] (denoted as *This study*) and Ou et al. [17] (denoted as *Ou [2]*).

According to Figure 2.1, for $B/L = 27.48/96.73 = 0.284$ and d of around 37.0m, RPS value is between 0.90 and 1.0. The value can be taken as more conservative, i.e. 1.0, which would mean that the real displacements are equal to the ones obtained in the two-dimensional analysis.

Since the measurements used in the inverse analysis shown in this report are synthetic, the derivation of genuine 3D factor is not of utmost importance. Nevertheless, when the real displacements taken from the site measurement system are used, the 3D factor needs to be empirically derived. This should be done by performing several simulations, in which the criterion for the comparison would be the settlements of the building settlements and the d-wall deflections. Also, more than one construction phase should be considered. The proposed phases would be 12, 14 and 15 since these are the faces with the lowest factor of safety.

2.3. Constitutive models in the deep excavation applications

The usual procedure in geotechnical design (forward-design approach) is to draw a geological works plan, where the number and type of soundings and tests are driven by a will to minimize the geotechnical-related risks, then collect the data and use it in finite-element modelling with an appropriate safety margin.

Geotechnical investigation program of good quality is essential to the successful accomplishment in every construction project. It is of utmost importance in constructions of deep building pits due to the high costs of construction, and big soil masses involved resulting in a high horizontal and vertical variability of strength parameters and costly consequences of unforeseen geotechnical risks or over-conservative design parameters adopted. A properly planned and performed site investigation program can successfully narrow down the estimated soil parameters distributions, hence increase the certainty in predicting the wall deformations and surface settlement.

The derived soil parameters are used in numerical modelling by means of material models. The simplest

material model that is being used in engineering practice is the Mohr-Coulomb (MC) model. The MC model depicts soil behaviour as two bi-linear lines, one showing elastic response and the second showing perfectly plastic response. Since the soil does not behave linearly in reality, and soil stiffness is stress-dependent, using the MC model can over-predict the soil displacement at the low-stress levels, and under-predict at the high-stress levels. It is especially important, since, in deep excavations, the soil behaviour is usually within a relatively small deformation region [86], so the pre-failure performance is more important than failure conditions [23]. Another reason for using other, hyperbolic models, is because of more accurate unloading-reloading soil response representation.

2.3.1. Hardening Soil Small-strain

The HSS model is often used in deep excavation practice and is referred to as the best standard model in the Plaxis software for this application [12]. The main advantages of the HSS model are that it is suitable for the analysis of both static and dynamic tasks, and is more suitable for deep excavation applications when compared to the HS model. It also allows making more accurate computations because of adding the strain dependency to the stress-strain relation for stress paths penetrating the elastic domain [12].

Based on the deep excavation of the metro station Case A in Kaohsiung city, Taiwan, it is reported that the HSS model gave results more accurately than the HS model, which was more accurate than the MC model [44]. Two cases, Rochor Complex Project in Singapore and Formosa Project in Taipei, have also proven that the HSS model predicts the settlement surface better than the MC model while keeping wall deflection prediction at the same level of accuracy [95].

However, it has also been reported, that the usage of the HSS model in the design of A19 metro station in Warsaw, Poland, has underestimated the bottom's uplift by 51% and the wall displacement by 26% in the final excavation stage [62]. The other models used in the FE simulations of this deep excavation, i.e. Mohr-Coulomb, Hardening Soil and Hypoplastic Clay, have resulted in values differing up to 19 – 25% from the observed displacements. Also, the analysis of a deep excavation in soft clay constructed as a part of Västlänken tunnel project in Gothenburg, Sweden, has shown that for the undrained analysis the HS model gave more accurate settlements prediction than the HSS model [21].

Summing up, the HSS model has reportedly being used in the deep excavation applications. Although modelling of the undrained conditions requires considerable caution, it is one of the most widely used models with good results in the displacement predictions. It is relatively simple to be calibrated with the most-important parameters being derived by means of triaxial tests.

2.3.2. NGI-ADP

NGI-ADP is elastoplastic constitutive soil model, which is based on the undrained shear strength approach and total stress analysis. The (undrained) shear strength parameters are directly inputted for three different stress paths/states: active (A), direct simple shear (D) and passive (P). The NGI-ADP model is formulated for a general stress state, matching both undrained failure shear strengths and strains to that of selected design profiles. Besides, the model provides output on two state variables: plastic shear strain γ_p and the hardening function r_κ . The insight into the soil behaviour given by those parameters helps to understand the reasons for diaphragm wall displacements, which helps in a proper configuration of inverse analysis.

Many geotechnical problems concern undrained behaviour of clay and the capacity in undrained loading, and the NGI-ADP model with its clear input parameters has a significant advantage for design analysis of undrained problems. The undrained shear strength is directly determined and does not require information on parameters such as over-consolidation ratio or earth pressure coefficient at rest. It is reasonably easier to calibrate it to the design profile of undrained shear strength when compared to the other methods that often require trial-and-error testing to match the prediction of the anisotropic shear strength to the profile obtained in laboratory tests [40].

The usage of NGI-ADP model was suggested in the stability verification against the basal heave failure mechanism at excavations in soft soils by [67] as a tool to analyze drained and undrained soil behaviour. The parameter optimization for the model of two laboratory soil data of Bangkok clay, AIT and Chula sites, has proven that a proper set of material model parameters allows reproducing the laboratory tests soil behaviour

with very high accuracy [92].

2.3.3. SHANSEP MC

The SHANSEP MC model (Stress History and Normalized Soil Engineering Properties) is a total stress model, which combines the Mohr-Coulomb model with the SHANSEP concept, and is intended for undrained soil loading conditions [72]. The additional extension allows simulating potential changes of the undrained shear strength depending on the effective stress state of the soil. It consists of two sets of parameters: one set of MC parameters and one set of SHANSEP parameters. Initially, the model behaves as the MC model until it is (manually) switched to the SHANSEP concept [72]. Then, the model works practically as a Tresca model, where the undrained shear strength, defined by the SHANSEP formula [13].

In this model, Over-Consolidation Ratio (OCR) and the undrained shear strength are computed based on the effective major principal stress σ'_1 . Soil stiffness is associated with the undrained shear strength S_u , by the introduced constant ratio of the shear modulus G_0 over S_u , which can allow modelling the increase of stiffness with depth [72]. One of the SHANSEP model's advantages is that it gives a more realistic, empirical way of modelling of the undrained shear strength. The model also provides output on two state variables: $\sigma'_{1,max}$ and S_u , what helps to understand the evolution of the shear strength as a function of depth (effective stress).

The SHANSEP concept has also been applied to a different material model, namely SHANSEP NGI-ADP. When applied to the NGI-ADP model, the model uses the undrained shear strength, defined by the SHANSEP formula, as the input for the undrained shear strength in triaxial compression. This constitutive soil model has been widely applied to dykes problems. So far, the SHANSEP formula has not been applied to other constitutive models. There are limitations for (hardening) models based on the effective stress principle, since SHANSEP is based on undrained shear strength. The usage of SHANSEP procedure was suggested by Ladd (1974) [53], however there are no reports on usage of the SHANSEP MC model in the deep excavation application available in the literature.

2.3.4. Generalized Hardening Soil

The Generalized Hardening Soil model is a more modular, user-defined soil model based on the original Hardening Soil model with small-strain stiffness. It possesses almost the same parameters as the HSS model. The significant advantage of this model is that it allows to use different configurations for the stress and strain dependency and to choose the appropriate yielding functions.

The workflow of the GHS model is summed up in Figure 2.2 below:

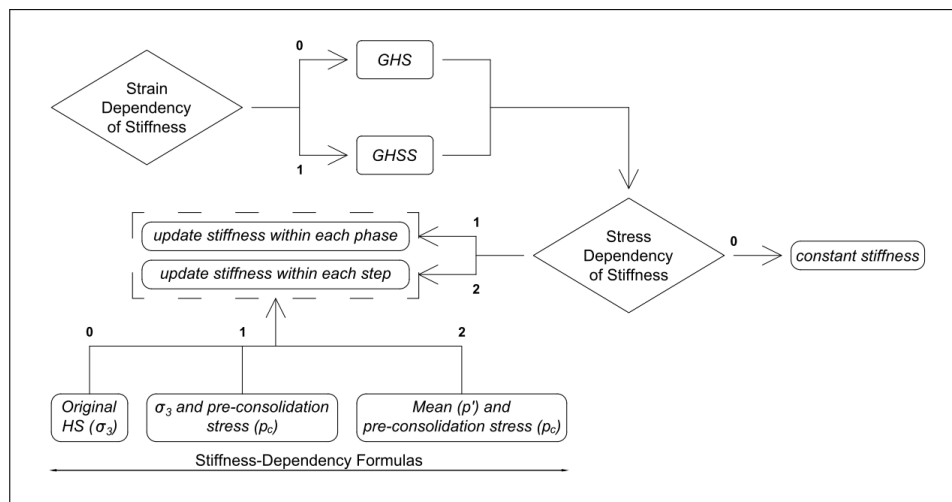


Figure 2.2: The workflow of the GHS model.

The stress-dependency of stiffness and stress-dependency formulas are as given in Table 2.1 below:

		S-D formula		
	S-D of stiffness	0	1	2
		S-D based on the original formula of the HS model	S-D based on σ_3 and pre-consolidation stress	S-D based on mean effective stress and pre-consolidation stress
	0	Constant E_{ur} equal to the input value	E_{ur}	E_{ur}
	1	Stiffness is updated within each calculation phase	$E_{ur} = E_{ur}^{ref} \left(\frac{\sigma_3 + c \cdot \cot \phi}{\sigma^{ref} + c \cot \phi} \right)^m$	$E_{ur} = E_{ur}^{ref} \left(\frac{0.5 \cdot (\sigma_3 + p_c)}{p^{ref}} \right)^m$
	2	Stiffness is updated within each calculation step	$E_{ur} = E_{ur}^{ref} \left(\frac{\sigma_3 + c \cdot \cot \phi}{\sigma^{ref} + c \cot \phi} \right)^m$	$E_{ur} = E_{ur}^{ref} \left(\frac{0.5 \cdot (p' + p_c)}{p^{ref}} \right)^m$

S-D is a shortcut for Stress-Dependency

Table 2.1: Switches of the GHS material model with respect to the stress-dependency of stiffness and the stress-dependency formulas

Regarding the plasticity model settings, the following options for the switch can be applied:

1. Mohr-Coulomb failure criterion;
2. Mohr-Coulomb failure criterion + shear hardening;
3. Mohr-Coulomb failure criterion + cap hardening;
4. Mohr-Coulomb failure criterion + cap hardening + shear hardening.

The GHS configurations names are created concerning these switches, for example, GHS2130 is where the stress-dependency of stiffness is set as 2, the plasticity model is set as 3, the strain-dependency of stiffness set as 1 and the stress-dependency formula are set as 0.

The GHS model has been used in the study of seismic response of a masonry structure to induced seismicity in Groningen, the Netherlands [68].

2.4. Inverse finite-element modelling

The numerical simulations, which are used in the deep excavation applications, can be combined with the measurement data, which might be a valuable source for the calibration and verification of the numerical analysis. This creates a link between the numerical analysis and the OM, where experience gained during calibration exercises, i.e. comparing results of the computational analysis and field measurements, can be used to suggest appropriate numerical procedures to adopt [24]. The estimation of the model parameters based on field measurements is often referred to as inverse problem or back-analysis [2].

2.4.1. Observational Method

To fill the gap between the predicted and the real observed behaviour, Terzaghi and Peck (1948) [89] proposed an observational procedure, which is an integrated design construction method for the earth structures [2]. The proposed method is focused on monitoring of the performance of the structures, with particular attention given to displacement measured during the construction process. Thanks to this procedure, the original design can be verified, and if necessary, modified towards the more certain parameters. Formally, the Observational Method has been introduced by Peck (1969 [69]). The usage of OM has already been reported in many geotechnical projects all around the world [2, 18, 30, 33, 36, 70, 77–79, 85, 97, 98]. The example of a calibration loop, which is the essence of a feedback loop-oriented design, is shown below:

- Selection of field observations;
- Comparison of model data with the monitoring data;
- Updating the design prediction by iteratively changing model input values until they match the observed values.

The optimized input parameters can be used in further design of the succeeding construction phases.

2.4.2. Inverse analysis procedure

In the design of the deep excavation, evaluating geomechanical parameters is of greatest importance due to the strong influence of these parameters on the design and applied construction methods. Usually, the parameters are evaluated using field and laboratory tests, and then, used in the conventional forward approach as an input in the numerical models to anticipate stress-strain behaviour of the soil domain. To tackle uncertainties related to the complexity and variability of geological conditions, the procedure of using the field monitoring to obtain input material parameters, called inverse analysis (back analysis) approach, can be used. [63].

In the inverse analysis, field measurements are used together with appropriate material models to calibrate the input parameters. Since the existing commercial modelling software is not suited (yet) for computing geomechanical parameters back from measurements data, an iterative procedure has to be adopted to obtain acceptable coincidence between measurements and computed output [63]. Basing on the field measurements data of how the diaphragm walls behaved during the sequential excavation, the model can be calibrated.

Primarily, the mathematical procedure of optimization consists of two parts: an objective function, consisting of a numerical model and an error function, formulated to measure the difference between computed values and experimental results and the optimization strategy that is used to search for the minimum of this objective function. The difference between the computed result and the observed value is measured by an objective function (error function), and an optimization algorithm is used to reduce that difference [59]. Minimization of the objective function is obtained by the optimization of the input parameters of the numerical model, and the procedure is repeated until the model is optimized [14].

2.4.3. Inverse analysis optimization algorithms

In general, two types of optimization methods could be distinguished: deterministic and probabilistic one [61]. To the deterministic approaches, we can include gradient-based algorithms and the Nelder-Mead simplex algorithm. Whereas, the probabilistic methods are, for example, Genetic Algorithms (GA), particle swarm optimization, simulated annealing, differential evolution algorithm and others [99]. The primary point of attention here is given to what the end product is. The first group of the algorithms may be faster, but end up on single value, whereas the second group results are provided as a distribution of the variable, what is more esteemed. The other division of mainly used optimization algorithms would be: classical optimization theory iterative algorithms and optimization methods from the evolutionary computation field [63].

The main differences between the classical optimization methods are related with the use or not of the first, $g(x)$, and second, $H(x)$, derivatives of the objective function, $f(x)$. Therefore, these methods can be divided into three main groups [96], [59]:

- Zero-order methods (direct methods): require the evaluation of $f(x)$ only. These are, for example, the Gauss, the Simplex method and the Rosenbrock algorithm.
- First-order methods (gradient methods): require the evaluation of $f(x)$ and $g(x)$, for example, the conjugate gradient method and the steepest descent. If $g(x)$ can not be obtained explicitly (in case of using numerical models), its computation is a complex problem but can be approximated by finite-differences or using method such as direct differentiation or the adjoint state method.
- Second-order methods: use information about $g(x)$ and $H(x)$ in the optimization process. If both can be evaluated directly, Newton's method is usually applied (due to its efficiency). If not, quasi-Newton methodologies can be used to apply indirect approximations to $g(x)$ and $H(x)$.

The evolutionary computation algorithms belong to stochastic search techniques and are characterized by searching for the solution in the entire parameter space [63]. There are several evolutionary algorithms, such as [22]:

- Genetic Algorithms: computational models are working on a population of potential solutions, or individuals, where individuals compete with each other for survival. When evaluated, best individuals have a higher probability of being selected as parents and create new individuals of offspring, which inherit some of the parents' characteristics. The generated offspring compete with themselves or with

themselves and parents (depending on the variation of the algorithm). Also, the mutation is applied so that the innovative features could appear. The genetic search process leads a better fit of the evolved population [63].

- Evolution Strategies: search procedures that are also based on natural evolution mechanisms, and are similar to GA. For instance, they only require data based on the objective function and constraints, and not derivatives or other auxiliary knowledge [60].
- Evolutionary Programming - independent paradigm created by Lawrence Fogel in 1960, which has become very similar to the ES and nowadays they are difficult to distinguish [63].

The optimization methods, which are frequently used in geotechnical engineering are [55], [87]:

- Maximum likelihood estimation - a probabilistic formulation that can be applied when the probability density function of the measurements error is known. The basis of this method is maximizing the likelihood of the measurements appearing.
- Bayesian approach - The parameters, p , are considered random variables and the estimation is performed by maximizing the probability density function of p given a set of measured values x . This is also called the maximum *a posteriori* approach because it estimates the parameters that are the most probable from the existing data.
- Kalman Filter (KF) approach - Filters are data processing schemes that separate desired signals from unwanted noise [28]. A general state equation relating measurements, parameters and noise (characterized in statistical terms) is adopted and optimal estimation of the parameters is proposed in a recursive form.
- Particle Filter (PF) method - Particle filters work with any arbitrary, non-analytic probability distribution. PF consist of a set of generic type Monte Carlo sampling algorithms to solve the state filtering problem [6, 37].
- The Markov Chain Monte Carlo method (MCMC) - a stochastic analysis method that aims to optimize a function by relying on a random sampling of input parameters. The MCMC utilizes a huge number of realizations that generate draws of parameter values out of a prior probability distribution, producing different input combinations [34].

2.4.4. Chosen optimisation method

The analyzed problem can be described as non-linear with the distribution of the parameters assumed to be Gaussian. The observations from the field are usually given for each construction phase and are given with an added sensor error, depending on the applied measuring method.

The sought solution, in the best scenario, would be a distribution of the soil parameters instead of a single, deterministic value. The method, which provides a distribution as a solution is the PF method, which might also be used in method merging [58]. However, despite PF being parallelizable, it still requires many particles, hence is computationally expensive. In PF as the algorithm runs, any particle that does not match the measurements will acquire a deficient weight. This can lead to creating a lot of particles, where only a few contribute meaningfully to the state estimate. It is so-called the filter degeneration. The solution to this problem is particle resampling. However, due to the complexity of the numerical model being used in the algorithm, this could lead to many problems, especially related to the soil parameters correlations.

For unimodal distributions using KF is an option, which works faster and is possibly viable to be applied [7]. The Kalman Filter (KF) itself is most widely used in GPS tracking and general positioning of the moving objects. In a non-linear geotechnical model, a more appropriate are other extensions, which allow modelling a complex soil behaviour more accurately. The Kalman filter requires the user to know the state model. Otherwise, the performance will be poor. Also, if the problem is multimodal, then the Kalman filter cannot represent it.

The versions of KF are as follows: Extended Kalman Filter (EKF), Iterated Extended Kalman Filter (IEKF),

Ensemble Kalman Filter (EnKF) and the recently developed Unscented Kalman Filter (UKF) The pattern for choosing an appropriate sub-method can be described as in Figure 2.3 below:

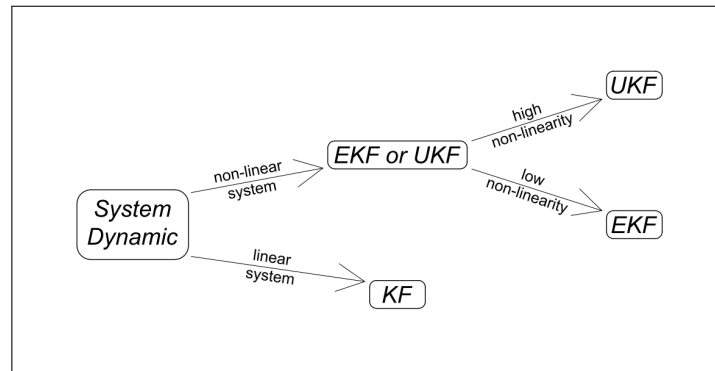


Figure 2.3: The extensions of the Kalman Filter optimization algorithm.

The EKF was used by [65] for identification of the system actual state (of soil parameters during tunnel excavation) using a number of synthetic settlements at observation positions. However, it was reported by the author that the linearization of the system is prone to inaccuracy, especially for highly nonlinear systems. Hence, UKF and EnKF were reported as ones which obviate the need for linearisation by directly applying nonlinear transformations of an ensemble of individual representatives of the state means and covariances [65].

The version, which will be eventually used to model the analyzed problem is the Ensemble Kalman Filter. The EnKF was introduced in 1994 [27] and uses the markovian structure of the state space to estimate sequentially the filtering distribution $p(x_t|y_{1:t})$ particle-based methods so that it can be described as a particle system with mean-field interaction. Comparing the EnKF to the KF, on the downside the fact that the EnKF is a suboptimal filter, so it will not produce the optimal solution that the KF produces can be mentioned. However, for a large number of sigma points, this problem tends to disappear.

3

Investigation of material models and calibration of soil parameters

The first section presents the workflow of this chapter, highlights the soil data used in this project and introduces the methodology used in the calibration of the material model parameters. The second section is focused on showing the results of the laboratory testing program in statistical terms. The next section presents the studies on the initial sets of the parameters based on the point estimations of the soil characteristics. Then, the calibration of the material model parameters based on the advanced laboratory testing program is performed.

The modelling is based on the site investigation data from Tel Aviv, Isreal, and consists of 35 soundings and the laboratory testing program (see Figure 3.1). The field tests consisted of twenty-four rotatory auger drillings with double and triple-core barrel drilling used for sampling, six Dynamic Probing Super Heavy (DPSH) tests, four cross-hole tests and one single cone penetration test (CPT) test. Besides, the monitoring system consisting of extensometers, inclinometers, tilt-meters, prisms and levelling balls was installed at the site. The measurement data comprising of the measured diaphragm walls deflections, adjacent buildings settlements, tilt, and strains were integrated with the construction works design.

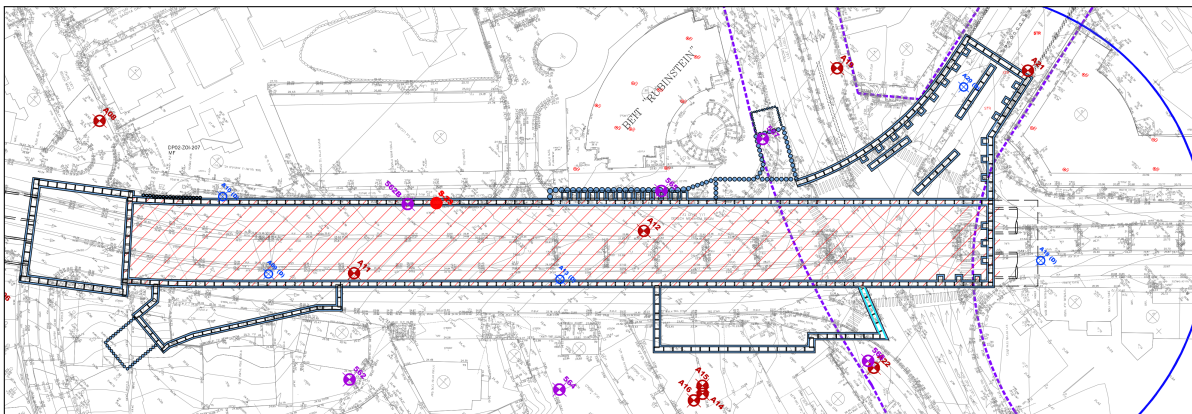


Figure 3.1: Top view of the project location with marked boreholes locations (marked as blue and red circles).

Also, in the boreholes, the following tests have been conducted: 656 Standard Penetration Tests (SPT), 255 Pressuremeter Tests (PMT) and the dissipation tests. The laboratory testing program consisted of: 389 single sieve analyses, 142 Atterberg limits tests, 178 Water Content (WC) tests, 199 Carbonate Content tests, 52 Free Swell tests, 48 organic matter analyses, 5 Unconfined Compressive Strength (UCS) tests performed on undisturbed clay samples, 84 Direct Shear Tests (DS) performed on compacted granular samples, 30 sets of Triaxial Consolidated Undrained (CU), 9 sets of Triaxial Unconsolidated Undrained (UU) tests done on undisturbed clay samples and 30 one-dimensional consolidation (1D) tests performed on undisturbed clay samples.

Based on the information gathered from the aforementioned tests, the local stratigraphy was defined as the following:

- Fill (thickness of around 1.0 m) – composed mostly of asphalt, dark brown silty to clayey sand with crushed limestone and Kurkar gravels.
- SC-CL (thickness of around 2.0 – 7.0 m) – composed of a poorly grade clayey sand to low plasticity clay. In the southern part, the layer contains more sand particles and is characterized by lower to even no plasticity.
- Kurkar (thickness of around 20.0 m) – the upper Kurkar layer is characterized medium to high strength and high gravel and carbonate content. In between the clay layer, another Kurkar layer is found, sometimes even two such layers appear (mostly in the southern part of the station, where the intermediate Kurkar layer is the thickest). Towards the northern part of the station, the intermediate Kurkar layers constrict.
- Clay (thickness of about 15.0 to over 20.0 m) – high plasticity, dark brown to blackish, soft, moderately organic clay layer, characterized by low SPT values, high fines, and water content. In the southern part of the station, the layer is divided into two (or even three) sub-layers.

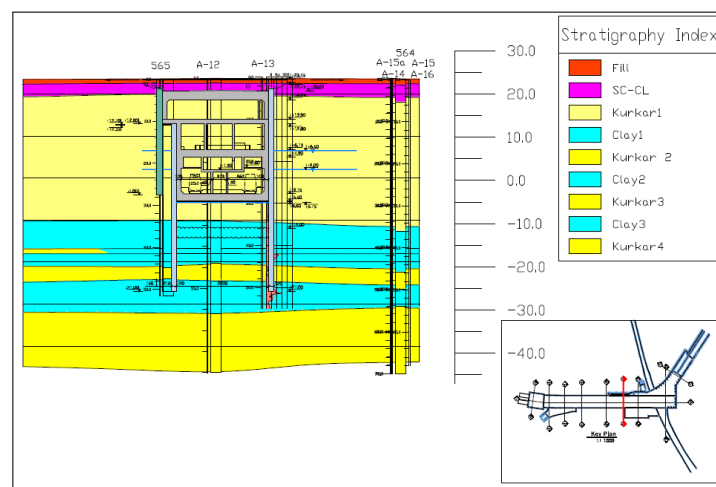


Figure 3.2: Longitudinal cross-section of building pit.

3.1. Introduction

Calibration of the material models was done by simulating the pressuremeter tests, the one-dimensional consolidation tests and the triaxial tests in the Plaxis SoilTest facility. The parameter assessment was based on point estimation of the parameters derived from the laboratory tests. The representative advanced laboratory tests were chosen and used to calibrate the parameters of the constitutive models, i.e. making the computed stress path fit the stress path obtained in the real laboratory tests. The modelling of the stress path is made until failure or a sample, or the strain of around 16% if no failure is reached. This procedure should allow making a comparison of the undrained behaviour, stress dependency of stiffness (through compression and extension tests), and different plastic yield functions between those models. Furthermore, the customizable switches of the GHS model were investigated to check if they can help to increase the accuracy of reproducing the stress paths obtained in the laboratory tests.

Following aspects for each test have been analyzed:

- changes in principal stress difference and the volumetric changes (or pore pressures) with axial strain for the drained (undrained) tests;
- weighting of the observations using coefficients of variation,
- visual examination of the stress-strain plots;
- the model fit statistics.

As a part of calibration, the stress paths obtained in triaxial CU and UU tests were compared with the computed stress paths in SoilTest for the set of parameters obtained in the real laboratory tests. Then, the parameters of the material models were adjusted, so to obtain a good fit between the real and computed stress paths. The difference, between the real and the computed stress paths, was calculated by means of Root Square Mean Error (RMSE), which measures the difference between the real and computed stress at one hundred, dispersed levels of strain symmetrically. The RMSE is calculated for each of the three cell pressures applied, and the comparison is made between the whole sets of tests (all three cell pressures applied treated as one test), with the values averaged for the whole tests. Another comparison is made for the averaged values of RMSE for the lowest, middle and the highest cell pressures. These averages are made for all two (or three) analyzed tests. The exemplary figure, which is used for the comparison of the results, is shown in Figure 3.3 below:

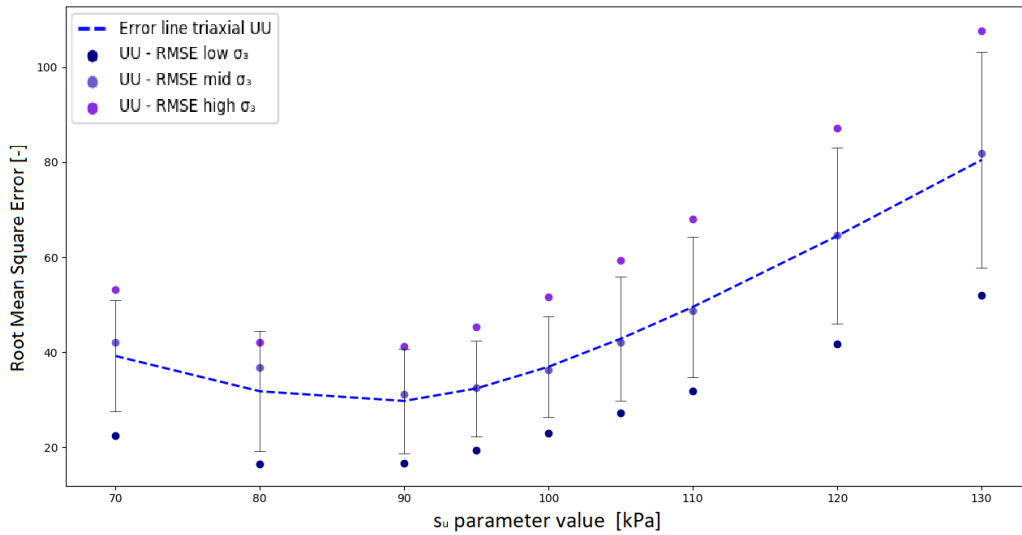


Figure 3.3: The method of calibration of soil parameters (in here, the s_{u1} in the NGI-ADP model based on triaxial UU1 test).

For finding the calibrated material model parameters, two approaches have been adopted, which are shown in Figure 3.4 and explained further.

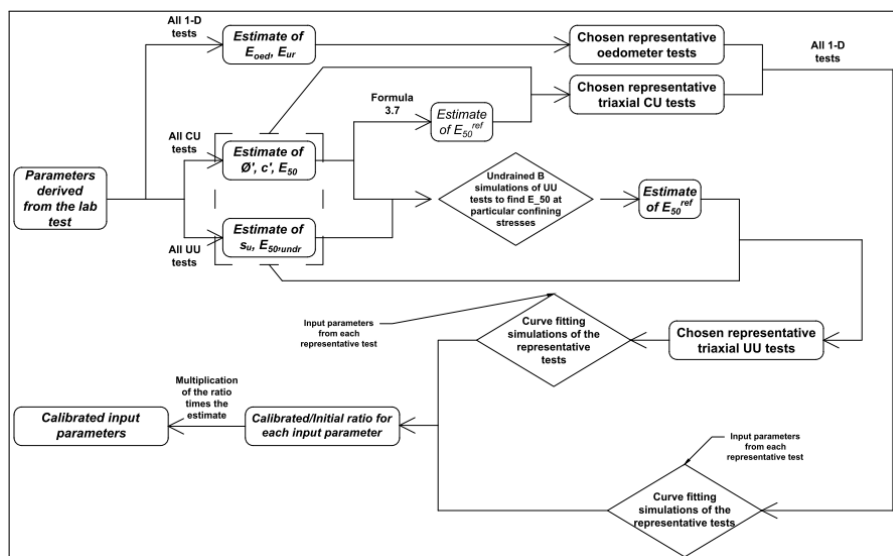


Figure 3.4: Workflow of calibration of the HSS model input parameters.

The first is that for each stress path, the ratio between the best-fit and the initial curves obtained in the lab-

oratory test is calculated. This ratio is then averaged for the whole space of the representative tests. Then, the mean is multiplied by this calculated ratio in order to obtain the initial input values. This method was adopted in the calibration of the HSS model. The workflow is shown in Figure 3.4 below. Since a dispersion between the mean values and the values obtained in each representative test is significant, the graphs show only the intermediate calibration plot, i.e. parameters derived in each test multiplied by the calibration ratio compared to the stress path in this laboratory test.

The second method tries to find one specific value, which fits all of the representative tests best. This method was applied in the calibration of the NGI-ADP (except for the s_u parameter), and SHANSEP MC models since most of the initial parameters are based on the assumptions.

3.2. Sub-soil parameters assessment

In this part, the material models' parameters will be set with respect to the sub-soil parameters obtained in the laboratory and field testing programs. Of the utmost interest are the low- and high- plasticity clay parameters. The parameters, which are given in the further section are based on the accomplished geological works, which have included 24 geological samplings of depth ranging from 24.45 to 70.1 meters, with an average value of 56.7 meters.

As a part of these soundings, 103 SPT tests and 86 pressuremeter tests were performed. Additionally, the laboratory testing program was introduced and it comprised of 107 sieve analyses, 127 Atterberg limits tests, 137 WC tests, 48 FS tests, 73 Dry Unit Weight tests, 4 UCS tests, 3 DS tests, 27 CU tests, 11 UU tests, 4 UC and 30 one-dimensional consolidation tests [50].

3.2.1. Triaxial tests

In total, 27 CU tests, 11 UU and 4 UC tests were performed. In order to find the best-fit test, several parameters shown below were taken into account:

- The reference secant stiffness E_{50}^{ref} for both CU and UU tests;
- The undrained shear strength s_u for UU tests;
- The (effective) internal friction angle ϕ' and the (effective) cohesion c' for CU tests.

Furthermore, the overburden pressure is an essential factor. In the triaxial tests, cell pressure in CU represents the effective overburden pressure multiplied by a lateral earth pressure coefficient at rest, and in UU tests, the horizontal water pressure value is added. For a better understanding of a cell pressure evolution with depth, the effective and total in-situ lateral confining pressure is shown in Figure 3.5. The wished-in place situation would be to choose tests with the cell pressure lying inside of the bounds.

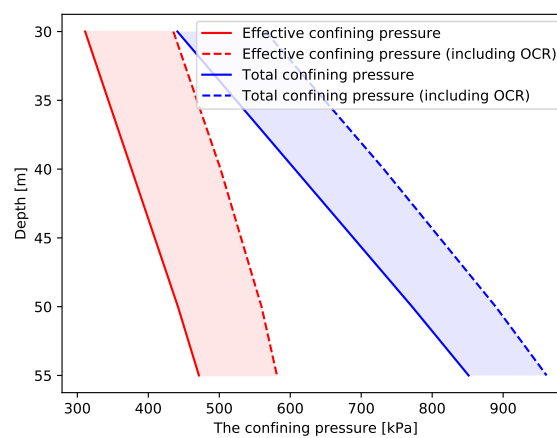


Figure 3.5: The confining pressure as a function of depth for the considered cross-section ($K_0 = 0.645$).

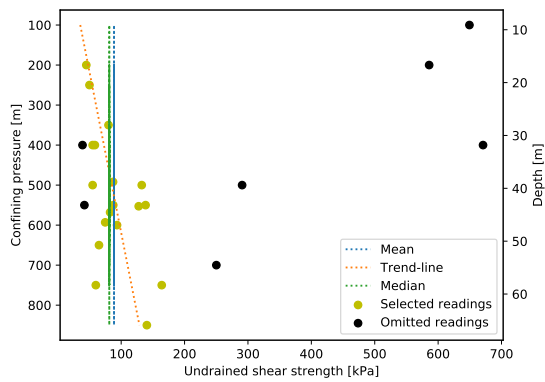


Figure 3.6: In-depth distribution of the undrained shear strength obtained from the UU and UC triaxial tests.

The distributions of parameters obtained in the performed CU and UU tests are assessed, as shown in Figure 3.6 on the left. The extreme readings (black dots) are omitted, and the rest of the readings (yellow dots) are used to calculate the mean, the median and standard deviation and to draw a corresponding trend-line. The procedure is presented in Figure 3.6 on an exemplary parameter, i.e. the undrained shear strength derived from UU and UC triaxial tests.

The assessment of the E_{50}^{ref} parameter started from describing the distribution of $E_{50,undrained}$ obtained in the CU tests as shown in Figure 3.7 below.

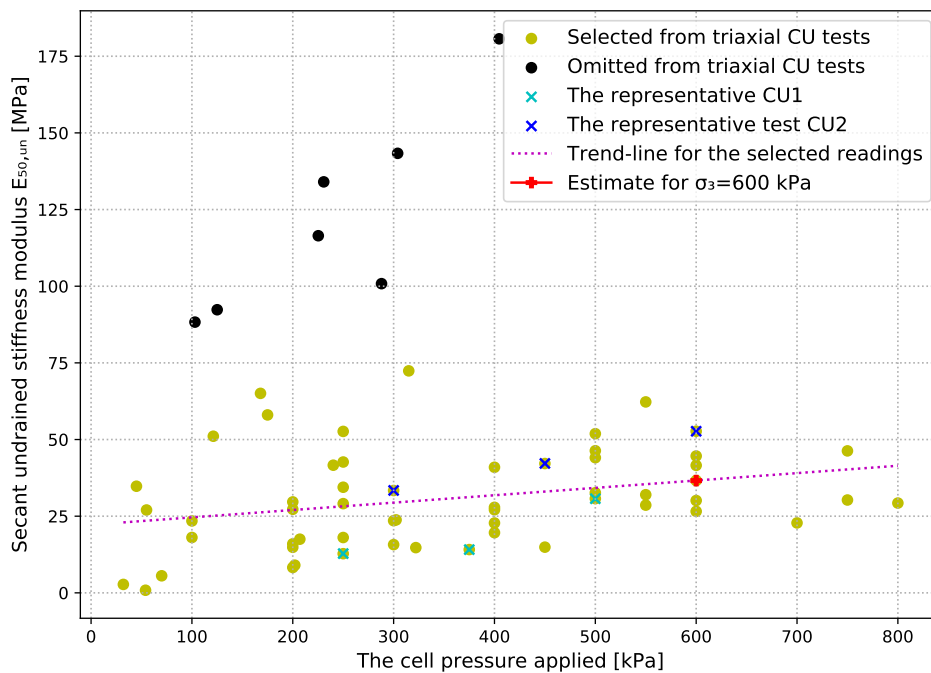


Figure 3.7: Distribution of the secant undrained stiffness obtained in the triaxial CU tests as a function of test confining pressure.

The SoilTest facility was used to investigate the E_{50}^{ref} input parameter value corresponding to the stress level applied in each test, and the average estimate is equal to 1.95 MPa. The strength parameters were as established in Table 3.7, vertical pre-consolidation pressure equal to 180 kPa (POP corresponding to the applied cell pressure and average OCR as in Table 3.7).

In the same manner, the results from the triaxial UU tests were assessed. The distribution of $E_{50,undrained}$ obtained in triaxial UU tests is shown in Figure 3.8 below.

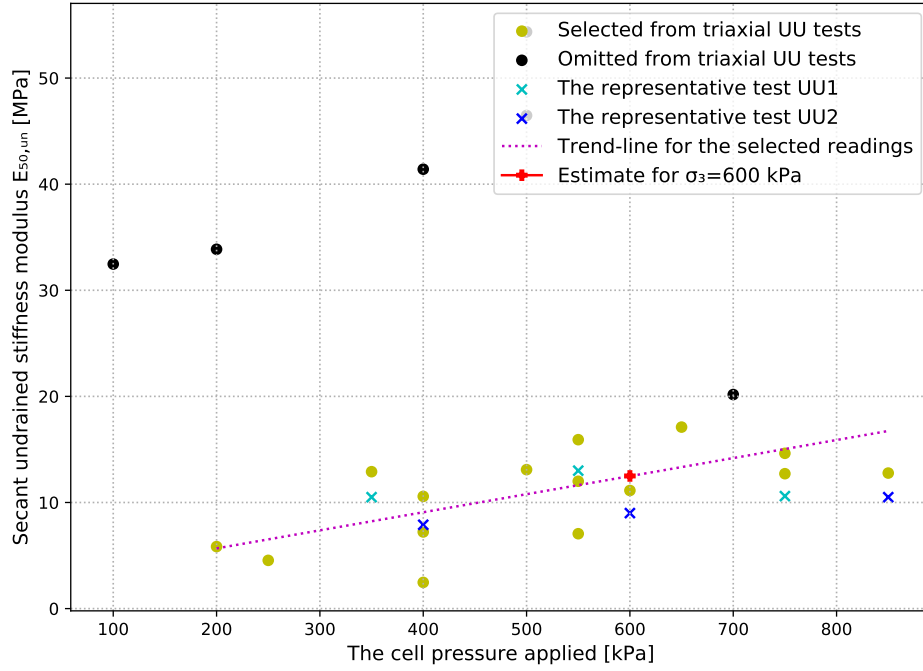


Figure 3.8: Distribution of the secant undrained stiffness obtained in the triaxial UU tests as a function of test confining pressure.

The corresponding input value was investigated using *Undrained B* drainage settings. Hence no stress-dependency is applied. The input E_{50} for $E_{50,undrained}$ of 12.5 MPa was calculated using Formula 3.1 at a confining pressure of 600 kPa. The estimated value is 9.3 MPa.

$$E_{50} = E_{50}^{ref} \left(\frac{c \cdot \cos\phi - \sigma'_3 \sin\phi}{c \cdot \cos\phi + p^{ref} \sin\phi} \right)^m \quad (3.1)$$

Repeating the derivation of E_{50}^{ref} value for each performed test (at each cell pressure) leads to the distribution of this parameter in-depth as shown in Figures A.3 and A.4 in Appendix A. In these figures, the depth was back-calculated from the applied cell pressure.

The point estimation for all the mentioned parameters is shown in Table 3.1 below.

Test	Parameter	Unit	Mean	Median	SD	Choice
CU	ϕ'	[°]	18.0	18.0	3.31	18.0
CU	c'	[kPa]	27.2	29.0	7.84	28.0
UU & UC	s_u	[kPa]	91.3	81.3	34.8	85.0
UU	E_{50}^{ref}	[MPa]	1.53	1.32	0.61	1.50
UU	E_{50}^{ref}	[MPa]	9.3	-	-	9.3
CU	E_{50}^{ref}	[MPa]	2.26	1.80	1.19	2.25

The reference pressure is 100 kPa, except for the stress-level in triaxial UU secant stiffness input in the 5th row, which is 600 kPa.

Table 3.1: Parameters obtained in the triaxial tests.

The best fit triaxial test should provide parameters as described in Table 3.1. The mean value of the undrained shear strength s_u refers to a depth of around 40.0 - 45.0 meters, i.e. where mean and linear regression lines cross. Also, in the same manner as for the consolidation test, it should have similar plasticity characteristics, a void ratio and a dry unit weight as given in Tables 3.5 and 3.6.

3.2.2. Pressuremeter tests

The first two parameters can be used to obtain secant shear and un-loading/reloading stiffness moduli through Formula 3.2 [41]. However, the obtained values for a reference stress level of $p^{ref} = 100$ kPa were unreasonably high ($E_{50}^{ref} \approx 20.3$ MPa, and $E_{ur_{PMT}}^{ref} \approx 40.6$ MPa) and will not be used later.

The last parameter, p_L , can be used to estimate the undrained shear strength s_u using Formula 3.3 [41]. The obtained s_u distribution is shown in Figure A.6 in Appendix A. As seen in the plot, the original distribution of the soil parameter is shown. Latter, the deviating extreme values (black dots on the plots) are omitted in order to receive a higher target score, and the new distribution (only the yellow dots on the plots) is used to give the point estimate. On the plots, the blue line is the mean value, and the green line indicates the median and the orange line shows the depth-trend.

$$E_{50} \iff E = 1.5 \div 2.0 \frac{E_M}{\alpha} [MPa] \quad (3.2)$$

where: E_M is pressuremeter stiffness modulus expressed in MPa, and α is between 0.22 and 1.0.

$$s_u = 85kPa + \frac{p_L}{35} [kPa] \quad (3.3)$$

where: p_L is in kPa.

The limit pressure test is of limited reliability because many tests have not reached the limit pressure, what may cause the undrained shear strength values to be underestimated. The summary of the averaged parameter values obtained for the low- and high- plasticity clay is shown in Table 3.2. The values in the table are for all clay types classified as *CL*, *CH*, *CL – CH*, *CH – CL* and *CH – SP*.

Parameter	Unit	Whole layer		Depth to 49.5 m		Depth from 49.5 m	
		Mean	SD	Mean	SD	Mean	SD
E_p	[MPa]	157	223	86.9	82.9	280.5	322.8
		Mean: <u>87.5</u>		Median: <u>70.1</u>		SD: <u>68.7</u>	
E_r	[MPa]	651	1481	392	1271	1169	1776
		Mean: <u>229</u>		Median: <u>178</u>		SD: <u>162</u>	
p_L	[MPa]	2.35	1.00	2.70	1.09	1.79	0.54
		Mean: <u>2.11</u>		Median: <u>2.04</u>		SD: <u>0.54</u>	
s_u	[kPa]	Mean: <u>139</u>		Median: <u>142</u>		SD: <u>13.8</u>	

Table 3.2: Clay parameters obtained in Pressuremeter tests.

The derivation of the parameters shown above is based on the field testing consisting of 86 Pressuremeter tests. The distribution of the Pressuremeter parameters, i.e. stiffness modulus E_p , rebound modulus E_r , limit pressure p_L obtained in these test is shown in Figures A.7, A.8 and A.5 in Appendix A.

3.2.3. One-dimensional consolidation tests

In total, 30 one-dimensional consolidation tests have been performed. For the analysis of the pre-consolidation ratio, the vertical effective and total stresses as a function of depth are shown in Figure 3.9 below.

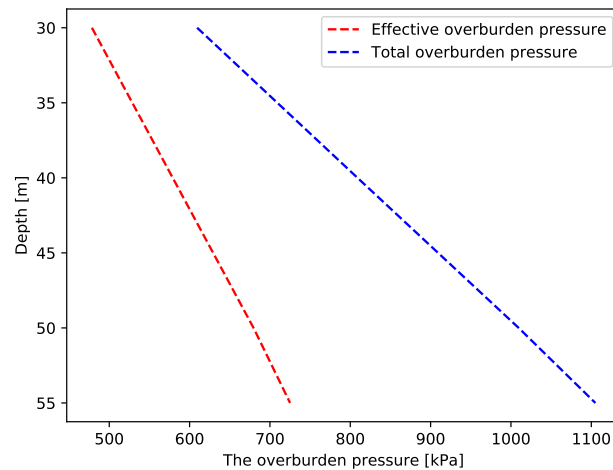


Figure 3.9: The vertical effective and total stresses as a function of depth for the considered cross-section ($OCR = 1.0$).

The statistics for the for low- and high- plasticity clay specimen parameters obtained in one-dimensional consolidation tests are shown in Table 3.3 below.

Layer	Parameter	Whole layer		Depth to 49.50 m		Depth from 49.51 m	
		Mean	SD	Mean	SD	Mean	SD
C_e	[-]	0.0843	0.0494	0.0726	0.0535	0.115	0.0479
		Mean: <u>0.069</u> ,		Median: <u>0.080</u> ,		SD: <u>0.018</u>	
C_c	[-]	0.213	0.135	0.285	0.150	0.146	0.086
		Mean: <u>0.207</u> ,		Median: <u>0.175</u> ,		SD: <u>0.119</u>	
σ'_p	[kPa]	904	301	858	308	946	310
		Mean: <u>825</u> ,		Median: <u>800</u> ,		SD: <u>133</u>	

Table 3.3: Clay parameters obtained from one-dimensional consolidation tests.

The mean value of the pre-consolidation pressure σ'_p obtained in the one-dimensional consolidation test is equal to 825 kPa, the median equal to 800 kPa and the standard deviation is 133 kPa. Two formulae were considered to calculate the Over-Consolidation Ratio (OCR):

Formula 3.4 based on the pre-consolidation pressure derived in the oedometer tests:

$$OCR = \frac{\sigma'_p}{\sigma'_{v0}} \quad (3.4)$$

Formula 3.5 by Ladd [54] based on the undrained shear strength:

$$OCR = \left(\frac{s_u}{0.22\sigma'_v} \right)^{\frac{5}{4}} \quad (3.5)$$

where: s_u is taken from Formula 3.8.

The Ladd [54] formula significantly underestimates the OCR level. The OCR value will be based on the pre-consolidation pressure from the oedometer tests and is estimated to be 1.40 for a depth of 30.0 meters and 1.20 for a depth of 60.0 meters and in between the mathematical interpolation method applies.

Based on all of the one-dimensional consolidation tests, the tangent oedometer stiffness E_{oed} and un/re-loading stiffness E_{ur} were derived according to the formulae 3.6 and 3.7 from [12] shown below:

$$E_{oed} = E_{oed}^{ref} \left(\frac{c \cdot \cos\varphi - \frac{\sigma'_3}{K_0^{nc}} \sin\varphi}{c \cdot \cos\varphi + p^{ref} \sin\varphi} \right)^m \quad (3.6)$$

$$E_{ur} = E_{ur}^{ref} \left(\frac{c \cdot \cos\varphi - \sigma'_3 \sin\varphi}{c \cdot \cos\varphi + p^{ref} \sin\varphi} \right)^m \quad (3.7)$$

where: $\sigma'_1 = \frac{\sigma'_3}{K_0^{nc}}$.

The distributions of these parameters are shown in Figures 3.10 and 3.11 below:

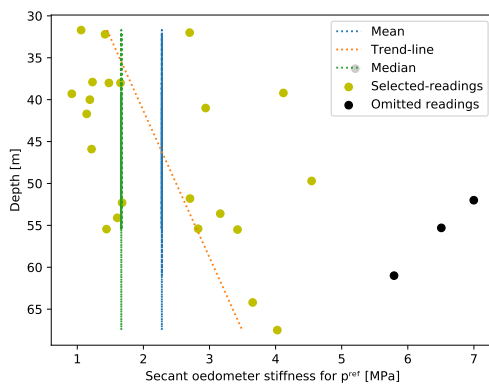


Figure 3.10: Reference tangent oedometer stiffness E_{oed}^{ref} as a function of depth.

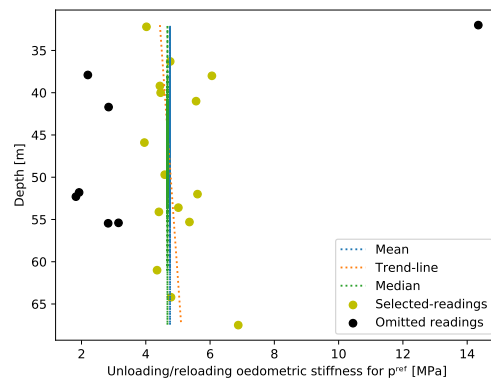


Figure 3.11: Reference un/re-loading stiffness E_{ur}^{ref} as a function of depth.

The point estimation for the parameters obtained in one-dimensional consolidation tests is given in Table 3.4 below.

Parameter	Symbol	Unit	Range	Mean	Median	SD	Choice
Secant oedometer stiffness	E_{oed}	[MPa]	-	2.28	1.67	1.13	2.00
Un/re-loading oed. stiffness	E_{ur}	[MPa]	-	4.95	4.67	0.78	4.95

Table 3.4: The stiffness parameters obtained from one-dimensional consolidation tests.

The best-fit clay specimen for the consolidation test should have the swelling index of around 0.08, the compression index of around 0.20 and the initial void ratio around 0.95. The dry unit weight of an average soil specimen is approximated as 14.0 kN/m^3 and saturated unit weight as 19.0 kN/m^3 . The average pre-consolidation pressure is around 820 kPa , but the range is between 700 kPa and 850 kPa .

3.2.4. Atterberg limits and index tests

In total, 127 Atterberg limits tests were performed, and the data on the plasticity characteristics obtained in these tests was used for a further assessment of the representative one-dimensional consolidation and triaxial tests and in the derivation of specific material model parameters.

In addition to the parameters mentioned above, four other parameters were derived in index tests performed as a part of the consolidation and triaxial tests. These parameters can be used, together with Atterberg limits to point out the most representative tests concerning the sample characteristics. Their distributions are shown in Figure A.13, A.17, A.18 and A.19 in Appendix A. The distributions and tables are shown as before.

The summary of the test results for the whole clay domain (of low- and high- plasticity) is shown in Table 3.5 below.

Parameter	Unit	Whole layer		Depth to 49.50 m		Depth from 49.51 m	
		Mean	SD	Mean	SD	Mean	SD
<i>L.L.</i>	[%]	64.0	17.9	58.2	20.3	74.2	17.5
		Mean: <u>64.1</u>		Median: <u>66.0</u>		SD: <u>12.9</u>	
<i>P.L.</i>	[%]	26.2	10.4	24.7	11.4	28.8	10.6
		Mean: <u>25.2</u>		Median: <u>23.0</u>		SD: <u>8.61</u>	
<i>P.I.</i>	[%]	37.8	14.4	33.5	14.6	45.2	14.8
		Mean: <u>38.2</u>		Median: <u>36.0</u>		SD: <u>12.9</u>	
<i>w</i>	[%]	30.5	9.1	29.2	9.83	33.2	14.0
		Mean: <u>30.4</u>		Median: <u>30.3</u>		SD: <u>8.19</u>	

Table 3.5: Parameters obtained from Atterberg Limits tests.

The best fit clay specimen should have following plasticity characteristics: Liquid Limit around 65%, Plastic Limit around 24%, Plasticity Index around 37% and natural water content around 30%.

The statistics of the four state parameters is shown in Table 3.6 below.

Layer	Parameter	Whole layer		Depth to 49.50 m		Depth from 49.51 m	
		Mean	SD	Mean	SD	Mean	SD
e_0	[-]	0.913	0.190	0.884	0.216	0.940	0.173
		Mean: <u>0.947</u> ,		Median: <u>0.940</u> ,		SD: <u>0.133</u>	
γ_d	[kN/m ³]	14.7	1.70	14.8	1.76	14.5	1.67
		Mean: <u>14.2</u> ,		Median: <u>14.0</u> ,		SD: <u>1.21</u>	
w_{test}	[%]	31.8	7.29	31.1	8.42	32.7	6.07
		Mean: <u>33.3</u> ,		Median: <u>33.1</u> ,		SD: <u>5.86</u>	
γ_{sat}	[kN/m ³]	19.2	1.44	19.1	1.08	19.2	1.78
		Mean: <u>19.0</u> ,		Median: <u>18.7</u> ,		SD: <u>0.97</u>	

Table 3.6: State parameters obtained from the index tests.

Based on all of the oedometer tests, the derived stiffness parameters are shown in Figures A.10 and A.11, the pre-consolidation pressure in Figure A.9, and the other parameters in Figures A.12, A.14, A.15 and A.16 in Appendix A.

3.2.5. Summary of the parameters assessment

To summarize the performed field and laboratory tests, this part refers to Geotechnical Interpretative Report [51] prepared for this project, where other tests such as SPT, correlations and assumptions, and knowledge of local experts is used to assess the final parameters. These parameters are: coefficient of lateral earth pressure K_0^{nc} , the Poisson's ratio ν , the characteristic values of effective friction angle φ' and the effective cohesion c' , which were characteristic values calculated with a confidence level of 95%, the stiffness moduli E_{50}^{ref} , E_{oed}^{ref} and E_{ur}^{ref} .

Besides, the undrained shear strength was derived in three different tests. In order to increase confidence in assessing its average value, point estimation will be based on both PMT, UC and UU tests. The combined

distribution is shown in Figure A.20 in Appendix A.

The trend-line describing the undrained shear strength is as in Formula 3.8 below. The mean value was estimated as 128 kPa (median 139 kPa) with a standard deviation of 40.0 kPa.

$$s_u = 0.1183\sigma'_v + 54.89y_{ref} [kPa] \quad (3.8)$$

where: y_{ref} is the reference depth.

Since there is a big spread between direct values from the UU and UC tests and the correlated values from PMT, it was agreed that s_u should be in a range between 90.0 kPa for a depth of 30.0 m and 150 kPa for a depth of 60.0 m.

The same applies to the secant triaxial and tangent oedometric stiffness. Since there is a big spread between CU ($E_{50}^{ref} \approx 5.90$ MPa), UU ($E_{50}^{ref} \approx 1.80$ MPa) and one-dimensional consolidation ($E_{oed}^{ref} \approx 2.25$ MPa) tests, it was agreed to use one value of 2.50 MPa. Also, the un/re-loading, which was estimated to be 4.95 MPa, is too low when compared to the tangent stiffness from primary oedometer loading. That is why the value 7.50 MPa is set as the initial value. The variance for both E_{50}^{ref} and E_{oed}^{ref} parameters is taken as a standard deviation for all of the results of the UU and 1D consolidation tests.

In the linear-elastic, perfectly-plastic analysis, the Poisson's ratio for clays can be taken as 0.30 – 0.40 [10] with an average value of 0.35 taken as the best-estimated value. In the undrained calculations, a value of 0.495 should be adopted for the ν_u parameter, because the value of 0.50 might cause computation errors in finite-element analysis software.

The final list of all relevant soil parameters derived in the site investigation program is shown in Table 3.7 below.

Parameter	Symbol	Range	Estimate	SD	Unit
Reference stiffness modulus	E_{50}^{ref}	-	2.50	1.10	[MPa]
Reference oedometer modulus	E_{oed}^{ref}	-	2.50	1.10	[MPa]
Reference un/re-loading modulus	E_{ur}^{ref}	-	7.5	-	[MPa]
Initial void ratio	e_0	-	0.945	0.13	[-]
Plasticity index	PI	-	37.0	13.0	[%]
Effective friction angle	φ'	-	22.0	3.3	[°]
Effective cohesion	c'	-	1.0	7.80	[kPa]
Undrained shear strength	s_u	90 - 150	120	40	[kPa]
Coefficient of lat. earth pressure at rest	$K_0 = K_0^{nc}$	0.62 – 0.73	0.65	0.25	[-]
Effective Poisson's ratio	ν'	-	0.35	-	[-]
Over-consolidation ratio	OCR	1.0 - 1.5	1.2 - 1.4	-	[-]

The reference stress level p^{ref} is equal to 100 kPa.
The average s_u value is given for depth of 45.0 m.

Table 3.7: Summary of the input parameters.

3.3. Studies on the material model parameters

3.3.1. Initial values of the material model parameters

In this section, parameters of the analyzed material models are described, the estimate and justification for each parameter's value will be given. Most of the parameters are taken as they are in Table 3.7 and the missing material model parameters are explained below.

HSS model

The default value of the threshold shear strain at $G_s = 0.722G_0$, i.e. the $\gamma_{0.7}$ parameter, is taken as equal to the default value 0.0001. This value has also been proven to have a good fit with the real laboratory tests results. The reference shear stiffness at small strains can be approximated with Formula 3.9 [3]:

$$G_0 = E_0 \frac{1}{2(1+\nu)} [MPa] \quad (3.9)$$

The ratio of $\frac{E_0}{E_{50}}$ can exceed 10 for very soft clays [3], but often a value of 3.0 [93] is assumed. For the clay domain in this project, the good fit was received for G_0^{ref} estimated as 40.0 MPa.

The HSS model parameters, which are the established averages for the whole clay domain, are listed in Table 3.11.

NGI-ADP model

The ratio un/reloading shear modulus over (plane strain) active shear strength G_{ur}/s_u^A is not defined in the laboratory tests, and its value can only be correlated from the un/reloading stiffness modulus using Formula 3.10.

$$\frac{G_{ur}}{s_u^A} = \frac{E_{ur}}{2(1+\nu_{ur}) s_u^A} \quad (3.10)$$

Using this formula for an average value of E_{ur}^{ref} and s_u^{ref} we obtain a value around 22.0. This value is considered too low to be applied, hence the ratio of 30.0 is taken.

The shear strain at failure in triaxial compression γ_f^C from the CU tests is equal to 7.2%, and γ_f^E as an average from the two available triaxial extension tests is equal to 2.1%. There is no direct simple shear test data available. In the literature [12] one can find a following approximations for the shear strain parameters: $\gamma_f^C = 0.5 - 4.0\%$, $\gamma_f^E = 3.0 - 8.0\%$ and $\gamma_f^{DSS} = 2.0 - 8.0\%$. Also, a following relation can be found: $\gamma_f^C < \gamma_f^{DSS} < \gamma_f^E$. Since there is no fully reliable data (very high standard deviation of the available results and too high results), initially, the parameters were taken as the upper range according to the literature, i.e. $\gamma_f^C = 4.0\%$, $\gamma_f^E = 6.0\%$ and $\gamma_f^{DSS} = 8.0\%$.

The ratio of triaxial compressive strength over active shear strength $s_u^{C,TX}/s_u^A$ is set to a default value. The ratio of passive shear strength over active shear strength s_u^P/s_u^A is estimated as 2.68 in the laboratory tests, which is a very high number. From the literature, values in the range of $0.2 \div 0.5$ can be found [12], hence the value of 0.35 was adopted. For the ratio of direct simple shear strength over active shear strength s_u^{DSS}/s_u^A , there is no available data to be used, hence the Formula 3.11 [12] was used, and the value of 0.68 was found as the best estimation.

$$s_u^{DSS}/s_u^A = \frac{1 + s_u^P/s_u^A}{2} \quad (3.11)$$

The reference depth y_{ref} is set as -35.0 m with s_u^{ref} taken as 100 kPa and $s_{u,inc}^A$ equal to $2.0 \text{ kN/m}^2/\text{m}$, so the undrained shear strength was equal to the established mean (120 kPa) at the depth of 45.0m, i.e. depth were the trend-line and mean-line usually cross for most of the parameters. The initial mobilization τ^0/s_u^A was taken as a default value.

The NGI-ADP model parameters, which are the established averages for the whole clay domain, are listed in Table 3.12.

SHANSEP MC model

Two formulae can be used to approximate the shear modulus over the undrained shear strength ratio G/S_u . The first one is described in Formulae 3.12 and 3.13 related to the undrained rigidity index I_R .

$$G \cong G_{50} = I_R s_u \quad (3.12)$$

where s_u is the undrained shear strength, and I_R is calculated using Formula 3.13:

$$I_R = \frac{e^{(137-PI)/23}}{[1 + \ln(1 + (OCR - 1)/26)^{3.2}]^{0.8}} \quad (3.13)$$

The other is as shown in Formula 3.14 [72].

$$\frac{G}{S_u} = \frac{5000}{I_p[\%]} = \frac{5000}{37} \approx 135 \quad (3.14)$$

where: I_p is a plasticity index.

Eventually, the second formula is used in this study, and the ratio is kept constant for each of the analyzed tests to avoid additional discrepancies between the parameters sets. The SHANSEP MC model parameters, which are the established averages for the whole clay domain, are listed in Table 3.13 below.

GHS model

All of the GHS model parameters are consistent with the parameters of the HSS model, and have been derived exactly in the same way as in HSS model.

3.3.2. Chosen representative tests

The point estimation of each soil parameter was used to choose the representative tests, which define clay behaviour as accurately as possible. In total, seven tests have been chosen to be used in the calibration: two triaxial CU tests summarised in Table 3.8, two triaxial UU tests summarised in Table 3.9 and three one-dimensional consolidation tests summed up in Table 3.10.

Sample description			Test parameters							
Test code	Depth [m]	Sample	σ_1 [kPa]	σ_3 [kPa]	$\sigma_1 - \sigma_3$ [kPa]	ε_f [%]	ε_{50} [%]	E_{50}^{ref} [MPa]	ϕ' [°]	c' [kPa]
CU1	46.15	CH	536	250	286	15.8	1.12	1.75	24.0	10.0
			797	375	424	15.8	1.50	1.33		
			1056	500	556	14.5	0.91	2.30		
CU2	52.15	CH	577	300	277	6.57	0.42	4.05	17.0	20.0
			838	450	388	5.26	0.46	3.62		
			1106	600	506	5.30	0.48	3.48		

Table 3.8: Parameters obtained in the representative triaxial CU tests.

Sample description			Test parameters						
Borehole	Depth [m]	Sample	σ_1 [kPa]	σ_3 [kPa]	$\sigma_1 - \sigma_3$ [kPa]	ε_f [%]	ε_{50} [%]	E_{50}^{ref} [MPa]	s_u [kPa]
UU1	60.60	CH	510	350	160	14.3	0.62	10.0	80.0
			827	550	277	9.2	0.87	12.1	139
			1078	750	338	10.3	1.29	9.2	164
UU2	67.35	CH	510	400	110	15.8	0.52	7.47	55.0
			787	600	187	15.8	0.84	8.03	93.5
			1131	850	281	15.8	1.10	9.43	141

E_{50}^{ref} input value for a given confining (cell) pressure.

Table 3.9: Parameters obtained in the representative triaxial UU tests.

Sample data			Parameters obtained in 1D the consolidation tests								
Test code	Depth [m]	Layer	C_e [-]	C_c [-]	σ_p [kPa]	e_0 [-]	$L.L.$ [%]	$P.I.$ [%]	γ_d [kN/m ³]	E_{oed}^{ref} [MPa]	E_{ur}^{ref} [MPa]
1D-1	37.90	CH	0.077	0.37	700	0.98	49	29	13.63	1.23	8.25
1D-2	54.10	CH	0.081	0.27	1600	0.88	77	50	14.32	1.60	7.46
1D-3	55.45	CH	0.095	0.30	700	0.88	73	50	14.32	1.44	6.35

Table 3.10: Parameters obtained in the representative one-dimensional consolidation tests.

The tables above are based on the tests shown in Figures A.27 and A.28 in Appendix A for the triaxial CU tests, Figures A.24 and A.25 in Appendix A for the triaxial UU tests and in Figures A.21, A.22 and A.23 in Appendix A for the one-dimensional consolidation tests.

3.3.3. Calibration of the parameters of the HSS model

There are three drainage types in the HSS constitutive soil model: *Drained*, *Undrained A* and *Undrained B*, whereas in the SoilTest simulations, there is no difference in the computed stresses between the *Drained* and *Undrained A* settings. The calibration of the material model parameters is possible only in the applicable stress range, so the oedometer tests simulations can only be simulated appropriately using the *Drained* settings. This is because in *Undrained B* settings after the vertical effective pressure reaches a double value of the undrained shear strength, the stress-strain curve follows the constant degree till the maximum vertical effective pressure is reached.

In total, the results of four triaxial tests (using three cell pressures in each test) and three oedometer tests were reproduced in the SoilTest facility in order to calibrate the material parameters. The triaxial CU tests were simulated using *Drained* approach and the triaxial UU tests were simulated using the *Undrained B* drainage type. For the *Drained* settings, Figures 3.12, 3.13 and 3.16 show stress paths for the calibrated material model parameters sets for triaxial CU1 and CU2 and one-dimensional consolidation tests. For the *Undrained B* settings, Figures 3.14 and 3.15 show the calibrated stress path for triaxial UU1, UU2 and extension UU tests, respectively.

The initial values obtained in the laboratory tests were taken as in Table A.1 in Appendix A. The calibrated stress paths are given for the initial values, whereas the stiffness parameters were multiplied by the ratio of 1.6 for the triaxial CU and oedometer tests and the ratio of 0.85 for the triaxial UU tests, the internal friction angle was increased by 3.0°.

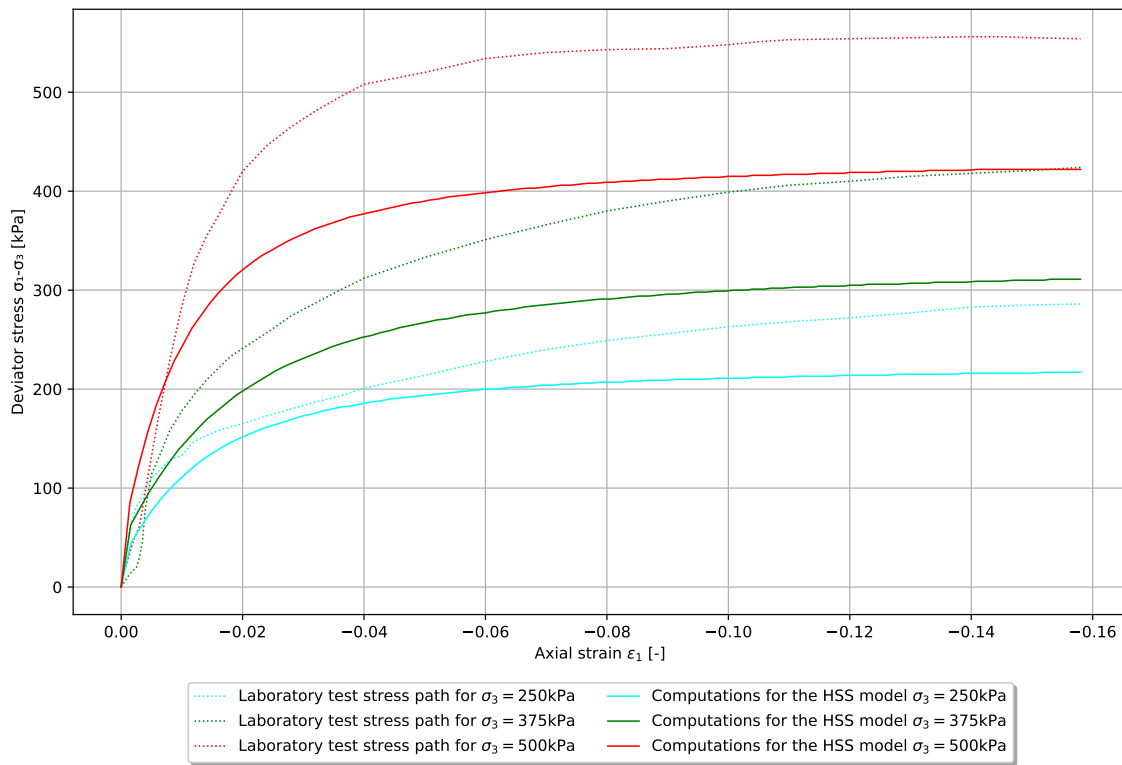


Figure 3.12: Stress paths computed for the calibrated HSS model parameters compared to the paths from the laboratory tests - triaxial CU1 test.

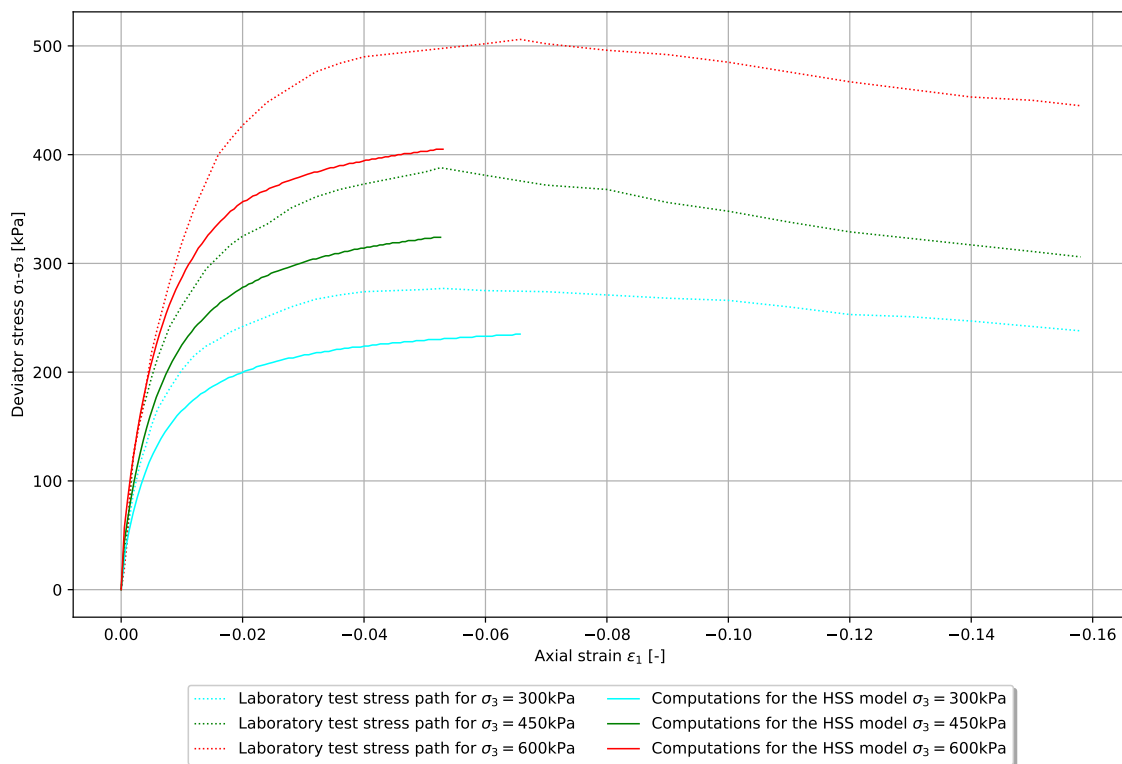


Figure 3.13: Stress paths computed for the calibrated HSS model parameters compared to the paths from the laboratory tests - triaxial CU2 test.

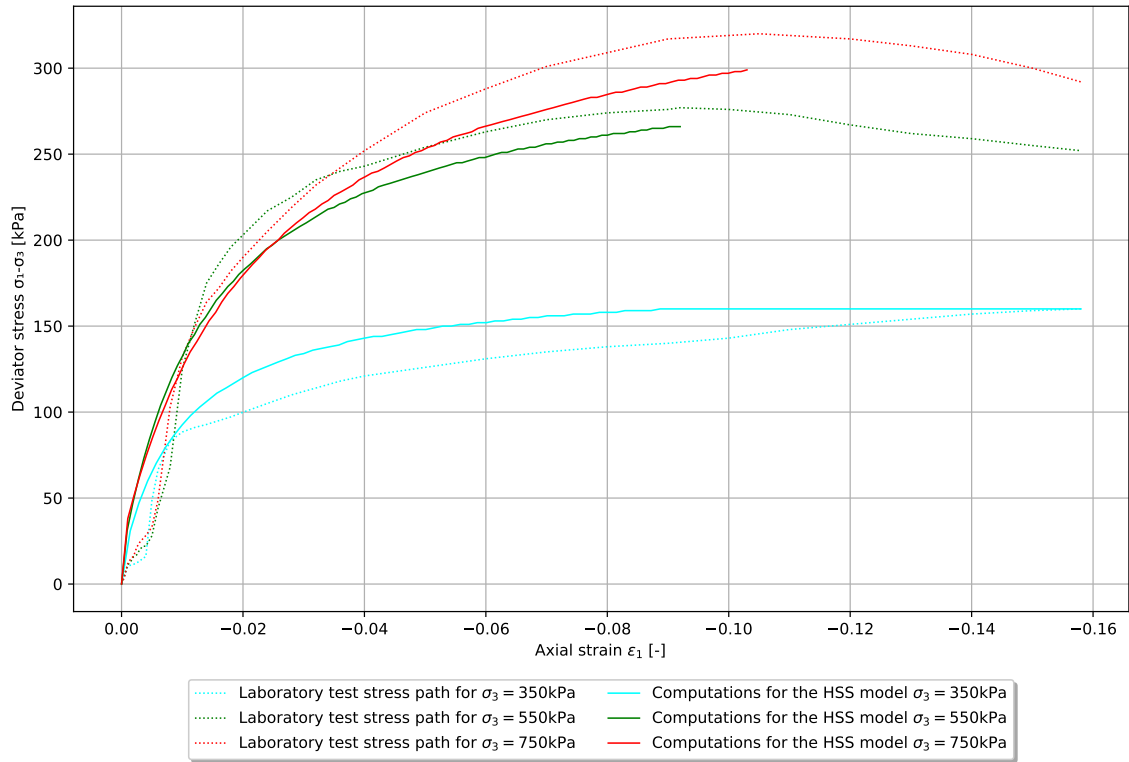


Figure 3.14: Stress paths computed for the calibrated HSS model parameters compared to the paths from the laboratory tests - triaxial UU1 test.

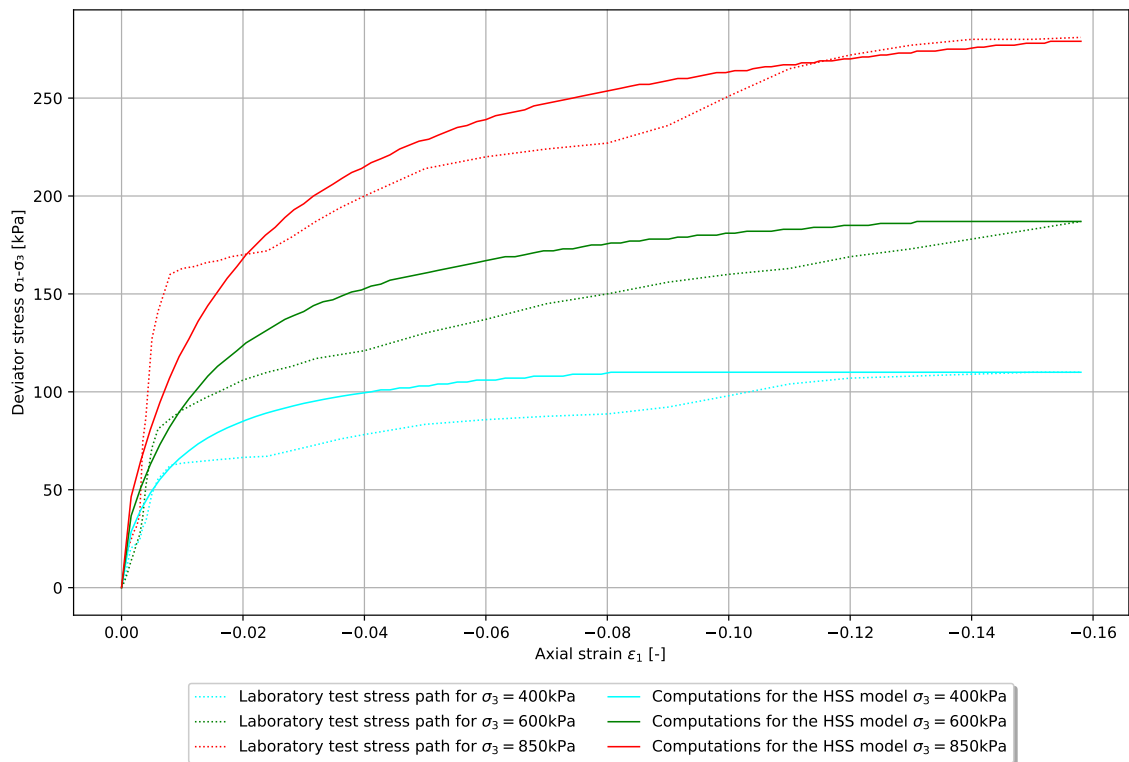


Figure 3.15: Stress paths computed for the calibrated HSS model parameters compared to the paths from the laboratory tests - triaxial UU2 test.

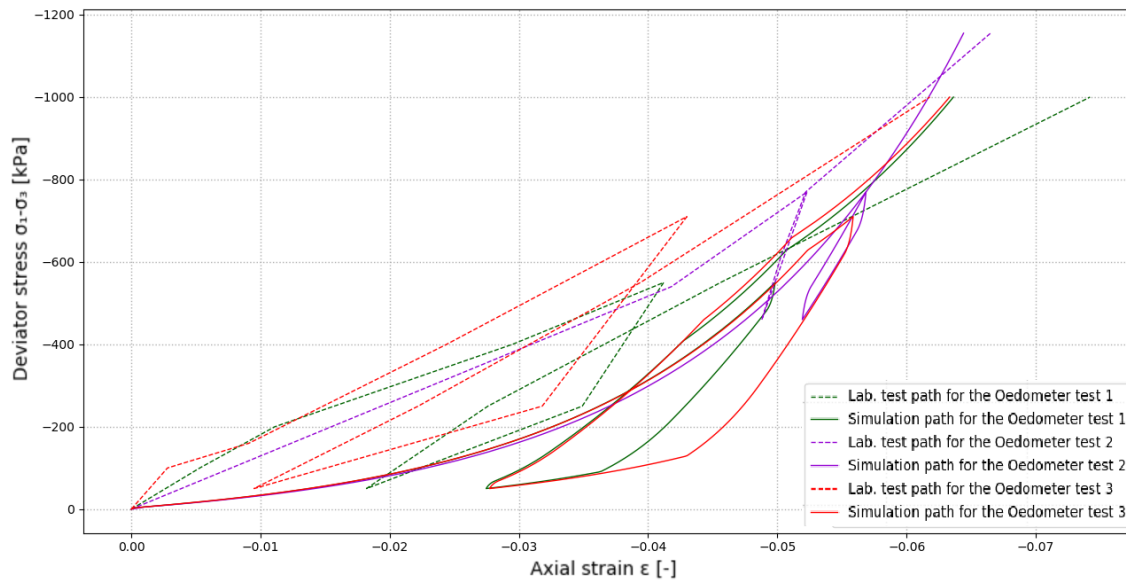


Figure 3.16: Stress paths computed for the calibrated HSS model parameters compared to the paths from the laboratory tests - oedometer tests.

The calibrated input parameters for the HSS model are shown in Table 3.11 below.

Parameter type	Symbol	Initial Estimate		Optimised Estimate		Unit
		Drained	Undrained B	Drained	Undrained B	
Failure parameters as in MC	φ	22.0	0.0	22.0	0.0	[°]
	c	1.0	120	10.0	120	[kPa]
	ψ	0	0	0	0	[°]
	σ_t	0	0	0	0	[kPa]
Basic parameters for soil stiffness	E_{50}^{ref}	2.50	10.1	4.0	8.6	[MPa]
	E_{oed}^{ref}	2.50	10.1	5.0	10.7	[MPa]
	E_{ur}^{ref}	7.5	30.3	15.0	32.2	[MPa]
	m	1.0	1.0	1.0	1.0	[-]
Small-strain stiffness	$\gamma_{0.7}$	0.0001	0.0001	0.0001	0.0001	[-]
	G_0^{ref}	40.0	75.0	35.0	70.0	[MPa]
Advanced parameters	ν_{ur}	0.20	0.20	0.20	0.20	[-]
	p^{ref}	100	600	100	600	[kPa]
	K_0^{nc}	0.65	0.65	0.65	0.65	[-]
	R_f	0.90	0.90	0.90	0.90	[-]

Parameters in *Undrained B* column are given for the confining pressure of 600 kPa.

Table 3.11: The initial and the calibrated parameters of the HSS model.

The stiffness in extension has not been calibrated since the only proper test shows the E_{50} parameter equal to 22.5 MPa at the stress level of 500 kPa, which is around two times higher than the stiffness in compression. Hence, the stiffness value for the clay at extension will be taken as one-third of the compression values adjusted to the stress level of 400 kPa.

3.3.4. Calibration of the parameters of the NGI-ADP model

There are three drainage types in the NGI-ADP model: *Drained*, *Undrained B* and *Undrained C*. The computed stress paths for the *Drained* and *Undrained B* models are identical, and the results using the *Undrained C* settings are slightly different (almost negligible). Since the only strength parameter is the undrained shear

strength s_u , which is pre-defined and is not influenced by the stress σ'_{yy} , the simulations of the one-dimensional consolidation tests were not be performed.

In total, the results of two triaxial UU tests, using three cell pressures in each test, were reproduced in SoilTest. Both tests have been simulated using the *Undrained C* settings. The results of the calibration for the triaxial tests UU1 and UU2 is shown in Figures 3.17 and 3.18 below.

The initial values were derived from the laboratory tests taken as in Table A.2 in Appendix A. In each tri-axial test, the computed $s_{u,ref}^A$ value was different and equal to the one directly derived from the test. The other values, by a trial-and-error method, were calibrated to a one, constant value.

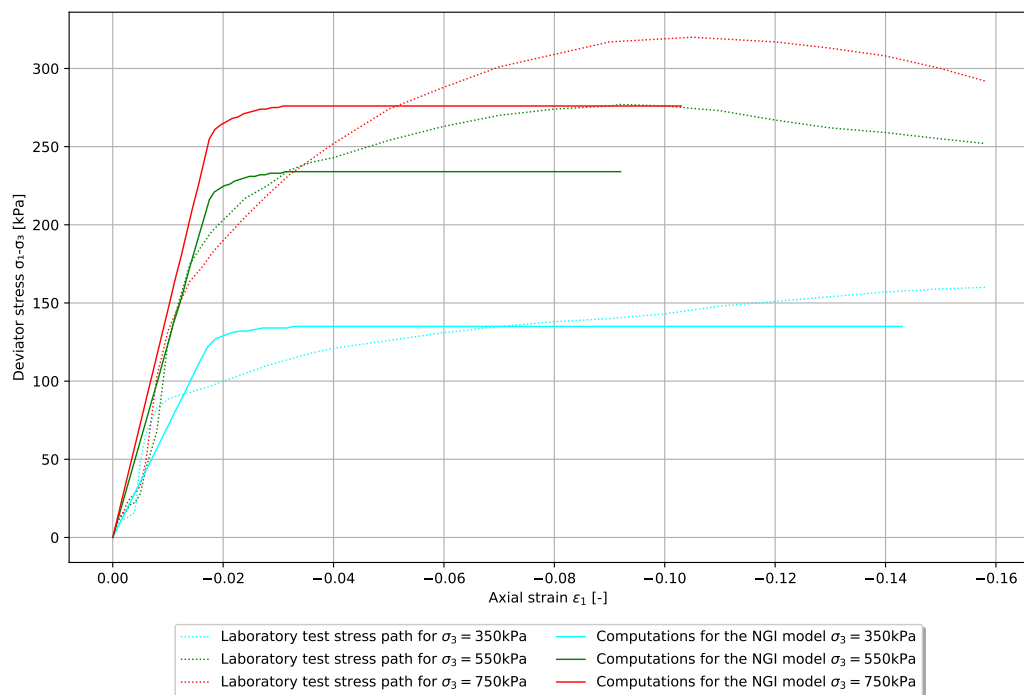


Figure 3.17: Stress paths computed for the calibrated NGI-ADP model parameters compared to the paths from the laboratory tests - triaxial UU1 test.

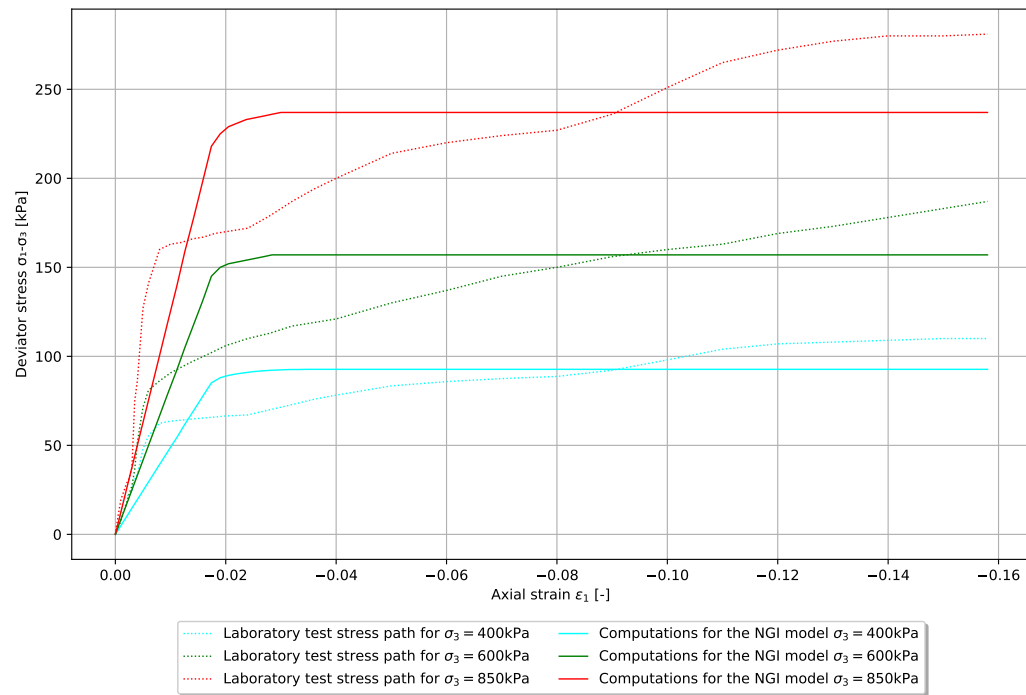


Figure 3.18: Stress paths computed for the calibrated NGI-ADP model parameters compared to the paths from the laboratory tests - triaxial UU2 test.

The calibrated input parameters for NGI-ADP model are showed in Table 3.12 below.

Parameter type	Symbol	Initial Estimate	Optimised Estimate	Unit
Stiffness parameters	G_{ur}/s_u^A	30.0	35.0	[-]
	γ_f^C	4.0	4.0	[-]
	γ_f^E	8.0	8.0	[-]
	γ_f^{DSS}	6.0	6.0	[-]
Strength parameters	$s_{u,ref}^A$	100	85	[kPa]
	$s_u^{C,TX}/s_u^A$	0.99	0.99	[-]
	y_{ref}	-35.0	-35.0	[m]
	$s_{u,inc}^A$	2.0	2.0	[kPa/m]
	s_u^B/s_u^A	0.35	0.35	[-]
	τ^0/s_u^A	0.70	0.70	[-]
Advanced parameter	s_u^{DSS}/s_u^A	0.68	0.68	[-]
	ν'	0.35	0.35	[-]

The input parameters are given for the *Drained* settings, while the values for the *Undrained C* settings are exactly same apart from Poisson's ratio, which is equal to = 0.495 then.

Table 3.12: The initial and the calibrated parameters of the NGI-ADP model.

3.3.5. Calibration of the parameters of the Shansep MC model

The SHANSEP MC model can be set with two drainage types: *Drained* and *Undrained A*. The computed stress paths for the *Drained* and *Undrained A* models are identical. The SHANSEP MC model, which is a total stress analysis model, is not appropriate for simulating a one-dimensional consolidation tests.

In total, the results of two triaxial UU tests, using three cell pressures in each test, were reproduced in SoilTest, both with the *Undrained A* drainage settings. The results of the calibration for the triaxial tests UU1 and UU2 is shown in Figures 3.19 and 3.20.

The initial values are derived from the laboratory tests were taken as in Table A.3 in A. In each triaxial test, the computed G/S_u value was different and equal to the one directly derived from the test, while α and m parameters were calibrated to a one, constant value. Eventually, all these parameters were calibrated to one value, which gave the best fit for all the stress paths.

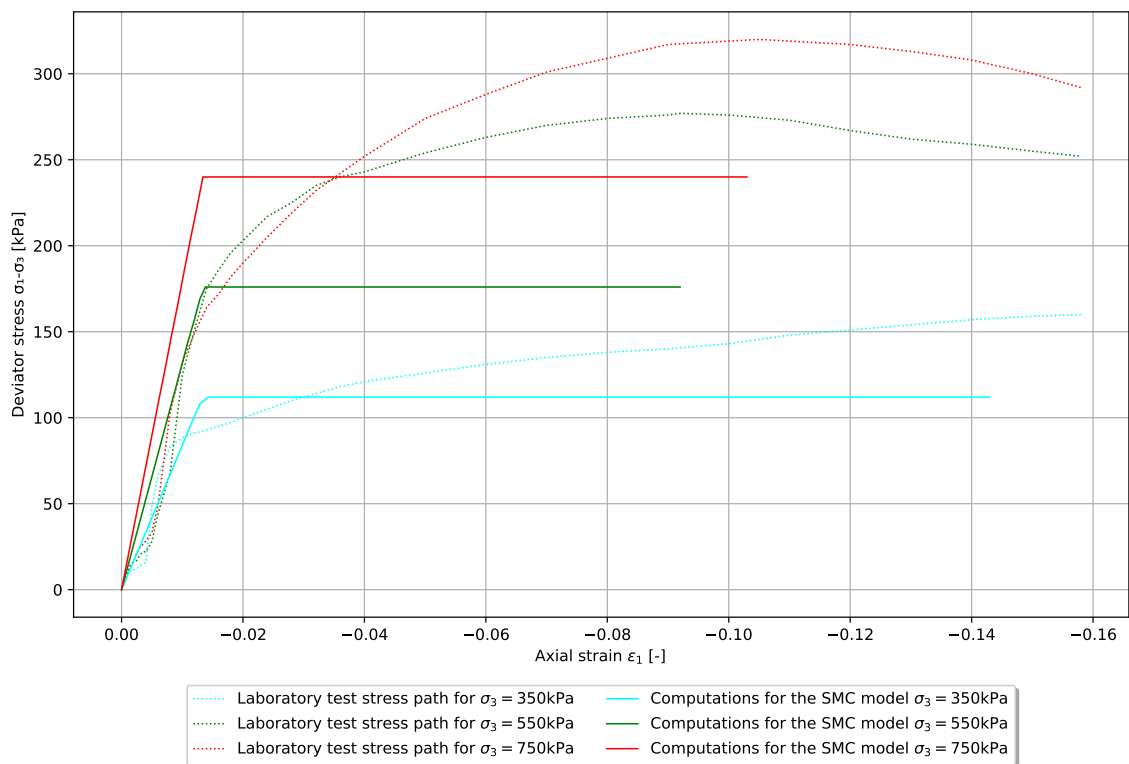


Figure 3.19: Stress paths computed for the calibrated SHANSEP MC model parameters compared to the paths from the laboratory tests - triaxial UU1 test.

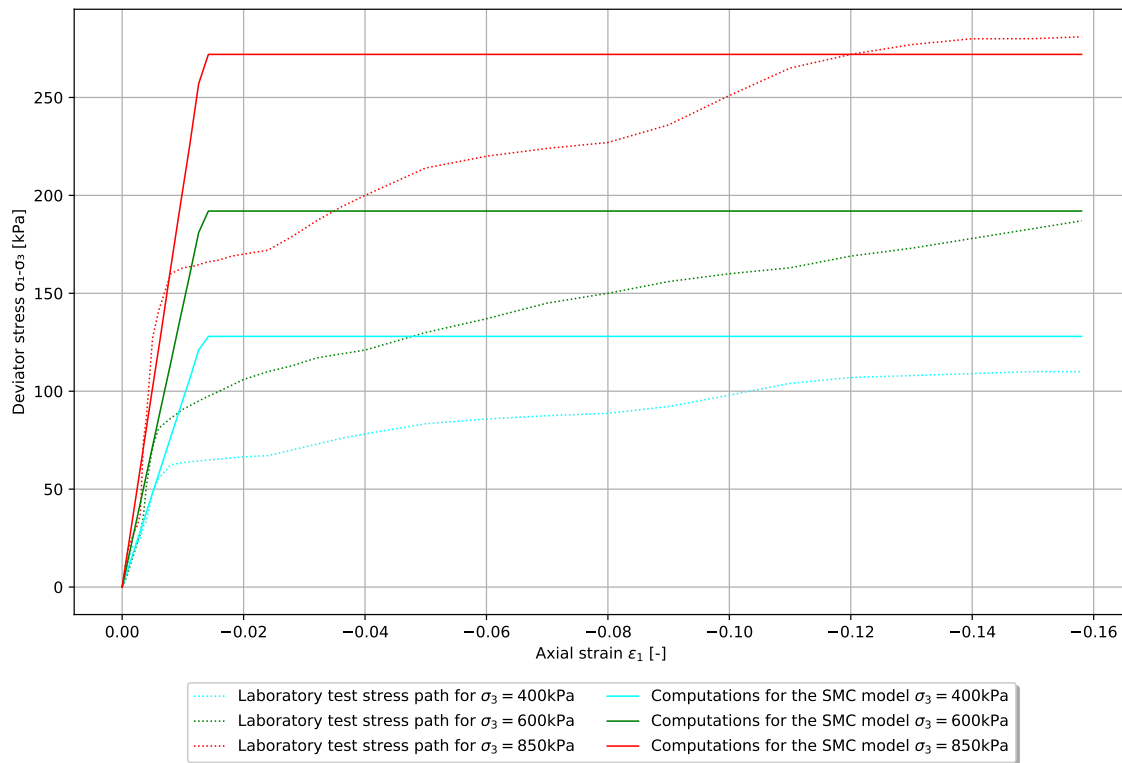


Figure 3.20: Stress paths computed for the calibrated SHANSEP MC model parameters compared to the paths from the laboratory tests - triaxial UU2 test.

The material model parameters calibrated for those two triaxial tests do differ from each other significantly. The final calibrated input parameters for SHANSEP MC model are the average values from those two triaxial tests and are shown in Table 3.13 below.

Parameter type	Symbol	Initial Estimate	Optimised Estimate	Unit
Mohr-Coulomb model parameters	G	4.89	4.89	[MPa]
	ν'	0.35	0.35	[-]
	φ	22.0	22.0	[°]
	c	1.0	1.0	[kPa]
	ψ	0	0	[°]
	σ_t	0	0	[kPa]
SHANSEP parameters	α	0.22	0.16	[-]
	m	0.80	0.79	[-]
	G/S_u	135	50.0	[-]
	$S_{u_{min}}$	5.0	5.0	[kPa]
	OCR_{min}	1.0	1.0	[-]

G/S_u parameter was changed from the calibrated value of 45 to the value of 50, because the lower value was causing a calculation errors.

Table 3.13: The initial and the calibrated parameters of the SHANSEP MC model.

3.3.6. Calibration of the parameters of the GHS model

The GHS constitutive soil model consists of the same set of input parameters as the HSS model. The triaxial CU tests were simulated with the parameters as in the HSS model. The triaxial UU tests were simulated with the internal friction angle set to 0° and the cohesion set to the effective cohesion, i.e. the s_u parameter as in HSS *Undrained B* model. The GHS model has two drainage settings types: *Drained* and *Undrained A*, whereas the computed stress paths are identical for both settings. Also, the GHS model has several other functionalities, which were studied further in this section.

To investigate how the GHS models' switches influence the stress/strain output generated in SoilTest facility, all of the possible variations have been considered. The plasticity model setting 1 has been omitted since it is the Mohr-Coulomb failure criterion with no hyperbolic stress-strain relation. In total, 28 sub-variations for each strain-dependency of stiffness setting could be distinguished, so in total 56 sub-variations.

The comparison between stress paths obtained with the selected GHS variations, the HSS material model and the ones obtained in laboratory tests are shown in Figures 3.21 and 3.22.

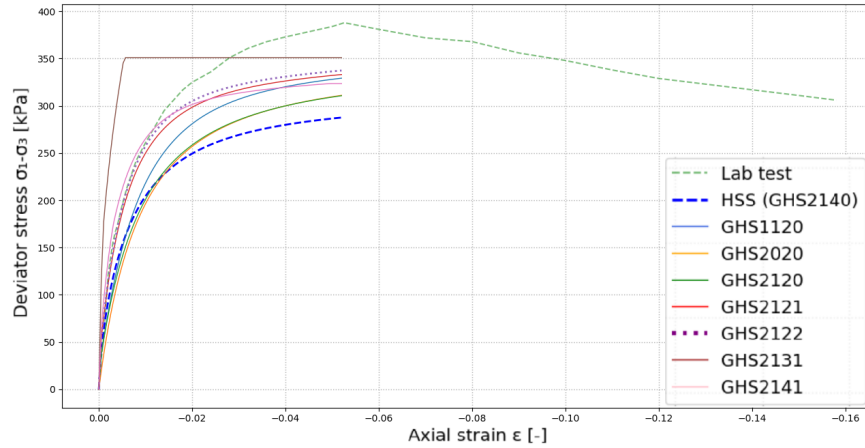


Figure 3.21: Stress paths for the calibrated parameters of the HSS model and the selected GHS model variations - triaxial CU2 test at $\sigma_3 = 450$ kPa.

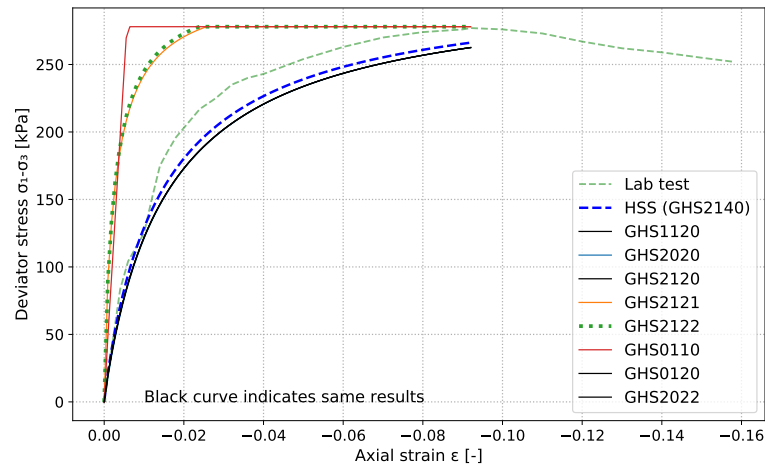


Figure 3.22: Stress paths computed for the calibrated parameters of the HSS model and the selected GHS model variations - triaxial UU1 at $\sigma_3 = 550$ kPa.

The plasticity models with no shear hardening (Formulae 1 and 3) do not have hyperbolic behaviour. Formula 4, which incorporates both shear and cap hardening, produces higher deviator stress than Formula 2. The original (HS) stress-dependency formula results in the smallest deviator stress, while adding pre-consolidation stress makes it higher, and changing the lower principal stress with the mean effective stress also increases the deviator stress slightly. The difference in the triaxial UU tests was much bigger than in the triaxial CU tests. Furthermore, the deviator stress was higher when it was updated in each calculation phase than when it is updated in each step. Deactivation of small-strain stiffness makes the deviator stress lower than in the real tests, for both triaxial tests types.

The GHS model variation, which had the best fit with stress paths obtained in the laboratory tests, is the GHS1120 model. The performance of this material model is shown in Figures 3.23, 3.24, 3.25 and 3.26. The parameters of all of the representative tests, which were used for the calibration are as in the HSS model. The calibration method is also the same as for the HSS model.

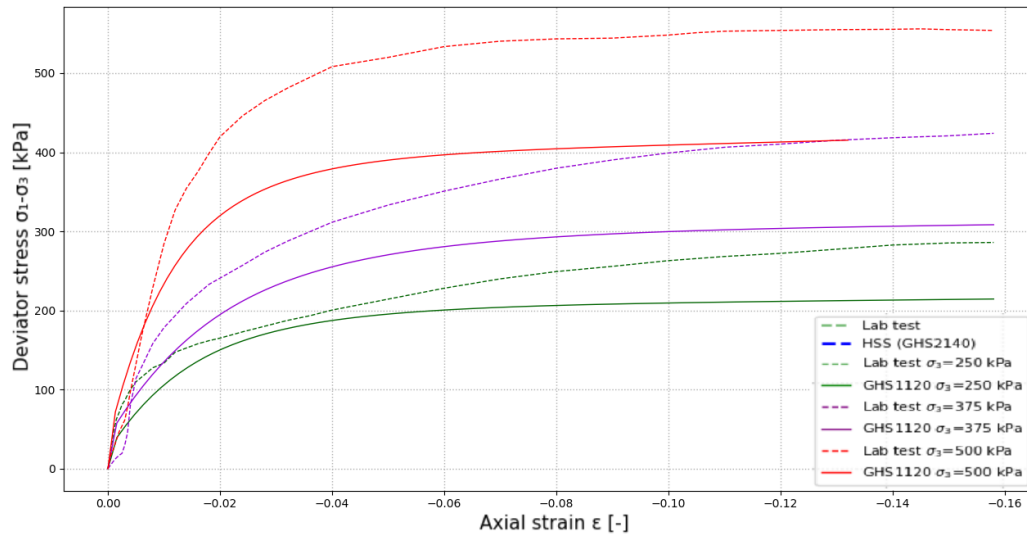


Figure 3.23: Stress paths computed for the calibrated GHS1120 model parameters compared to the paths from the laboratory tests - triaxial CU1 test.

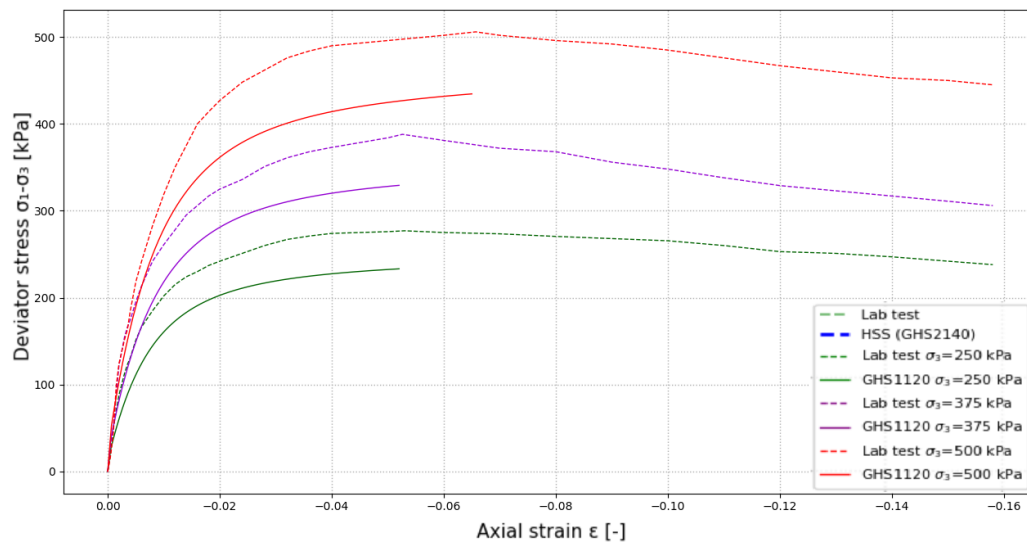


Figure 3.24: Stress paths computed for the calibrated GHS1120 model parameters compared to the paths from the laboratory tests - triaxial CU2 test.

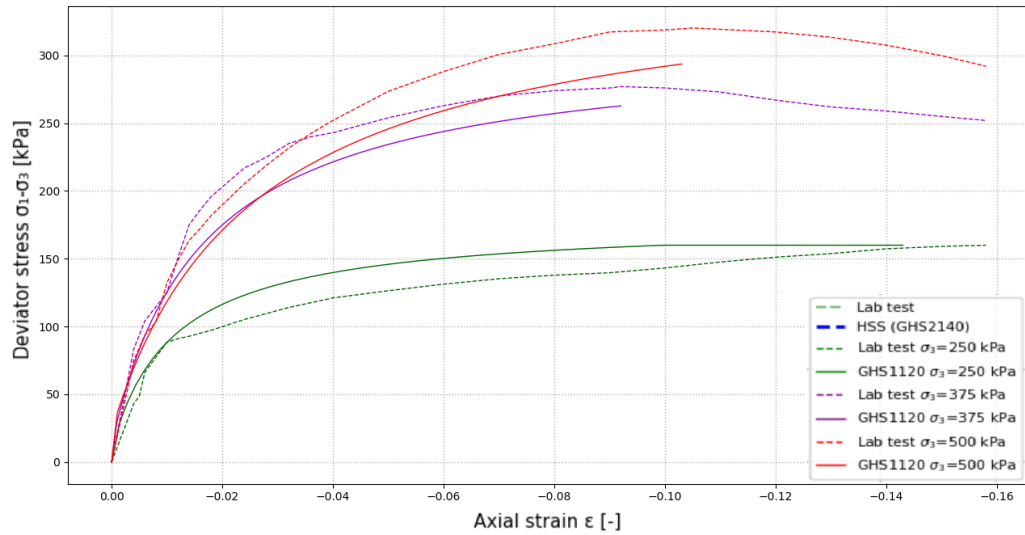


Figure 3.25: Stress paths computed for the calibrated GHS1120 model parameters compared to the paths from the laboratory tests - triaxial UU1 test.

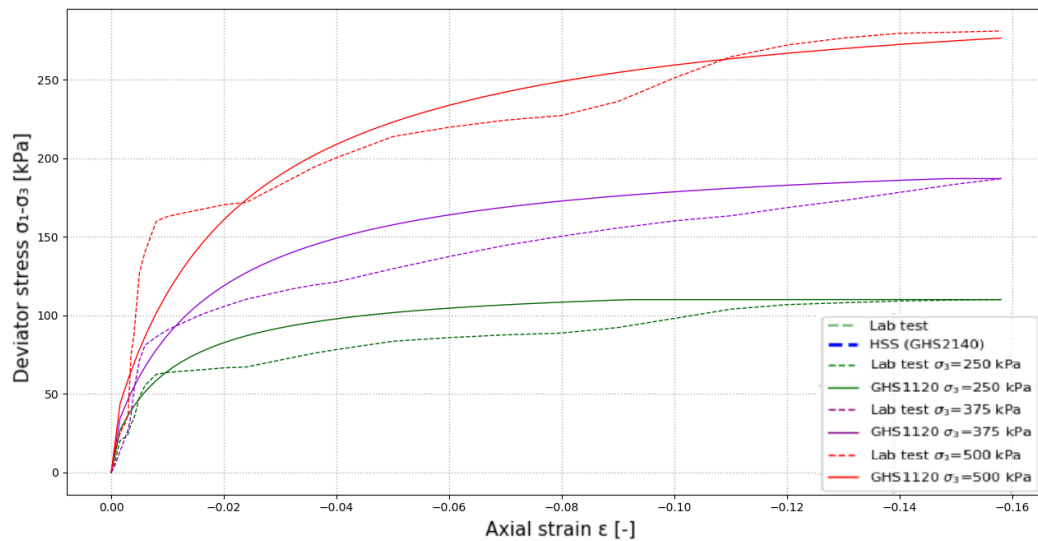


Figure 3.26: Stress paths computed for the calibrated GHS1120 model parameters compared to the paths from the laboratory tests - triaxial UU2 test.

The calibrated input parameters for the GHS model are same as for the HSS model presented in Table 3.11. The drainage settings used for the GHS model is the *Undrained A* type.

In addition to the calibration presented above, a comparison of models with and without activated small-strain stiffness is given. The comparison between GHS2021 and GHS2121 models is shown on triaxial CU2 test in Figure 3.27 and the comparison between GHS1020 and GHS1120 models are shown on the triaxial UU1 test in Figure 3.28.

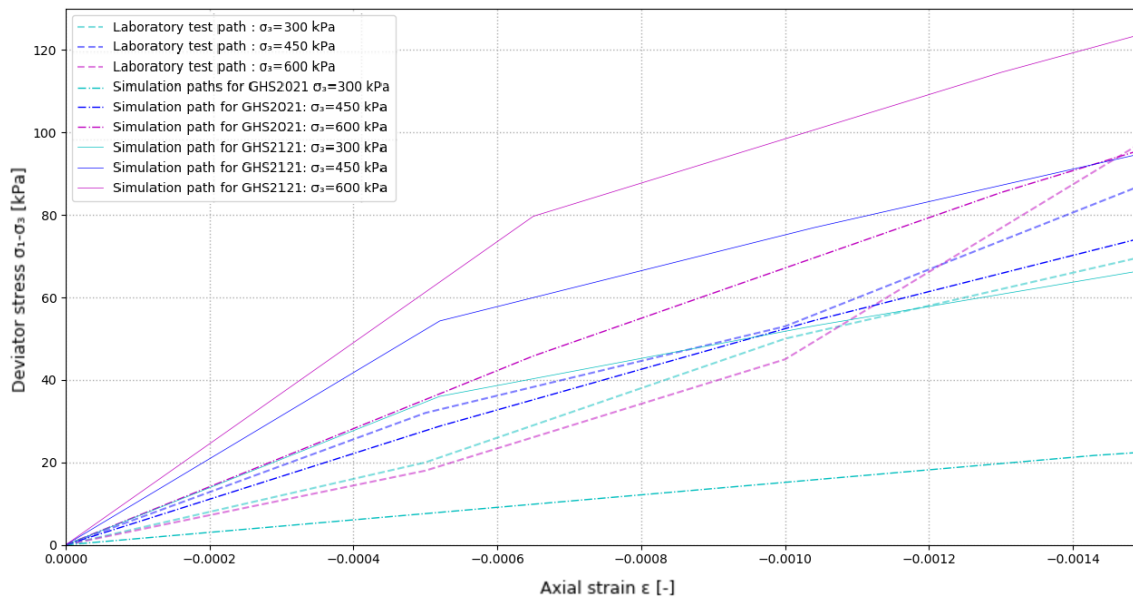


Figure 3.27: Stress paths for the small strain range for the calibrated GHS2021 and GHS2121 models' parameters compared to the stress path from the laboratory test - triaxial CU2 test.

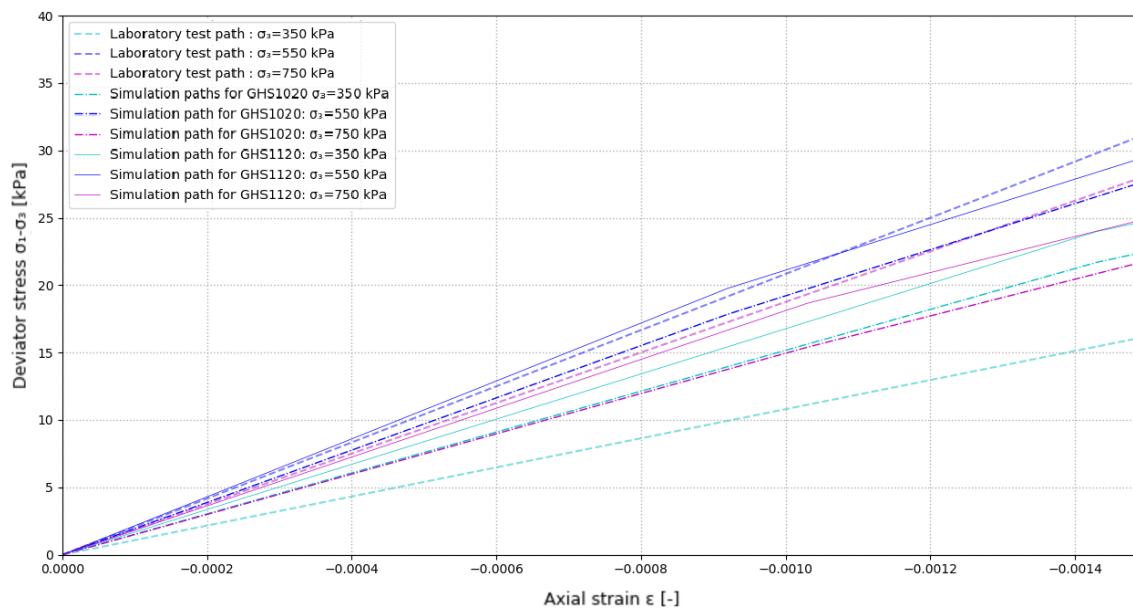


Figure 3.28: Stress paths for the small strain range for the calibrated GHS1120 and GHS1121 models' parameters compared to the stress path from the laboratory test - triaxial UU1 test.

Based on the comparison of the computed and real stress paths, it cannot be stated if the small-strain stiffness should or should not be activated. Nevertheless, according to Yo-Ming Hsieh et al. (2017) [43], ignoring small-strain stiffness can overestimate deformations by as much as 80%, leading to conservative and costly design (the case of deep excavation in silty clay). The influence of the activation of the small-strain stiffness was further investigated in the full 2D Plaxis analyses.

3.3.7. Comparison of the models performance

Both the HSS and the GHS1120 models were capable of reproducing the triaxial tests' results in terms of the effective stress, and the computed stress paths imitate the laboratory test curves very accurately compared to the other models.

The comparison between performance of the HSS and GHS models is shown on the triaxial CU2 test at the cell pressure $\sigma_3 = 550$ kPa in Figure 3.29.

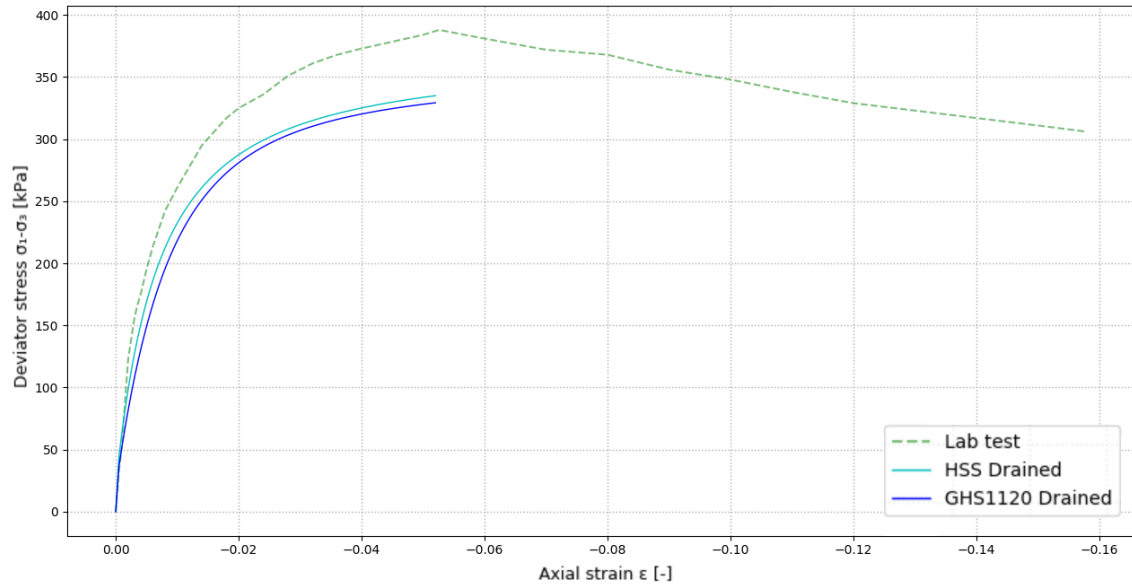


Figure 3.29: Comparison of the performance of the calibrated HSS and GHS models parameters - triaxial CU2 test at $\sigma_3 = 450$ kPa.

The NGI-ADP model is suited to the calculations in terms of the undrained analysis only. The values of the stiffness parameters (apart from the G_{ur}/s_u^A parameter) derived from the laboratory tests were higher than a reasonable range of these parameters, what is caused by a limited laboratory tests data.

The SHANSEP MC model lacks the hyperbolic behaviour for all the parameter combinations. Therefore, for most levels of strain, the computed deviator stress was relatively far away from the real one. However, the deviator stress for the small-strain range in the triaxial tests was reproduced accurately, so the SHANSEP MC model is a better choice than the NGI-ADP model.

The performance of all four material models considered is presented on the triaxial UU1 test at the cell pressure $\sigma_3 = 450$ kPa in Figure 3.30.

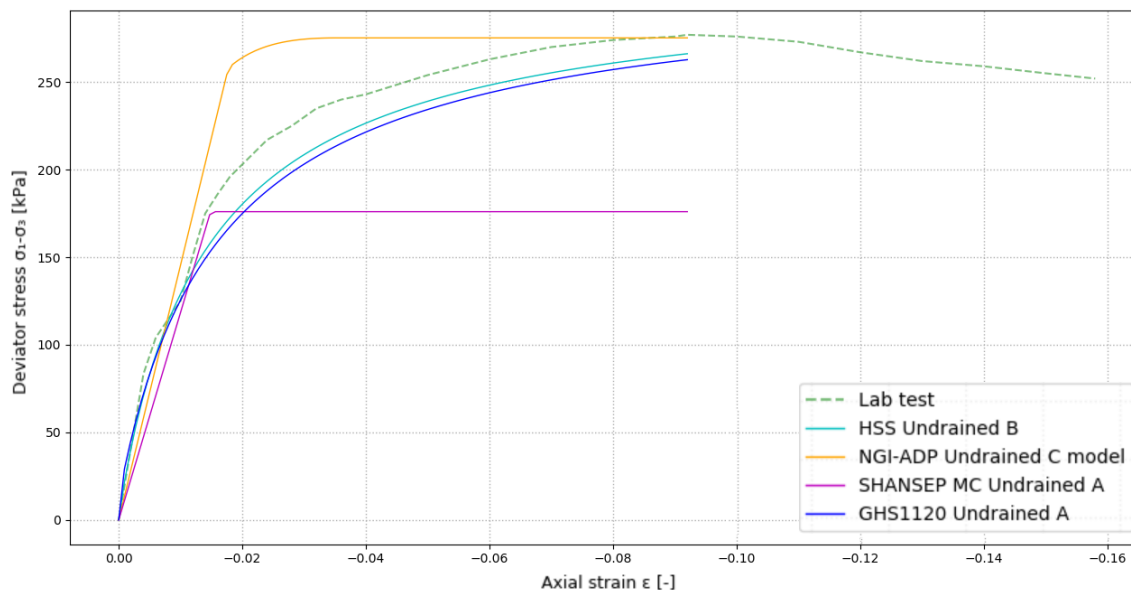


Figure 3.30: Comparison of the performance of the calibrated HSS, NGI-ADP, Shanssep MC and GHS1120 models' parameters - the triaxial UU1 test at $\sigma_3 = 550$ kPa.

The HSS model, compared to the HS model, incorporates the small-strain stiffness and is the best standard material model for deep excavation applications (loading/unloading problems) [73]. Also, it is possible to fully calibrate its parameters using the triaxial test only. However, applying it in undrained calculations using Undrained B brings difficulties in the calibration of undrained parameters, especially in problems associated with an extension. Another disadvantage is that the stiffness based on σ'_3 only is often underestimated in unloading problems.

The advantage of the NGI-ADP model is a direct input of the undrained shear strength, which can be depth-dependent. In addition, the initially mobilised shear strength τ_0^A/s_u^A can be changed, which has a major impact on initial stiffness. The model can also be merged with the SHANSEP concept what has been widely used in the dikes design. A disadvantage of this model is the complexity of its calibration due to the many types of tests needed. Also, for not horizontal (inclined) soil layers, usage of the depth-dependency of the undrained shear strength leads to a non-realistic distribution of the undrained shear strength.

The SHANSEP MC model, contrary to the MC model, gives a realistic way of modelling the undrained shear strength according to the major principal stress σ'_1 and stress-dependent stiffness based on the S_u parameter. However, the SHANSEP MC failure criterion is limited to the Mohr-Coulomb criterion. Also, the SHANSEP concept is unsuitable for modelling behaviour of a highly sensitive clays and cemented clays in which deformation modifies their structure[81].

The GHS model allows the user to keep a chosen stress-/strain-dependency of stiffness setting, stress-dependency formulae and plasticity models depending on the considered case making it more problem-specific. Another advantage is that the stress-dependency formula can incorporate the mean effective stress or pre-consolidation stress, which can help to solve the problem of stiffness reduction due to low minor principal stress σ_3 . A disadvantage of the GHS model is that it is less robust than the HSS model, i.e. it requires more understanding, knowledge and user experience than the HSS model. Also, it is not possible to perform undrained calculations based on the undrained shear strength.

3.4. Conclusions

The main differences regarding the excavation problems between the four material models, which were investigated in this section, are summed up in Table 3.14 below.

Aspect	HSS	GHS	NGI-ADP	SHANSEP MC
Analysis type	Effective stress analysis		Total stress analysis	
Stress-dependency of stiffness	σ_3	σ_3 or σ_3 and p' or σ_3 and p_c	G_{ur} / s_u^A	G/S_u where S_u is updated based on σ'_1
Stiffness in undrained calculations	Constant (Undrained B)	Stress-dependent	Depth-dependent (via s_u)	Stress-dependent (via s_u^A)
Calculations of the undrained shear strength	Depth-dependent (Undrained B)	-	Depth-dependent	Stress-dependent
Plasticity model	MC + cap + hardening	MC + / cap + / hardening	Tresca + hardening	MC
Laboratory tests required	Triaxial test or Oedometer test	Triaxial test, DSS or Cyclic triaxial test and extension test	Undrained DSS or Cyclic triaxial test and undrained compression test	Triaxial undrained test or Oedometer test

Table 3.14: Differences between the material models.

The conclusions formulated specifically for the considered triaxial tests, including the limitations of using only primary loading kind of tests, are:

- The GHS1120 model captured the stiffness in the small-strain range (ε_1 up to 0.5%) best from all of the models. The HSS model also gave a very good estimation of stiffness in that range, whereas the best estimation for the total stress analysis was received for the SHANSEP MC model.
- Regarding the stress-dependency formulae tested on the available triaxial tests, the most accurate estimation of deviator stress at strain between 0.0% and 0.5% was received for stiffness calculated based on the lower principal stress and the pre-consolidation stress.
- Plasticity models 1 and 3 do not include shear hardening, hence do not capture a hyperbolic behaviour of soil. For the triaxial tests' considered, Formula 2 (without cap hardening) more accurately simulated the stiffness in the small-strain range and was more conservative.

The conclusions formulated concerning the specific, deep excavations application considered are:

- The difference between updating the stiffness in each calculation step and each calculation phase is almost negligible and is slightly less conservative in the second case. In unloading problems, this difference is a result of omitting computations of relaxation of the soil domain caused by reducing the vertical effective stress in each step. Considering the small difference in computed stress, the usage of stress-dependency formula updating stiffness in each phase can increase computation's robustness. The influence of this setting should be studied for each problem individually.
- For the undrained analysis, both the stiffness and the undrained shear strength is depth-dependent in the NGI-ADP model and stress-dependent in the SHANSEP MC model. In the Undrained B settings of the HSS model, the undrained shear strength is depth-dependent (what is quite often ignored by the users), but the stiffness is constant according to the input.

4

Target measurements in the 2D finite-element model

4.1. Introduction

4.1.1. Finite-element model and construction phases

The two-dimensional finite-element model, which is used in the further calculations, is as shown in Figure 4.1 below. Two loads are considered in the model, namely: a building load of 400 kN/m^2 and a surface load of 20 kN/m^2 .

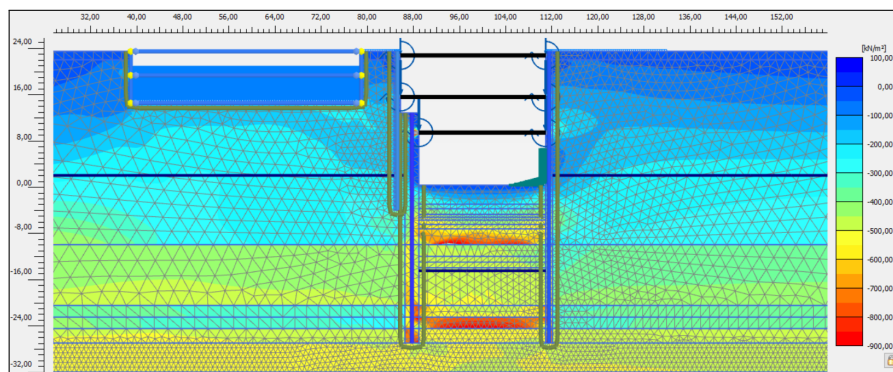


Figure 4.1: The effective stress distribution in the two-dimensional Plaxis model.

In Table 4.1 all of the construction phases used in the computations are shown. Phases from 0 to 15 were modelled and compared with the measurements from the site, and were used in the inverse analysis. Phases from 16 to 25 are scheduled to happen latter and were not a part of the inverse analysis.

Phase	Description
0	Initial Phase
1	Building Load
2	Surface Load
3	D-wall installation
4	Excavation to +20.45 m
5	Strut N1 installation at +22.75 m
6	Excavation to +14.55 m
7	Strut N2 installation at +15.55 m
8	Excavation to +8.40 m
9	Strut N3 installation at +9.40 m
10	Excavation to +2.00 m
11	Dewatering to -14.50 m
12	Excavation to +0.30 m
13	Strut N4 installation at +1.30 m
14	Excavation to -3.00 m
15	Excavation to -5.75 m

Table 4.1: Construction phases as in the Plaxis 2D model.

In addition, ten construction phases were distinguished, which modelled casting the base slab, the walls and roof inside the pit, dismantling the struts, stopping the dewatering process and back-filling to the ground level. However, these phases are irrelevant in the inverse analysis procedure and are omitted. The phase 15 is characterised by the lowest factor of safety, because the excavation level reached is the deepest from all phases considered. The evolution of the building displacements throughout the excavation steps is shown in Figure 4.2 below.

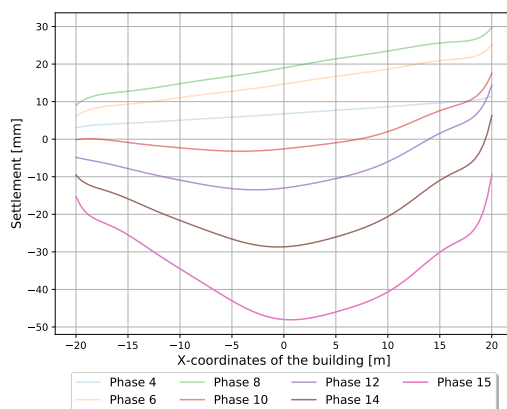


Figure 4.2: The evolution of the building displacements throughout the excavation steps for the SHANSEP MC Undrained A model.

There were two drainage settings distinguished: up to 12th phase the behaviour is modelled as drained since the excavation has not reached the cohesive layer and no significant deformations happened yet, and up to phase 12, and from phase 13 onward, the excavation inside of the pit starts to proceed in the clay layer, hence the behaviour is modelled as undrained from this point onward. The type of drainage has a significant impact on the material models, which can be modelled in a twofold manner (as drained and undrained), such as the HSS model.

Furthermore, a dominant behaviour inside and outside of the d-box is different. Due to swelling of the clay layer and the resulting movement of the diaphragm walls, the clay layer behaviour inside and outside of the d-box is different, namely extension in the inside and compression outside of the d-box.

When a chosen model's drainage type is drained, stiffness properties are automatically configured according to confining pressure. However, for the HSS model's *Undrained B* configuration, the stiffness needs to be input manually. Therefore, depending on the model, different drainage configurations and different material model properties are applied in specific phases. This is summed up in Table 4.2 below.

Material model	Material model's settings			
	Phases 0 - 12		Phases 13 - 15	
	Inside the d-box	Outside of the d-box	Inside the d-box	Outside of the d-box
HSS	Drained		Undrained B***	Undrained B**
NGI-ADP	Drained		Undrained C	
SHANSEP MC	Mohr-Coulomb		Shansep MC - Undrained A	
GHS	Undrained A*		Undrained A	

"*" denotes that the undrained behaviour is ignored.

"**" denotes that the values are taken for compression as shown in Table 3.11.

"***" denotes that the values are taken for extension, i.e. as one-third of the compression values adjusted to the stress level of 400 kPa.

Table 4.2: Configurations of material model parameters and drainage approach depending on construction phases.

For a comparison between different material models' performance, displacements for two phases are considered. The first is phase 12, which is the last phase characterised by drained behaviour, and the other is phase 15, which is the last in general and is modelled as undrained.

4.2. Material models' performance comparison

4.2.1. Simulations with different material models

The material models' parameters used in the following computations were as in Tables 3.11 - 3.13. In order to compare the performance of different material models used, the displacements were checked for construction phases 12 and 15 (see Table 4.1).

The comparison between the performance of the four material models was made in a twofold manner: concerning settlements of the building adjacent to the excavation (Figures 4.3 and 4.4) and the diaphragm wall deflections (Figures 4.5 and 4.6). In addition, the evolution of the building displacements throughout the excavation steps is shown in Figure 4.7.

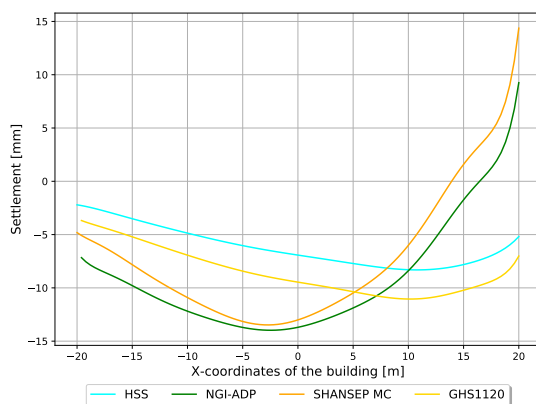


Figure 4.3: Comparison of the computed settlements of the building for different material models - phase 12.

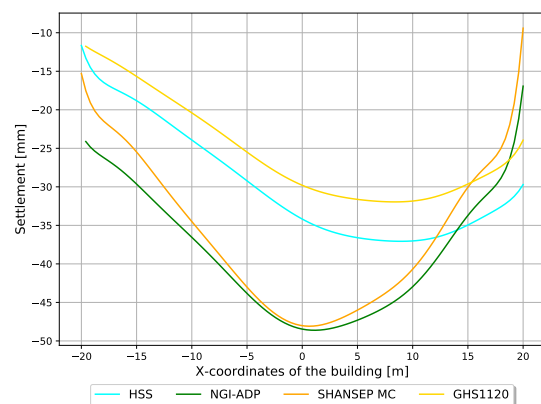


Figure 4.4: Comparison of the computed settlements of the building for different material models - phase 15.

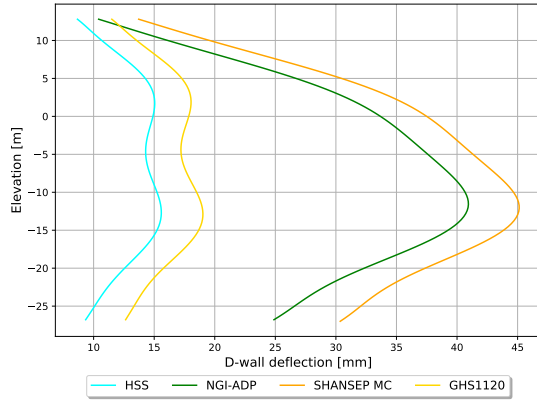


Figure 4.5: Comparison of the computed d-wall deflections for different material models - phase 12.

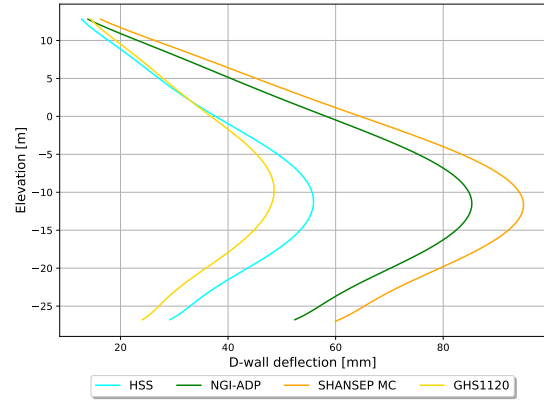


Figure 4.6: Comparison of the computed d-wall deflections for different material models - phase 15.

For this specific case, the total stress methods, i.e. the NGI-ADP and SHANSEP MC models, gave much larger diaphragm wall's deflections than the models based on the effective stress analysis, i.e. the HSS and GHS models. The building settlements size is also larger for the NGI-ADP and SHANSEP MC models, but also the shape of the deflections curve is different. The total stress analysis models have foreseen heave of the front part of the building, whereas the other models computed almost uniform settlements.

Another point is that both Phase 12 and Phase 15, the results for the HSS and GHS models are very similar, even though in phase 15, the GHS1120 model is set with the *Undrained A* drainage type, whereas the drainage behaviour of the HSS model was set to *Undrained B*. This means that for the given parameters' set, there is no big difference between the drained and the undrained computations for the given parameters sets. Using the drained model may help to make the inverse analysis process more manageable by reducing the number of parameters used, hence reducing the number of unknowns.

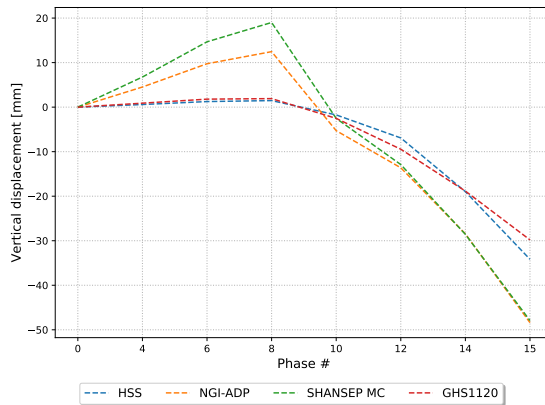


Figure 4.7: The evolution of the displacements of the building (middle node) throughout the excavation steps for different material models.

As seen in Figure 4.7 on the left, there is a strong coherence of computed displacements between the HSS and GHS material models (the effective stress analysis models) and between the NGI-ADP and SHANSEP MC models (the total stress analysis models). In the first three unloading phases (phases 0 to 8), the cap surface was reached in much more spots in the total stress methods than for the effective stress analysis. In the later four unloading phases (phases 10 to 15), the failure was observed in relatively more places in the soil domain for the total stress methods.

The resulted displacements are caused by a difference in computed stiffness and mobilised shear strength. In all of the unloading phases, the computed stiffness was higher in all the distinguished soil layers for the total stress methods, while the mobilised shear strength was similar for both methods in all layers, but the clay layer in which the effective stress methods shown higher values.

Two reasons for such a high difference can be considered. Firstly, the way how the stiffness is computed in those two methods, i.e. governed by σ'_3 in effective stress methods, σ'_1 in the SHANSEP MC and both principal stresses in the NGI-ADP model. Also, for the total stress methods, the ratio of σ'_1 to σ'_3 computed in the FE model was lower than for the effective stress methods and the computed principal effective stresses

were higher for the total stress methods. Secondly, the NGI-ADP and SHANSEP MC material models were calibrated based on limited soil data. Hence, the calibrated parameters, especially related to the shear strain, might be inaccurately assessed.

4.2.2. Simulations with different GHS model settings

In addition to the comparison between different GHS model settings was based on the SoilTest facility only, another comparison between a different GHS model settings performance was made by checking the building settlements (Figures 4.8 and 4.9) and the diaphragm wall deflections (Figures 4.10 and 4.11).

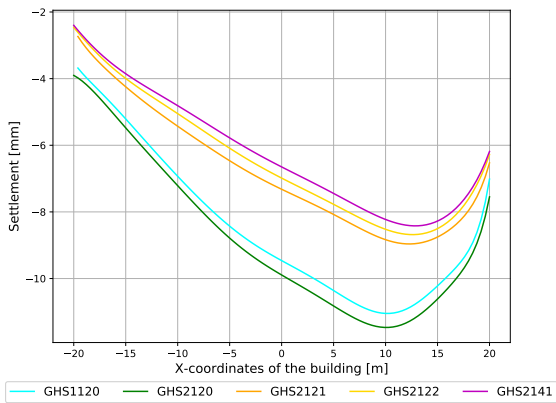


Figure 4.8: Comparison of the computed settlements of the building for different settings of the GHS model - phase 12.

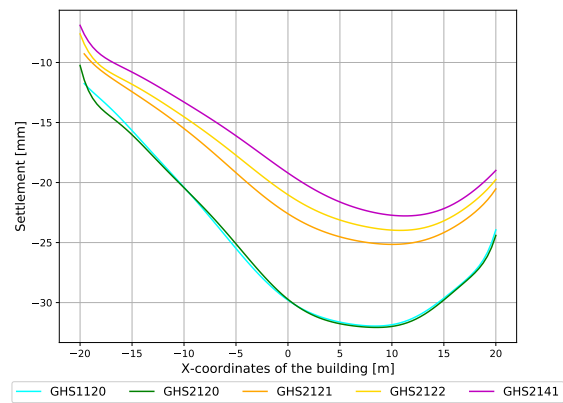


Figure 4.9: Comparison of the computed settlements of the building for different settings of the GHS model - phase 15.

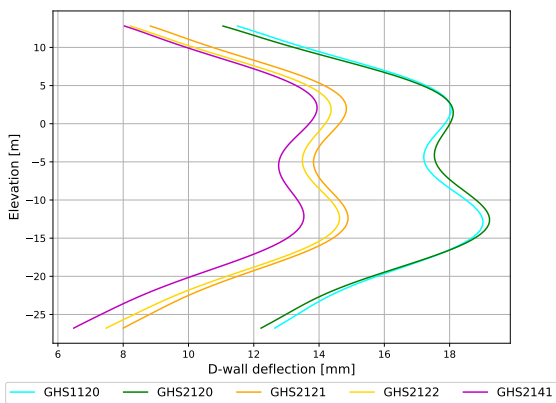


Figure 4.10: Comparison of the computed d-wall deflections for different settings of the GHS model - phase 12.

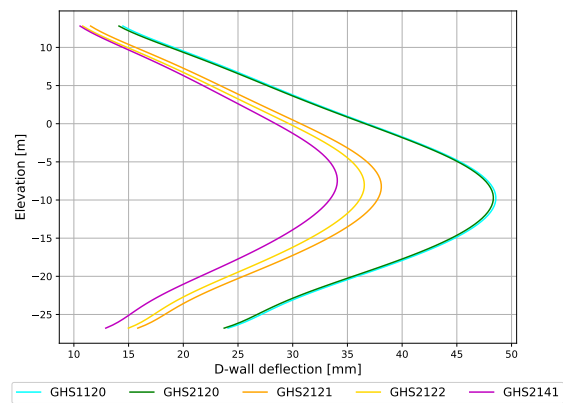


Figure 4.11: Comparison of the computed d-wall deflections for different settings of the GHS model - phase 15.

An additional comparison between the models HSS, GHS2140, GHS2141, GHS2142 and GHS2040 was made. Analogically to the previous computations, also in here four plots (Figures 4.12, 4.13, 4.14 and 4.15) are used to compare the model behaviour.

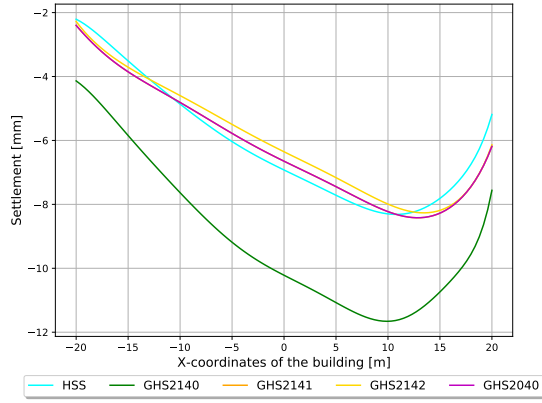


Figure 4.12: Comparison of the computed settlements of the building for different settings of the GHS model - phase 12.

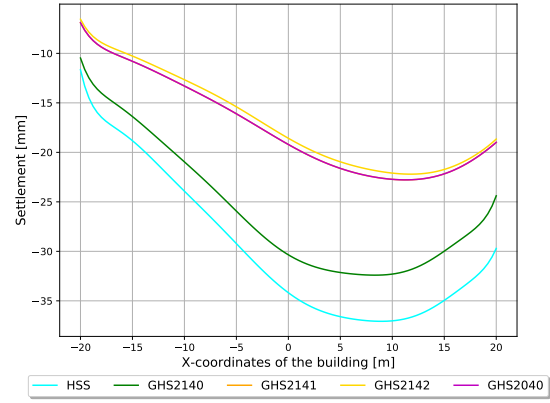


Figure 4.13: Comparison of the computed settlements of the building for different settings of the GHS model - phase 15.

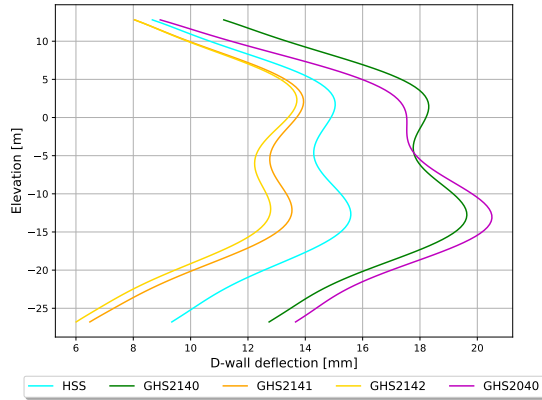


Figure 4.14: Comparison of the computed d-wall deflections for different settings of the GHS model - phase 12.

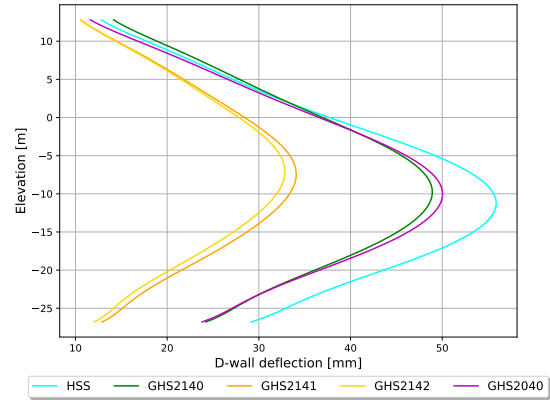


Figure 4.15: Comparison of the computed d-wall deflections for different settings of the GHS model - phase 15.

Regarding the simulations with the GHS model, following observations have been drawn:

- Due to a higher deviator stress computed, the usage of the stiffness formula incorporating the mean stress p' and the pre-consolidation stress p_c generates smaller displacements than the formula incorporating lower principal stress σ_3 only (as in the HS model) and the formula incorporating lower principal stress σ_3 and the pre-consolidation stress p_c .
- The usage of the model with no small-strain stiffness (GHS2040) resulted in very similar d-wall displacements as the one with small-strain stiffness activated (GHS2140) for phase 12. However, the computed building displacements were much higher for the GHS2140 model for phase 15.
- When stiffness is updated in each phase instead of each step, the diaphragm wall deflections computations are more conservative, and the computations are faster.

4.3. Sensitivity analysis of the input parameters

To verify, which material model parameters has the highest influence on the diaphragm wall displacements, simplified sensitivity studies were performed. The procedure was to decrease and increase all of the considered material models' parameters values by 25%. Then, the average difference of the output is translated into the factor of how each parameter influences the displacements. Sensitivity studies are divided into two parts: sensitivity of the parameters in the drained calculations, i.e. phases from 0 (the initial one) to the phase 12 (excavation to +0.30 m), and sensitivity of the parameters in the undrained calculations, i.e. phases from 13 (Strut N4 installation at +1.30 m) onward.

The output of each parameters' variation is judged by the error between the computed results and the established, constant synthetic observations. For the building settlements, there are three values, which are being compared, namely: the settlements of the front, the middle and the rear part of the building. For the d-wall deflections, there are five different similarity measures [47] and one additional value, which is a weighted average of those five measures.

The errors are measured in the same way for both phases (12 and 15), i.e. they are compared to the observations made at the end of phase 12. Although comparing different phases does not provide any information on the accuracy of the results, it provides certain values for different parameters sensitivity, what is the ultimate goal of this section.

The next step is to relate the difference in the computed errors between the initial and a new value expressed in percentages to the relative change the parameter value. Afterwards, having these ratios for each considered material models' parameters, the numerical proportion between these ratios is derived, which is the final sensitivity of each parameter.

In addition, the sensitivity of different model parameters can also be investigated via the built-in Plaxis feature called *Sensitivity and parameter variation*. This feature allows to investigate sensitivity based on horizontal, vertical and total displacements, stress-strain relations or reached force/moment values in an arbitrarily chosen nodes. Also, construction phase can be chosen, which one should be the criterion for the analysis.

In order to calculate a sensitivity values, a program runs a significant number of simulations with different values of a chosen parameters. The higher number of chosen parameters, the higher number of variations to be studied; hence, a time needed for computation can reach days or even weeks. However, the accuracy of this method is undoubtedly higher than the one demonstrated in the latter part of this paragraph.

4.3.1. Error measurement method

In order to assess how the observed and computed results are close to each other, the measurements and computations of the settlements in the three parts of the building and the deflections of the diaphragm wall adjacent to this building were used.

Measuring how close are the computed building's settlements to the synthetic measurements is done by subtracting the computed settlements from the established measurements. The resulting negative values mean that the computed settlements are bigger. However, to compare the exemplary and the computed d-wall deflection, one needs to take into account all of the characteristics of the curves, i.e. shape, arc-lengths and distances between curves at different depths. Some of the complexities that may lead to the need for incorporating more sophisticated similarity measures are:

- The measurements from the site may not cover the same section of the d-wall as the one which is computed in Plaxis;
- Curves can have multiple deflection points, and these can be localised at different depths;
- Not only the maximum/minimum deflection is important, but also the general shape of the deflection curve, which has a significant meaning for the adjacent buildings settlements.

The d-wall deflections comparison first starts from interpolating through the measurements from the site and the FE software. Both are described as a set of points containing depth and corresponding deflection. In order to derive a smooth curve showing the deflections in-depth, coefficients of a eleventh-degree polynomial are fitted to this data, and corresponding deflections readings are matched to these coefficients. Afterwards, in order to measure an error between each of the derived curves, several methods for measuring the error have been considered including but not limited to [47]:

- The Hausdorff distance (DH) method: Measures the longest distance one can be forced to travel by an adversary who chooses a point in one of the two sets;
- Partial Curve Mapping (PCM) method: Matches the area of a subset between the two curves [94];

- Area method: An algorithm for calculating the area between two curves in 2D space [47];
- Discrete Fréchet distance (DF): The shortest distance in-between two curves, where one is allowed to vary the speed at which one travel along each curve independently (walking dog problem) [4, 11, 25, 26, 32, 83];
- Curve Length method: Assumes that the only true independent variable of the curves is the arc-length distance along the curve from the origin [5, 15];
- Dynamic Time Warping (DTW): A non-metric distance between two time-series curves that have been proven useful for a variety of applications [8, 35, 71, 80, 82, 91].

In order to be as precise as possible, all five methods were used. The final equation for measuring error is as below:

$$D_{error} = PCM + Area + \frac{DH^2}{3} + 5DF + \left(\frac{DTW}{100}\right)^{\frac{3}{2}} \quad (4.1)$$

4.3.2. Sensitivity of the HSS model parameters

Since there are two drainage types in the model (*Drained* and *Undrained B*), and the dominant behaviour in between the diaphragm walls is an extension, while outside of the d-box the dominant behaviour is compression, sensitivity analysis of eleven input parameters was performed.

Parameter	Sensitivity [%]						
	Phase 12			Phase 15			
	D-wall	Building	AVG	D-wall	Building	AVG	
DCE	E_{50}^{ref}	28.9	5.7	17.3	6.9	4.8	5.8
	E_{oed}^{ref}	4.8	3.6	4.2	3.8	2.8	3.3
	E_{ur}^{ref}	11.1	10.1	10.6	6.4	5.6	6.0
	$\gamma_{0.7}$	13.3	17.9	15.6	5.2	4.6	4.9
	G_0^{ref}	19.1	24.1	21.6	19.3	15.3	17.3
	ϕ	18.0	34.8	26.4	23.7	25.0	24.3
	c	4.8	3.8	4.3	3.6	2.1	2.9
UDC	E_{50}^{ref}	-	-	-	6.5	9.7	8.1
	E_{oed}^{ref}	-	-	-	0.9	0.2	0.6
	E_{ur}^{ref}	-	-	-	5.0	6.6	5.8
	$\gamma_{0.7}$	-	-	-	0.9	1.2	1.1
	G_0	-	-	-	1.5	2.1	1.8
	s_u	-	-	-	2.9	5.3	4.1
	UDE	E_{50}^{ref}	-	-	-	3.0	4.2
E_{oed}^{ref}		-	-	-	0.1	0.1	0.1
E_{ur}^{ref}		-	-	-	7.9	7.7	7.8
$\gamma_{0.7}$		-	-	-	0.4	0.4	0.4
G_0		-	-	-	0.4	0.4	0.4
s_u		-	-	-	1.5	1.9	1.7

The sensitivity criterion *D-wall* stands for the d-wall displacements, *Building* stands for the building settlements, and *AVG* is their average.

DCE is the drained behaviour of clay under both compression and extension. UDC and UDE is the undrained behaviour of clay under compression and extension, respectively. In both cases, the *Undrained B* drainage types were used.

The internal friction angle has been being changed while keeping K_0^{nc} at a constant level of 0.645.

Table 4.3: Sensitivity of the HSS model parameters for construction phases 12 and 15.

For the *Drained* phases (0-11), sensitivity of five input parameters has been analysed: the reference un/reloading stiffness E_{ur}^{ref} , the reference shear stiffness at very small strains G_0^{ref} , the internal friction angle ϕ (with the K_0^{nc} value kept constant) and the cohesion c . For the *Undrained B* phases (12-15), the sensitivity of three input parameters has been analysed: the reference un/reloading stiffness E_{ur}^{ref} , the shear stiffness at very small strains G_0 and the undrained shear strength s_u . This part was repeated independently for the compression- and extension- dominated soil sections.

The computed displacements and errors for the sensitivity analysis used to calculate the sensitivity are separated in two sections. The results for the phase 12, i.e. the last phase modelled as drained in Tables B.1 and B.2, and for the last excavation phase modelled as undrained (phase 15) in Tables B.3 and B.4 in Appendix B.

After performing the procedure explained in the introduction of this section, the independent sensitivity of each input parameter is found. This is shown in Table 4.3, and has been done by varying only one parameter's value, what is a significant simplification of the sensitivity studies.

Apart from the limitations of this method stated above, another limitation is that there are several parameters, which were not included in the analysis, namely: K_0^{nc} , R_f , OCR , m and c_{inc} .

4.3.3. Sensitivity of the NGI-ADP model parameters

In the NGI-ADP model, phases from 0 to 12 are modelled as *Drained* type, whereas phases from 13 to 15 are modelled as *Undrained C* type. Therefore, the sensitivity of two sets of parameters was analysed: the parameter G_{ur}/s_u and the undrained shear strength s_u for both cases, so four different parameters in total.

The computed displacements and errors for the sensitivity analysis, for the phase 12 are summed up in Table B.5 and for phase 15 in Table B.6 in Appendix B. The independent sensitivity of each input parameter is shown in Table 4.4. As previously, this has been done by varying only one parameter's value.

Parameter		Sensitivity [%]					
		Phase 12			Phase 15		
		D-wall	Building	AVG	D-wall	Building	AVG
Drained	G_{ur}/s_u^A	56.6	84.6	70.6	23.7	16.4	20.1
	$s_{u,ref}^A$	43.4	15.4	29.4	7.1	17.3	13.5
Undrained	G_{ur}/s_u^A	-	-	-	11.0	16.1	13.5
	$s_{u,ref}^A$	-	-	-	58.2	50.1	54.2

Table 4.4: Sensitivity of the NGI-ADP model parameters for construction phases 12 and 15.

Sensitivity of parameters γ_f^C , γ_f^E , γ_f^{DSS} , $s_u^{C,TX}/s_u^A$, s_u^P/s_u^A , τ^0/s_u^A , s_u^{DSS}/s_u^A and ν' was not included in the studies.

4.3.4. Sensitivity of the SHANSEP MC model parameters

In the SHANSEP MC, there are two drainage settings possible: *Drained* and *Undrained A*. All of the phases are modelled as *Undrained A*. However, phases from 0 to 12 ignore undrained behaviour. Therefore, the sensitivity of the two parameters was analysed: the parameter α and the parameter G/s_u .

The computed displacements and errors for the sensitivity analysis, for the phase 12 are summed up in Table B.7 and for phase 15 in Table B.8 in Appendix B. The independent sensitivity of each input parameter is shown in Table 4.5 below.

Parameter		Sensitivity [%]					
		Phase 12			Phase 15		
		D-wall	Building	AVG	D-wall	Building	AVG
Undrained	α	51.6	63.3	57.4	64.6	78.3	71.5
	G/s_u	48.4	36.7	42.6	35.4	21.7	28.5

Table 4.5: Sensitivity of the SHANSEP MC model parameters for construction phases 12 and 15.

The parameters, which sensitivity has been not investigated are: m , $S_{u_{min}}$ and OCR_{min} .

4.3.5. Sensitivity of the GHS2142 model parameters

In the GHS model, there are two drainage settings possible: *Drained* and *Undrained A*. All of the phases are modelled as *Undrained A*. Phases from 0 to 12 are modelled to ignore undrained behaviour. The sensitivity of five parameters were analysed: the un/reloading stiffness at a reference pressure E_{ur}^{ref} , the secant stiffness at a reference pressure (while keeping the initial ratio between E_{50}^{ref} , E_{oed}^{ref} and E_{ur}^{ref}), the undrained shear strength s_u , the internal friction angle ϕ and the cohesion c .

The computed displacements and errors for the sensitivity analysis, for the phase 12 are summed up in Table B.9 and for phase 15 in Table B.10 in Appendix B. The independent sensitivity of each input parameter is shown in Table 4.6 below.

Parameter	Sensitivity [%]					
	Phase 12			Phase 15		
	D-wall	Building	AVG	D-wall	Building	AVG
E_{50}^{ref}	2.6	3.5	3.0	1.8	3.2	2.5
E_{oed}^{ref}	22.8	24.1	23.5	28.6	25.2	26.9
E_{ur}^{ref}	19.2	23.1	21.1	22.4	25.2	23.8
$\gamma_{0.7}$	14.3	13.7	14.0	14.5	15.6	15.0
G_0^{ref}	19.6	12.7	16.2	5.1	6.6	5.9
ϕ	19.7	20.7	20.2	22.8	22.1	21.9
c	1.8	2.3	2.0	4.8	3.2	4.0

Table 4.6: Sensitivity of the GHS2142 model parameters for construction phases 12 and 15.

The parameters which were not taken into account are: K_0^{nc} , R_f , OCR , POP , m , v_{ur} and c_{inc} .

4.4. Summary and the model selection

4.4.1. Conclusions regarding the material models' performance

Based on the computed displacements, it was observed that the soil response in the total stress methods was stiffer than in the effective stress methods causing a higher heave in the beginning and higher settlements in the latter parts. The discrepancies between the results can be caused by the fact that the stiffness is updated based on a different principle stresses, i.e. either σ'_1 or both σ'_1 and σ'_3 in the total stress analysis compared to σ'_3 only in the HSS model and because of calibration of the NGI-ADP and the SHANSEP MC models based on limited soil data (especially, concerning the shear parameters).

The computation time needed for the FE model run is of utmost importance in the inverse analysis and this time depends not only on the model but also on the given parameters set. For the GHS model, the computation time differs also between its stress and strain dependency and plasticity configurations model configurations. The averaged time needed for one model run are summarised in Table 4.7 below.

Material model	HSS	SHANSEP MC	NGI-ADP	GHS
Time-expensiveness	100%	200%	140%	190%

The time needed for one full 2D model run with the HSS material model used for the clay layer is around 10 minutes.

Table 4.7: Comparison of the time-expensiveness of calculation with different material models.

In conclusion, the HSS model is chosen, because of its robustness, accurate modelling of soil behaviour in terms of the effective stress and its wide applicability in excavation applications.

5

Set-up of the inverse analysis method

5.1. Introduction

In the numerical modelling applied in the forward design of the problem analysed in this report, the material model parameters are the input values, and the diaphragm wall deflections are the output values. The goal of the inverse analysis algorithm is to back-figure the corresponding soil parameters based on the provided observations as input values.

Since developing a script for such analyses is not a trivial problem and needs certainty in parameters estimation, a simple, physically similar problem was first presented. In the considered problem, both input and output values are known, so it was possible to prove that the created algorithm certainly provides the correct solution.

The Kalman Filter algorithm is usually used for the optimisation of the dynamics system. The algorithm is often used for estimating the trajectory of objects navigated by the GPS, where the estimated variable is updated according to the observations, given in each time-step. The equivalent in geotechnical engineering would be a quasi-static system, i.e. a building process consisting of a number of construction phases. However, in this study, only one construction phase is considered (static system).

Therefore, the chosen exemplary problem for developing the algorithm is a single-degree-of-freedom mass-spring system consisting of two springs with a block of a mass attached to each of the spring. The calculation model in the objective function is a differential equation based on Newton's law, but the only value which is calculated as the last, equilibrium state displacement.

5.2. Kalman Filter

The EKF, in contrast to the KF can tackle nonlinear problems. The problem can be nonlinear in a twofold manner. Either, the process model can be nonlinear, i.e. when the behaviour resulting is nonlinear, hence the linear equations cannot be used, or the measurement can be nonlinear. The EnKF, same as the EKF, can solve the nonlinear problems. The EnKF can be applied at any time measurements are acquired, but in the considered case, only one time-step is considered, i.e. at the final equilibrium state [48].

5.2.1. Workflow of the Extended Kalman Filter

The analysis in the EKF starts by initialisation, i.e. creating a parameters space based on the initial guess consisting of the variables means and covariance matrix.

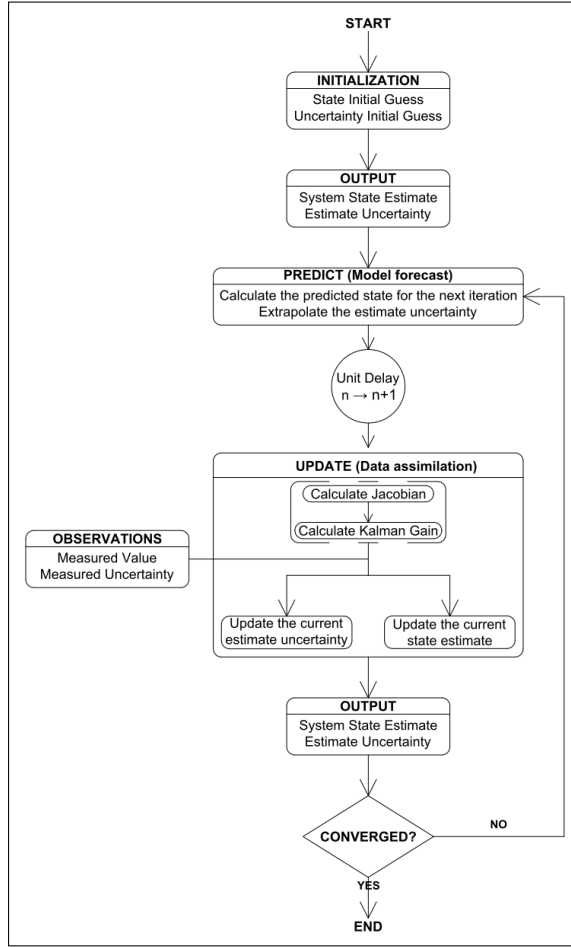


Figure 5.1: The workflow of Extended Kalman Filter algorithm.

Then, the first step of the optimisation is proceeded, i.e. the prediction step. System state estimate with its uncertainty (error covariance) is calculated based on the nonlinear process function, and the process white-noise is added. In the considered case, the function is not nonlinear, so the estimate is the same as the initial guess is, but with the added white-noise.

The next step of the optimisation procedure is the assimilation step. In this step, firstly the Jacobian matrix is calculated, which translates the predicted variables estimates to the estimated displacements. Then, the Kalman Gain is calculated based on the Jacobian matrix, forecasted error covariance and the measurement noise. After that, the error covariance is updated with the computed Kalman Gain matrix, Jacobian matrix and the forecasted error covariance. In the end, the assimilated parameters state is calculated based on the predicted variables estimate, the Kalman Gain Matrix, the observations inputted into the system and the estimated displacements.

The output of the assimilation step is the updated variables estimate and the updated error covariance. The displacements corresponding to the updated values are compared to the observations. If the error computed with error function is above the tolerance, the procedure (iteration) is repeated until the error is acceptable, i.e. lower than the tolerance.

5.2.2. Formulation of the Extended Kalman Filter

In formulation of the EKF, the model's nonlinear system space is governed by Formula 5.1 describing the difference equation and Formula 5.2 describing the observations model with additive noise [88].

For the dynamic system, the k parameter describes the time-step, however, for a static scheme, k denotes the iteration, i.e. the assimilation step currently being calculated.

$$x_k = f(x_{k-1}) + w_{k-1} \quad (5.1)$$

where: x_k is a state vector of dimensions $n \times 1$, $f(\cdot)$ is a process nonlinear vector function and w_k is a process noise vector of dimensions $n \times 1$.

$$y_k = h(x_k) + v_k \quad (5.2)$$

where y_k is a measurements vector of dimensions $m \times 1$, $h(\cdot)$ and v_k is a measurement noise vector of dimensions $m \times 1$.

The initial state x_0 (the initial guess), from which the optimization starts, is a random vector with known mean $\mu_0 = E[x_0]$ and covariance $P_0 = E[(x_0 - \mu_0)(x_0 - \mu_0)^T]$.

In the following, we assume that the random vector w_k captures uncertainties in the model and v_k denotes the measurement noise. Both are uncorrelated white noise processes with a mean equal to zero and known covariances. Also, no correlation between those values is considered at consecutive iterations (in static systems) or at different times (in dynamic or quasi-static systems) is present. Moreover, both of them are uncorrelated with the initial state x_0 [88].

$$E[w_k] = 0 \quad E[w_k w_k^T] = Q_k \quad E[w_k x_0^T] = 0 \quad (5.3)$$

where Q_k is a process noise covariance matrix of dimensions $n \times n$.

$$E[v_k] = 0 \quad E[v_k v_k^T] = R_k \quad E[v_k x_0^T] = 0 \quad (5.4)$$

where R_k is a measurement noise covariance matrix of dimensions $m \times m$.

The two random vectors w_k and v_k are uncorrelated:

$$E[w_k v_k^T] = 0 \quad (5.5)$$

Since the analyzed example is considered to be a static problem, the vectorial function $f(\cdot)$ is a vector equal to 1. The observation nonlinear vector function $h(\cdot)$ converts the variable value into the displacement measurement, which is further compared with the observations. For this purpose, the Equation 5.24 is used, so basing on the input stiffness values, the output displacements are calculated.

The main two steps of estimating the values of the variables in the EKF algorithm are the model forecast (prediction step) and data assimilation (correction step).

The model forecast is governed by two equations:

$$x_k^f = f(x_{k-1}^a) \quad (5.6)$$

$$P_k^f = J_f(x_{k-1}^a) P_{k-1} J_f^T(x_{k-1}^a) + Q_{k-1} \quad (5.7)$$

Because of a static/quasi-static system with no time-steps, hence no influence of the previous state on the next state, the equations can be simplified to:

$$x_k^f = x_{k-1}^a \quad (5.8)$$

$$P_k^f = P_{k-1} + Q_{k-1} \quad (5.9)$$

It means that for the first iteration, the predicted value x_1^f is equal to the initial state value x_0 and the forecast error covariance P_1^f is the covariance of the initial state P_0 but with and added process white noise.

The data assimilation step consists of three equations:

$$x_k^a \approx x_k^f + K_k (z_k - h(x_k^f)) \quad (5.10)$$

$$K_k = P_k^f J_h^T(x_k^f) (J_h(x_k^f) P_k^f J_h^T(x_k^f) + R_k)^{-1} \quad (5.11)$$

$$P_k = (I - K_k J_h(x_k^f)) P_k^f \quad (5.12)$$

The Jacobian J_h is given by Equation 5.13:

$$J_h \equiv \begin{bmatrix} \frac{\lambda h_1}{\lambda x_1} & \frac{\lambda h_1}{\lambda x_2} & \cdots & \frac{\lambda h_1}{\lambda x_n} \\ \vdots & \vdots & \ddots & \vdots \\ \frac{\lambda h_m}{\lambda x_1} & \frac{\lambda h_m}{\lambda x_2} & \cdots & \frac{\lambda h_m}{\lambda x_n} \end{bmatrix} \quad (5.13)$$

5.2.3. Workflow of the Ensemble Kalman Filter

The first step of the optimisation process in the EnKF, the initialisation, is exactly the same as in the EKF algorithm. In contrast to the EKF algorithm, the next step does not use the process nonlinear vector function. Instead, the so-called ensemble members are drawn around the mean values and covariance of the normally-distributed variables. The state transition function is used in the prediction step.

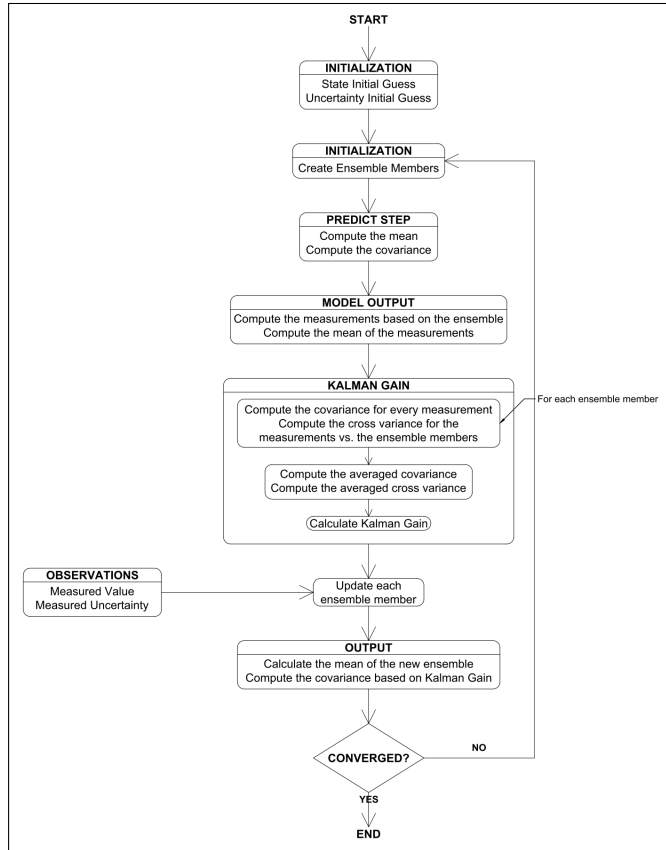


Figure 5.2: The workflow of Ensemble Kalman Filter algorithm.

In the last step, the calculation model is used to calculate the measurements based on the updated means and the corresponding covariance, and the error function is used to calculate the corresponding error. Similarly to EKF, if the computed RMSE is higher than the tolerance, the procedure is repeated.

In the dynamic or quasi-static system, the number of these procedures (iteration) is equal to the time-steps considered. For static schemes, there are two ways to find convergence. Either to use as many iterations as it is needed for the convergence or to use ensemble size big enough to solve the problem in one iteration.

5.2.4. Formulation of the Ensemble Kalman Filter

In the EnKF, an ensemble of n state vectors is used to simulate the initial estimation of the stiffness parameters, that is, $x = [x_1, x_2, \dots, x_n]$ [48].

In the prediction step of each iteration, the ensemble of state vectors is forecasted in the second (assimilation) step by the model describing the problem, as shown in Equation 5.14.

$$x_t^f = M_t x_{t-1} + w_t \quad (5.14)$$

where t is the time-step number in the EnKF, x_t is the n -dimensional unobserved state vector of interest, and w_t is the process (innovation) error given by $w_t \approx N(0, Q_t)$ where Q_t is the process noise matrix and M_t determines how the process evolves in time [49].

For the static system, which is considered in this report, the transition function M_t is not necessary to forecast the variable's value, and it can be neglected. The predicted covariance of the mean is calculated, as shown in Equation 5.15 [52].

The prediction step passes all the ensemble members through a supplied state transition function and adds the process of white noise, calculates the mean and covariance of the so created ensemble [52]. The predicted mean and the sample covariance is precisely same as the initial state for the ensemble size $N \rightarrow \infty$ and the process white-noise $\sigma_{process}^2 \rightarrow 0$. For the reasonable process noise, and tens of ensemble members, the discrepancies between the initial state and the predicted values for the first ensemble is almost negligible.

The next step (assimilation step) utilises the calculation model for computing the measurements for each variable set, i.e. for each ensemble member. After that, the Kalman Gain is calculated in a formula, which multiplies the cross-covariance for the measurements versus the ensemble members and the inversed covariance for every ensemble member. Then, each ensemble member is updated with the Kalman Gain matrix and the perturbed observations. Eventually, the filter's mean and covariance is re-computed [52].

$$P^f = \frac{1}{N-1} \sum_1^N [x_t - \tilde{x}_t][x_t - \tilde{x}_t]^T \quad (5.15)$$

where N is the ensemble size and \tilde{x}_t is the mean of the ensemble for a given time-step (iteration).

After the forecasting step, the assimilation of the predicted values starts. The displacements y_t are computed for each ensemble member and the mean of these displacements \tilde{y}_t is calculated (Equations 5.16 and 5.17, respectively).

$$y_t = h(x_t, u) \quad (5.16)$$

where h is the measurement function (calculation model), and u refers to how the measurements of the previous time-step influence the measurements of the following step. In the static example, u can be omitted.

$$\tilde{y}_t = \frac{1}{N} \sum_1^N y_t \quad (5.17)$$

The Kalman Gain is calculated as in Equation 5.18 below [52].

$$K_G = P_{xz} P_{zz}^{-1} \quad (5.18)$$

where P_{xz} is the cross variance for each computed measurement vs each ensemble member given by Equation 5.19 and P_{zz} is the covariance for every ensemble member given by Equation 5.20.

$$P_{zz} = \frac{1}{N-1} \sum_1^N [y_t - \tilde{y}_t][y_t - \tilde{y}_t]^T + R \quad (5.19)$$

where R is the measurement noise matrix.

$$P_{xz} = \frac{1}{N-1} \sum_1^N [x_t - \tilde{x}_t][y_t - \tilde{y}_t]^T \quad (5.20)$$

The next action in the assimilation step is to update each ensemble member with the computed Kalman Gain matrix and the observations, as shown in Equation 5.21.

$$x_t^a = x_t + K_G[z - y_t + v_t] \quad (5.21)$$

where z is the observation vector and v_t is the perturbation added to the observations according to $v_t = N(0, R_t)$ where R_t is the measurement noise matrix.

Finally, the updated mean and the updated covariance of the ensemble is calculated as in Equations 5.22 and 5.23.

$$\tilde{x}_t^a = \frac{1}{N} \sum_1^N x_t^a \quad (5.22)$$

$$P^a = P - K_G P_{zz} K_G^T \quad (5.23)$$

At the end of the iteration process, the ensemble mean is considered to be the best estimate of the stiffness variable and utilised to generate correlated stiffness parameters.

5.3. Optimisation process experiment

5.3.1. Problem formulation

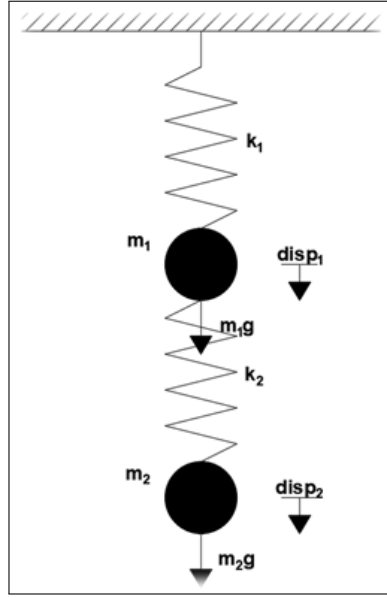


Figure 5.3: Scheme of coupled springs problem.

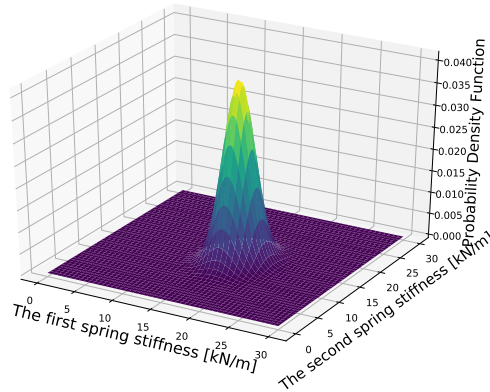


Figure 5.4: The probability distribution plotted for the initial mean and covariance of the two springs stiffness values.

For developing a tried-and-true algorithm, a simple problem consisting of two springs and two blocks of mass is used. The quantities sought in the real problem (the soil stiffness parameters) are represented by the springs' stiffness values, while the diaphragm wall displacements are represented by the displacements of the blocks. The scheme is shown in Figure 5.3 below.

The problem shown above is governed by the following equation:

$$\begin{bmatrix} disp_1 \\ disp_2 \end{bmatrix} \times \begin{bmatrix} k_1+k_2 & -k_2 \\ -k_2 & k_2 \end{bmatrix} = \begin{bmatrix} m_1 \\ m_2 \end{bmatrix} \times g \quad (5.24)$$

The scheme was considered as a static problem, i.e. the only displacement that is observed is the final one, calculated using Equation 5.24. It corresponds to using the FE computation results from one construction phase only. Also, we assume that the stiffness values of the springs do not depend on their lengths.

The convergence of the algorithm is tested on the spring model example, where the masses were equal to $m = [5, 10]$ and the observations computed as $z = [14.72, 19.62]$, what was based on the target values of the variables $x = [10, 20]$. The initial mean and covariance were set to $\mu = [x_1, x_2] = [17, 14]$ and $Cov(X_1, X_2) = \begin{bmatrix} 9 & 0 \\ 0 & 16 \end{bmatrix}$, respectively. The corresponding probability distribution of the described initial state is shown in Figure 5.4 below.

Since the process variance represents the measurements uncertainty the updating function of the algorithm, the measurement and process variance values were set to: $\sigma_{measurements}^2 = \sigma_{process}^2 = 0.001$ of the maximum observation value.

5.3.2. Formulation of an objective function

To perform an inverse analysis, a function that estimates the error between the computed and experimental results is needed. This error is measured after each time step (iteration in the case considered) of the optimisation procedure, by the so-called individual norm that forms an error function $Error(x)$.

$$Error(x) \longrightarrow 0 \quad (5.25)$$

where x is a parameter that needs to be optimized, expressed as a vector function.

The commonly used error function is the least square equation given by Equation 5.26 [63], where the parameters are computed by minimizing a function based on the squared difference between the measured and computed values.

$$\epsilon = \frac{1}{m} \sum_{j=1}^m \left[\frac{\eta_j - f_j(\hat{x})}{\eta_j} \right]^2 = \frac{1}{m} \sum_{j=1}^m \left[1 - \frac{f_j(\hat{x})}{\eta_j} \right]^2 \quad (5.26)$$

where: ϵ is the Mean Squared Error (MSE), \hat{x} is the vector of n components of the parameters to estimate, η_j is the j obtained measurement, f_j is the computed value correspondent to the j measurement, and m is the *in situ* measurement number.

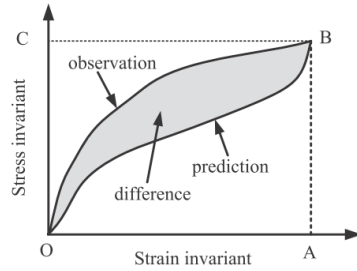


Figure 5.5: Definition of an error function [99]

The error function used in the script is Equation 5.26 adopted for the considered problem. The function is the same for both the spring example and the application with Plaxis FE software used as the calculation model application and is formulated below:

$$RMSE = \frac{1}{n \times |z_{max}|} \sqrt{\sum_{i=1}^m \sum_{j=1}^n |(y_{i,j} - z_{i,j})|^2} \tag{5.27}$$

where: y is the measurement, z is the observation and n is the size of the observation vector.

5.3.3. Convergence of the EKF algorithm

In the analysis of the EKF convergence, the model characteristics were set as in Subsection 5.3.3. After 875 iterations, the mean and the error covariance found are $x = [9.98, 19.97]$ and $cov = \begin{bmatrix} 1.01E-7 & -6.0E-7 \\ -6.0E-7 & 7.22E-6 \end{bmatrix}$.

In Figure 5.6, the evolution of the computed displacements of the two springs in a function of the algorithm iterations is shown. At the same time, the estimates of springs stiffness are plotted. The target displacement and stiffness values are highlighted as solid lines.

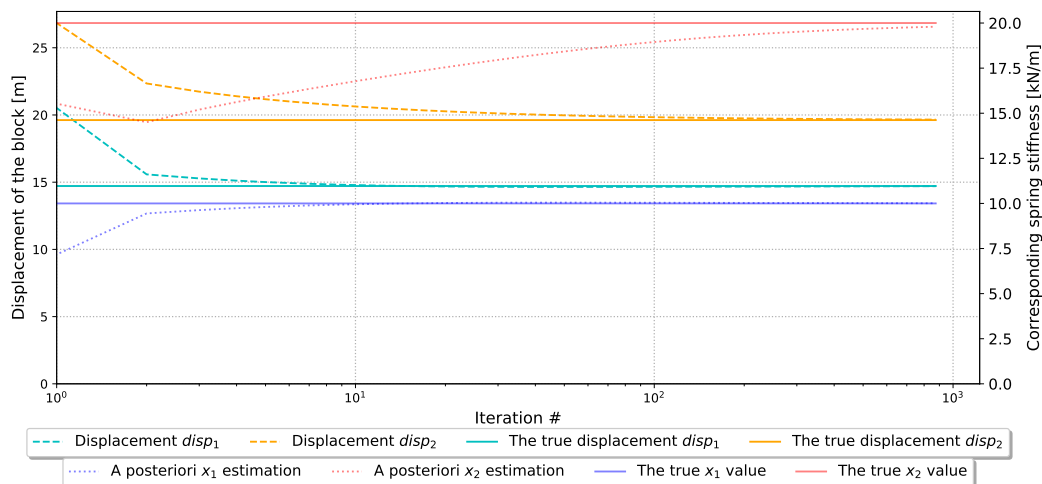


Figure 5.6: The optimisation of the spring problem using the EKF algorithm - the evolution of the estimated variables and measurements throughout the iterations.

In Figure 5.7, the evolution of the RMSE error in a function of the algorithm iterations is shown with translation to the required calculation model runs in Figure 5.8. The tolerance was set to 0.001, what accounts for the average displacement difference of 0.048 m per spring.

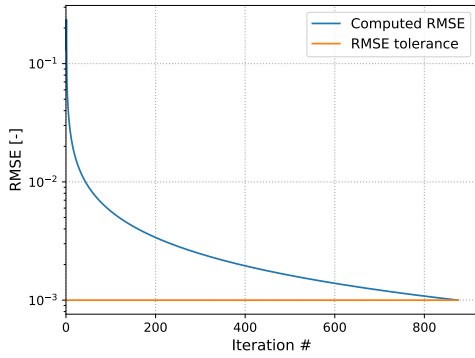


Figure 5.7: The optimisation of the spring problem using the EKF algorithm - the evolution of RMSE throughout the iterations.

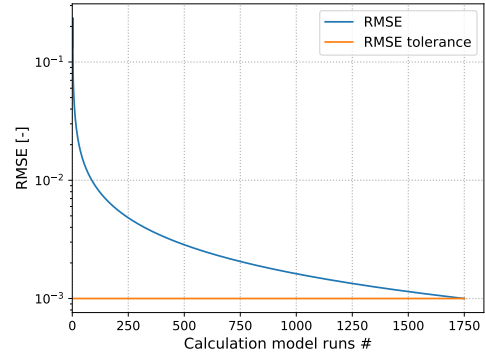


Figure 5.8: The optimisation of the spring problem using the EKF algorithm - the evolution of RMSE throughout the calculation model runs.

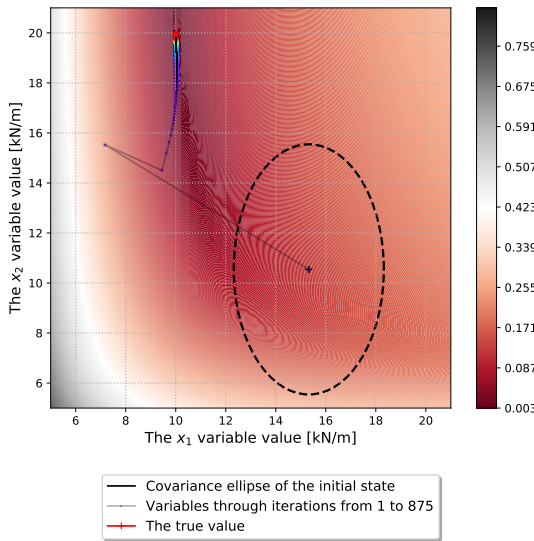


Figure 5.9: The variables evolution throughout the iterations in the two-spring problem optimisation using the EKF algorithm.

In Figure 5.9, the evolution of the variables estimates throughout the iterations is shown, where the initial state is circumscribed with a covariance ellipse. The covariance ellipse is calculated using the eigenvalues of the error covariance matrix. The actual radii of the ellipse being $\sqrt{\lambda_1}$ and $\sqrt{\lambda_2}$ for two eigenvectors. In the plot, it is shown that the algorithm is capable of finding the solution, which is located outside of this ellipse is shown. Also, it ignores the state spaces with very low RMSE to go directly to the sought solution.

Eventually, as a part of Principal Component Analysis (PCA), the evolution of the Pearson's product-moment correlation coefficient evolution throughout the iterations is shown in Figure 5.10 and the evolution of the variance values from the covariance matrix taken for the updated estimates of each iteration is shown in Figure 5.11.

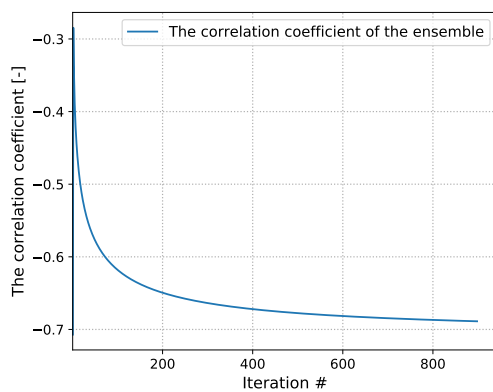


Figure 5.10: The optimisation of the spring problem using the EKF algorithm - the Pearson's coefficient evolution throughout the iterations.

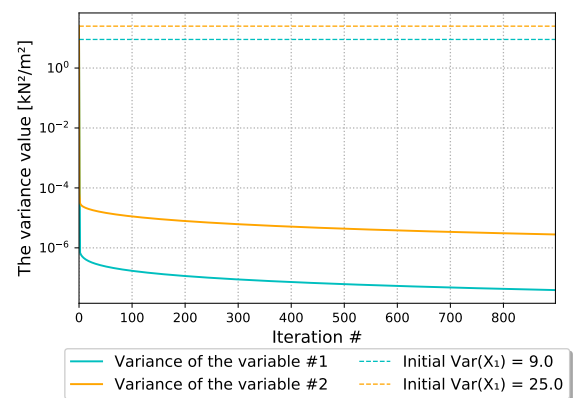


Figure 5.11: The optimisation of the spring problem using the EKF algorithm - the evolution of the variables' variances and covariance.

Pearson’s coefficient was plotted for the EKF algorithm for further comparison to the EnKF algorithm. However, in the EKF algorithm, the evolution of this coefficient and the variables’ variance are overlinearised, because the covariance matrix is calculated based on a singular estimation of the variables. In the EnKF algorithm, it is based on the number of estimation of the variables equal to the ensemble size.

5.3.4. Convergence of the EnKF algorithm

In this analysis, the model characteristics were also set as in Subsection 5.3.3 and the ensemble size was set to $N = 20$. The means of the variables in the initial ensembles was $x = [15.95, 14.16]$, while after the first iteration were equal to $x = [6.65, 16.22]$ with computed RMSE = 0.288 and corresponding displacements $y = [22.12, 28.17]$.

The convergence of the EnKF algorithm is presented analogous to the EKF algorithm. Figure 5.12 shows the evolution of the displacements based on the estimated mean values of the variables. Besides, the displayed grey areas are indicating the 2σ bandwidth around the estimated means.

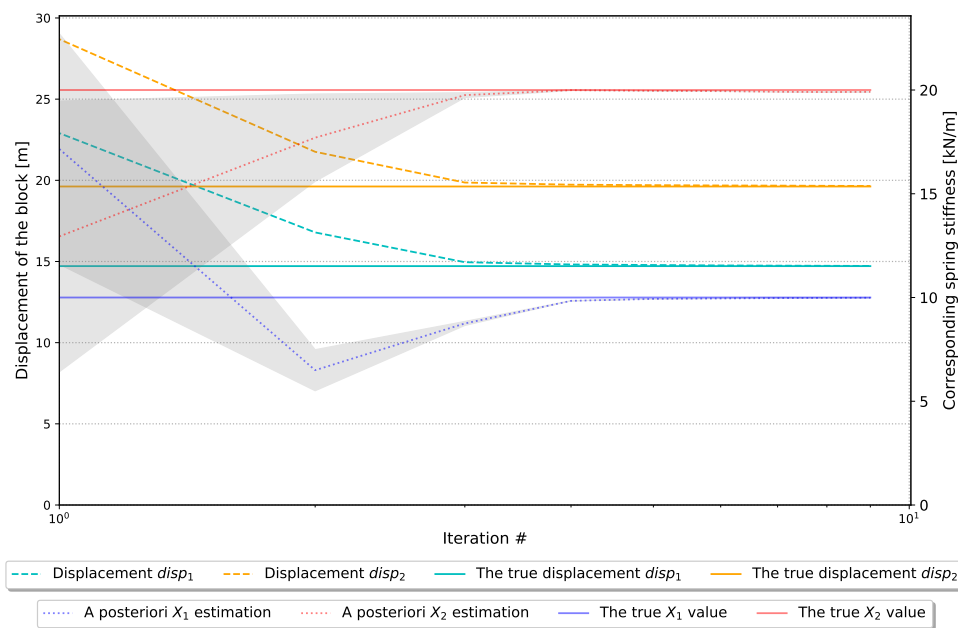


Figure 5.12: The optimisation of the spring problem using the EnKF algorithm - the evolution of the estimated variables and measurements throughout the iterations.

As in the subsection presenting the EKF algorithm convergence, the evolution of the RMSE error is shown in two plots (Figures 5.7 and 5.14). In comparison to EKF, fewer iterations are needed. Hence the error curve is less smooth.

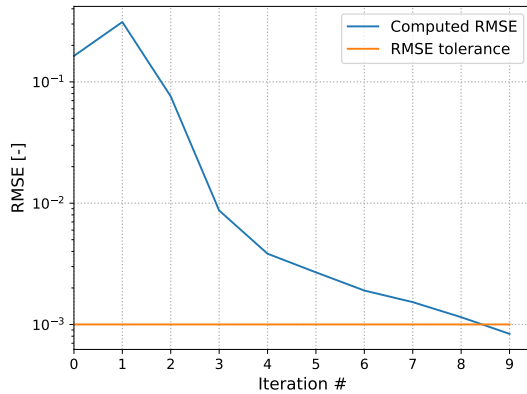


Figure 5.13: The optimisation of the spring problem using the EnKF algorithm - the evolution of RMSE throughout the iterations.

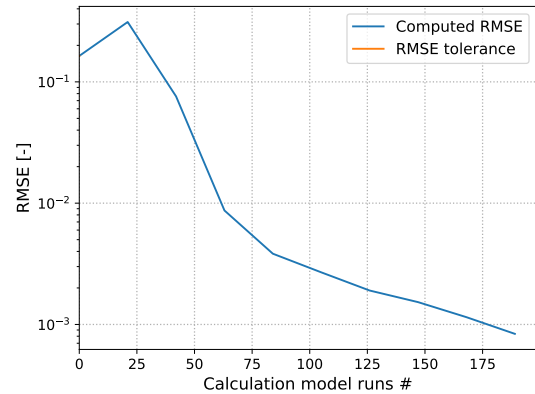


Figure 5.14: The optimisation of the spring problem using the EnKF algorithm - the evolution of RMSE throughout the calculation model runs.

The same plot showing the evolution of the variables estimates throughout the iterations for the EnKF is shown in Figure 5.15.

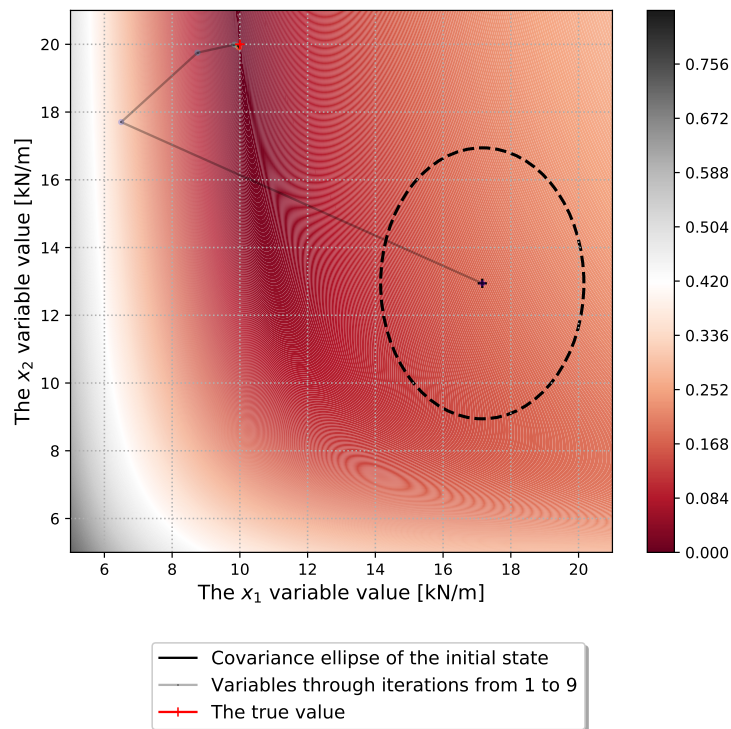


Figure 5.15: The variables evolution throughout the iterations in the two-spring problem optimisation using the EnKF algorithm.

In Figure 5.16, the evolution of the ensemble members with the variables means throughout the iterations is shown. Each dot (member) represents one variable estimate with solid lines being the means of these estimates. Throughout the iterations, the sample covariance matrix is getting smaller and smaller; hence, the ensemble's spread is getting smaller as well.

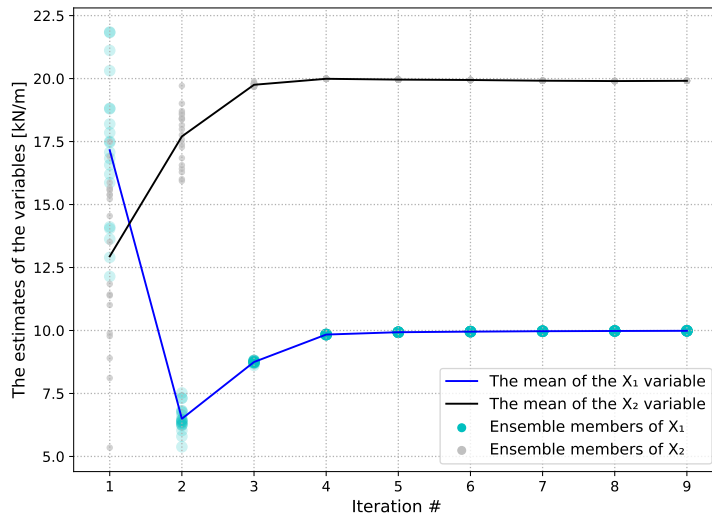


Figure 5.16: The optimisation of the spring problem using the EnKF algorithm - the ensemble evolution throughout the iterations.

In Figure 5.17, the ensemble is shown in the parameters space. The blue dots are the initial ensemble members drawn around the initial point estimation. The covariance ellipses for 1σ , 2σ and 3σ stipulate the borders of 68, 95 and ~ 100 percents of all of the ensemble members drawn.

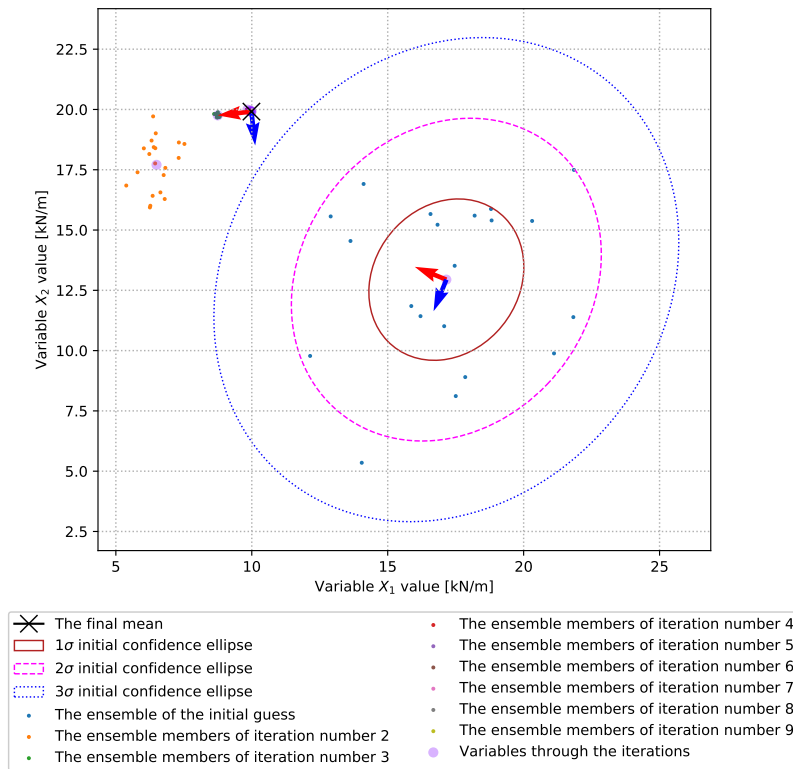


Figure 5.17: The optimisation of the spring problem using the EnKF algorithm - ensemble evolution in parameters space (focus on the initial ensemble).

As shown in Figure 5.17, for the configurations applied, the second ensemble moves beyond the 3σ covari-

ance ellipse in searching for the solution. The estimated variables' values are already very close to the solution after three updated only. In the next plot, Figure 5.18, the focus is given to the ensembles of the fourth and subsequent iterations are shown.

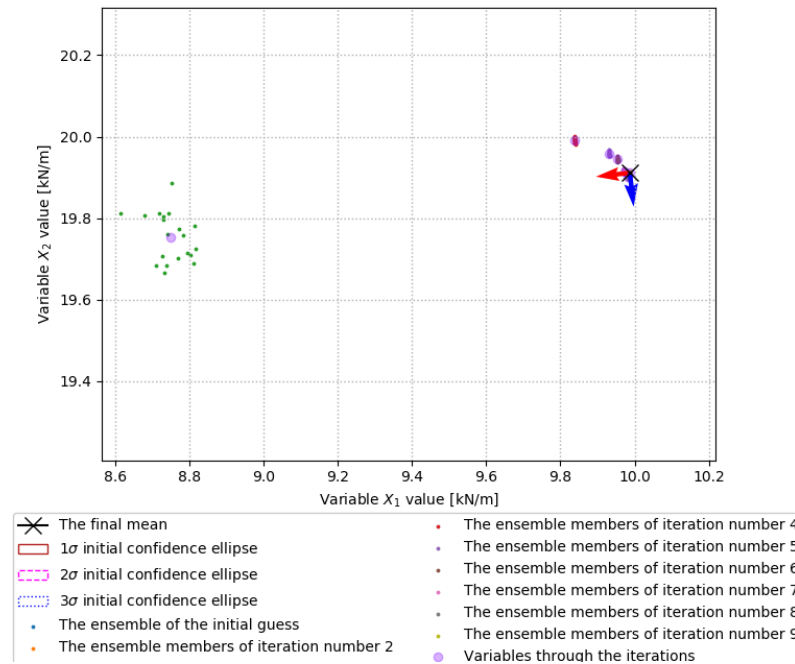


Figure 5.18: The optimisation of the spring problem using the EnKF algorithm - ensemble evolution in parameters space (focus on the last ensembles).

Plots related to PCA for EnKF are shown in Figures 5.19 and 5.20.

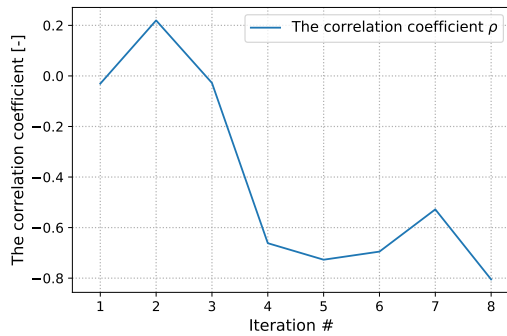


Figure 5.19: The optimisation of the spring problem using the EnKF algorithm - the Pearson's coefficient evolution throughout the iterations.

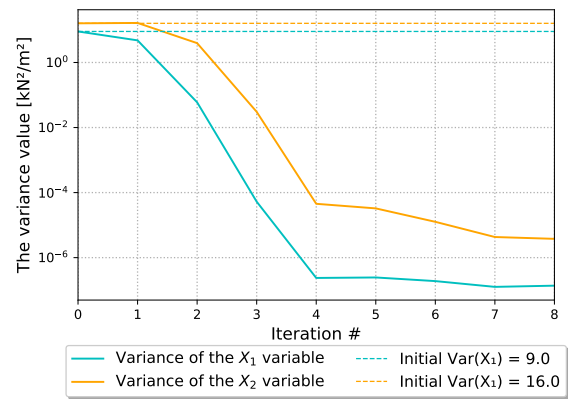


Figure 5.20: The optimisation of the spring problem using the EnKF algorithm - the evolution of the variables' variances and covariance.

5.3.5. Method selection

In the presented example, a tolerance of 0.001 was reached by the EKF algorithm after 875 iterations and 9 for the EnKF algorithm.

It is not possible to directly compare one run of the EKF to one run of EnKF since in the EKF the first estimate drawn from a normal distribution of the initial state happens to be far from the mean. In the EnKF algorithm, the mean of the initial ensemble tends to the mean of the initial state as the ensemble size tends to infinity. Even for a small ensemble size, such as 5, the mean of the ensemble is relatively close to the initial state estimation. Therefore, an exemplary run of the EKF can overestimate (or underestimate) the robustness of the algorithm. Still, the vast majority of the EnKF runs was finished incomparably faster than when using the EKF algorithm.

Another pitfall of the EKF algorithm is that in each iteration, the state is updated based on the results of only one run of the calculation model. Calculation of the RMSE can either be based on the estimates updated in the previous iteration or on the newly updated estimates for which an additional calculation model run is needed. Since the calculation model is the most time-costly part of the process, the first way is more reasonable, but can also be considered as a limitation. In the EnKF algorithm, the calculation model can be run one more time for the calculation of RMSE, since in each iteration at least 10-20 runs are needed regardless.

One of the main differences in the formulation of these algorithms is a need for Jacobian matrix in the Extended Kalman Filter. Two ways of inputting the Jacobian matrix were tested: using the analytical Jacobian calculated from Equation 5.24 and using the perturbation method. The algorithm was able to back-figure the sought solution in both cases. However, the usage of the analytical Jacobian is only possible when we know the governing equation of the physical problem, which is often impossible. For example, the nonlinearity of the Plaxis FE model cannot be shown as a simple equation with a known Jacobian. The perturbation method can be applied to more systems, but still, the necessity of using the Jacobian matrix is a substantial limitation. Therefore, the EnKF method is considered to be much more adequate for the considered problem.

One of the limitations of the EKF algorithm is the randomness of the initial guess. In case the initial guess of the variables is taken from the farthest parts of the initial distribution's ties, many more iterations are needed for the script to find the solution, as shown in Figures C.1 to C.5 in Appendix C. In that example, a total of 105119 iterations are needed, and the final estimates and covariance are $x = [9.97, 20.11]$ and $cov = \begin{bmatrix} 4.14E-10 & -2.63E-9 \\ -2.63E-9 & 3.39E-8 \end{bmatrix}$. In that example, it can be noticed that the final covariance is smaller by three orders of magnitude than in the example in Subsection 5.3.3. An associated phenomenon is so-called degeneration of the error covariance, where the estimate is not close to the solution yet while the covariance matrix already became too low to allow for big changes in the estimates.

5.4. Calibration of the method

5.4.1. Variance of the input parameters

In the real-life scenario, we obtain point estimations of some soil parameters from the field and laboratory testing. Direct input of the point estimation without consideration of how the variability of data influence the convergence of the regression algorithm may lead to not reaching an optimal solution or any solution at all. In the EnKF, each variable is described by a mean and covariance. While the established means are unambiguous, the influence of the initial variance values on the algorithm convergence should be investigated beforehand.

As shown in Figure 5.21, it is indicated that, when the initial mean is uncertain, it is better to choose a larger standard deviation in order to get acceptable back-calculated results [48]. The reason for this is that for the uncertain sample data, choosing a larger standard deviation for generating the initial ensemble enables the realisation to cover a broader range of values, which, in turn, helps in searching out the correct values of the sought variables during the data assimilation process.

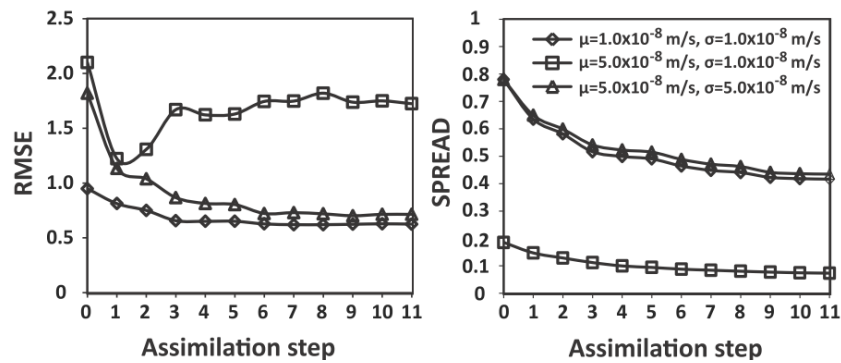


Figure 5.21: Variation of RMSE and SPREAD for cases with accurate and inaccurate initial conditions [48].

5.4.2. Negative values of the parameters

One of the problems spotted during the development of the EnKF script was an issue of the ensemble members, which were drawn as negative values. If the members represent the variables, which cannot be smaller than zero, for example, spring stiffness, internal friction angle of soil or Young's modulus, applying a negative value in the calculation model is not allowed. Since the whole ensemble is based on the (positive) mean and non-zero covariance, there is always a chance (even for very high mean and low variance) of drawing a negative value. Since in both simple application and the FE model, the parameters are stiffness (and strength) related, negative values must not be drawn.

In order to assure that the negative values do not appear, one can either use a lognormal transformation of the drawn members or a truncated distribution. Since using a lognormal distribution influences not only the performance of the algorithm but should not be used if the variable's distribution is not normal, sometimes truncated distribution is the only viable solution. In the script, the truncated distribution is achieved by introducing a small change to the random normal distribution function, which redraws the member each time it lies outside of the permitted range.

5.4.3. Measurement and process noises

In the Kalman Filter algorithm, two types of noises are usually added [88]: the measurement noise and the process noise. These are represented by the measurement noise covariance matrix R and the process noise covariance matrix Q , respectively.

In order to better understand how the measurement and process covariance matrices influence the computed error, a studies comprising of 25 configurations between the measurement and process variances with a following values of variance have been used: 1.0%, 0.5%, 0.1%, 0.05% and 0.01% of the average observation value. The measurement and process variances in the simulations above were expressed as percentage values of the average observation value $\bar{z} = 17.17$.

In the studies, the model characteristics were set as following: the masses were set to $m = [5, 10]$, the observations to $z = [14.72, 19.62]$. The initial mean and covariance were equal to $\mu = [17, 14]$ and $cov = \begin{bmatrix} 9 & 0 \\ 0 & 16 \end{bmatrix}$, respectively. The chosen ensemble size was equal to $N = 75$.

To assess how the convergence criterion, i.e. the computed error, changes throughout the iterations, 100 simulations for each model configuration were performed. Then, the error was plotted against the total number of members needed in the calculation process, i.e. the ensemble size multiplied by the number of iterations ($Runs = N \times i$).

The sensitivity of the model with respect to the measurement and process variances is shown in a twofold manner: by showing the average total number of members needed for reaching a tolerance of $RMSE = 0.01$ (Figure 5.22) and by showing the lowest RMSE error reached after updating 7500 members in a total of 100 iterations in Figure 5.23.

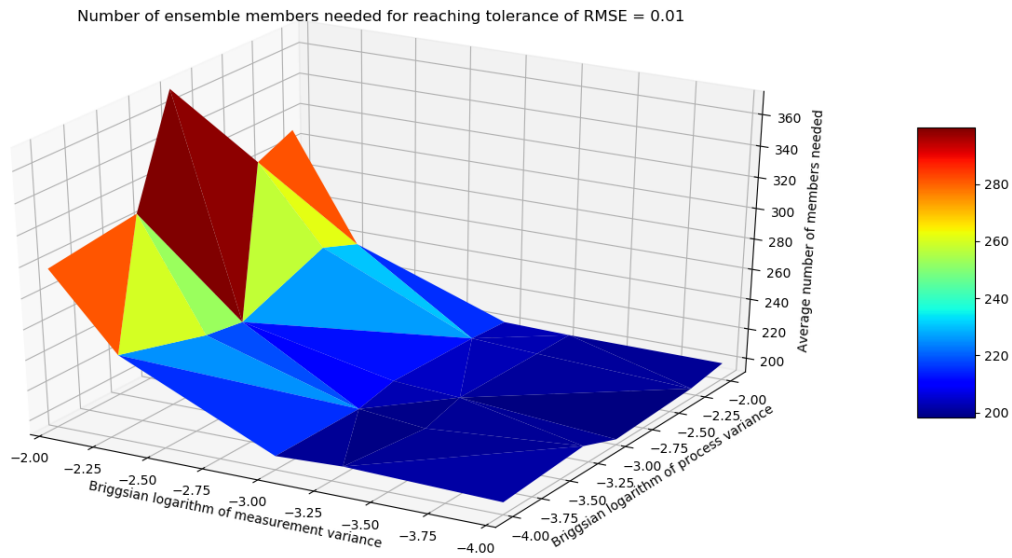


Figure 5.22: Measurement and process variances sensitivity studies - total number of *Runs* (calculated ensemble members in all iterations summed) needed to reach tolerance of 0.01.

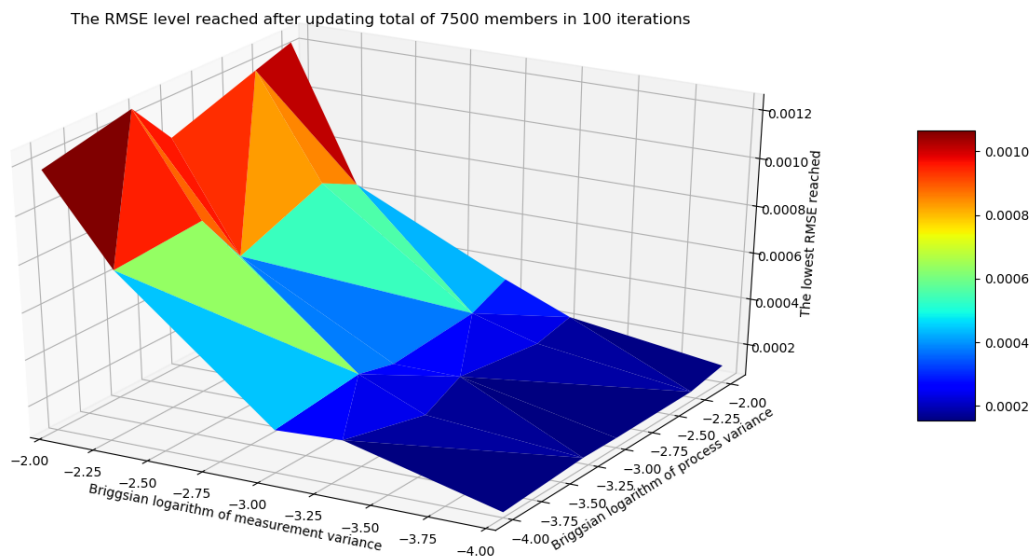


Figure 5.23: Measurement and process variances sensitivity studies - the lowest RMSE reached for a total of 7500 members calculated.

The measurement and process variance studies have shown that increasing the measurement and process variance negatively influences the robustness of the script. However, in the real applications, the measurement noise is a pre-defined value specified by the accuracy of the sensors, whereas the process noise represents the measurement noise in the optimisation algorithm and is user-defined. The noises also provide an additional spread of the computed estimates what can help to avoid collapsing of the ensemble.

5.4.4. Ensemble size studies

One of the settings that have the most significant influence on the robustness of the script is the number of members in the ensemble. The model chosen for testing the influence of the ensemble size on the number of iterations required for convergence is the two-springs problem.

In the model, the masses were set to $m = [5, 10]$, the observations to $z = [14.72, 19.62]$. The initial mean and covariance were equal to $\mu = [17, 14]$ and $cov = \begin{bmatrix} 9 & 0 \\ 0 & 16 \end{bmatrix}$, respectively. The measurement variance was set

to 0.5% of the maximum observed value, whereas the process variance was set to 0.05%. The robustness of the script was tested for a following ensemble sizes: $N = [10, 15, 20, 25, 40, 50, 75, 100]$.

For these sensitivity studies, 25 simulations with constant model settings were run for each ensemble size considered. Then, evolution of the error between the computed and observed displacements in a function of performed iterations was plotted for each of the 25 simulations (Figures C.6 to C.21). Afterwards, the error was plotted against the iterations and the resulting total number of calculation model runs needed for reaching a particular tolerance levels. Finally, the derived average values of the computed errors with a corresponding bandwidth (2σ) for each ensemble size are plotted in Figures C.22 to C.29. These results are summed up in Figures 5.24 and 5.25 below.

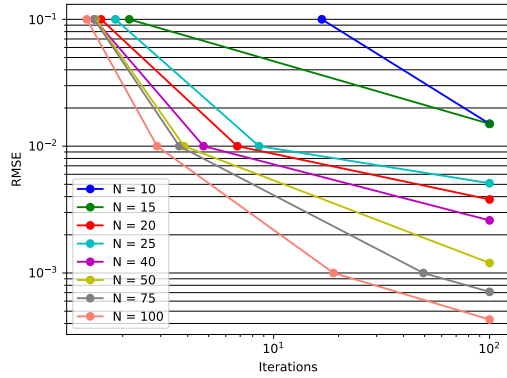


Figure 5.24: The total number of iterations needed to reach particular tolerance levels.

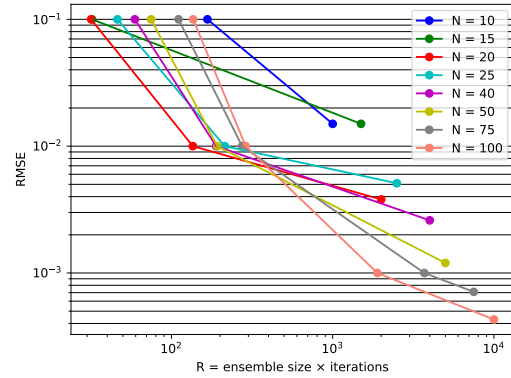


Figure 5.25: The total number of calculated ensemble members (*Runs*) needed to reach particular tolerance levels.

An associated aspect is the percentage of the script runs in which the computed error managed to converge, i.e. to fall below a specified tolerance. This was called the 'success rate' and was studied using the aforementioned 25 simulations with a predefined tolerance $RMSE = 0.01$. Summary of this analysis is shown in Table 5.1 below and are based on the plots shown in Figures C.30 and C.31 in Appendix C.

<i>Runs</i>	Success rates for ensemble sizes N [%]								
	N	10	15	20	25	40	50	75	100
100		41	51	48	54	26	7	4	0
200		50	62	66	70	64	60	47	8
300		51	63	73	80	82	77	61	58
400		51	65	75	85	90	82	74	86
500		51	65	77	87	93	89	90	93
1000		51	66	80	88	94	97	98	99
2000		51	66	81	89	96	98	98	100

Table 5.1: Studies of the 'success rate', i.e. the number of runs where error fell below the tolerance specified as $RMSE = 0.01$, for ensemble sizes $N = [10, 15, 20, 25, 40, 50, 75, 100]$.

Although the 'success rate' for the ensemble sizes of 25 and 40 is higher than the one for 20 members, the ensemble size considered as the best one to be used in the optimisation analysis together with Plaxis software, is $N = 20$.

5.5. Conclusions

In conclusion, the algorithm chosen to be used in the further inverse analysis is the Ensemble Kalman Filter because:

- It is more robust than the Extended Kalman Filter and its efficiency and robustness is less influenced by the starting selection created around the initial state.
- It requires less calculation model runs, which is a big advantage when dealing with time-expensive finite-element calculations.
- For reasonably high ensemble sizes, it gives a better variance estimation, because a high N value preserves the covariance from collapsing.
- The Extended Kalman Filter algorithm needs a gradient vector of multiple outputs (in here, a Jacobian matrix), which is not necessary for the Ensemble Kalman Filter algorithm.

Nevertheless, for the given variables settings, both methods were capable of successfully solving the presented spring problem. Also, both algorithms are capable of capturing a dependency between the variables after a few calculation model runs only. It can be seen that the algorithm finds the sought value of the first variable (the upper spring) faster because both observations are in inverse proportion with this variable. The second variable (the lower spring), however, influences only the second observation, while the first observation remains unaffected. Also, it was observed that the smaller the initial variance of the variables is, the smaller is the initial covariance, and the harder it is for the algorithm to find the solution.

The ensemble size studies presented in this chapter resulted in the suggested ensemble size of 20 members. However, the algorithm was configured for the presented spring problem, so for a problem of a lower level of non-linearity of the response and lower number of degrees of freedom. Therefore, for using Plaxis as a calculation model, the required ensemble size is expected to be higher.

6

Application of the inverse analysis in the FEM

6.1. Introduction

In this chapter, the Plaxis 2D software has been used as the calculation model. In order to verify whether the solution found by the EnKF is exactly the one that is sought, the algorithm is tested against target displacements, which are known beforehand.

The material model chosen for the inverse analysis is the HSS model. The 2D FE model is simplified, so the computation time is less. All of the construction phases are modelled using *Drained* drainage type of the HSS model, what according to the results from Chapter 4, has a limited influence on the accuracy of the results. At the same time, it helps to drastically limit the number of the input parameters involved in the optimisation process.

The calculation model used in this study, i.e. the Plaxis software, allows the user to use the remote scripting interface based on the Python language to control both Input and Output program via an external Python handler. The usage of Plaxis in the algorithm is pretty straightforward and was involved in the algorithm, as a part of the objective function (calculation model) according to as a subroutine with the following workflow:

- Opening Plaxis 2D Input;
- Loading the drawn variables;
- Transforming the variables into the material model parameters;
- Running the 2D model with the parameters;
- Opening Plaxis 2D Output;
- Loading the computed displacements from the plate used in the diaphragm wall.

Since in real cases, the exact solution is unknown, one cannot be sure if the found estimate is the only correct solution. Considering that the usage of the optimisation algorithm for back-figuring the soil distribution needs some confidence, the problematics of many possible solutions (same error computed) for the same provided observations is one of the biggest challenges in the optimisation process.

The number of sub-optimal solution, which would result in the same error depends on several aspects, including but not limited to: the ensemble size N , the size of the observation vector z , the calculation model used, the applied error function and other factors. The certainty of usage of the algorithm in the practical application should be preceded with the studies on how these factors influence the algorithm efficiency. The influence of the number and spacing of the sensors was studied by performing runs using different observation vectors and different target deflection curves given.

One of the main problems with showing reliable and repeatable results of this analysis is the structure of the starting point of the optimisation process, the so-called ‘initial guess’. The first ensemble consists of N draws taken from the normal distribution around the means and the covariance matrix; therefore, each time the generated ensemble is slightly different for low N values.

For a sensitivity analysis performed on a simple model (the spring problem), the randomness of the initial guess was tackled easily by running many analyses. The other way would be to set N so high that the drawn number would create a more continuous distribution, i.e. where the mean of the first ensemble would be same as the mean of the initial guess. However, when the Plaxis software is used as a calculation model, both solutions are hard to be implemented because of a high calculation time needed. Nevertheless, this limitation mostly touches upon the results of the first iteration, but in the next iteration, this randomness is tackled by an accurate performance of the algorithm.

6.2. Setting up the problem

6.2.1. Setting up the FE model

The Plaxis FE model used in the inverse analysis was adopted from Chapter 4, which consisted of 7 layers, from top to bottom: the fill, the silty clay, the first Kurkar layer, the first clay layer, the second Kurkar layer, the second clay layer and the last, third Kurkar layer.

In the original model, all of the layers were modelled using the HSS model, but to make the optimisation process more robust, the 2D Plaxis FE model has been slightly simplified. Instead of using a complex material model for each distinguished soil layer, all of the layers but the clay layer were changed to the Linear Elastic (LE) model. Moreover, the first Kurkar layer was split into seven sub-layers with stiffness values interpolated in a way, so the results were similar to the ones obtained when using the original model.

The FE model also consists of 15 phases, but only phase number 12 is used in the analysis. The meshing size was equal to 0.04002 and the mesh coarseness nearby the diaphragm walls was set according to the sensitivity analysis of the domain.

6.2.2. Variables selection

Since it is desired to limit down the number variables representing the sought material model parameters, a procedure of eliminating the least-important parameters was performed. Firstly, the simplified sensitivity analysis presented in Subsection 4.3.2 eliminated the strength parameters based on their lower influence on the final result and a common understanding of the problem considered. Secondly, the optimisation of 5 variables would be still computationally expensive, and modelling of the relationship between these parameters is considerably difficult, so simplification based on grouping of the parameters has been applied.

The parameters chosen to be used as variables in the optimisation process are E_{50}^{ref} and γ_{07} , and are represented by variables X_E and X_γ , respectively. The remaining parameters are bonded to these variables with a chosen ratio, so eventually two systems are considered: one using only one variable X_E and the system using two variables X_E and X_γ . In the one-variable system, the parameters are bound with the following relation:

$$X_E = E_{50}^{ref} = E_{oed}^{ref} = \frac{1}{3} E_{ur}^{ref} = \frac{1}{16} G_0^{ref} = \frac{0.0004}{\gamma_{07}} \quad (6.1)$$

Whereas in the two-variables system, the relation is as below:

$$X_E = E_{50}^{ref} = E_{oed}^{ref} = \frac{1}{3} E_{ur}^{ref} = \frac{1}{16} G_0^{ref} \quad (6.2)$$

and the small strain stiffness parameter γ_{07} is the second, independent variable X_γ .

6.2.3. Target measurements set-up

In the optimization problem, parameters can be assessed with higher reliability if the database for the optimization is diversified, i.e. contains results of many different tests [63]. Usually, the monitoring program at the construction site provides two model components, i.e. lateral wall deflection δ_{hm} and surface settlement δ_{vm} . Up to this, the deformation ratio $R = \frac{\delta_{vm}}{\delta_{hm}}$ can be calculated as an additional indicator.

However, building settlements can be influenced by several factors, such as depth of excavation, the height of the building, distance from pit edge to the building, considered geology and others. Therefore, wall deflections seem to be much more directly connected to changes in the material model used in the numerical model than the other observation types. For the sake of this analysis, the only site measurements type that are taken as the observations are the diaphragm wall deflections.

In the optimisation process, the required number of calculation model runs can be huge, hence very time-expensive. Therefore, a proper choice of parameters to be optimised is important for the robustness of the process. Since the cumulative relative sensitivity of the stiffness properties is higher than one of the strength parameters, and the problem is more related to the serviceable limit state, the stiffness parameters have been chosen.

Parameter	Targets for the X_E variable				
	1.0	2.0	3.0	5.0	10.0
φ	22.0	22.0	22.0	22.0	22.0
c	10.0	10.0	10.0	10.0	10.0
E_{50}^{ref}	1.0	2.0	3.0	5.0	10.0
E_{oed}^{ref}	1.0	2.0	3.0	5.0	10.0
E_{ur}^{ref}	3.0	6.0	9.0	15.0	30.0
$\gamma_{0.7}$	0.0004	0.0002	0.000133	0.00008	0.00004
G_0^{ref}	16.0	32.0	48.0	80.0	160.0

The units of the parameters and the missing material model parameters values are as in Table 3.11.

Table 6.1: The sets of HSS model parameters used to compute the target diaphragm wall displacements.

Eventually, the target deflections are created for varying stiffness parameters as explained in Table 6.1. The target displacements computed for the values shown in that table are presented in Figure 6.1 below.

The initial state in the inverse analysis is given equal to the calibrated parameters set shown in Table 3.11 and is described as $X_E = 4.0$ MPa. The other targets are dispersed from 1σ to 6σ from the initial value.

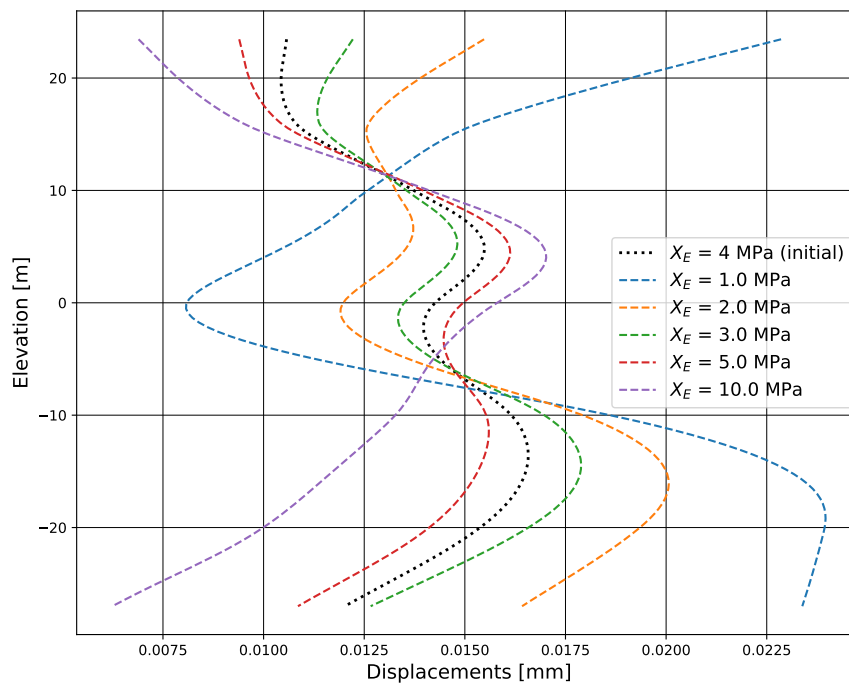


Figure 6.1: The diaphragm wall deflections computed for the established targets.

6.2.4. Input parameters distribution

The E_{50}^{ref} parameter initial distribution is shown in Figure 6.2 as a histogram with a corresponding PDF. The readings are cleared after the data directly derived from the lab tests with a criterion, that only the readings lower than 12.0 MPa are taken into account. Since the distribution of the E_{50}^{ref} derived from CU and UU triaxial tests are lognormal, the distribution of X_E variable is lognormal as well. In Chapter 3, the calibrated mean of the E_{50}^{ref} parameter was established as 4.0 MPa. The initial distribution of the variable X_E was adjusted to this mean (shown as the red line on the plot).

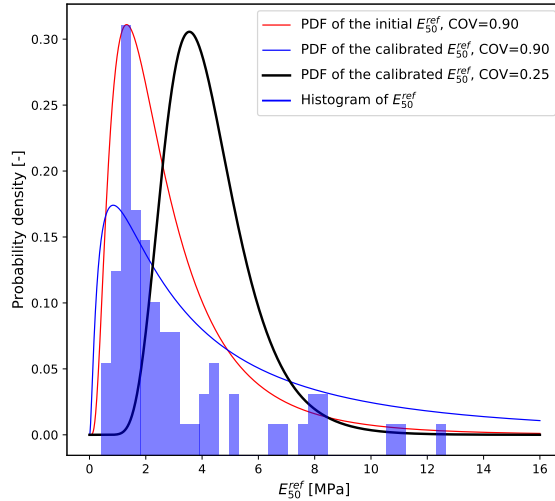


Figure 6.2: Histogram and PDF of log-normally distributed E_{50}^{ref} parameter and the input variable based on it.

The calculated COV of the underlying normal distribution of E_{50}^{ref} parameter was estimated as 0.90, what is an acceptable value for a lognormal distribution. However, for most of the normally distributed soil parameters, the COV usually does not exceed 0.25 – 0.30. Therefore, in the analysis, a comparison between different COV values, namely 0.1, 0.25, 0.5 and 0.9, was made, whereas the value of 0.25 is mostly used, so to test efficiency of the algorithm when some values have a very low probability density.

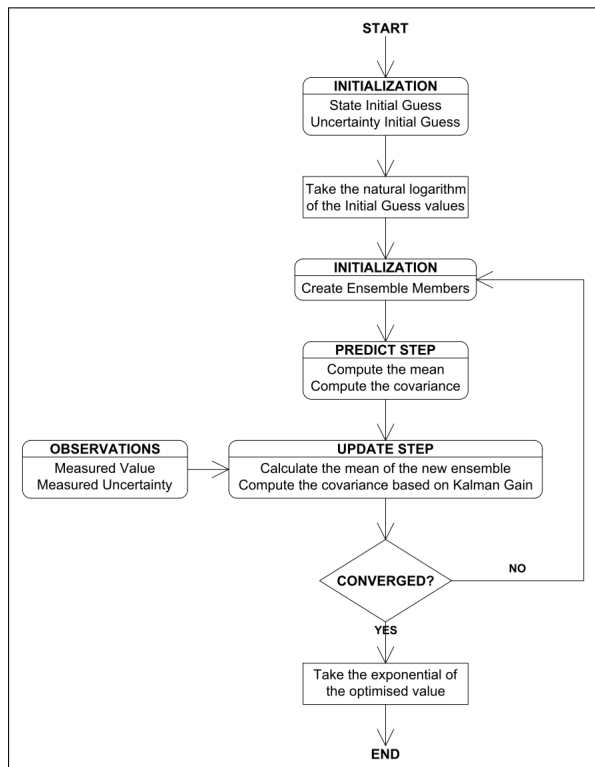


Figure 6.3: Workflow of the lognormal - normal - lognormal transformation in the EnKF script.

Since the analysis error of EnKF uses a linear analysis algorithm that is sub-optimal for all distributions except Gaussian, the ensemble is created using the normal distribution around the mean equal to $\ln(E_{50}^{ref})$ and COV as explained above. The variables are drawn from this distribution, and then the input to Plaxis software is an exponential of the drawn member. This assures that all operations are performed on the normally distributed ensemble members, what is especially relevant for the calculation of the Kalman Gain, and its components (covariance and cross variance). The whole procedure is shown in Figure 6.3 below.

In the first part of the analysis, where the one-variable system is considered, the variable X_E is lognormally distributed. In the second part, where the system consists of two variables, the X_E variable is lognormally distributed, whereas the X_γ variable is normally distributed.

6.2.5. Synthetic measurements

Two types of target observations were considered. The first was created using the same numerical model as in the inverse analysis procedure and explained at the end of Chapter 4. In addition, the other observations were considered, where the displacements of 140 nodes are semi-random, i.e. are were not created using a specific numerical model, but have a shape possible to be observed in a real scenario.

In the 2D Plaxis FE model, which is used in this analysis, the observation vector predominantly consists of 140 nodes displacements, which is a relatively high value. It was proven that as the number of measurement points increases, the standard deviation of the calculated variables decreases and the precision of the estimation increases [48]. Therefore, a high number of observations available in the output of Plaxis 2D model, i.e. the d-wall displacements represented by tens to hundreds of nodes with computed displacements, is a factor positively influencing the robustness of the algorithm. This aspect was also investigated by performing a number of analyses with a full observation vector, and vectors of a limited number of nodes displacements.

Since the measurements are synthetic, and the focus of this part is on testing the robustness and capabilities of the script, the measurements error is set to a considerably low value of $\sigma_{measurement}^2 = 0.001$ of the maximum lateral wall deflection. The process variance is also set to cause the lowest error possible, so the process variance is set to $\sigma_{process}^2 = 0.0001$ of the maximum lateral wall deflection. The pitfall of this approach is that the spread of the ensemble is low, and the covariance tends to collapse after a few iterations.

An important factor influencing the computational cost of the algorithm is the number of degrees of freedom of the system (the observed deflections curve) and with the rising number of degrees of freedom, the robustness of the algorithm is reduced. Also, for the number of degrees of freedom n much higher than the number of observations, computing the covariance matrix is the major part of the computational cost [74]. The investigation of the n value was made by the trial-and-errors method using *polyfit* function from the Python's library *numpy*. The results of this analysis are shown in Figure 6.4 below.

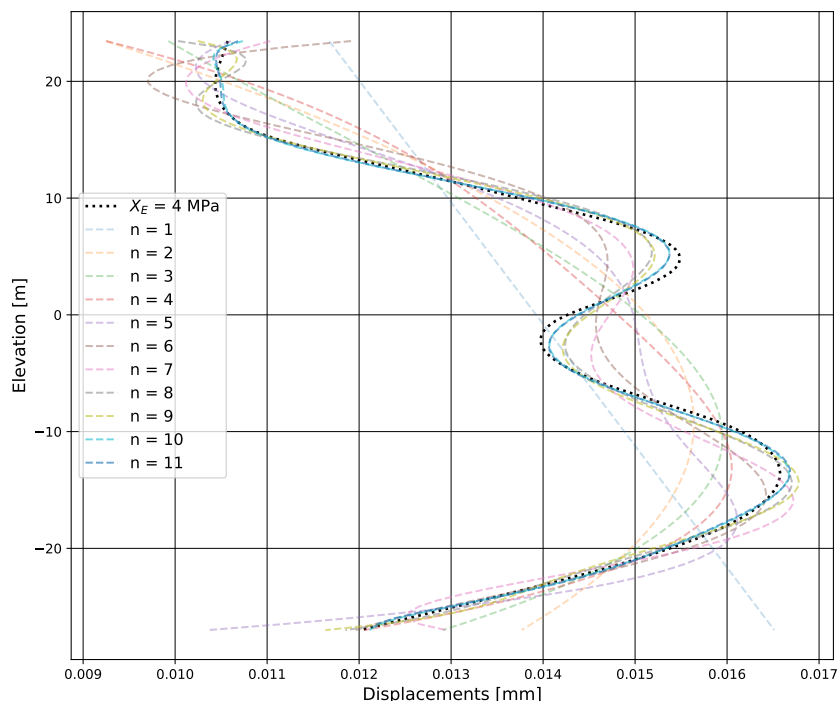


Figure 6.4: Derivation of the degrees of freedom of the diaphragm wall deflections curve for the initial variable value.

Even though the target displacements may be characterised by a different n value, the relative difference would be small, i.e. no more than a few degrees. Also, the number of degrees of freedom of the initial displacements curve is either around the number of observations delivered or smaller, so the data assimilation

process should require neither cost reduction methods nor approximations to covariance matrix calculations.

6.3. Post-processing of the algorithm performance

In order to test the performance of the developed algorithm, studies regarding the ability to find the established solution and the robustness of the algorithm were performed with respect to:

- the influence of the ensemble size;
- the aspect of how far from the solution is the initial guess;
- the size and the number of the observation given;
- the correlation between the variables.

As explained before, for the one-variable system, the distribution shown in Figure 6.2 was used with COV of 0.25. For the two-variables system, the initial distribution of X_E is the same, and the distribution of the X_Y variable is normal around the mean of 0.0001 with a COV of 0.25.

6.3.1. Example of the algorithm performance

To present how the algorithm works, the observations were set to the target displacements for the variable X_E set to 10.0 MPa and X_Y set to 0.00004. The initial distribution is same for the whole analysis, and is as given in Chapter 3, i.e. $X_E = 4.0$ MPa with a COV = 0.90. Firstly, the evolution of the ensemble with the mean of the variables throughout the iterations is shown in Figures 6.5 and 6.6.

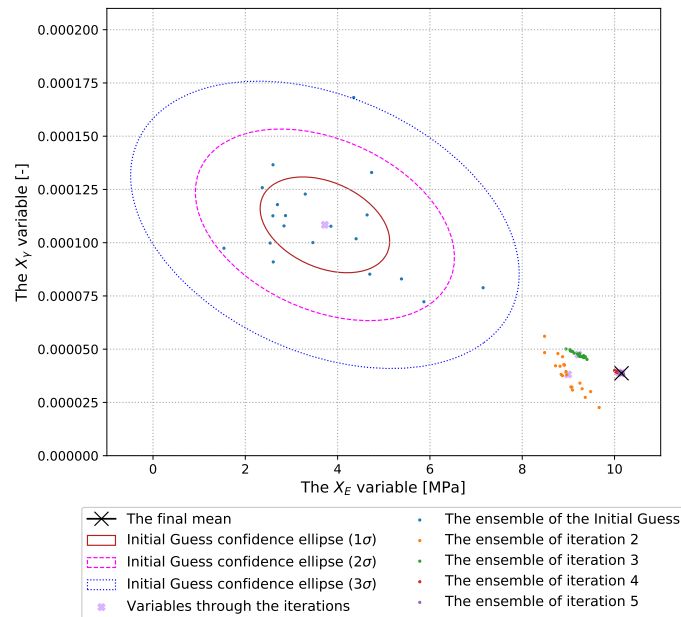


Figure 6.5: The ensembles created in each iteration for the run with targets set to $X_E = 10.0$ MPa and $X_Y = 0.00004$.

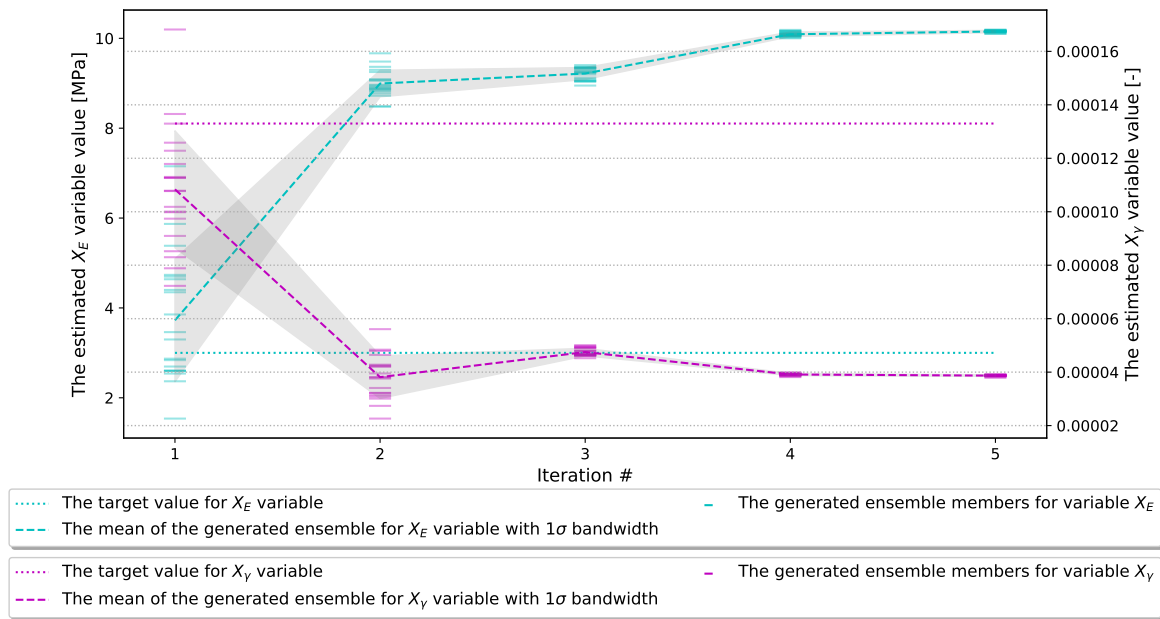


Figure 6.6: The members with the mean throughout the iterations for the run with targets set to $X_E = 10.0$ MPa and $X_\gamma = 0.00004$.

The corresponding RMSE and the diaphragm wall displacements computed for the means of the ensemble of each iteration are shown in Figures 6.7 and 6.8.

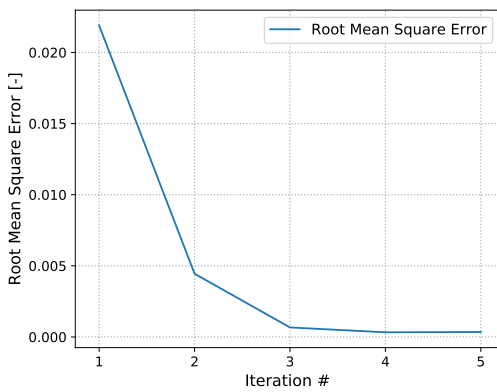


Figure 6.7: The RMSE computed for the mean output of each iteration for the run with targets set to $X_E = 10.0$ MPa and $X_\gamma = 0.00004$.

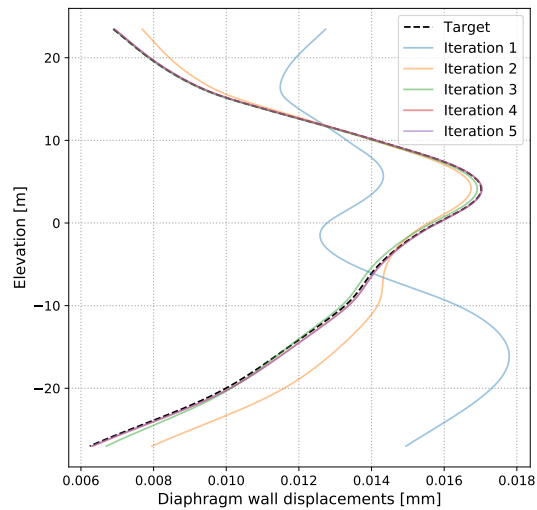


Figure 6.8: The d-wall deflections computed for the means of the ensemble of each iteration for the run with targets set to $X_E = 10.0$ MPa and $X_\gamma = 0.00004$.

In addition, the d-wall deflections computed for all of the members of the first ensemble are shown in Figure 6.9 below. As seen in the plot, the displacements computed for each member differ significantly between each other. In the next iterations, the discrepancies between the displacements computed for each member are much smaller.

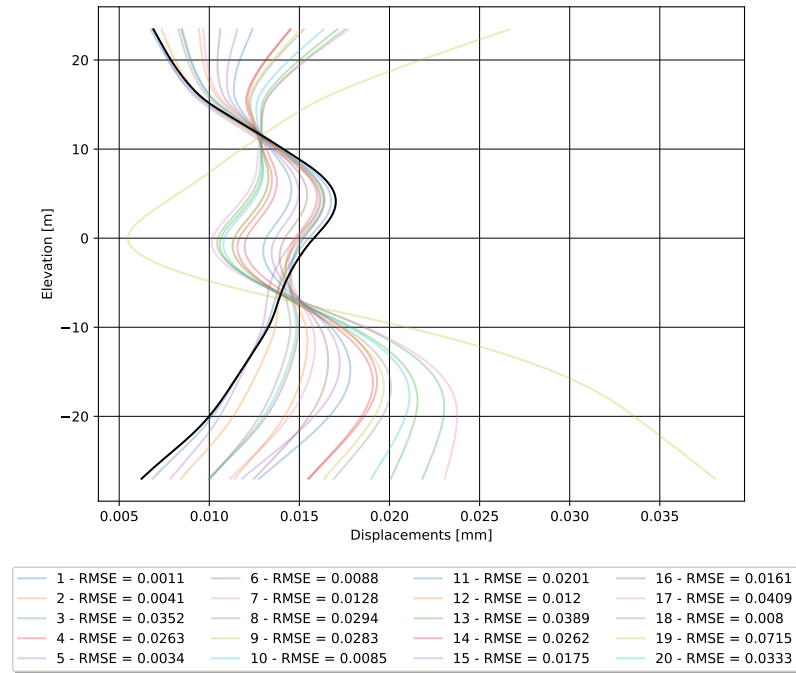


Figure 6.9: The d-wall deflections computed for the members of the first iteration for the run with the targets set to $X_E = 10.0$ MPa and $X_\gamma = 0.00004$.

6.3.2. Performance depending on the ensemble size

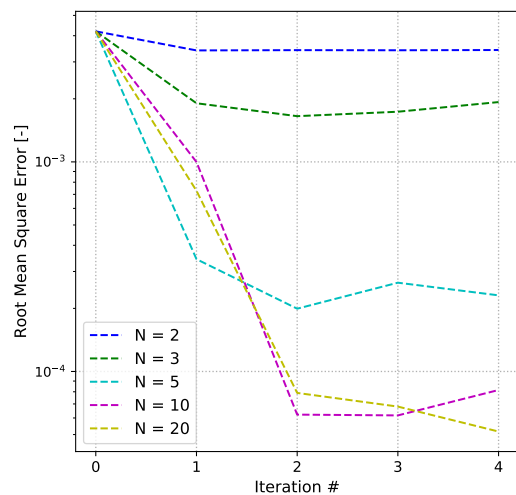


Figure 6.10: The comparison of the RMSE computed for the mean output of each iteration for different ensemble sizes - case of one variable X_E .

The studies on the most efficient ensemble size were performed in a previous chapter, with results are summed up in Figure 5.25. The studies were repeated here in order to compare the robustness of the algorithm when using Plaxis 2D as a calculation model.

The performance was tested for the one-variable system on ensemble sizes of $N = [2, 3, 5, 10, 20]$. In Figure 6.10 the evolution of RMSE in a function if iterations is shown, whereas in Figure 6.11 the evolution of the mean of the computed ensembles in a function if iterations is shown.

For the one-variable system, the run with 10 ensemble members gave practically the same error as the run with 20 ensemble members. For the ensemble size of 2, 3 and 5 members, the covariance collapsed quickly leading to the new ensembles being 'stuck' at an estimate, which was not a correct solution.

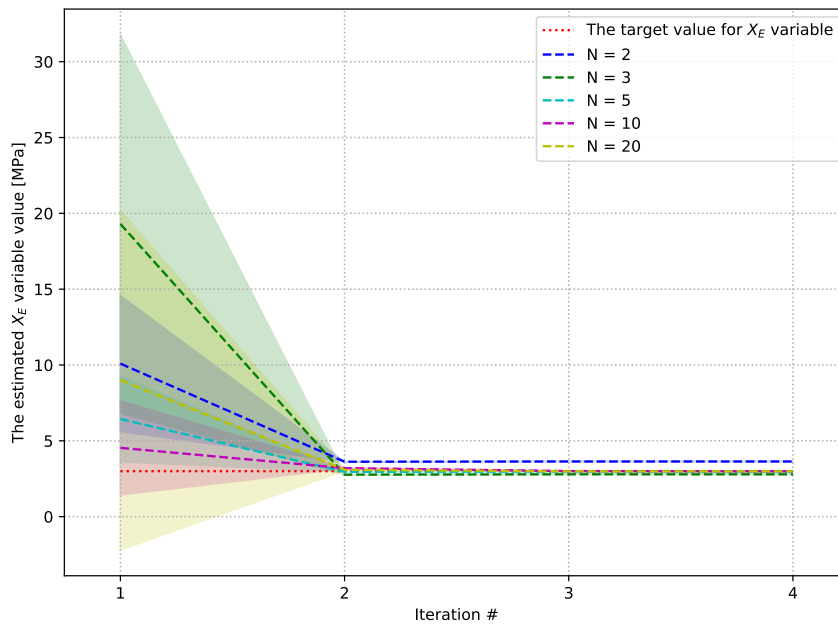


Figure 6.11: The comparison of the estimated mean of the ensemble of each iteration for different ensemble sizes - case of one variable (X_E).

When the computed error is considered, the run with five ensemble members was apparently less accurate than the runs with ten and twenty members. When the absolute values are considered, the run with $N = 5$ gave a final estimation of $X_E = 2.97$ MPa, that is a relative error smaller than 1%. Summing up, ten ensemble size, which was a suitable value for the one-variable system is ten, while for the two-variables system twenty ensemble members should be used, as concluded in Chapter 3.

6.3.3. Performance depending on the specified target

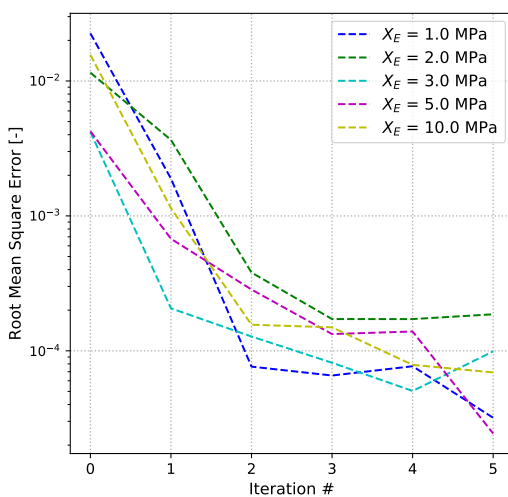


Figure 6.12: The comparison of the RMSE computed for the mean output of each iteration for different targets - one variable case.

In order to test the robustness of the script and its ability to reach a solution, which is relatively far away from the initial value, a set of runs with the solution set 1σ ($X_E = 3.0$ MPa and $X_E = 5.0$ MPa), 2σ ($X_E = 2.0$ MPa), 3σ ($X_E = 1.0$ MPa) and 6σ ($X_E = 10.0$ MPa) from the initial mean were performed. This was done for both one-variable and two-variables cases.

The evolution of the RMSE and the evolution of the estimated mean of the ensemble for the one variable system is shown in Figures 6.12 and 6.13 below.

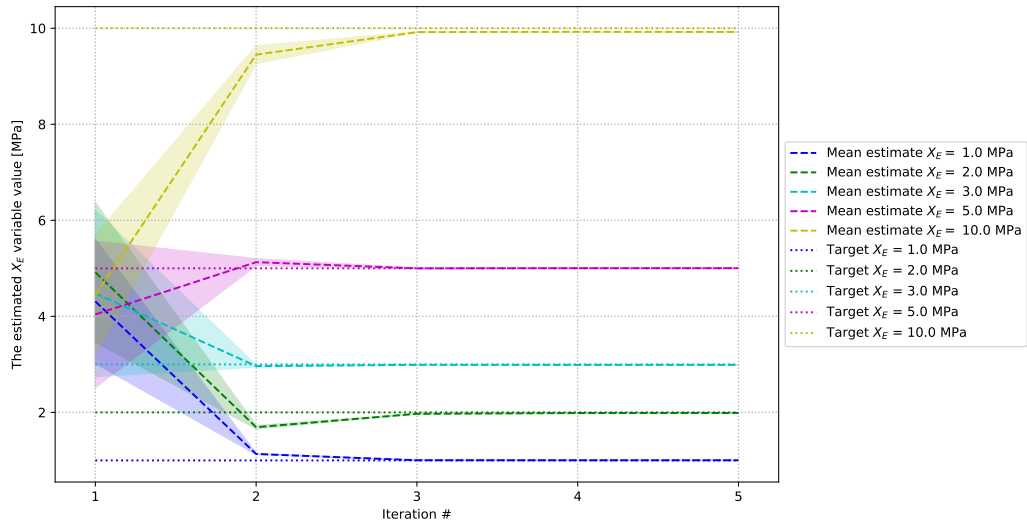


Figure 6.13: The evolution of the estimated mean of the ensembles throughout the iterations for a different targets - one variable case.

Three iterations of ten ensemble members each are enough to reach the established target, whereas the targets set to be 1σ from the initial mean reached in the second iteration already. From the third iteration onward, the computed error was almost constant and of negligible value for all of the runs. It was proven that the algorithm can find a solution, regardless of how far the solution is from the mean.

For the two variables system, the evolution of the RMSE in a function of iterations is shown in Figure 6.14 and the evolution of the means of the ensembles in a function of iterations is shown in Figures 6.15 and 6.16.

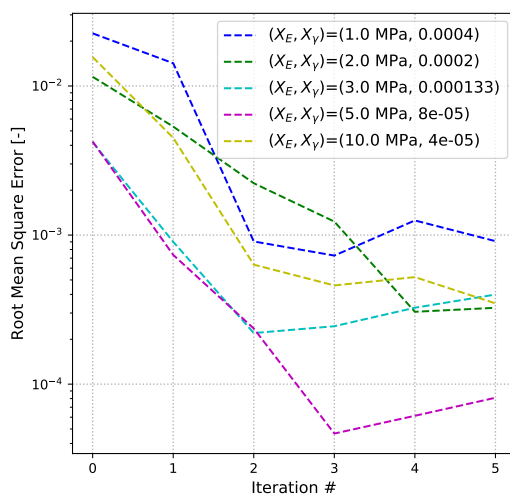


Figure 6.14: The comparison of the RMSE computed for the mean output of each iteration for different targets - two variables case.

For the targets with the X_E variable set 1σ from the initial mean, the computed error remains almost constant from the second iteration onwards, whereas for the other targets, more iterations are needed for the convergence. Furthermore, for the targets set 3σ and 6σ from the initial mean, even five iterations with 20 members each is not enough to reach acceptable RMSE.

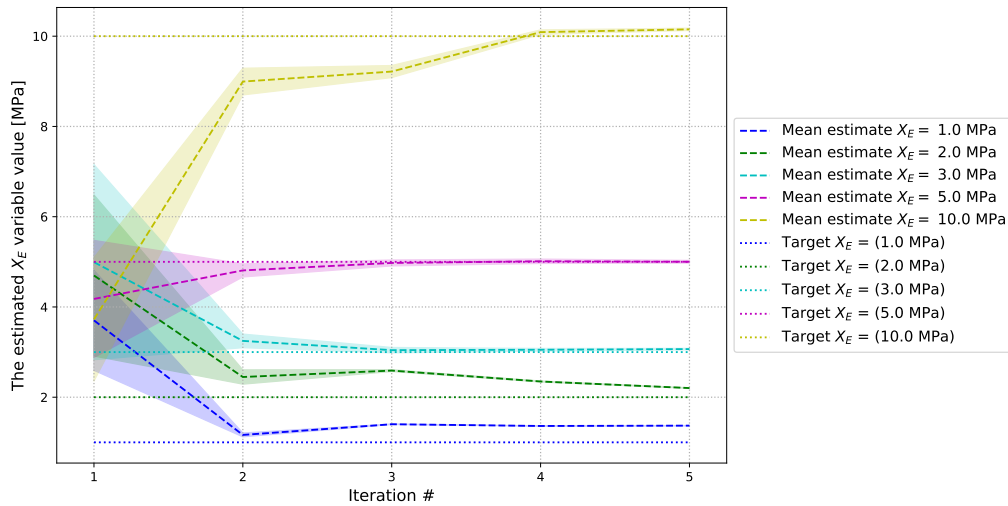


Figure 6.15: The evolution of the estimated mean of the ensembles (for X_E variable) throughout the iterations for a different targets - two variables case.

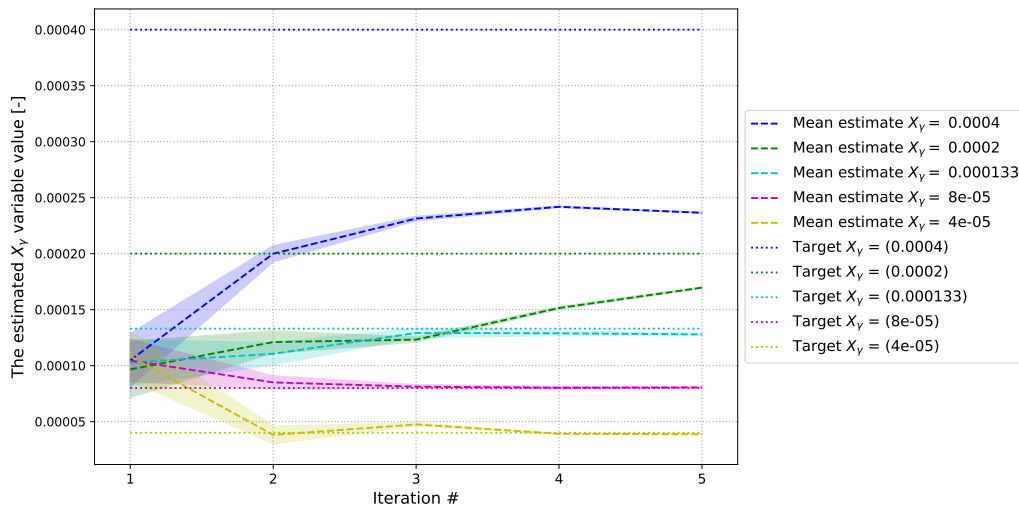


Figure 6.16: The evolution of the estimated mean of the ensembles (for X_γ variable) throughout the iterations for a different targets - two variables case.

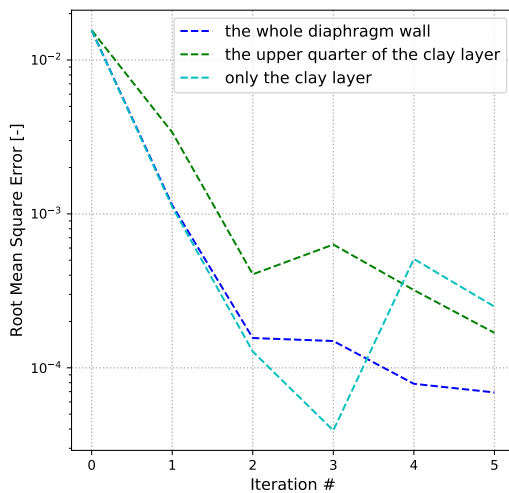
The run with the target set 6σ from the initial mean, needs more members to be generated so that it can reach the designated target. Nevertheless, the estimate is only around 1% from the solution in the fourth iteration onward.

Regarding the X_γ variable, the solution was not reached for the runs with targets of 0.00004 and 0.00008. The estimates for the other targets were correct in the third iteration onwards. The low values of the X_γ variable were problematic for the algorithm, because of a narrow ($COV = 0.25$) log-normal distribution in which low values have very low probability density. For higher values of the X_γ variable, the algorithm finds the solution appropriately, because of a higher probability density of such values in the distribution even though the solution lies 6σ away from the initial mean.

6.3.4. Performance depending on the observation vector

To investigate how the size of the observations input influences the performance of the script, three different types of observation vectors have been studied for the system with one variable:

1. Observation vector consisted of displacements of 140 nodes located throughout the whole diaphragm wall.
2. Vector consisting of displacements of 45 nodes, which were located only in the clay layer.
3. Vector consisting of displacements of only 10 nodes located in the upper part of the clay layer (nodes number 4 to 13 out of 45).



The trend is that the bigger the size of the observation vector, the faster the computed RMSE is reduced. Also, the convergence of the algorithm for the observation vector consisting only of the lateral wall displacement in the clay layer is almost as robust as for the observation vector taking all of the displacements values. Two factors are affecting the behaviour of the algorithm: the clay layer is the most sensitive one because this is the layer of which the model parameters are being changed. It is also because 45 nodes displacements are already informative enough.

Figure 6.17: The comparison of the RMSE computed for the mean output of each iteration for different observation vectors - one variable case.

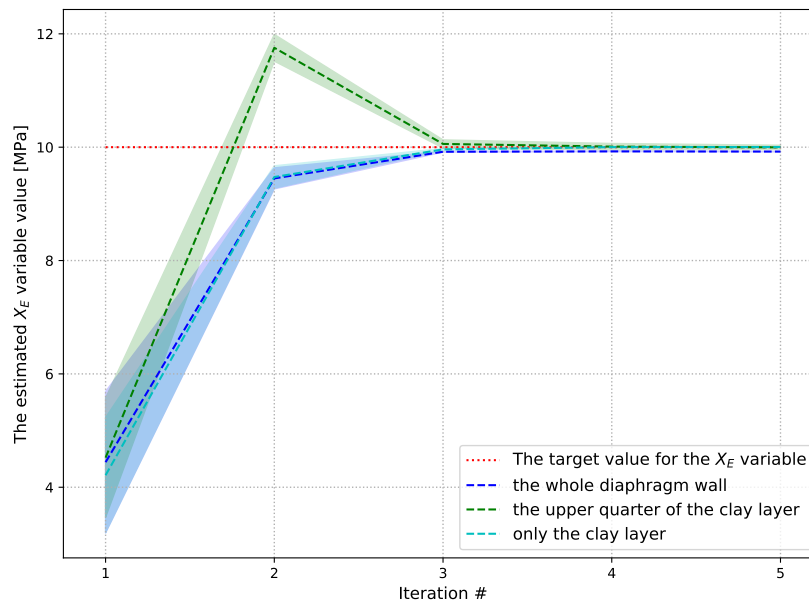


Figure 6.18: The evolution of the estimated mean of the ensembles throughout the iterations for a different observation types - one variable case.

The evolution of the mean estimates show one additional information: the ensemble created in the second iteration for the run with the smallest observation vector overestimated the variable value. Although in that run the algorithm converged to the sought value, the small observation factor can lead to a substantial overestimation of the ensemble would collapse before convergence. Concluding, using a small observation vector might lead over- or under-prediction, especially when the initial COV of the variables is very small.

The second part of this analysis used manually created observations, which imitate true readings from the field, i.e. when a perfect fit between the estimate and the target variables does not exist. The displacement curve, which was set as the target observation, together with the solutions obtained for those three observation vectors after the fifth iteration is shown in Figure 6.19 below. This analysis was done for two variables in the system.

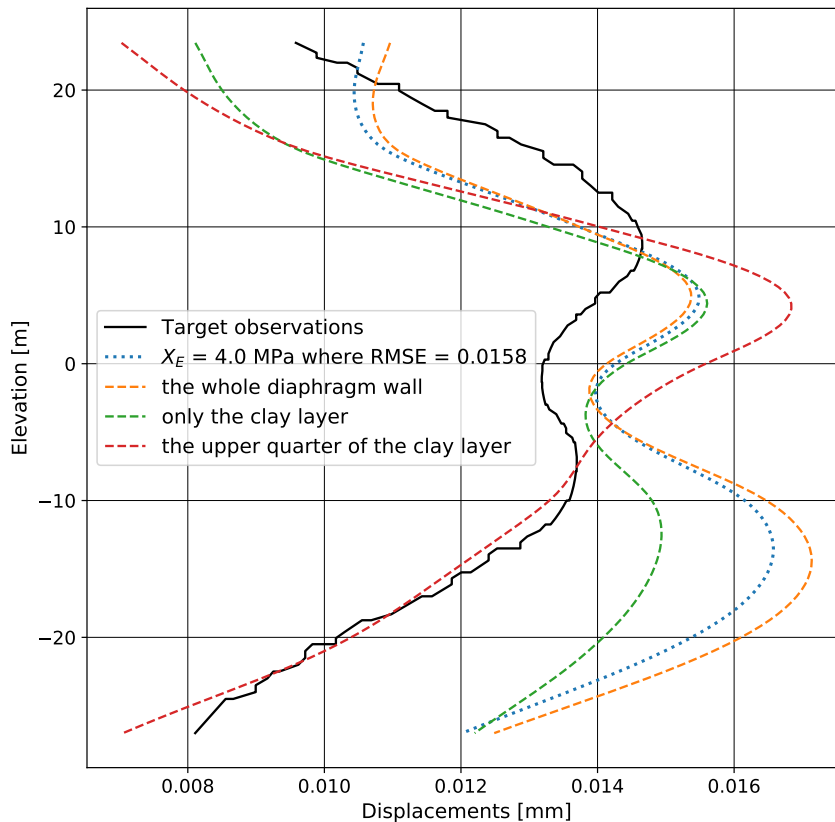


Figure 6.19: The computed diaphragm wall deflection for the runs with different observation vectors and the deflections imitating a true case.

The plots showing the corresponding evolution of the RMSE in a function of iterations is shown in Figure D.1, and the evolution of the estimated variables in a function of iterations are shown in Figures D.2 and D.3 in Appendix D.

The smallest RMSE was calculated for the run with the smallest observation vector and at the same time these results are the least conservative; however, the displacements computed for the estimated variables did not capture the second deflection of the diaphragm wall. Also, contrary to the previous analysis with only one variable, the error computed for the smallest observation vector was the smallest from the very beginning of the run.

Both of the runs with 45 and 140 displacements nodes provided have overestimated the displacements. Also, both analyses for systems with one and two variables indicated that the fewer observations are given, the higher the variance of the estimates.

6.3.5. Performance depending on the correlation coefficient

The covariance matrix of the initial state is as shown in Equation 6.3 below:

$$P_{init} = \begin{bmatrix} \sigma_{X_{E_{init}}}^2 & \text{Cov}(X_{E_{init}}, X_{Y_{init}}) \\ \text{Cov}(X_{E_{init}}, X_{Y_{init}}) & \sigma_{X_{Y_{init}}}^2 \end{bmatrix} \quad (6.3)$$

where: $\text{Cov}(X_{E_{init}}, X_{Y_{init}})$ is equal to the correlation coefficient $\rho_{X_E X_Y}$ multiplied by a standard deviation of $X_{E_{init}}$ and the standard deviation of $X_{Y_{init}}$.

Usually, this covariance between the variables is set as zero, because the initial estimates are given as single (mean) values with an unknown correlation between them. However, if the correlation was estimated beforehand, it can be used as an input.

In order to investigate how the additional input of this coefficient influences the convergence of the algorithm, four runs with different correlations of $\rho_{X_E X_Y} = \rho = [0.0, -0.50, -0.70, -0.90]$ were tested. In these runs, the target variables were set as $X_E = 10.0$ MPa and $X_Y = 0.00004$.

The evolution of the computed RMSE throughout the iterations is shown in Figure 6.20. The evolution of Pearson's coefficient itself for all of the runs mentioned above is shown in Figure 6.21.

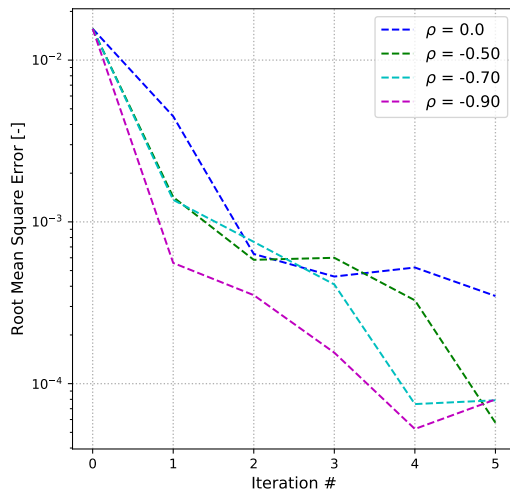


Figure 6.20: The comparison of the RMSE computed for the mean output of each iteration for different correlation coefficients - two variables case.

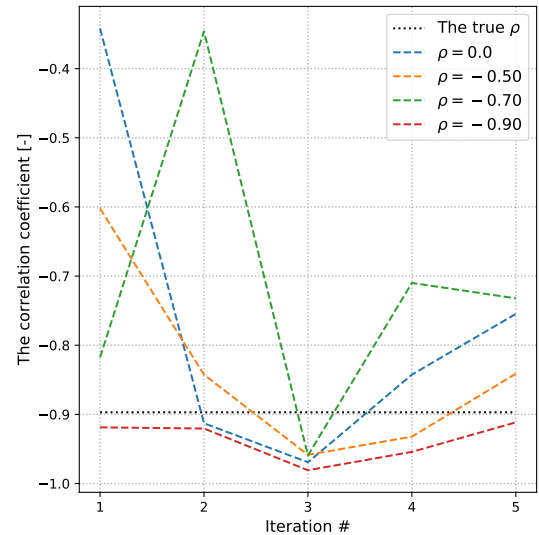


Figure 6.21: Pearson's correlation coefficient evolution throughout the iterations for different initial correlation values.

The correlation coefficient has a visible influence on the computed error, especially after the first iteration, where the initial correlation coefficient has the most prominent meaning. The true correlation coefficient was equal to $\rho = -0.90$, and from the first iteration till the penultimate one, the best estimate is given for the run with the initial coefficient of $\rho = -0.90$. The biggest influence of this input is visible in the first two iterations and then it gradually disappears.

As seen in Figure 6.21, after the third iteration the estimation of the correlation coefficient gets worse for most of the runs. From an accurate estimation of around 0.95 towards the true value of 0.90, the estimation changed to the correlation coefficient varying from ~ 0.70 to ~ 0.95 , what was caused by collapsing of the covariance. Even though the covariance collapsed, the best estimation was received for the correct input of $\rho = 0.90$, while for the other input higher discrepancies were noticed, especially in the first two iterations.

The evolution of the sought variables X_E and X_Y is shown in Figures 6.22 and 6.23.

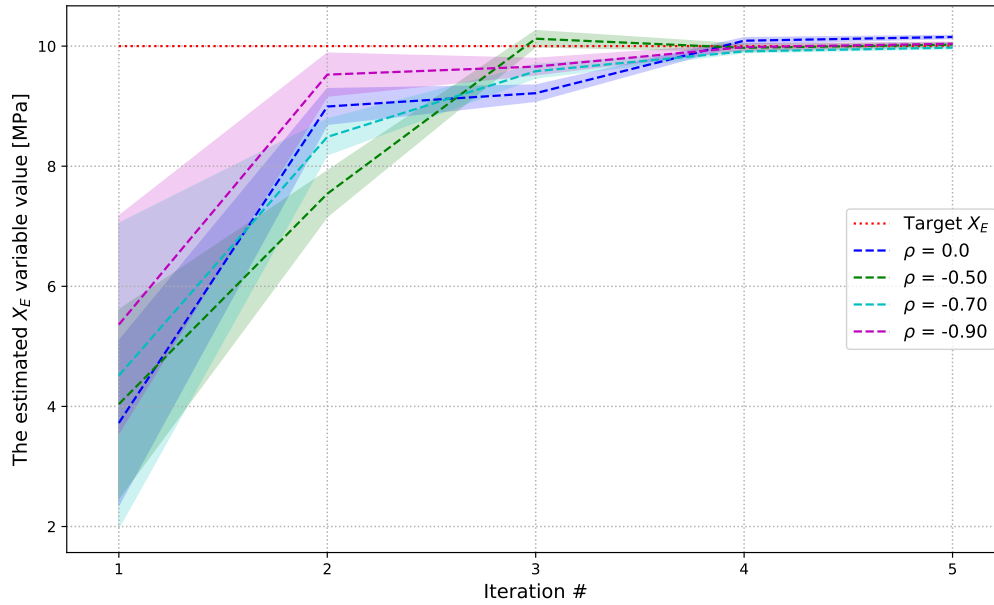


Figure 6.22: The evolution of the estimated mean (the X_E variable) of the ensembles throughout the iterations for different correlation coefficients - two variables case.

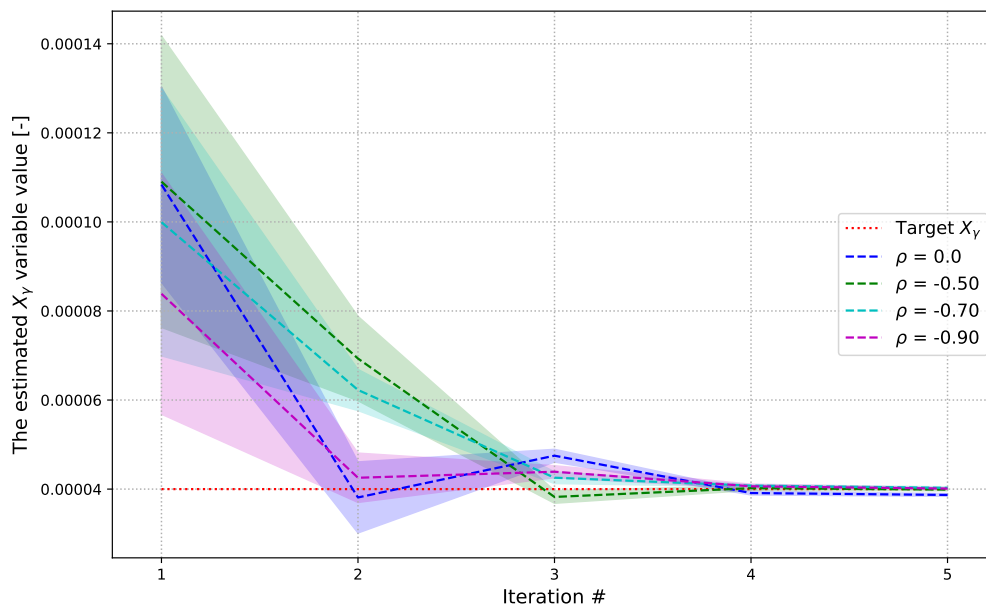


Figure 6.23: The evolution of the estimated mean (the X_γ variable) of the ensembles throughout the iterations for different correlation coefficients - two variables case.

The input of correct estimation of Pearson’s coefficient helped the algorithm to find both of the sought variables faster. Also, as seen in the second iteration, the second-best estimate was received for no initial correlation coefficient given; however, in the third iteration, this run gave the least accurate estimation. The results of the second iteration might indicate that no correlation specified can be better than the input of incorrect correlation value.

The next phenomenon that was investigated is the variances evolution throughout the iterations, what is shown in Figures 6.24 and 6.25 below.

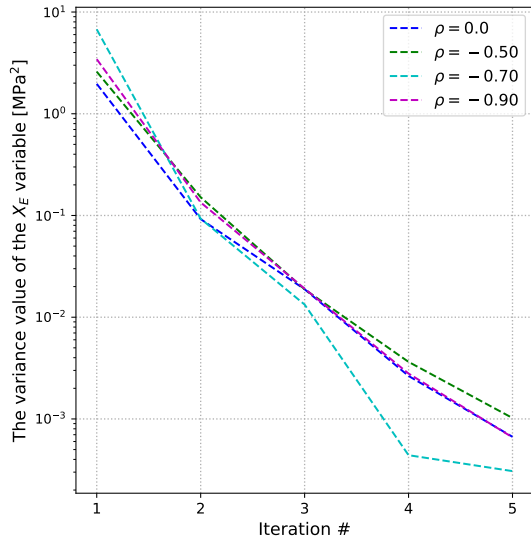


Figure 6.24: The evolution of the estimated variance of the X_E variable throughout the iterations for different initial correlation values.

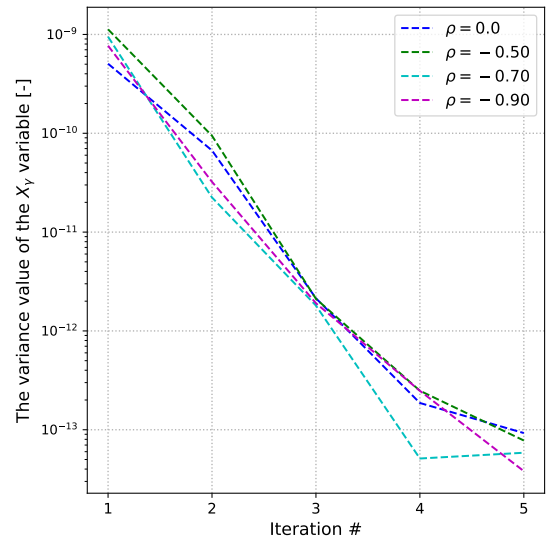


Figure 6.25: The evolution of the estimated variance of the X_γ variable throughout the iterations for different initial correlation values.

As we can see, the covariance for the run with the initial value of $\rho = -0.70$ is the smallest for most of the optimisation process. The variances and the covariance after the first iteration are the smallest for the initial coefficient of $\rho = 0.0$. Using values other than 0.0 for the correlation coefficient helped the algorithm to converge faster; however, it also increased the risk of covariance collapsing sooner. Therefore, one needs to be extremely careful and confident with using predefined values of the variables correlation, since for incorrectly specified values, the convergence might be impossible, and the final estimate might be erroneous.

Finally, the influence of the correlation coefficient on the algorithm performance is explained on the ensembles generated throughout the optimisation process. Starting from the general overview of the created ensembles shown in Figures 6.26 to 6.31.

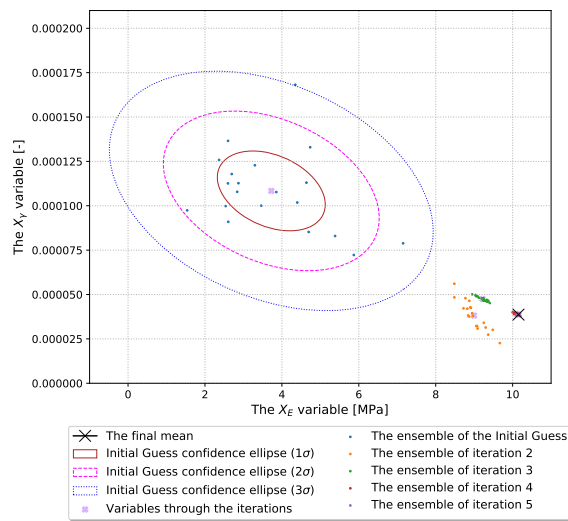


Figure 6.26: The ensemble created in each iteration for the initial value of $\rho = 0.0$.

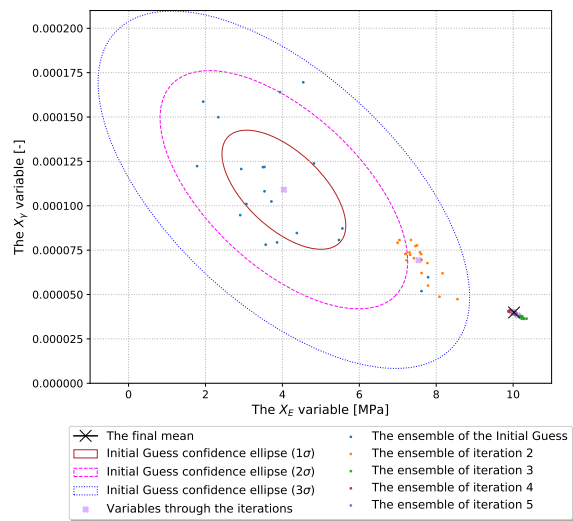


Figure 6.27: The ensemble created in each iteration for the initial value of $\rho = -0.50$.

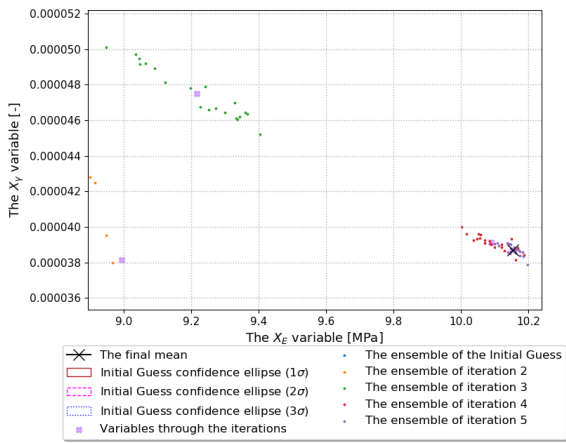


Figure 6.28: The ensemble created in each iteration for the initial value of $\rho = 0.0$ - focus on the last iterations.

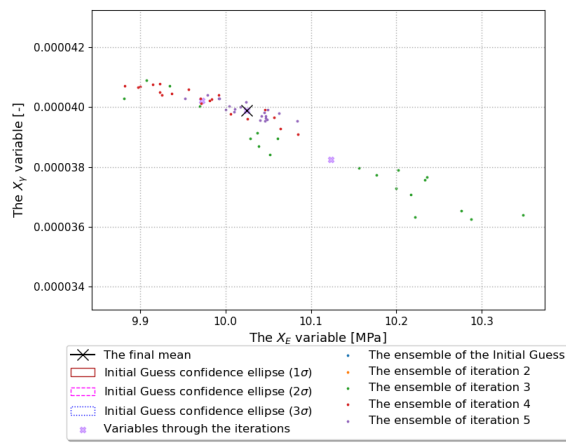


Figure 6.29: The ensemble created in each iteration for the initial value of $\rho = -0.50$ - focus on the last iterations.

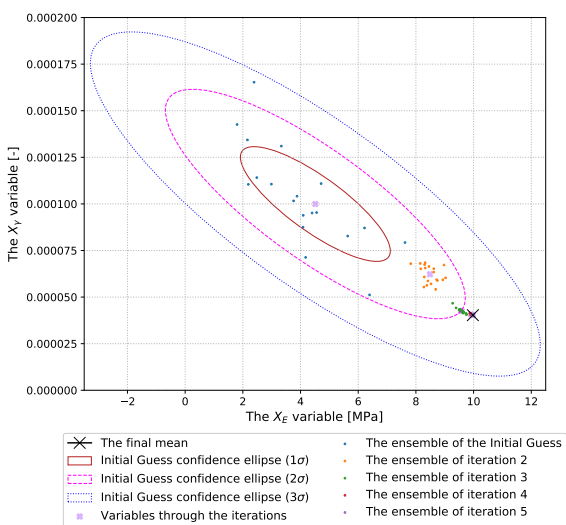


Figure 6.30: The ensemble created in each iteration for the initial value of $\rho = -0.70$.

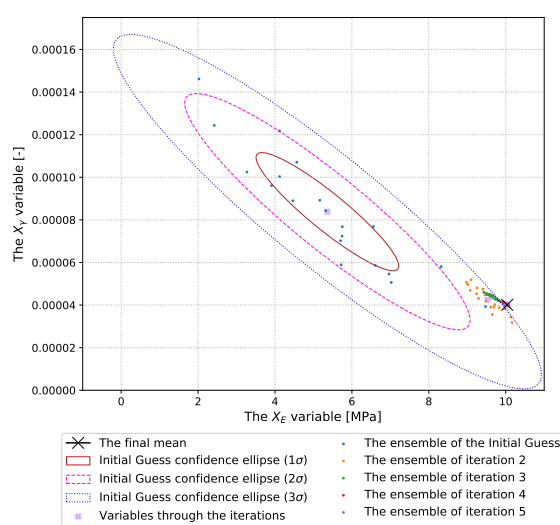


Figure 6.31: The ensemble created in each iteration for the initial value of $\rho = -0.90$.

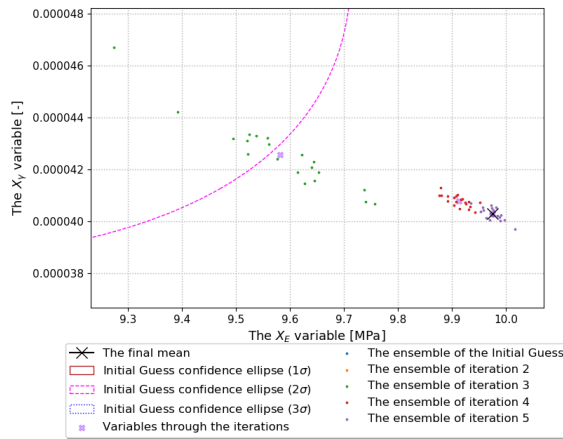


Figure 6.32: The ensemble created in each iteration for the initial value of $\rho = -0.70$ - focus on the last iterations.

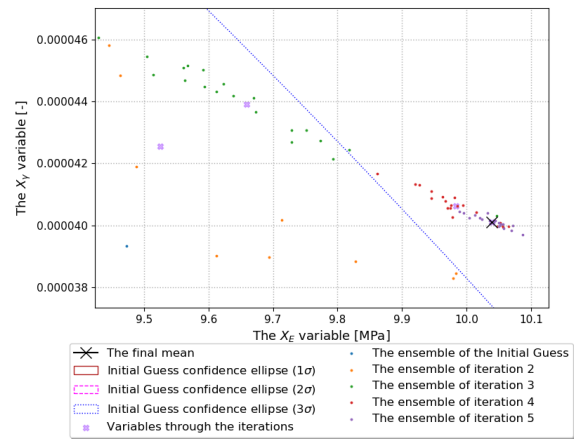


Figure 6.33: The ensemble created in each iteration for the initial value of $\rho = -0.90$ - focus on the last iterations.

As shown in plots above, the shapes of the covariance ellipses created around the first ensemble for $\rho = -0.50$ and $\rho = -0.90$ are much more analogous to the shape of the ensembles created in the successive iterations. When the consecutive iterations are zoomed, it is seen that the ensemble created in the second and third iterations is circumscribed much closer to the solution for coefficient ρ equal to -0.70 and -0.90 than for the other values, what is correct for the established targets with the Pearson's coefficient equal to $\rho \sim 0.90$.

As the analysis proved, the initial ensemble is circumscribed according to the input of the initial correlation. It resulted in steering the optimisation in a specific space governed by the initial and true correlations. The EnKF algorithm approximated the correlation coefficient starting from the first assimilation step and is capable of back-figuring the correlation coefficient between the variables used for creating the target measurements.

When the correlation coefficient of the initial guess is close to the one corresponding to the target parameters set, the robustness and the efficiency of the algorithm were influenced positively. This gives an additional tool for judging the outcome of the optimisation, and the coefficient can be used to judge a final solution or to add specific bounds between different parameters to create a limitation not to allow the algorithm to draw members, which lay beyond cap hardening surface, for example.

The pitfall of this is that deriving the coefficient from the laboratory tests is usually not easy, because of the limited number of the tests performed and noisy data. Nevertheless, the optimisation process is susceptible to changes in Pearson's coefficient, so one needs to fully understand how the input of correlation coefficient influences the output of the optimisation procedure.

6.4. Conclusions

The analyses shown in this section demonstrated following capabilities of the Ensemble Kalman Filter: The analyses showed in this section demonstrated the following capabilities of the Ensemble Kalman Filter:

- The algorithm is capable of finding the sought variable laying from one to six standard deviations from the initial estimate, with very high accuracy (the difference between the estimate and the solution lower than 1 per cent) using only 10 ensemble members and a maximum of 3 iterations.
- The algorithm is capable of finding two sought variables laying from one to six standard deviations from the initial guess with very high accuracy using only 20 ensemble members and a maximum of 3 iterations, provided that the stiffness was high enough, i.e. E_{50}^{ref} higher or equal to 3.0 MPa. The algorithm's efficiency and accuracy for stiffer soil are much higher, and its low efficiency for very weak soils rises a need for using a higher ensemble size for more than one variable.
- The algorithm is capable of finding a dependency between variables by approximating a correlation coefficient in the covariance matrix of the sample. The correlation is being back-figured based on the provided observations starting from the very first assimilation step. The coefficient can also be used as an input to the initial state. For the correct coefficient provided, the robustness and accuracy of the optimisation process are significantly increased.

Regarding the configurations of the algorithm, the following conclusions were stated:

- The efficiency of the algorithm after 20 calculation model runs was same for the observation vector consisting of displacements of 140 nodes located throughout the whole diaphragm wall as for one consisting of displacements of 40 nodes located only in the clay layer. The efficiency for the run with displacements provided from only 10 nodes located in the clay layer was much less. After 40 calculation model runs, the estimates for all of the three observation vectors balanced out.
- The ensemble size of 20 members was enough to solve most of the established targets of the presented problem consisting of 2 variables in a maximum of 3 iterations, what accounts for around 60 calculation model (Plaxis 2D) runs. Comparing a complexity of one- and two- variables system, the ensemble size, which allowed the algorithm to reduce the error to below 1.0% when the target is one standard deviation from the initial state, was equal to 5 and 20, respectively.

Last but not least, following limitations and reasons for accuracy and efficiency issues were formulated:

- Considering computations made in Plaxis 2D model for very weak soils (E_{50}^{ref} lower than 2.0 MPa), the level of non-linearity was too high for the algorithm using 20 ensemble members to capture the dependency between the parameters and the computed deflections.
- How a material model reproduces a true soil behaviour is never perfect and each simplification leads to decrease in efficiency of the algorithm, what highlights the importance of a proper choice of a material model and its accurate calibration.
- Constitutive soil models are formulated based on numerous soil mechanics laws, so the relations between their parameters (algorithm's variables) are characterised by specific bounds caused by, for example, shear yield surfaces and hardening cap surfaces. In order not to allow the algorithm to draw members, which break these bounds and cannot be an input to the FE model, one either has to reproduce the material model's code or use truncated distribution or log-normal distribution or both. This implies a need for a very good understanding of what is happening in the model, which solutions should be omitted and which are the optimal ones. The usage of truncated distribution also negatively influences the efficiency of the algorithm.
- The calculations in the optimisation process can take even several days, but due to limitations of Plaxis connection to Windows-proxy settings it is not possible to use Python's library *multiprocessing* together with the Plaxis software to create parallel processes, where each process would be an independent model run.

Conclusions and recommendations

7.1. Conclusions

In the presented thesis, a method of reducing the uncertainty in the soil parameters distribution using the field measurements and the Ensemble Kalman Filter algorithm is shown. The motivation was to make use of the displacements measurements from the construction site (synthetic measurements in the presented report) to directly correct the estimation of the soil parameters. The updated estimation of the soil parameters distribution can be used to improve predicting the soil behaviour and in the reliability updating through the construction phases by utilizing the data gathered in the less critical construction phases in the more critical ones.

The synthetic data-set of the diaphragm wall deflections generated in the FE software Plaxis was presented, so to prove the concept that the algorithm scripted in the Python environment successfully back-figures the sought variables (soil stiffness parameters) based only on a set of observed displacements. It is anticipated that this may contribute to the projects employing the Observational Method by a more confident assessment of switching between established construction's scenarios.

The presented algorithm was developed for a static scheme, where both observations and estimates concern only one construction phase; however, it is also possible to use the algorithm in a quasi-dynamic scheme in which the observations are provided from consecutive construction phases. This not only can help to better predict the behaviour in an advancing construction but also can reduce the amount of measurement data points required.

Specific conclusions, which were formulated based on the presented research, are divided into two groups and presented below:

a) Conclusions regarding the usage of the material models:

- Based on the available soil data, the best estimation of soil stiffness in the most crucial for deep excavation small-strain range was obtained for the GHS1120 model. Hence, in the considered soil conditions is considered as the best model for deep excavation applications. A big advantage of both the HSS and GHS models require only a triaxial compression test for a full calibration. Also, from all four models considered, the HSS model was the most robust in 2D FE calculations.
- Considering the GHS configurations independently, from all stress-dependency formulae the best estimate was received for stiffness calculated based on the lower principal and the pre-consolidation stresses. Regarding the plasticity model, the most accurate estimate was received for the formula with MC criterion with shear hardening added.
- Changing the stress-dependency of stiffness to be updated in each phase increases the robustness of the calculations due to ignoring the calculations of the relaxation of the soil domain in each step. Although the difference in the computed stiffness is negligible, this setting is slightly less conservative.

b) Regarding the inverse analysis algorithm used and optimisation of the costs of providing necessary data:

- The Ensemble Kalman Filter was chosen as the algorithm, which robustness was better and less influenced by the starting selection created around the initial guess than in the EKF. It required less calculation model runs, it did not need a gradient vector (a Jacobian matrix) and was giving a better estimation of sample variance.
- The developed algorithm successfully back-figured the sought variables' set from one to six standard deviations from the initial estimate with a relative error lower than 1% for one variable in only 20 calculation model (Plaxis 2D model) runs. For two variables, same efficiency was received for targets with stiffness of $E_{50}^{ref} = 3.0$ MPa and higher requiring only 40 calculation model runs.
- The algorithm is capable of deriving the correlation between the parameters based on the updated ensemble covariance. Furthermore, if the correlation is known beforehand, its certain input results in a more accurately circumscribed initial ensemble, hence in better robustness and accuracy of the algorithm.
- The robustness and accuracy of the algorithm are influenced by both the location, type and number of the displacements provided in the observation vector, and they increase up to a certain volume of the information provided after which additional input does not have any impact on the estimates. Performing a sensitivity studies of the influence of the number and spacing of the readings obtained from the FE model on the algorithm's response can optimise the number of the sensors installed at the site as a part of a monitoring program. The analysis has shown that focus on the layer, which parameters are to be optimised, is a reasonable solution. However, the spacing should allow the algorithm to capture all the inflexions in the diaphragm wall, which are caused by a bending moments distribution.

7.2. Limitations of the research

The main limitations of the research and reasons for inaccuracies are as follows:

- A repetitive incoherence between the results of the triaxial CU tests and typical CU tests was spotted in the form of almost not developed pore pressures, what could have led to an overestimation of the deviator stress, hence inaccuracies in the SoilTest simulations of the undrained tests.
- The calibration procedure was based on primary loading triaxial tests, whereas the true nature of the considered problem involves also unloading and reloading and these tests were not covered.
- There is a limited number of extension tests, and there are no direct, simple shear tests performed on clay samples. Therefore, the assumptions used to evaluate the lacking parameters are characterized by high uncertainty.
- The probability distributions of many parameters derived in the laboratory tests are characterised by a high variance what imposed considerable difficulty in finding representative tests with the parameters laying close to the mean.
- In order to derive the effective stiffness from the undrained tests, simulations in the SoilTest facility were used. The values were derived by iteratively changing the values of the input parameters, to fit the resulting stiffness. However, this method does not cover the correlation between the parameters fully, so is characterised by some inaccuracy.
- In some of the inverse analysis runs, the covariance collapsed. The effect of it is most visible in the last iterations, and it was visibly leading to inaccuracies in the estimation of, for example, correlation coefficient.

The limitations mentioned above may lead to several issues in the application of the inverse analysis in a real case. The most important risk is that the site investigation of poor quality, i.e. a one lacking some types of tests and parameters characterised by a high variance, lead to the decrease of efficiency of the inverse analysis by improper initial state description. In extreme cases, a high variance may rise a necessity to use, for example, a truncated distribution reducing the efficiency of the algorithm.

7.3. Recommendations for further studies

The fact that the estimation of parameters was improved for one layer gives an optimistic view of the further development of the method. Nevertheless, the developed method still needs many improvements, and many aspects have not been investigated in this thesis due to time and knowledge limitations. For future research, a few recommendations are formulated:

- The focus of the presented inverse analysis was on reducing the uncertainty of the parameters of one distinguished soil layer and included only two variables. Further improvement should bring more layers, which would significantly increase the number of variables in the system. This would require extensive knowledge about the correlation of the parameters and experience in Plaxis remote scripting.
- For a static and quasi-static scheme, a better solution than the Ensemble Kalman Filter would be to use Ensemble Smoother with Multiple Data Assimilation (ES-MDA) proposed by Emerick and Reynolds in 2011. Also, in order to maintain a higher variance of a sample and to avoid collapsing of the covariance the number of iterations should be reduced and the ensemble size increased instead. In the last iterations, the ensemble is very sensitive to changes in the estimates, so degeneration of the covariance can lead to wrong estimates of, for example, the correlation between variables.
- Accuracy and robustness of the optimisation process can be positively influenced by circumscribing the initial state closer the sought solution and by accurate input of correlation between the sought variables. Both can be received by a good site investigation program. Furthermore, good soil data can be a valuable factor for a judgement of the estimated values and their reliability and increase the certainty of the predictions.
- One of the most important factors governing the efficiency of the algorithm is the observation vector provided. Studies defining how the number, spacing and type (displacements of nodes and deflections of plates of particular structures) of the observations influence the efficiency would greatly increase the knowledge regarding the certainty of the inverse analysis.
- Since the usage of truncated distribution negatively influences the efficiency of the algorithm, a thorough understanding of soil mechanics law governing the chosen material model can help to script an ensemble sampler, which would allow to efficiently use more variables (soil layers and their parameters) in the optimisation process.
- A time needed for computations and complexity of the problem turned out to be less than expected, however, if the level of complexity would be higher, the Response Surface Method can be the way of creating measurements while keeping robustness at an acceptable level.
- Since the availability of guidebooks about the remote scripting with the Python wrapper is very limited, it is recommended to reserve a reasonable amount of time for getting familiar with the scripting commands and creating a fully functional connection to a Plaxis model.
- Using Python's library *Multithreading* to run a calculation model run in Plaxis gives a more prominent control over the calculation process and the possibility of, for example, stopping and restarting a calculation if an error or exception was raised.
- Additional studies regarding how and if to gradually reduce the process noise R throughout the iterations (and time-steps in quasi-static schemes) can bring another way to increase the algorithm's robustness.

Bibliography

- [1] Adem, H. H. and Vanapalli, S. K. (2013). Constitutive modeling approach for estimating 1-D heave with respect to time for expansive soils. *International Journal of Geotechnical Engineering*, 7(2):199–204.
- [2] Alipour, A. and Eslami, A. (2019). Design adaptations in a large and deep urban excavation: Case study. *Journal of Rock Mechanics and Geotechnical Engineering*, 11(2):389–399.
- [3] Alpan, I. (1970). The geotechnical properties of soils. *Earth Science Reviews*, 6(1):5–49.
- [4] Alt, H. and Godau, M. (1995). Computing the Fréchet Distance between Two Polygonal Curves. *International Journal of Computational Geometry & Applications*, 5(1):75–91.
- [5] Andrade-Campos, A., De-Carvalho, R., and Valente, R. A. F. (2012). Novel criterion for determination of material model parameters. *International Journal of Mechanical Sciences*, 54(1):294–305.
- [6] Arulampalam, M. S., Maskell, S., Gordon, N., and Clapp, T. (2002). A tutorial on Particle Filters for Online Nonlinear/Non-Gaussian Bayesian Tracking. *IEEE Transactions on Signal Processing*, 50(2):723–737.
- [7] Bagnell, D. (2014). Good , Bad , and Ugly of Particle Filters The Good.
- [8] Berndt, D. J. and Clifford, J. (1994). Using Dynamic Time Warping to Find Patterns in Time Series. In *Proceedings of the 3rd International Conference on Knowledge Discovery and Data Mining*, AAAIWS'94, pages 359–370. AAAI Press.
- [9] Bolt, G. H. (1956). Physico-Chemical Analysis of the Compressibility of Pure Clays. *Géotechnique*, 6(2):86–93.
- [10] Bowles, J. E. (1997). *Foundation Analysis and Design*, volume 20. The McGraw-Hill Companies, Inc., 5 edition.
- [11] Bringmann, K. (2014). Why walking the dog takes time: Frechet distance has no strongly subquadratic algorithms unless SETH fails. In *2014 IEEE 55th Annual Symposium on Foundations of Computer Science*, pages 661–670, Philadelphia, PA, USA.
- [12] Brinkgreve, R., Kumarswamy, S., Swolfs, W., and Foria, F. (2018). PLAXIS 2D Material Models Manual.
- [13] Brinkgreve, R. B. J. (2019). Private correspondence. Delft.
- [14] Calvello, M. and Finno, R. J. (2004). Selecting parameters to optimize in model calibration by inverse analysis. *Computers and Geotechnics*, 31(5):410–424.
- [15] Cao, J. and Lin, J. (2008). A study on formulation of objective functions for determining material models. *International Journal of Mechanical Sciences*, 50(2):193–204.
- [16] Chang-Yü, O., Dar-Chang, C., and Tzong-Shiann, W. (1996a). Three-Dimensional Finite Element Analysis of Deep Excavation. *Journal of Geotechnical Engineering*, 122(5):769–774.
- [17] Chang-Yü, O., Dar-Chang, C., and Tzong-Shiann, W. (1996b). Three-Dimensional Finite Element Analysis of Deep Excavations. *Journal of Geotechnical Engineering*, 122(5):337–345.
- [18] Chapman, T. and Green, G. (2004). Observational method looks set to cut city building costs. *Proceedings of the Institution of Civil Engineers - Civil Engineering*, 157(3):125–133.
- [19] Chen, F. H. (1988). *Foundations on expansive soils*. Elsevier ; Distributors for the U.S. and Canada, Elsevier Science Pub. Co., Amsterdam; New York; New York, NY, U.S.A.
- [20] Chew, S. H., Young, K. Y., and Lim, A. (1997). Three-dimensional finite element analysis of a strutted excavation. In *Computer methods and advances in geomechanics*, pages 1915–1920, Wuhan, China. Balkema.

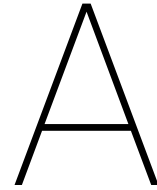
- [21] Contractor, D., Desai, C. S., Harpalani, S., Kemeny, J., and Kundu, T. (2001). Computer methods and advances in geomechanics. In Chandra S. Desai, editor, *Proceedings of the Tenth International Conference on Computer Methods and Advances in Geomechanics*, Tucson.
- [22] Dianati, M., Song, I., and Treiber, M. (2019). *An Introduction to Genetic Algorithms and Evolution Strategies*.
- [23] Dong, Y. (2014). *Advanced Finite Element Analysis of Deep Excavation Case Histories*. PhD thesis, University of Oxford.
- [24] Dong, Y. P., Burd, H. J., and Houlsby, G. T. (2016). Finite-element analysis of a deep excavation case history. *Géotechnique*, 66(1):1–15.
- [25] Driemel, A., Har-Peled, S., and Wenk, C. (2012). Approximating the Fréchet Distance for Realistic Curves in Near Linear Time. *Discrete & Computational Geometry*, 48(1):94–127.
- [26] Eiter, T., Mannila, H., and Eiter, T. (1994). Computing Discrete Fréchet Distance.
- [27] Evensen, G. (1994). Sequential data assimilation with a nonlinear quasi-geostrophic model using Monte Carlo methods to forecast error statistics. *Journal of Geophysical Research*, 99(C5).
- [28] Eykhoff, P. (1974). System identification: parameter and state estimation.
- [29] Finno, R. J., Blackburn, J. T., and Roboski, J. F. (2007). Three-Dimensional Effects for Supported Excavations in Clay. *Journal of Geotechnical and Geoenvironmental Engineering*, 133(1).
- [30] Finno, R. J. and Calvello, M. (2005). Supported Excavations: Observational Method and Inverse Modeling. *Journal of Geotechnical and Geoenvironmental Engineering*, 131(7):826–836.
- [31] Fook-Hou, L., Kwet-Yew, Y., N., Q. K. C., and Kum-Thong, C. (1998). Effect of Corners in Struttred Excavations: Field Monitoring and Case Histories. *Journal of Geotechnical and Geoenvironmental Engineering*, 124(4):339–349.
- [32] Fréchet, M. M. (1906). Sur quelques points du calcul fonctionnel. *Rendiconti del Circolo Matematico di Palermo (1884-1940)*, 22(1):1–72.
- [33] Fuentes, R., Pillai, A., and Ferreira, P. (2018). Lessons learnt from a deep excavation for future application of the observational method. *Journal of Rock Mechanics and Geotechnical Engineering*, 10(3):468–485.
- [34] Gilks, W. R., Richardson, S., and Spiegelhalter, S. J. (2000). *Markov Chain Monte Carlo in Practice*, volume 1. Chapman & Hall, London.
- [35] Giorgino, T. (2009). Computing and visualizing dynamic time warping alignments in R: The dtw package. *Journal of Statistical Software*, 31(7):1–24.
- [36] Glass, P. R. and Powderham, A. J. (1994). Application of the observational method at the Limehouse Link. *Géotechnique*, 44(4):665–679.
- [37] Gordon, N. J., Salmond, D. J., and Smith, A. F. M. (1993). Novel approach to nonlinear/non-Gaussian Bayesian state estimation. *IEE Proceedings F Radar and Signal Processing*, 140(2):107–113.
- [38] Gourvenec, S., Powrie, W., and De Moor, E. K. (2009). Three-dimensional effects in the construction of a long retaining wall. *Proceedings of the Institution of Civil Engineers - Geotechnical Engineering*, 155(3):163–173.
- [39] Gouw, T. L. (2014). Common mistakes on the application of plaxis 2D in analyzing excavation problems. *International Journal of Applied Engineering Research*, 9(21):8291–8311.
- [40] Grimstad, G., Andresen, L., and Jostad, H. P. (2012). NGI-ADP: Anisotropic shear strength model for clay. *International Journal for Numerical and Analytical Methods in Geomechanics*, 36(2012):483–497.
- [41] Gutjahr, I. (2017). Project correspondence. Technical report, Soletanche Bachy.

- [42] Hongyu, T. (2015). Prediction of the Variation of Swelling Pressure and 1-D Heave of Expansive Soils With Respect To Suction.
- [43] Hsieh, Y.-M., Dang, P. M., and Lin, H.-D. (2017). How Small Strain Stiffness and Yield Surface Affect Undrained Excavation Predictions. *International Journal of Geomechanics*, 17(3).
- [44] Hsiung, B. C. B. and Dao, S. D. (2014). Evaluation of constitutive soil models for predicting movements caused by a deep excavation in sands. *Electronic Journal of Geotechnical Engineering*, 19(Z5):17325–17344.
- [45] Hsiung, B. C. B., Yang, K. H., Aila, W., and Hung, C. (2016). Three-dimensional effects of a deep excavation on wall deflections in loose to medium dense sands. *Computers and Geotechnics*, 80:138–151.
- [46] Israel Science and Technology Directory (2019). Climate and Seasons in Israel.
- [47] Jekel, C. F., Venter, G., Venter, M. P., Stander, N., and Haftka, R. T. (2019). Similarity measures for identifying material parameters from hysteresis loops using inverse analysis. *International Journal of Material Forming*, 12(3):355–378.
- [48] Kang, L. (2017). *Reduction of Uncertainty in Stability Calculations for Slopes Under Seepage*. PhD thesis, TU Delft, Delft.
- [49] Katzfuss, M., Stroud, J. R., and Wikle, C. K. (2016). Understanding the Ensemble Kalman Filter. *American Statistician*, 70(4):350–357.
- [50] Klein, J. (2015a). Geotechnical Factual Report. Technical report, IBI Group + DHV BV Collaborative Design Team, Tel Aviv-Yafo.
- [51] Klein, J. (2015b). Geotechnical Interpretative Report. Technical report, IBI, Royal HaskoningDHV Collaborative Design Team, Tel Aviv-Yafo.
- [52] Labbe, R. R. (2018). *Kalman and Bayesian Filters in Python*. GitHub repository.
- [53] Ladd, C. C. and Foott, R. (1974). New Design Procedure for Stability of Soft Clays. *Journal of the Geotechnical Engineering Division*, 100(7):763–786.
- [54] Ladd, C. C., Young, G. A., Kraemer, S. R., and Burke, D. M. (1999). Engineering Properties of Boston Blue Clay from Special Testing Program. In *Special Geotechnical Testing: Central Artery/Tunnel Project in Boston, Massachusetts*, pages 1–24, Boston. Haley & Aldrich, Inc.
- [55] Ledesma, A., Gens, A., and Alonso, E. E. (1996). Parameter and variance estimation in geotechnical backanalysis using prior information. *International Journal for Numerical and Analytical Methods in Geomechanics*, 20(2):119–141.
- [56] Lee, F.-H., Hong, S.-H., Gu, Q., and Zhao, P. (2010). Application of Large Three-Dimensional Finite-Element Analyses to Practical Problems. *International Journal of Geomechanics*, 11(6):529–539.
- [57] Lin, D. G., Chung, T. C., and Phien-wej, N. (2003). Quantitative evaluation of corner effect on deformation behavior of multi-strutted deep excavation in Bangkok subsoil. 34:41–57.
- [58] Mavritsakis, A. (2017). Evaluation of Inverse Analysis Methods with Numerical Simulation of Slope Excavation.
- [59] Miranda, T. (2007). Geomechanical Parameters Evaluation in Underground Structures. Artificial Intelligence, Bayesian Probabilities and Inverse Methods.
- [60] Miranda, T., Dias, D., Eclaircy-Caudron, S., Gomes Correia, A., and Costa, L. (2011). Back analysis of geomechanical parameters by optimisation of a 3D model of an underground structure. *Tunnelling and Underground Space Technology*, 26(6):659–673.
- [61] Miranda, T., Dias, D., Kastner, R., Sousa, L., Eclaircy-Caudron, S., and Correia, A. (2010). Inverse analysis on two geotechnical works. *Applications of Computational Mechanics in Geotechnical Engineering V*, (February 2015):4–7.

- [62] Mitew-Czajewska, M. (2018). Parametric study of deep excavation in clays. *Bulletin of the Polish Academy of Sciences - Technical Sciences*, 66(5).
- [63] Moreira, N., Miranda, T., Pinheiro, M., Fernandes, P., Dias, D., Costa, L., and Sena-Cruz, J. (2013). Back analysis of geomechanical parameters in underground works using an Evolution Strategy algorithm. *Tunnelling and Underground Space Technology*, 33:143–158.
- [64] Murillo, C., Hoyos, L., Colmenares, J. E., and Berdugo, I. R. (2013). *Advances in Unsaturated Soils*. CRC Press, 1 edition.
- [65] Nguyen, L. T. and Nestorovi, T. (2013). Application of the Extended Kalman Filter for Soil Parameter Identification during Tunnel Excavation. In *3rd International Conference on Computational Methods in Tunneling and Subsurface Engineering*, pages 17–19, Bochum, Germany.
- [66] Ni, P., Mei, G., Zhao, Y., and Chen, H. (2018). Plane strain evaluation of stress paths for supported excavations under lateral loading and unloading. *Soils and Foundations*, 58(1):146–159.
- [67] Núñez, G., Borghei, Z., and Perau, E. (2014). Stability verification against the basal heave failure mechanism at excavations in soft soils with FEM and classical methods. In *Numerical Methods in Geotechnical Engineering*, pages 229–234.
- [68] Panagoulas, S., Laera, A., and Brinkgreve, R. B. J. (2017). A practical study on the induced seismicity in Groningen and the seismic response of a masonry structure. *The 3rd International Conference on Performance Based Design in Earthquake Geotechnical Engineering*, (2010):9.
- [69] Peck, R. B. (1969). Advantages and Limitations of the Observational Method in Applied Soil Mechanics. *Géotechnique*, 19(2):171–187.
- [70] Peck, R. B. (2001). The observational method can be simple. *Proceedings of the Institution of Civil Engineers - Geotechnical Engineering*, 149(2):71–74.
- [71] Petitjean, F., Ketterlin, A., and Gançarski, P. (2011). A global averaging method for dynamic time warping, with applications to clustering. *Pattern Recognition*, 44:678–693.
- [72] Plaxis (2016). *The SHANSEP MC model*.
- [73] Plaxis (2019). *Material Models Manual - Plaxis*. Technical report.
- [74] Polavarapu, S. (2014). *The Linear Kalman Filter*. Technical report, Toronto University, Toronto.
- [75] Potts, D. M. and Fourie, A. B. (1986). Discussion: The behaviour of a propped retaining wall: results of a numerical experiment. *Géotechnique*, 36(1):119–121.
- [76] Potts, D. M. and Zdravković, L. (2001). *Finite Element Analysis in Geotechnical Engineering: Volume two - Application*. Thomas Telford Publishing.
- [77] Powderham, A. J. (2002). *The observational method—learning from projects*, volume 155.
- [78] Powderham, A. J. and Rutty, P. C. (1994). The observational method in value engineering. In *Proceedings of the 5th International Conference on Pilling and Deep Foundations*, pages 1–5.
- [79] Sakurai, S., Akutagawa, S., Takeuchi, K., Shinji, M., and Shimizu, N. (2003). Back analysis for tunnel engineering as a modern observational method. *Tunnelling and Underground Space Technology*, 18(2):185–196.
- [80] Salvador, S. and Chan, P. (2007). Toward Accurate Dynamic Time Warping in Linear Time and Space. *Mathematics*, 11(5):561–580.
- [81] Seah, T. H. and Lai, K. C. (2003). Strength and Deformation Behavior of Soft Bangkok Clay. *Geotechnical Testing Journal*, 26(4):421–431.
- [82] Senin, P. (2008). Dynamic Time Warping Algorithm Review. (December):1–23.

- [83] Seyler, S. L., Kumar, A., Thorpe, M. F., and Beckstein, O. (2015). Path Similarity Analysis: A Method for Quantifying Macromolecular Pathways. *PLOS Computational Biology*, 15(6).
- [84] Simpson, B. (1992). Retaining structures: displacement and design. *Géotechnique*, 42(4):541–576.
- [85] Spross, J. and Johansson, F. (2017). When is the observational method in geotechnical engineering favourable? *Structural Safety*, 66:17–26.
- [86] Take, W. A., Bolton, M. D., and Munachen, S. E. (2001). A deformation measurement system for geotechnical testing based on digital imaging, close-range photogrammetry, and PIV image analysis. *15th International Conference on Soil Mechanics and Geotechnical Engineering*, (May 2016):539–542.
- [87] Tavares, C. (1997). *Back analysis methods in the interpretation of concrete dams behaviour (in Portuguese)*. PhD thesis, Technical University of Lisbon.
- [88] Terejanu, G. A. (2003). Extended Kalman Filter Tutorial. Technical report, University at Buffalo, Buffalo, NY, USA.
- [89] Terzaghi, K. and Peck, R. B. (1948). *Soil Mechanics in Engineering Practice*. Wiley ; Chapman & Hall, New York : London, 3 edition.
- [90] Tomilson, M. J. (1980). *Foundation Design and Construction*. Pitman Publishing Inc., London, England, 4th edition.
- [91] Tormene, P., Giorgino, T., Quaglini, S., and Stefanelli, M. (2009). Matching incomplete time series with dynamic time warping: an algorithm and an application to post-stroke rehabilitation. *Artificial Intelligence in Medicine*, 45(1):11–34.
- [92] Ukritchon, B. and Boonyatee, T. (2015). Soil Parameter Optimization of the NGI-ADP Constitutive Model for Bangkok Soft Clay. *Geotechnical Engineering Journal of the SEAGS & AGSSEA*, 46(1):28–36.
- [93] Wichtmann, T. and Triantafyllidis, T. (2009). On the correlation of “static” and “dynamic” stiffness moduli of non-cohesive soils. *Bautechnik*, 86(S1):28–39.
- [94] Witowski, K. and Stander, N. (2012). Parameter Identification of Hysteretic Models Using Partial Curve Mapping. In *12th AIAA Aviation Technology, Integration, and Operations (ATIO) Conference and 14th AIAA/ISSMO Multidisciplinary Analysis and Optimization Conference*, Aviation Technology, Integration, and Operations (ATIO) Conferences, Indianapolis, Indiana. American Institute of Aeronautics and Astronautics.
- [95] Xuan, F., Xia, X. H., and Wang, J. H. (2009). The Application of a Small Strain Model in Excavations. *Journal of Shanghai Jiaotong University (Science)*, 14(4):418–422.
- [96] Yang, Z. and Elgamal, A. (2003). Application of unconstrained optimization and sensitivity analysis to calibration of a soil constitutive model. *International Journal for Numerical and Analytical Methods in Geomechanics*, (27):1277–1297.
- [97] Yeow, H.-c. and Feltham, I. (2008). Case Histories Back Analyses for the Application of the Observational Method under Eurocodes for the Scout Project. *Sixth International Conference on Case Histories in Geotechnical Engineering*, (8):1–13.
- [98] Yeow, H.-C., Nicholson, D., Man, C.-L., Ringer, A., Glass, P., and Black, M. (2014). Application of observational method at Crossrail Tottenham Court Road station, UK. *Proceedings of the Institution of Civil Engineers - Geotechnical Engineering*, 167(2):182–193.
- [99] Yin, Z. Y., Jin, Y. F., Shen, J. S., and Hicher, P. Y. (2018). Optimization techniques for identifying soil parameters in geotechnical engineering: Comparative study and enhancement. *International Journal for Numerical and Analytical Methods in Geomechanics*, 42(1):70–94.
- [100] Zdravkovic, L., Potts, D. M., and St John, H. D. (2005). Modelling of a 3D excavation in finite element analysis. *Géotechnique*, 55(7):497–513.

Appendices



Calibration of the material models parameters

A.1. Subsoil parameters assessment

A.1.1. Triaxial test parameters

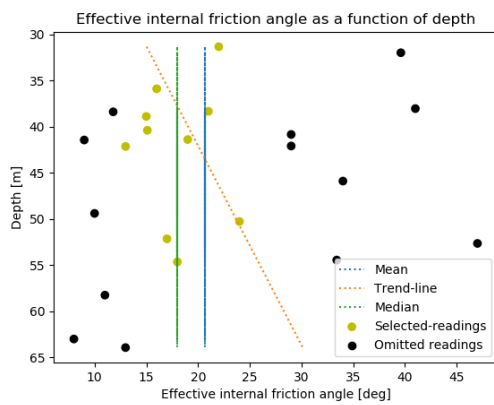


Figure A.1: Distribution of the effective internal friction angle obtained in the CU triaxial tests as a function of depth.

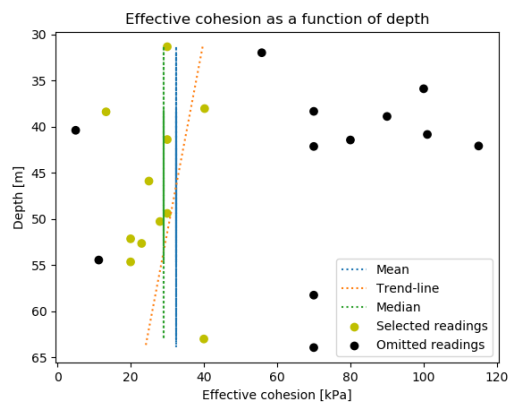


Figure A.2: Distribution of the effective cohesion value obtained in the CU triaxial tests as a function of depth.

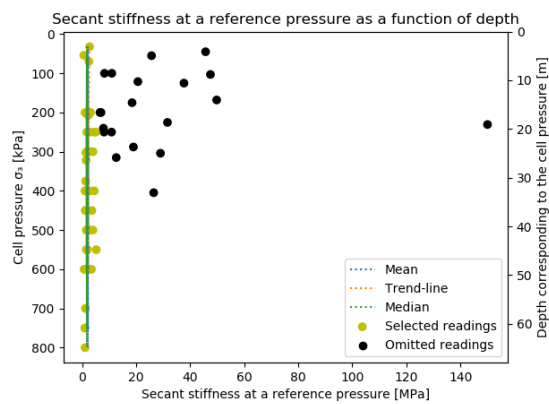


Figure A.3: Distribution of the secant stiffness as a function of depth obtained in triaxial CU tests.

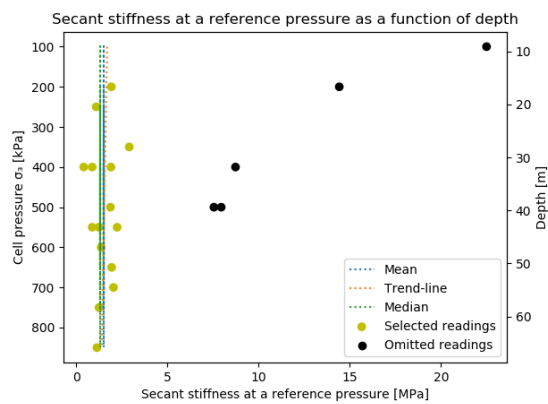


Figure A.4: Distribution of the secant stiffness as a function of depth obtained in triaxial UU tests.

A.1.2. Pressuremeter test parameters

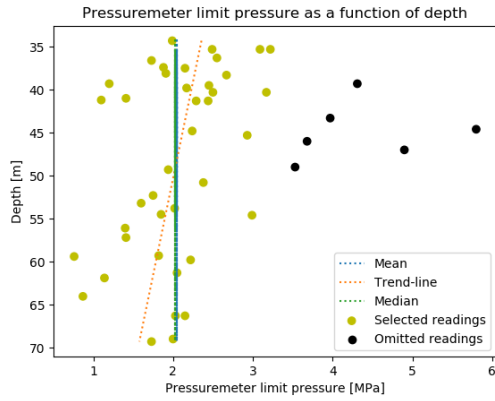


Figure A.5: Pressuremeter limit pressure p_L as a function of depth.

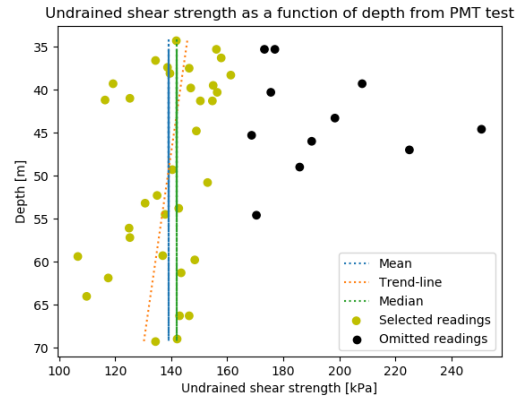


Figure A.6: The undrained shear strength s_u obtained in the PMT testing.

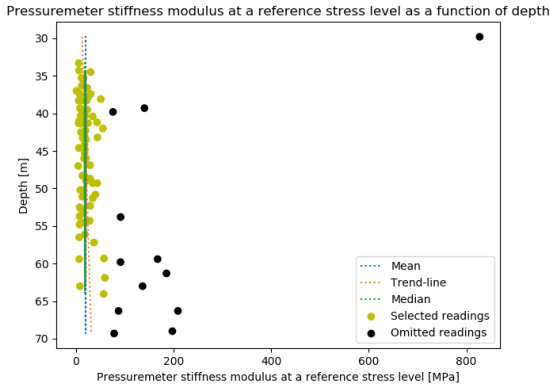


Figure A.7: Pressuremeter stiffness modulus E_M as a function of depth.

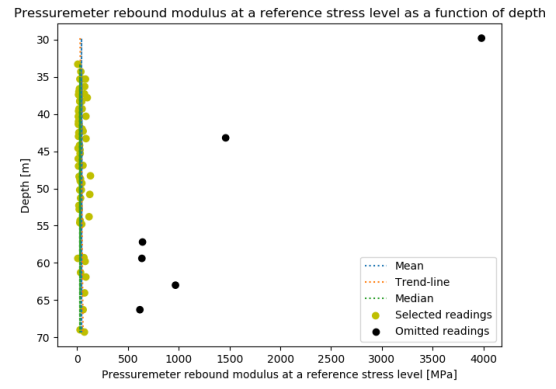


Figure A.8: Pressuremeter rebound modulus E_{ur} as a function of depth.

A.1.3. Consolidation test parameters

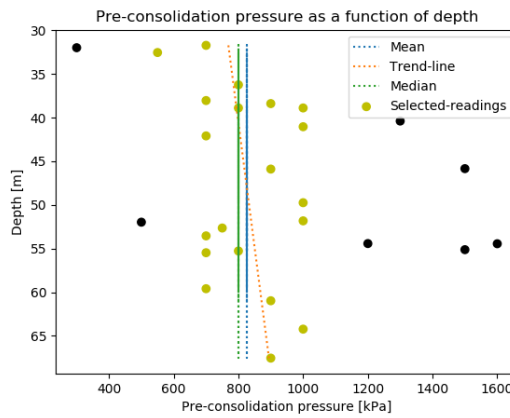


Figure A.9: The one-dimensional consolidation test pre-consolidation pressure σ'_p as a function of depth.

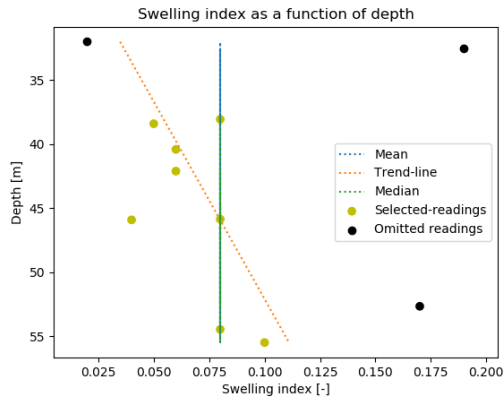


Figure A.10: The consolidation test swelling index C_e as a function of depth.

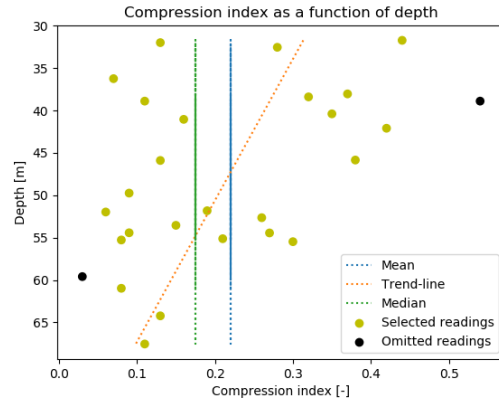


Figure A.11: The consolidation test compression index C_c as a function of depth.

A.1.4. Atterberg limits and index tests parameters

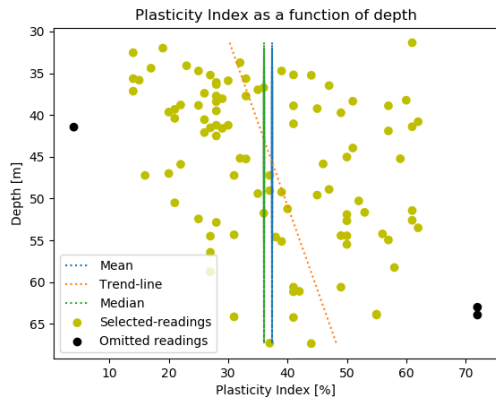


Figure A.12: Atterberg test Plasticity Index PI as a function of depth.

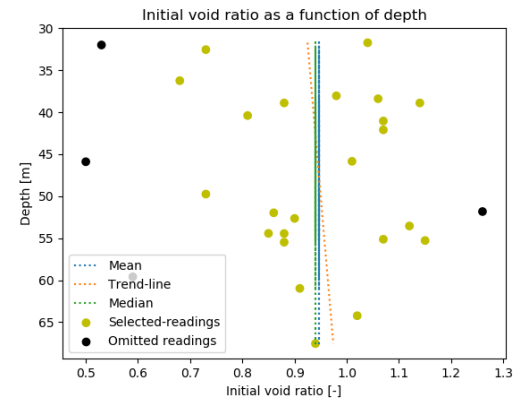


Figure A.13: The consolidation test initial void ratio e_0 as a function of depth.

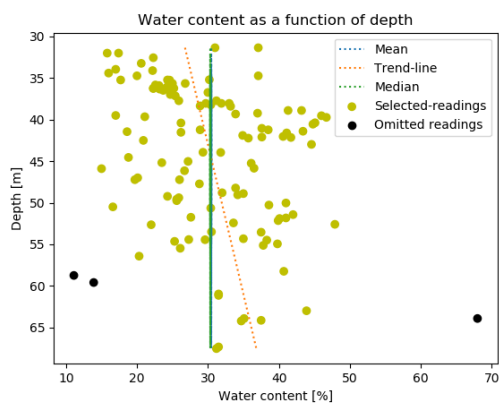


Figure A.14: Natural water content w as a function of depth.

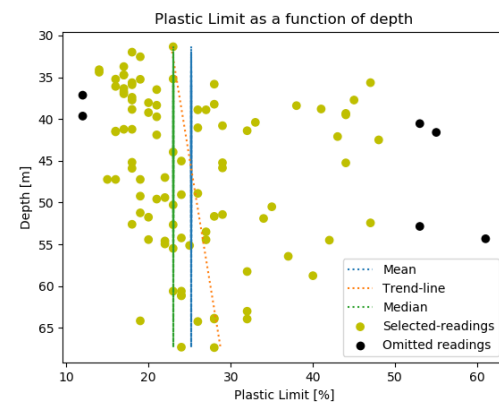


Figure A.15: Atterberg test Plasticity Limit PL as a function of depth.

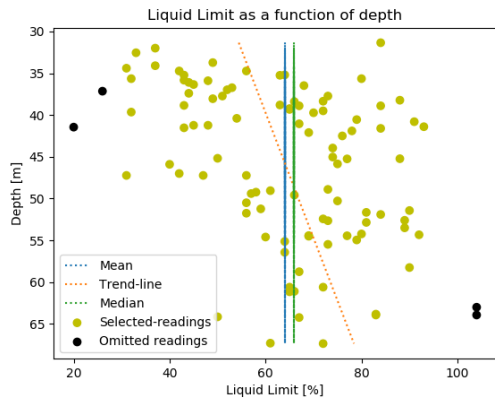


Figure A.16: Atterberg test Liquid Limit LL as a function of depth.

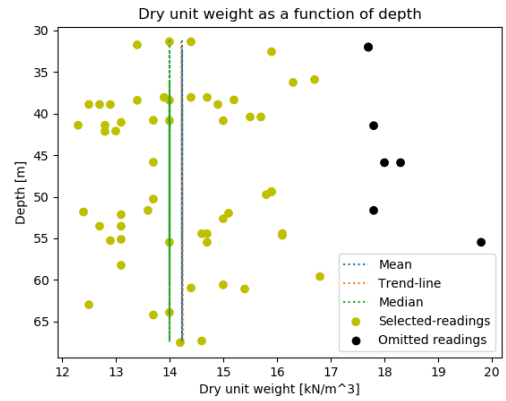


Figure A.17: Dry unit weight γ_d as a function of depth.

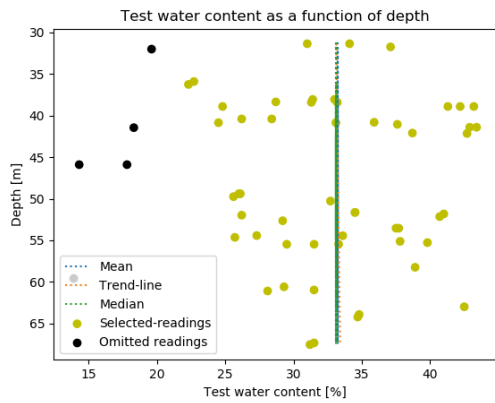


Figure A.18: Test water content w_{test} as a function of depth.

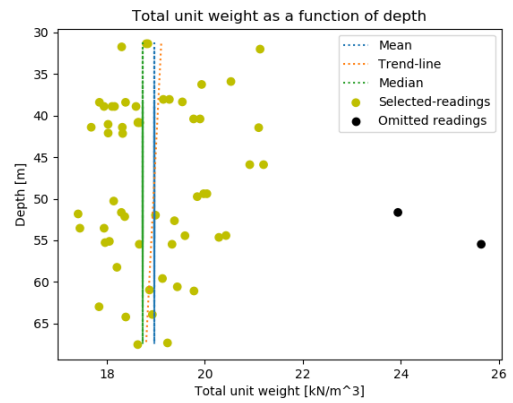


Figure A.19: Total unit weight γ_{sat} as a function of depth.

A.1.5. Summary - final parameters assessment

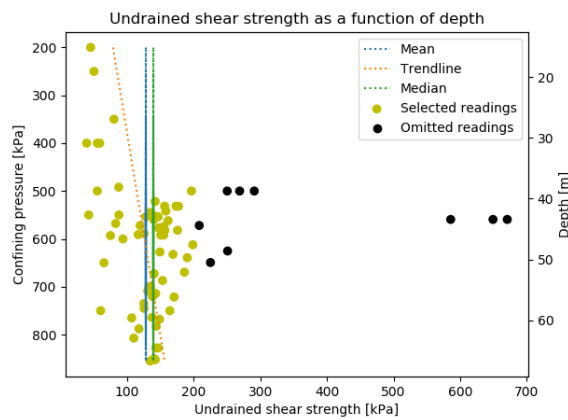


Figure A.20: The undrained shear strength s_u obtained in the PMT, UC and UU tests as a function of confining pressure (with corresponding averaged depth).

A.2. Studies on the material model parameters

A.2.1. Chosen representative tests

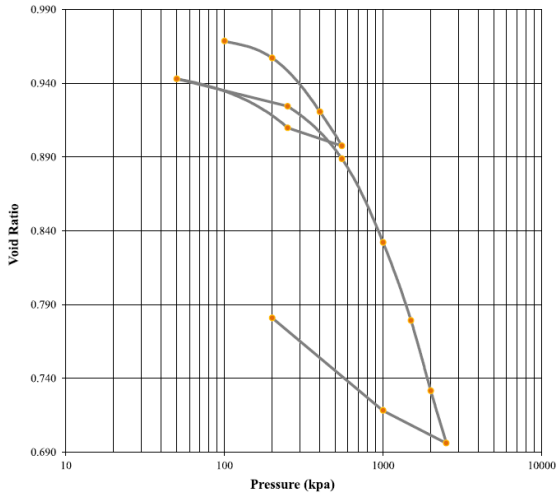


Figure A.21: Test results from the consolidation test: borehole CR-19, depth 37.90 m, CH clay type.

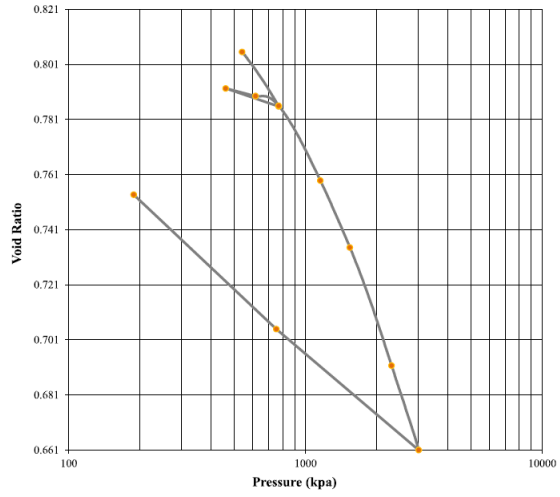


Figure A.22: Test results from the consolidation test: borehole CR-A6, depth 54.10 m, CH clay type.

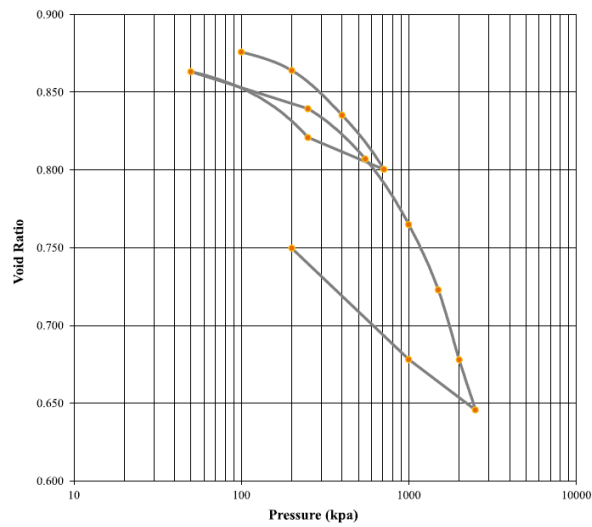


Figure A.23: Test results from the consolidation test: borehole CR-A19, depth 55.45 m, CH clay type.

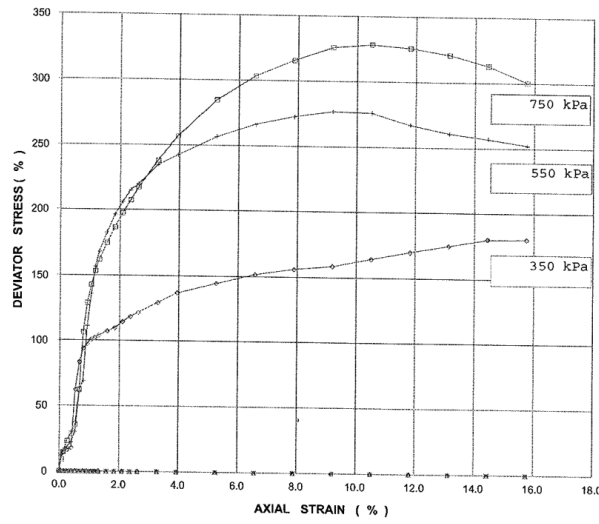


Figure A.24: Test results from the triaxial UU1 test: borehole CR-A-4 and depth of around 60.60 m.

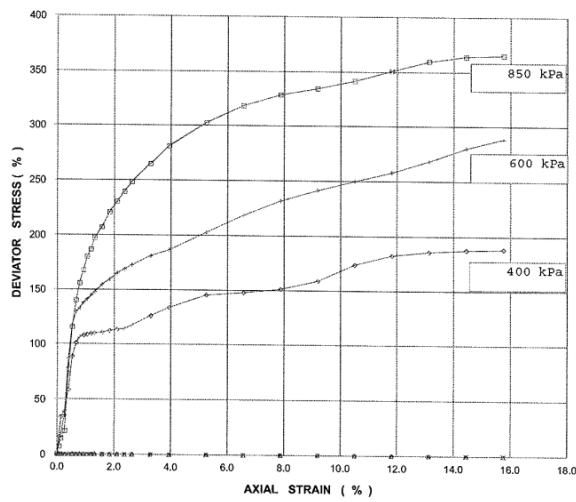


Figure A.25: Test results from the triaxial UU2 test: borehole CR-A-1 and depth of around 67.35 m.

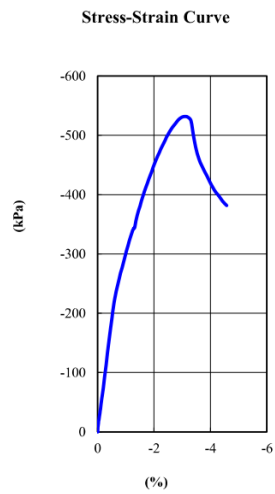


Figure A.26: Test results from the extension triaxial: borehole CR-A-19-51 and depth of around 51.65 m.

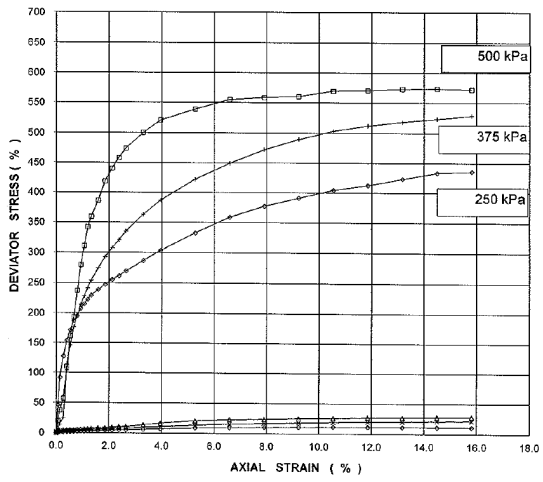


Figure A.27: Test results from the triaxial CU test: borehole CR-A-15 and depth of around 46.15 m.

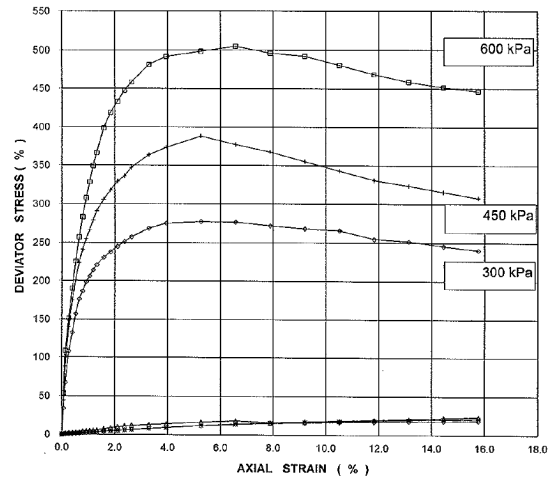


Figure A.28: Test results from the triaxial CU test: borehole CR-A-15 and depth of around 52.15 m.

Parameter	Test							Unit
	CU1	CU2	UU1	UU2	1D-1	1D-2	1D-3	
ϕ'	24.0	17.0	0	0	22.0	22.0	22.0	[°]
c'	10.0	20.0	80, 139, 164	55, 93.5, 141	1.0	1.0	1.0	[kPa]
ψ	0	0	0	0	0	0	0	[°]
σ_t	0	0	0	0	0	0	0	[kPa]
E_{50}^{ref}	1.75, 1.33, 2.30	4.05, 3.62, 3.48	8.7, 10.3, 7.8	6.4, 6.8, 8.0	1.23	1.60	1.44	[MPa]
E_{oed}^{ref}	1.75, 1.33, 2.30	4.05, 3.62, 3.48	8.7, 10.3, 7.8	6.4, 6.8, 8.0	1.23	1.60	1.44	[MPa]
E_{ur}^{ref}	5.3, 4.0, 6.9	12.2, 10.9, 10.4	32.5, 38.6, 29.3	23.9, 25.5, 30.0	8.25	7.46	6.35	[MPa]
m	1.0	1.0	1.0	1.0	1.0	1.0	1.0	[-]
C_c	-	-	-	-	0.37	0.27	0.30	[-]
C_s	-	-	-	-	0.08	0.08	0.10	[-]
e_{init}	0.95	0.95	0.95	0.95	0.98	0.88	0.88	[-]
$\gamma_{0.7}$	0.0001	0.0001	0.0001	0.0001	0.0001	0.0001	0.0001	[-]
G_0^{ref}	40.0	40.0	57.5, 71.5, 85.5	61.0, 75.0, 92.5	40.0	40.0	40.0	[MPa]
ν_{ur}	0.20	0.20	0.20	0.20	0.20	0.20	[-]	
p^{ref}	100	100	-	-	100	100	100	[kPa]
K_0^{nc}	0.65	0.65	0.65	0.65	0.65	0.65	0.65	[-]
R_f	0.90	0.90	0.90	0.90	0.90	0.90	0.90	[-]
σ_{tens}	0	0	0	0	0	0	0	[kPa]
c_{inc}	0	0	0	0	0	0	0	[kN/m ³]

For each triaxial test there are 3 values of parameters $s_u, E_{50}^{ref}, E_{oed}^{ref}, E_{ur}^{ref}$ given for the each cell pressure applied.
Stiffness moduli for triaxial UU test are shown for stress-level of 600 kPa.

Table A.1: HSS and GHS material models' initial input parameters for the representative tests.

Parameter	Test		Unit
	UU1	UU2	
G_{ur}/s_u^A	26.0	26.0	[-]
γ_f^C	4.0	4.0	[%]
γ_f^E	8.0	8.0	[%]
γ_f^{DSS}	6.0	6.0	[%]
$s_{u,ref}^A$	80, 139, 164	55, 93.5, 141	[kN/m ²]
$s_u^{C,TX}/s_u^A$	0.99	0.99	[-]
y_{ref}	-	-	[m]
$s_{u,inc}^A$	-	-	[kN/m ² /m]
s_u^P/s_u^A	0.35	0.35	[-]
τ^0/s_u^A	0.70	0.70	[kPa]
s_u^{DSS}/s_u^A	0.68	0.68	[-]
ν'	0.35	0.35	[-]

For the triaxial test there are 3 values of parameter $s_{u,ref}^A$ given for the each cell pressure applied.

Table A.2: NGI-ADP material model initial input parameters for the representative tests.

Parameter	Test		Unit
	UU1	UU2	
G	3.53, 5.62, 6.38	2.56, 3.83, 5.51	[MPa]
ν'	0.35	0.35	[-]
φ	0	0	[°]
c	80, 139, 164	55, 93.5, 141	[kPa]
ψ	0	0	[°]
σ_t	0	0	[kPa]
α	0.22	0.22	[-]
m	0.8	0.8	[-]
G/S_u	135	135	[-]
$S_{u,min}$	50	50	[kPa]
OCR_{min}	1.0	1.0	[-]

For each triaxial test there are 3 values of parameters G and $S_{u,min}$ given for the each cell pressure applied.

Table A.3: Shansep MC material model initial input parameters for the representative tests.

B

Target measurements in the two-dimensional finite-element model

B.1. Sensitivity analysis of the input parameters

B.1.1. Sensitivity analysis of the HSS model parameters

Input Parameter	Value	D-wall deflection errors [-]						Building settlement differences [mm]				
		DH	DF	DTW	PCM	Area	D_{error}	Front	Middle	Back	RMSE	
Drained	E_{50}^{ref}	3.2	18.34	18.34	1649	100.8	61.36	433.0	-6.537	-5.123	-12.510	8.670
	E_{oed}^{ref}	4.0	18.47	18.47	1645	99.82	62.26	434.9	-6.595	-4.985	-12.296	8.554
	E_{ur}^{ref}	12.0	18.54	18.54	1702	105.8	62.24	445.6	-6.702	-5.397	-12.562	8.791
	$\gamma_{0.7}$	0.00007	18.77	18.77	1730	106.9	62.82	453.0	-6.933	-5.697	-12.360	8.818
	G_0^{ref}	28.0	18.69	18.69	1731	107.6	62.97	452.4	-6.971	-5.484	-11.654	8.456
	ϕ^*	18.5	18.73	18.73	1723	105.7	63.67	451.5	-6.799	-5.859	-13.035	9.137
	c	0.1	18.02	18.02	1562	92.62	62.40	415.1	-6.304	-4.611	-12.617	8.567
UDC	E_{50}	6.0	18.40	18.40	1660	102.0	62.64	437.2	-6.611	-5.117	-12.409	8.638
	E_{oed}	7.5	18.40	18.40	1660	102.0	62.62	437.2	-6.611	-5.119	-12.411	8.640
	E_{ur}	25.8	18.40	18.40	1660	102.0	62.63	437.2	-6.611	-5.119	-12.411	8.640
	$\gamma_{0.7}$	0.00007	18.40	18.40	1660	102.0	62.63	437.2	-6.611	-5.118	-12.411	8.639
	G_0	56.0	18.40	18.40	1660	102.1	62.64	437.2	-6.611	-5.118	-12.410	8.639
	s_u	96.0	18.40	18.40	1660	102.1	62.63	437.2	-6.611	-5.119	-12.411	8.640
UDE	E_{50}	2.1	18.40	18.40	1660	102.0	62.62	437.2	-6.611	-5.117	-12.409	8.638
	E_{oed}	2.5	18.40	18.40	1660	102.1	62.64	437.2	-6.611	-5.118	-12.410	8.639
	E_{ur}	8.6	18.40	18.40	1660	102.1	62.64	437.2	-6.612	-5.119	-12.410	8.640
	$\gamma_{0.7}$	0.00007	18.40	18.40	1660	102.0	62.63	437.2	-6.611	-5.119	-12.411	8.640
	G_0	23.2	18.40	18.40	1660	102.0	62.62	437.2	-6.611	-5.119	-12.411	8.640
	s_u	96.0	18.40	18.40	1660	102.1	62.63	437.2	-6.612	-5.120	-12.412	8.641
Initial HSS Values			18.403	18.403	1659.7	102.05	62.639	437.22	-6.611	-5.118	-12.409	8.639

The units of the parameters are as in Table 3.11.

* means that in variation of the ϕ parameter, K_0^{nc} was kept constant

Drained stands for changing the parameter for phases 0 - 11 only, i.e. where material behaviour is set to drained.

UDC stands for changing the parameter for phases 12-15 only, i.e. where material behaviour is set to undrained and the parameter is changed only for the outside of the excavation (compression behaviour is dominant).

UDE stands for changing the parameter for phases 12-15 only, i.e. where material behaviour is set to undrained and the parameter is changed only for the outside of the excavation (extension behaviour is dominant).

Table B.1: The d-wall deflection errors and the building settlements differences computed for the lower-bound values of the HSS model parameters sensitivity studies (phase 12).

Input		D-wall deflection errors [-]						Building settlement differences [mm]				
Parameter	Value	DH	DF	DTW	PCM	Area	D_{error}	Front	Middle	Back	RMSE	
Initial HSS Values		18.403	18.403	1659.7	102.05	62.639	437.22	-6.611	-5.118	-12.409	8.639	
Drained	E_{50}^{ref}	4.8	18.40	18.40	1628	98.47	61.92	431.0	-6.545	-4.826	-12.150	8.441
	E_{oed}^{ref}	6.0	18.48	18.48	1663	101.6	62.55	438.2	-6.623	-5.169	-12.402	8.648
	E_{ur}^{ref}	18.0	18.35	18.35	1616	96.85	62.59	428.5	-6.537	-4.880	-12.170	8.459
	$\gamma_{0.7}$	0.00013	18.07	18.07	1556	92.80	62.09	415.4	-6.254	-4.167	-11.793	8.074
	G_0^{ref}	42.0	17.98	18.69	1569	94.38	62.56	416.8	-6.237	-4.445	-12.478	8.453
	ϕ^*	25.5	17.71	17.71	1564	96.48	61.04	412.5	-6.255	-3.961	-11.108	7.707
	c	20.0	18.68	18.68	1728	107.9	62.39	451.8	-6.805	-5.463	-12.119	8.622
UDC	E_{50}	11.2	18.40	18.40	1660	102.0	62.64	437.2	-6.612	-5.118	-12.409	8.639
	E_{oed}	13.9	18.40	18.40	1660	102.0	62.63	437.2	-6.611	-5.119	-12.411	8.640
	E_{ur}	38.6	18.40	18.40	1660	102.0	62.63	437.2	-6.611	-5.119	-12.411	8.640
	$\gamma_{0.7}$	0.00013	18.40	18.40	1660	102.0	62.64	437.2	-6.611	-5.118	-12.409	8.639
	G_0	84.0	18.40	18.40	1660	102.0	62.64	437.2	-6.611	-5.118	-12.410	8.639
	s_u	144.0	18.40	18.40	1660	102.0	62.64	437.2	-6.611	-5.117	-12.409	8.638
UDE	E_{50}	3.7	18.40	18.40	1660	102.0	62.63	437.2	-6.612	-5.119	-12.411	8.640
	E_{oed}	4.7	18.40	18.40	1660	102.0	62.63	437.2	-6.611	-5.119	-12.411	8.640
	E_{ur}	13.0	18.40	18.40	1660	102.1	62.63	437.2	-6.612	-5.119	-12.412	8.640
	$\gamma_{0.7}$	0.00013	18.40	18.40	1660	102.0	62.63	437.2	-6.612	-5.119	-12.411	8.640
	G_0	34.8	18.40	18.40	1660	102.0	62.62	437.2	-6.611	-5.118	-12.410	8.640
	s_u	144.0	18.40	18.40	1660	102.0	62.64	437.2	-6.611	-5.118	-12.409	8.639

The units of the parameters are as in Table 3.11.

* means that in variation of the ϕ parameter, K_0^{nc} was kept constant

Drained stands for changing the parameter for phases 0 - 11 only, i.e. where material behaviour is set to drained.

UDC stands for changing the parameter for phases 12-15 only, i.e. where material behaviour is set to undrained and the parameter is changed only for the outside of the excavation (compression behaviour is dominant).

UDE stands for changing the parameter for phases 12-15 only, i.e. where material behaviour is set to undrained and the parameter is changed only for the outside of the excavation (extension behaviour is dominant).

Table B.2: The d-wall deflection errors and the building settlements differences computed for the higher-bound values of the HSS model parameters sensitivity studies (phase 12).

Input		D-wall deflection errors [-]							Building settlement differences [mm]			
Parameter	Value	DH	DF	DTW	PCM	Area	D_{error}	Front	Middle	Back	RMSE	
Drained	E_{50}^{ref}	3.2	30.11	55.06	4104	274.2	336.9	1451.1	-14.859	-32.220	-36.835	29.528
	E_{oed}^{ref}	4.0	30.39	54.83	4107	276.4	326.9	1448.6	-14.946	-32.187	-36.668	29.461
	E_{ur}^{ref}	12.0	30.47	55.97	4189	283.5	333.2	1477.1	-15.149	-32.893	-37.197	29.972
	$\gamma_{0.7}$	0.00007	30.61	56.74	4238	284.5	339.5	1497.9	-15.354	-33.361	-36.966	30.084
	G_0^{ref}	28.0	30.56	57.13	4261	288.8	342.4	1506.4	-15.391	-33.452	-36.401	29.894
	ϕ^*	18.5	30.16	56.32	4179	278.5	249.4	1482.9	-15.122	-33.079	-36.995	29.953
	c	0.1	29.54	53.08	3974	265.3	321.8	1393.8	-14.850	-30.936	-36.442	28.90
UDC	E_{50}	6.0	30.50	56.32	4221	287.6	330.1	1483.7	-15.332	-33.374	-38.114	30.559
	E_{oed}	7.5	30.34	55.30	4131	278.5	331.9	1459.2	-15.025	-32.342	-36.913	29.633
	E_{ur}	25.8	30.33	55.80	4174	284.0	329.7	1469.0	-15.212	-32.625	-37.621	30.062
	$\gamma_{0.7}$	0.00007	30.33	55.48	4139	279.0	333.9	1463.3	-15.084	-32.471	-36.795	29.641
	G_0	56.0	30.35	55.48	4139	279.0	334.0	1463.6	-15.067	-32.559	-36.826	29.863
	s_u	96.0	30.40	55.68	4160	281.2	332.5	1468.4	-15.147	-32.740	-37.281	29.951
UDE	E_{50}	2.1	30.38	54.86	4164	281.3	334.7	1471.3	-15.142	-32.742	-37.428	30.009
	E_{oed}	2.5	30.34	55.33	4132	278.5	332.2	1459.9	-15.028	-32.362	-36.925	29.646
	E_{ur}	8.6	30.36	56.41	4196	283.6	340.7	1485.5	-15.243	-33.056	-37.448	30.152
	$\gamma_{0.7}$	0.00007	30.35	55.39	4136	278.8	332.7	1461.4	-15.043	-32.399	-36.955	29.674
	G_0	23.2	30.35	55.40	4136	278.9	332.7	1461.6	-15.049	-32.411	-36.954	29.679
	s_u	96.0	30.36	55.50	4143	279.4	333.4	1464.2	-15.065	-32.484	-37.083	29.762
Initial HSS			30.344	55.338	4132.6	278.58	332.28	1460.1	-15.031	-32.367	-36.930	29.650

The units of the parameters are as in Table 3.11.

* means that in variation of the ϕ parameter, K_0^{nc} was kept constant

Drained stands for changing the parameter for phases 0 - 11 only, i.e. where material behaviour is set to drained.

UDC stands for changing the parameter for phases 12-15 only, i.e. where material behaviour is set to undrained and the parameter is changed only for the outside of the excavation (compression behaviour is dominant).

UDE stands for changing the parameter for phases 12-15 only, i.e. where material behaviour is set to undrained and the parameter is changed only for the outside of the excavation (extension behaviour is dominant).

Table B.3: The d-wall deflection errors and the building settlements differences computed for the lower-bound values of the HSS model parameters sensitivity studies (phase 15).

Input		D-wall deflection errors [-]						Building settlement differences [mm]				
Parameter	Value	DH	DF	DTW	PCM	Area	D_{error}	Front	Middle	Back	RMSE	
Initial HSS		30.344	55.338	4132.6	278.58	332.28	1460.1	-15.031	-32.367	-36.930	29.650	
Drained	E_{50}^{ref}	4.8	30.34	54.38	4084	275.3	322.1	1437.3	-14.926	-31.871	-36.434	29.246
	E_{oed}^{ref}	6.0	30.40	55.11	4121	277.1	330.6	1455.9	-14.994	-32.251	-36.782	29.540
	E_{ur}^{ref}	18.0	30.28	54.49	4074	272.8	329.5	1440.4	-14.979	-32.072	-36.369	29.301
	$\gamma_{0.7}$	0.00013	29.84	53.53	4007	267.9	322.9	1408.8	-14.640	-31.670	-36.184	29.021
	G_0^{ref}	42.0	29.16	53.04	3961	263.4	325.1	1386.3	-14.528	-30.931	-36.219	28.750
	ϕ^*	25.5	28.61	51.58	3849	256.4	316.9	1342.9	-14.333	-28.505	-34.005	26.922
	c	20.0	30.54	56.65	4228	286.0	339.3	1494.4	-15.173	-33.054	-36.825	29.882
UDC	E_{50}	11.2	29.87	54.56	4061	271.2	334.7	1434.8	-14.799	-31.539	-35.871	28.870
	E_{oed}	13.9	30.33	55.32	4145.2	277.7	338.4	1466.3	-15.027	-32.350	-36.915	29.637
	E_{ur}	38.6	30.30	54.96	4101	274.4	333.9	1451.7	-14.881	-32.183	-36.434	29.352
	$\gamma_{0.7}$	0.00013	30.37	55.18	4127	278.1	330.4	1456.8	-14.969	-32.312	-37.059	29.673
	G_0	84.0	30.35	55.15	4124	277.9	330.2	1455.8	-14.979	-32.193	-37.001	29.607
	s_u	144.0	30.30	55.01	4106	276.2	331.7	1452.0	-14.923	-32.022	-36.597	29.368
UDE	E_{50}	3.7	30.31	54.86	4102	276.0	329.5	1448.9	-14.937	-32.009	-36.493	29.323
	E_{oed}	4.7	30.34	55.33	4132	278.5	332.2	1459.9	-15.029	-32.361	-36.926	29.646
	E_{ur}	13.0	30.33	54.63	4092	275.4	326.4	1443.6	-14.898	-31.936	-36.635	29.349
	$\gamma_{0.7}$	0.00013	30.34	55.23	4126	278.1	331.5	1457.6	-15.013	-32.295	-36.871	29.596
	G_0	34.8	30.35	55.31	4131	278.4	332.1	1459.6	-15.030	-32.353	-36.942	29.650
	s_u	144.0	30.33	55.17	4122	277.8	331.1	1456.0	-14.995	-32.250	-36.781	29.539

The units of the parameters are as in Table 3.11.

* means that in variation of the ϕ parameter, K_0^{nc} was kept constant

Drained stands for changing the parameter for phases 0 - 11 only, i.e. where material behaviour is set to drained.

UDC stands for changing the parameter for phases 12-15 only, i.e. where material behaviour is set to undrained and the parameter is changed only for the outside of the excavation (compression behaviour is dominant).

UDE stands for changing the parameter for phases 12-15 only, i.e. where material behaviour is set to undrained and the parameter is changed only for the outside of the excavation (extension behaviour is dominant).

Table B.4: The d-wall deflection errors and the building settlements differences computed for the higher-bound values of the HSS model parameters sensitivity studies (phase 15).

B.1.2. Sensitivity analysis of the NGI-ADP model parameters

Input		Value	D-wall deflection errors [-]						Building settlement differences [mm]			
Parameter			DH	DF	DTW	PCM	Area	D_{error}	Front	Middle	Back	RMSE
Drained	G_{ur}/S_u	50	24.40	31.87	2755	175.5	146.6	824.6	-10.930	-12.370	-5.107	9.976
	s_u	90	28.84	42.43	3530	237.1	178.2	1137	-11.586	-14.128	1.735	10.596
Undrained	G_{ur}/S_u	50	28.14	40.60	3403	227.6	192.5	1085.6	-11.280	-13.279	1.561	10.010
	s_u	90	28.13	40.69	3409	228.0	190.3	1084.6	-11.294	-13.346	1.522	10.132
Initial NGI-ADP Values			28.132	40.696	3409.7	228.05	193.28	1087.7	-11.300	-13.361	1.523	10.141
Drained	G_{ur}/S_u	65	23.41	28.91	2546	159.3	127.2	742.2	-10.853	-12.602	-8.471	10.776
	s_u	120	27.53	38.62	3260	217.3	200.9	1137	-10.972	-12.143	1.340	9.480
Undrained	G_{ur}/S_u	65	28.13	40.68	3409	228.0	193.1	1087.3	-11.294	-13.346	1.519	10.132
	s_u	120	28.13	40.56	3400	227.4	192.3	1084.6	-11.270	-13.242	1.589	10.081

The units of the parameters are as in Table 3.12.

Drained stands for changing the parameter for phases 0 - 11 only, i.e. where material behaviour is set to drained.

Undrained stands for changing the parameter for phases 12-15 only, i.e. where material behaviour is set to undrained.

Table B.5: The d-wall deflection errors and the building settlements differences computed for the NGI-ADP model parameters sensitivity studies (phase 12).

	Input		D-wall deflection errors [-]						Building settlement differences [mm]			
	Parameter	Value	DH	DF	DTW	PCM	Area	D_{error}	Front	Middle	Back	RMSE
Drained	G_{ur}/S_u	50	31.00	79.95	5849	425.0	455.9	2048.3	-26.640	-53.207	-36.327	40.251
	s_u	90	31.21	85.35	6293	460.8	469.9	2181.4	-25.735	-50.332	-23.80	35.412
Undrained	G_{ur}/S_u	50	31.37	82.51	6098	441.1	463.5	2121.4	-22.789	-47.907	-21.536	33.056
	s_u	90	31.56	92.15	6765	501.8	500.1	2351.0	-28.221	-58.265	-29.701	41.123
Initial NGI-ADP Values			31.268	86.634	6374.3	467.7	477.44	2213.1	-26.315	-52.789	-25.878	37.178
Drained	G_{ur}/S_u	65	30.72	72.59	5327	380.8	421.9	1869.2	-25.890	-49.921	-36.565	38.730
	s_u	120	31.25	86.72	6367	467.8	479.1	2214.0	-26.678	-53.90	-27.185	38.105
Undrained	G_{ur}/S_u	65	31.46	81.41	6031	434.3	459.4	2099.1	-21.598	-46.469	-20.426	31.849
	s_u	120	30.97	80.86	5969	433.6	455.3	2074.0	-24.566	-46.996	-21.888	33.122

The units of the parameters are as in Table 3.12.

Drained stands for changing the parameter for phases 0 - 11 only, i.e. where material behaviour is set to drained.

Undrained stands for changing the parameter for phases 12-15 only, i.e. where material behaviour is set to undrained.

Table B.6: The d-wall deflection errors and the building settlements differences computed for the NGI-ADP model parameters sensitivity studies (phase 15).

B.1.3. Sensitivity analysis of the SHANSEP-MC model parameters

Input Parameter	Value	D-wall deflection errors [-]						Building settlement differences [mm]				
		DH	DF	DTW	PCM	Area	D_{error}	Front	Middle	Back	RMSE	
Drained	α	0.14	31.74	51.49	4281	296.0	232.7	1402.1	-8.866	-12.771	12.715	11.596
	G/S_u	60	29.50	39.96	3382	227.3	174.7	1088.5	-9.937	-9.228	8.323	8.995
Initial SHANSEP MC Values			30.957	44.688	3769.7	257.87	195.934	1228.15	-9.4060	-11.1652	9.3966	10.0238
Drained	α	0.18	30.98	46.26	3872	264.1	207.9	1264.2	-9.974	-12.397	9.064	10.572
	G/S_u	75	27.29	36.33	3102	204.4	157.7	964.8	-9.794	-9.210	4.974	8.276

The units of the parameters are as in Table 3.13.

Table B.7: The d-wall deflection errors and the building settlements differences computed for the SHANSEP MC model parameters sensitivity studies (phase 12).

Input Parameter	Value	D-wall deflection errors [-]						Building settlement differences [mm]				
		DH	DF	DTW	PCM	Area	D_{error}	Front	Middle	Back	RMSE	
Undrained	α	0.14	34.20	120.0	8929	694.2	568.4	3096.1	-23.278	-67.021	-26.240	43.674
	G/S_u	60	32.50	92.74	6877	511.8	493.0	2390.8	-19.619	-50.617	-21.363	33.682
Initial SHANSEP MC Values			32.874	106.927	7846.88	592.356	563.031	2745.357	-21.7811	-58.2587	-22.1845	38.1254
Undrained	α	0.18	32.51	94.87	7094	529.2	493.3	2446.7	-19.550	-49.761	-16.113	32.238
	G/S_u	75	32.15	85.97	6338	461.8	481.8	2222.5	-19.222	-48.094	-23.251	32.778

The units of the parameters are as in Table 3.13.

Table B.8: The d-wall deflection errors and the building settlements differences computed for the SHANSEP MC model parameters sensitivity studies (phase 15).

B.1.4. Sensitivity analysis of the GHS2142 model parameters

Input Parameter	Value	D-wall deflection errors [-]						Building settlement differences [mm]				
		DH	DF	DTW	PCM	Area	D_{error}	Front	Middle	Back	RMSE	
Drained	E_{50}^{ref}	3.2	17.79	17.79	1449	80.73	67.11	397.5	-6.643	-4.495	-13.271	8.953
	E_{oed}^{ref}	4.0	17.87	17.87	1493	85.41	67.40	406.3	-6.740	-4.813	-13.503	9.146
	E_{ur}^{ref}	12.0	17.52	17.52	1347	71.10	64.18	374.58	-6.124	-3.409	-12.624	8.337
	$\gamma_{0.7}$	0.00007	18.07	1807	1523	88.02	66.66	413.2	-6.901	-4.988	-13.680	9.303
	ϕ	18.5	18.31	18.31	1553	90.48	67.94	422.87	-6.644	-5.040	-14.040	9.428
	c	0.1	17.84	17.84	1458	81.39	66.49	398.90	-6.636	-4.535	-13.651	9.146
	G_0^{ref}	28.0	17.89	17.89	1509	87.69	66.05	408.48	-6.822	-4.694	-13.021	8.909
Initial GHS Values		17.895	17.895	1458.8	81.027	66.776	399.74	-6.680	-4.558	-13.487	9.079	
Drained	E_{50}^{ref}	4.8	17.85	17.85	1458	81.45	66.64	399.1	-6.636	-4.515	-13.371	9.004
	E_{oed}^{ref}	6.0	17.58	17.58	1374	73.76	64.78	380.4	-6.258	-3.639	-12.696	8.438
	E_{ur}^{ref}	18.0	17.73	17.73	1453	81.99	66.12	396.96	-6.614	-4.542	-13.294	8.965
	$\gamma_{0.7}$	0.00013	17.62	17.62	1393	75.32	66.07	385.0	-6.392	-3.985	-13.028	8.688
	ϕ	25.5	17.71	17.71	1421	78.12	67.94	389.63	-6.519	-3.921	-12.456	8.427
	c	20.0	17.72	17.72	1424	78.50	65.24	390.78	-6.569	-4.126	-12.878	8.860
	G_0^{ref}	42.0	17.69	17.69	1393	74.54	66.92	386.24	-6.456	-4.154	-13.420	8.927

The units of the parameters are as in Table ??.

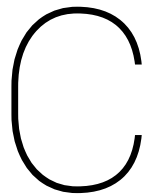
For variations of the ϕ parameter, K_0^{nc} was kept constant.

Table B.9: The d-wall deflection errors and the building settlements differences computed for the GHS model parameters sensitivity studies (phase 12).

Input		D-wall deflection errors [-]							Building settlement differences [mm]			
Parameter	Value	DH	DF	DTW	PCM	Area	D_{error}	Front	Middle	Back	RMSE	
Undrained	E_{50}^{ref}	3.2	21.99	32.23	2632	151.9	190.5	799.8	-10.697	-16.608	-25.824	18.772
	E_{oed}^{ref}	4.0	22.52	33.30	2714	159.2	194.6	830.8	-11.055	-17.353	-26.355	19.304
	E_{ur}^{ref}	12.0	21.06	29.55	2440	137.43	174.12	727.70	-9.754	-14.391	-24.249	17.226
	E_{50}^{ref}	3.2	22.60	33.86	2751	162.53	197.25	843.66	-11.351	-18.177	-26.773	19.799
	$\gamma_{0.7}$	0.00007	22.74	34.11	2769	163.8	198.7	851.2	-11.324	-18.189	-26.582	19.712
	G_0^{ref}	28.0	22.58	33.58	2730	161.59	195.27	837.41	-11.150	-16.976	-25.620	18.876
	ϕ	18.5	23.15	34.72	2825	168.6	198.0	868.90	-10.872	-19.205	-27.201	20.223
	c	0.1	22.09	32.23	2635	152.63	189.09	800.82	-10.772	-16.599	-26.072	18.897
	Initial GHS Values		22.150	32.319	2644.77	153.092	189.317	803.56	-10.763	-16.795	-26.093	18.963
Undrained	E_{50}^{ref}	4.8	22.13	32.26	2642	153.2	188.5	802.1	-10.692	-16.646	-25.942	18.836
	E_{oed}^{ref}	6.0	21.11	29.84	2461	138.6	176.7	735.1	-9.818	-14.215	-24.254	17.192
	E_{ur}^{ref}	18.0	21.98	31.62	2599	150.90	183.04	785.64	-10.633	-15.935	-25.514	18.420
	E_{50}^{ref}	4.8	21.84	21.84	2631	151.09	193.69	800.49	-10.740	-16.255	-25.455	18.507
	$\gamma_{0.7}$	0.00013	21.22	30.67	2507	141.8	182.4	752.7	-10.137	-14.889	-24.896	17.741
	G_0^{ref}	42.0	21.28	30.55	2505	140.51	184.08	753.65	-10.207	-15.251	-25.224	18.010
	ϕ	25.5	21.73	31.53	2583	148.7	185.8	780.89	-10.475	-15.597	-24.554	17.850
	c	20.0	21.92	31.82	2606	150.46	186.78	789.53	-10.589	-16.12	-25.291	18.364

The units of the parameters are as in Table ??.
For variations of the ϕ parameter, K_0^{nc} was kept constant.

Table B.10: The d-wall deflection errors and the building settlements differences computed for the GHS model parameters sensitivity studies (phase 15).



Estimation method in the inverse analysis

C.1. Extended Kalman Filter

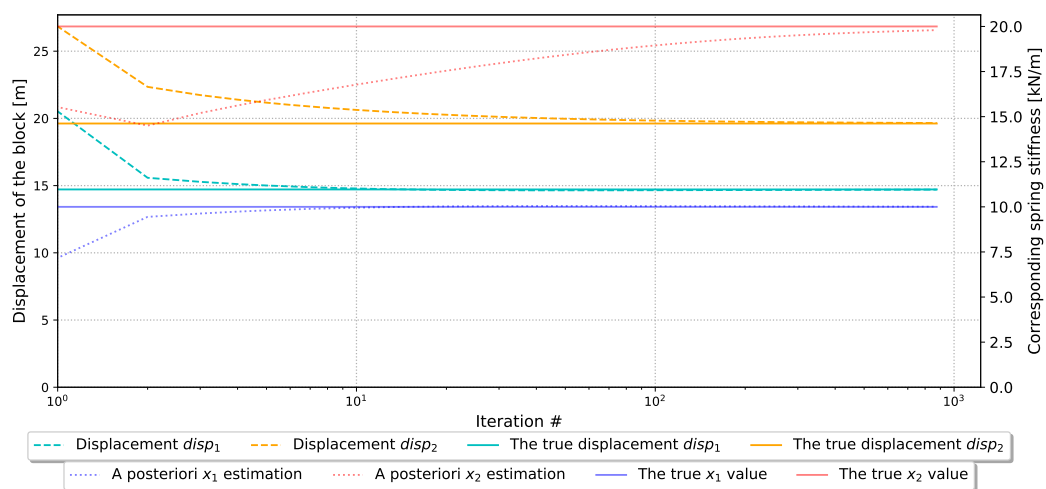


Figure C.1: The optimisation of the spring problem using the EKF algorithm - the evolution of the estimated variables and measurements throughout the iterations for tough initial conditions.

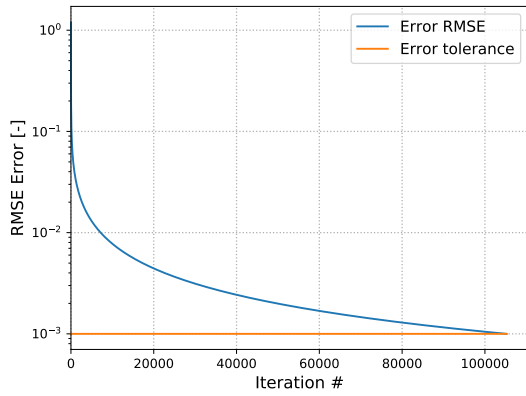


Figure C.2: The optimisation of the spring problem using the EKF algorithm - the evolution of RMSE throughout the iterations for tough initial conditions.

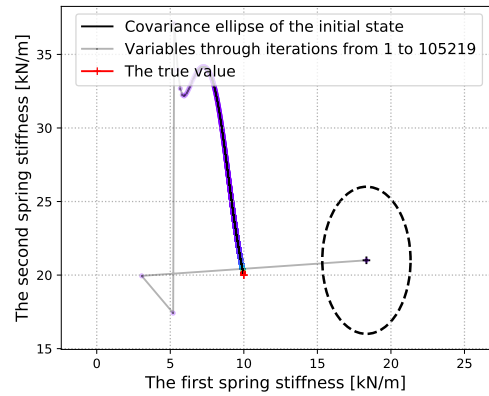


Figure C.3: The variables evolution throughout the iterations in the two-spring problem optimisation using the EKF algorithm for tough initial conditions.

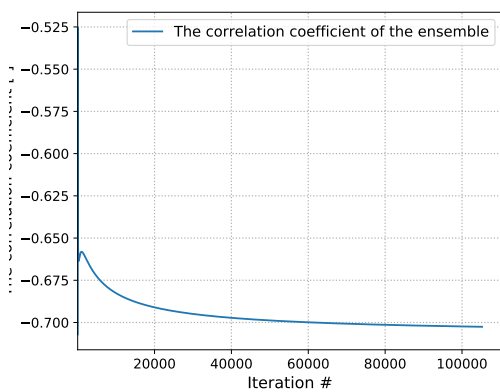


Figure C.4: The optimisation of the spring problem using the EKF algorithm - the Pearson's coefficient evolution throughout the iterations for tough initial conditions.

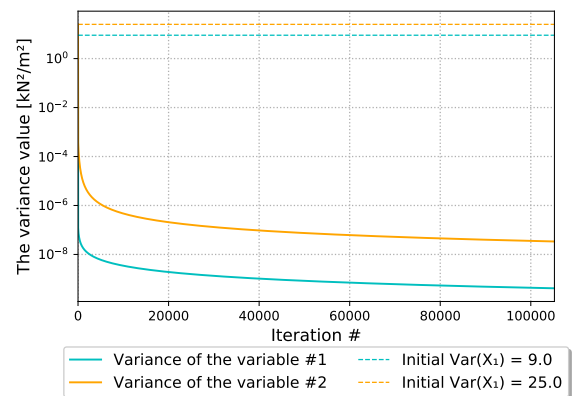


Figure C.5: The optimisation of the spring problem using the EKF algorithm - the evolution of the variables' variances for tough initial conditions.

C.2. Configuration of the script's functions

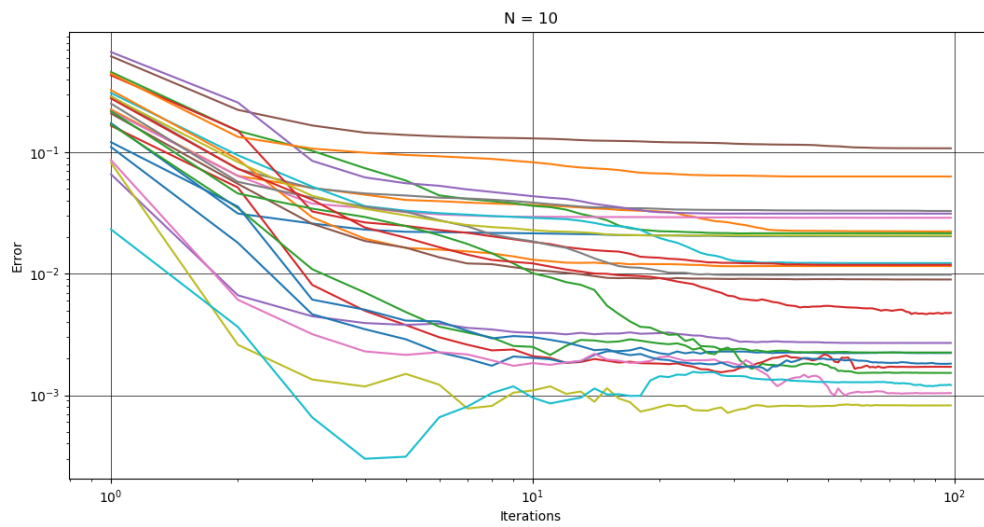


Figure C.6: The error evolution throughout the iterations for the ensemble size of $N = 10$.

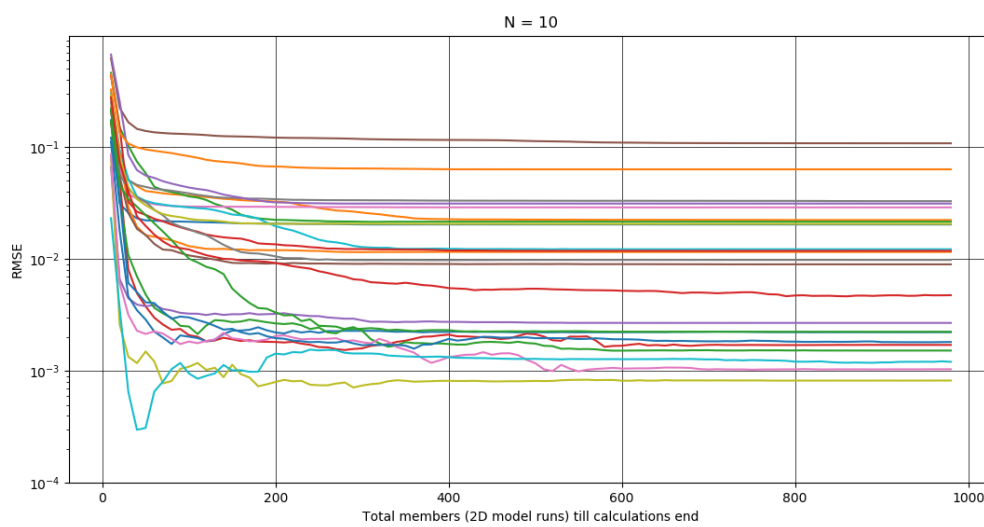


Figure C.7: The error evolution throughout the iterations for the ensemble size of $N = 10$.

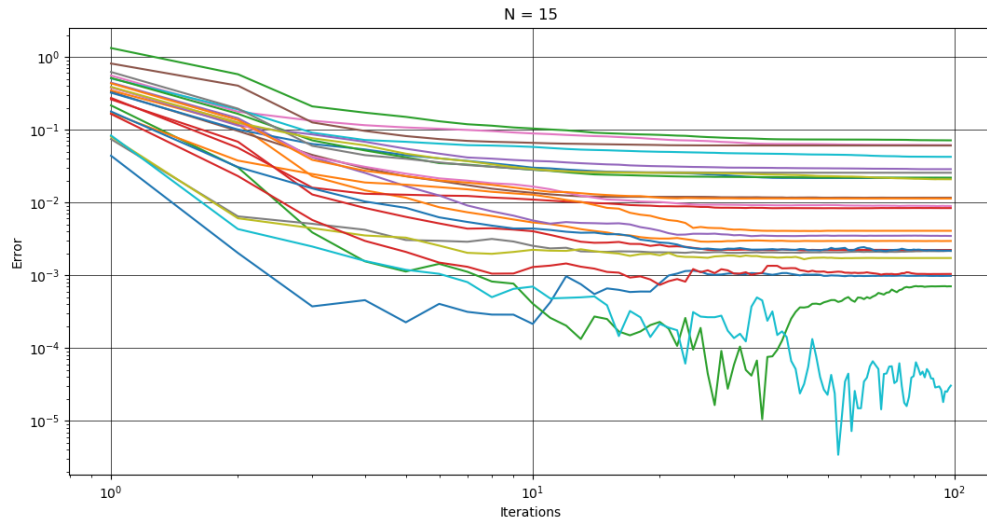


Figure C.8: The error evolution throughout the iterations for the ensemble size of $N = 15$.

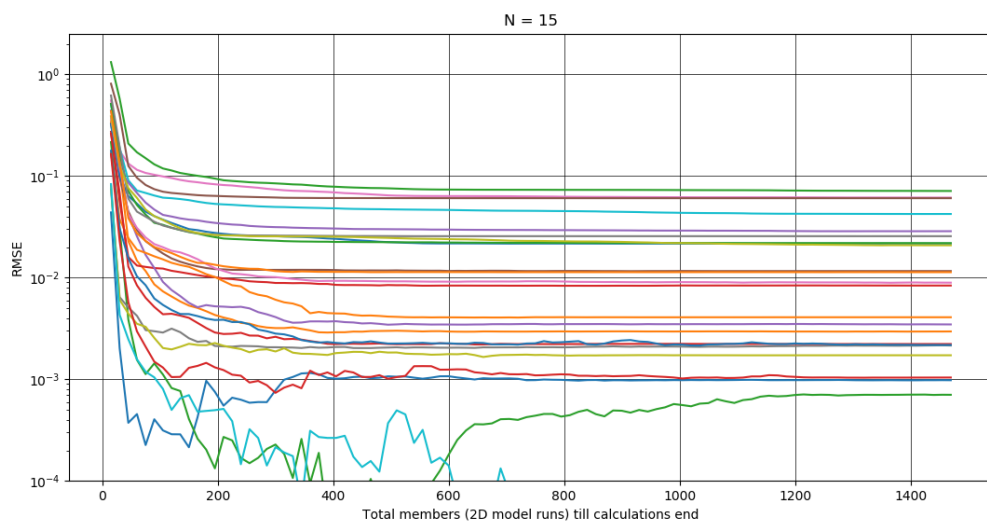


Figure C.9: The error evolution throughout the iterations for the ensemble size of $N = 15$.

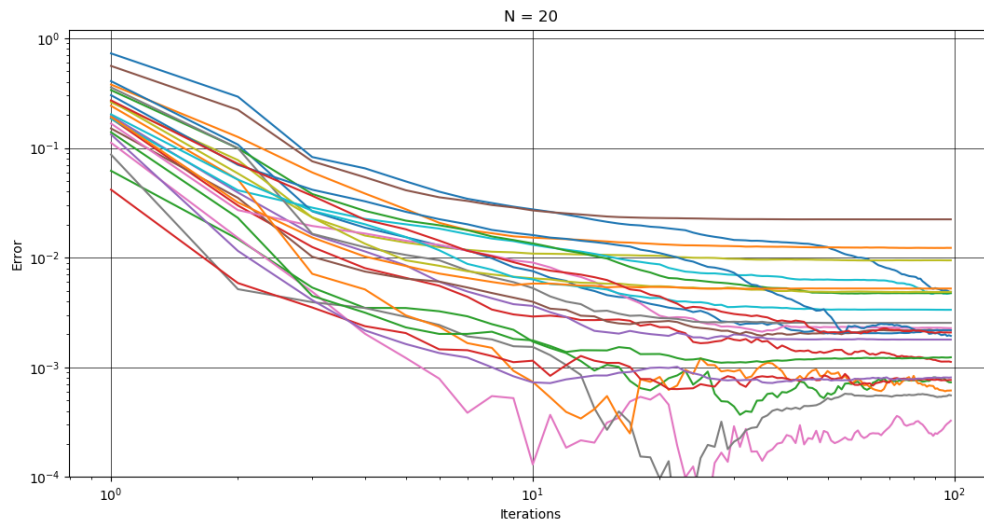


Figure C.10: The error evolution throughout the iterations for the ensemble size of $N = 20$.

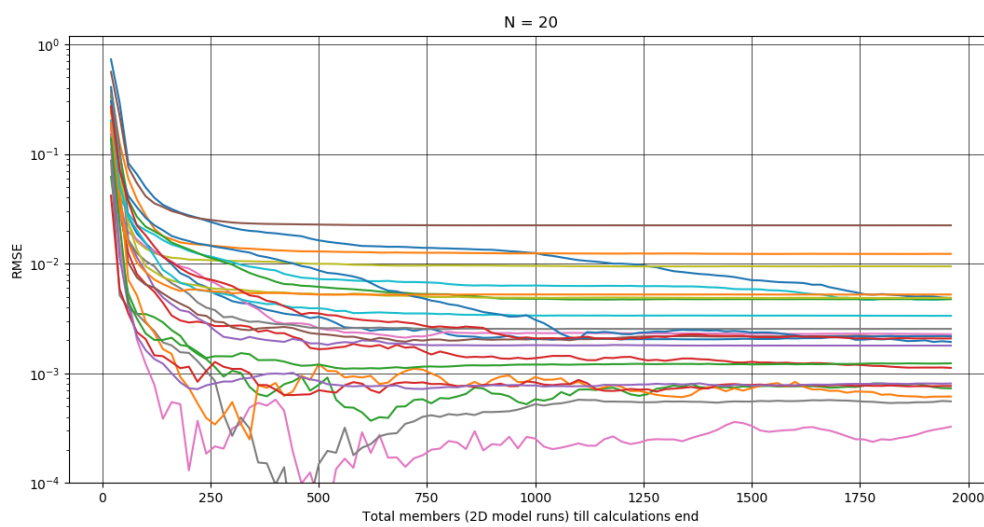


Figure C.11: The error evolution throughout the iterations for the ensemble size of $N = 20$.

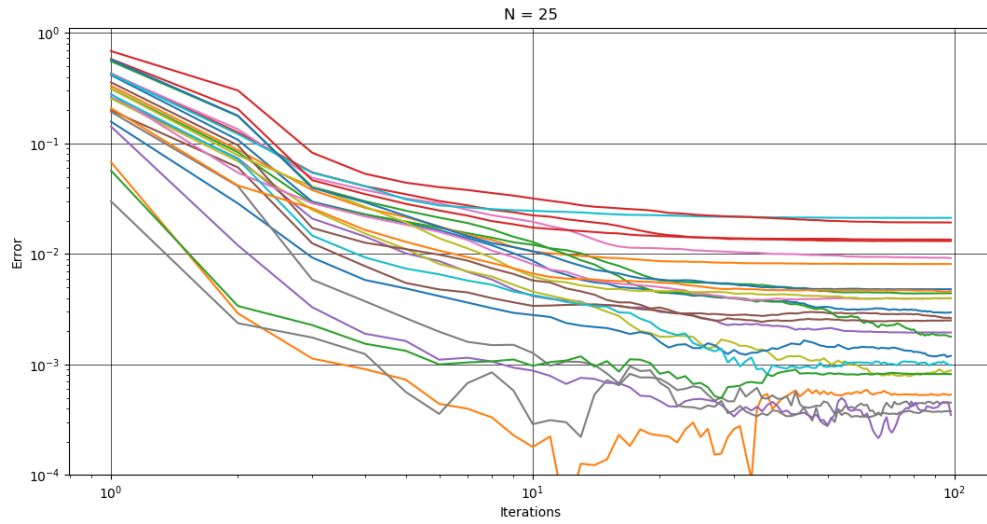


Figure C.12: The error evolution throughout the iterations for the ensemble size of $N = 25$.

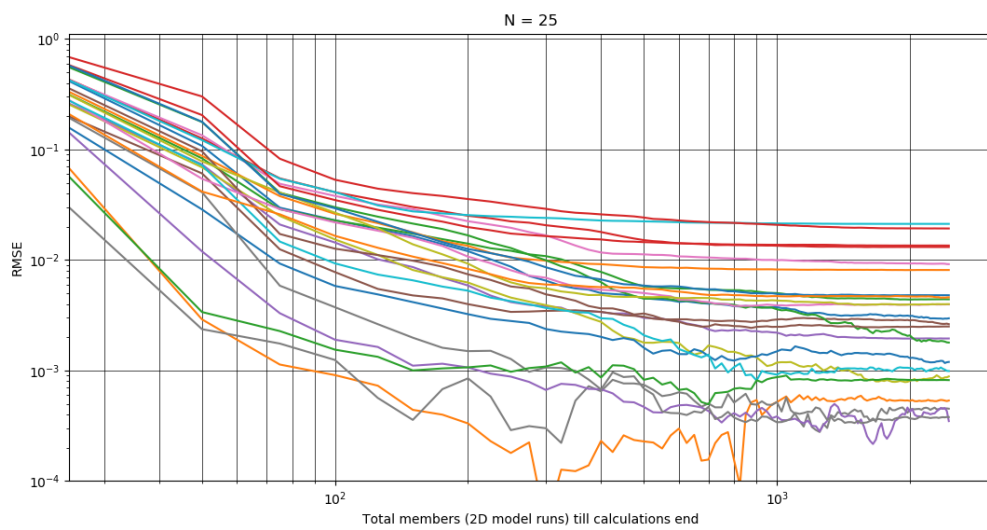


Figure C.13: The error evolution throughout the iterations for the ensemble size of $N = 25$.

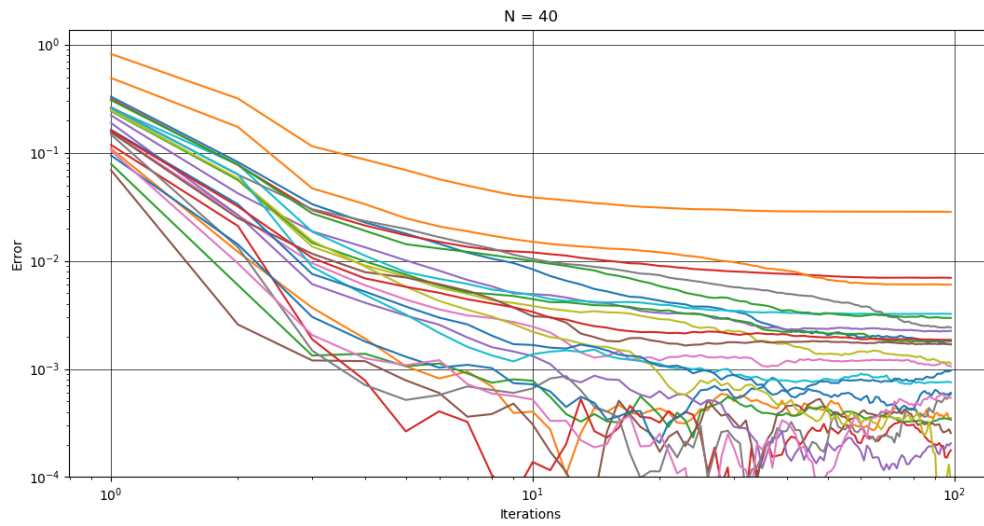


Figure C.14: The error evolution throughout the iterations for the ensemble size of $N = 40$.

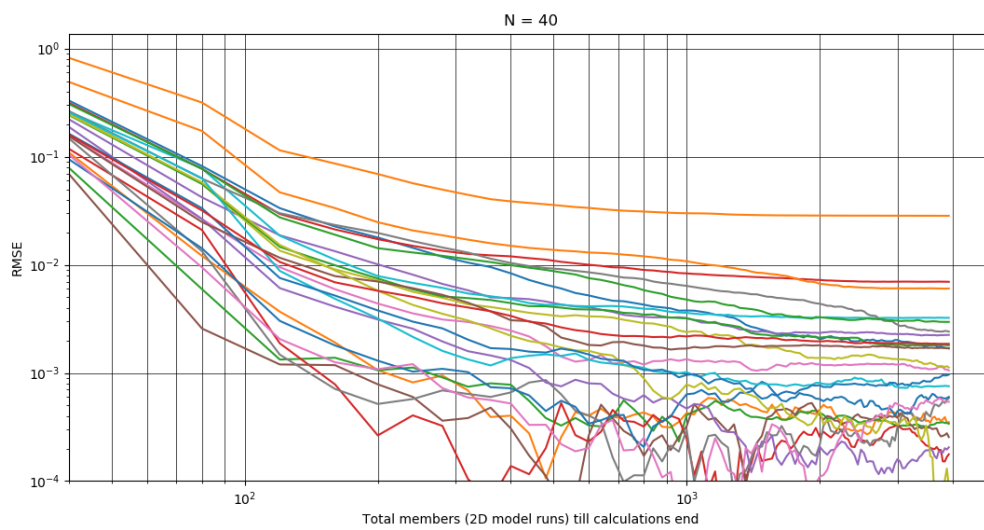


Figure C.15: The error evolution throughout the iterations for the ensemble size of $N = 40$.

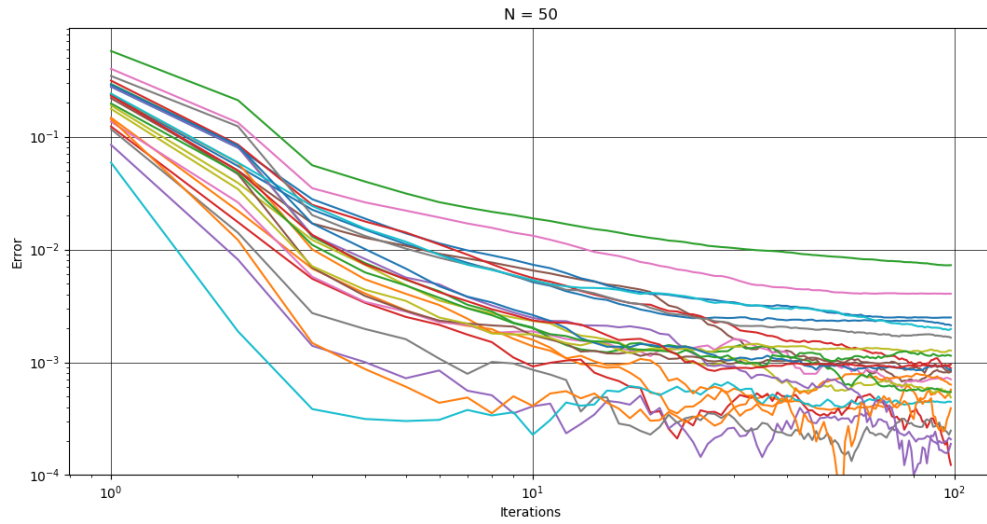


Figure C.16: The error evolution throughout the iterations for the ensemble size of $N = 50$.

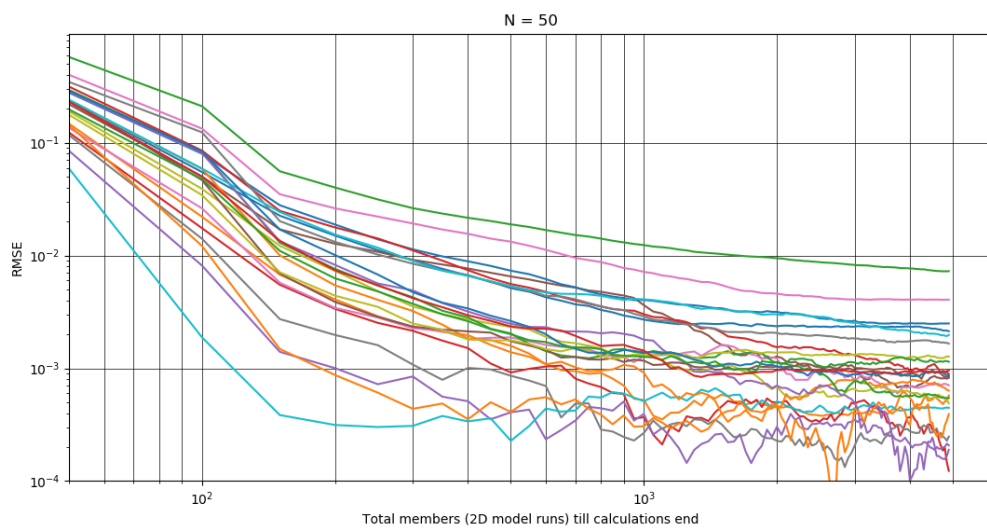


Figure C.17: The error evolution throughout the iterations for the ensemble size of $N = 50$.

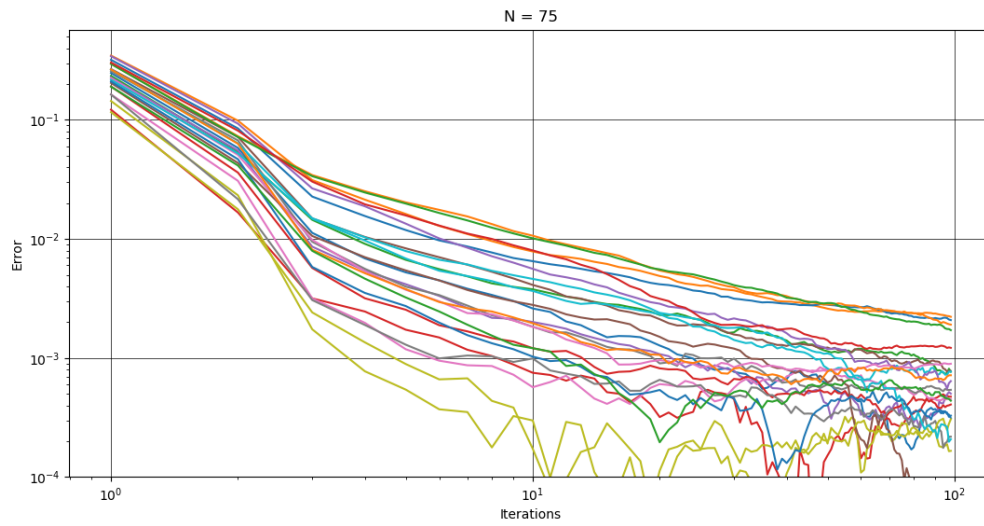


Figure C.18: The error evolution throughout the iterations for the ensemble size of $N = 75$.

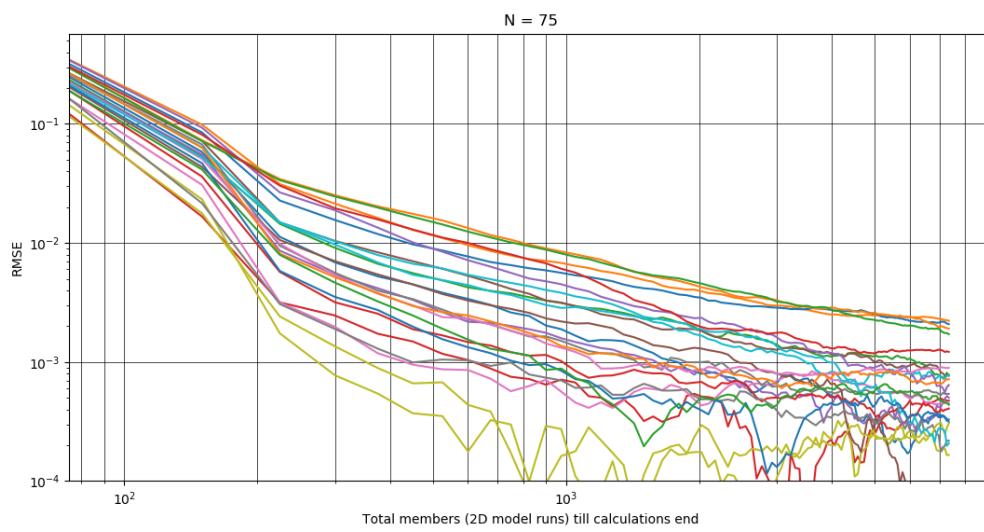


Figure C.19: The error evolution throughout the iterations for the ensemble size of $N = 75$.

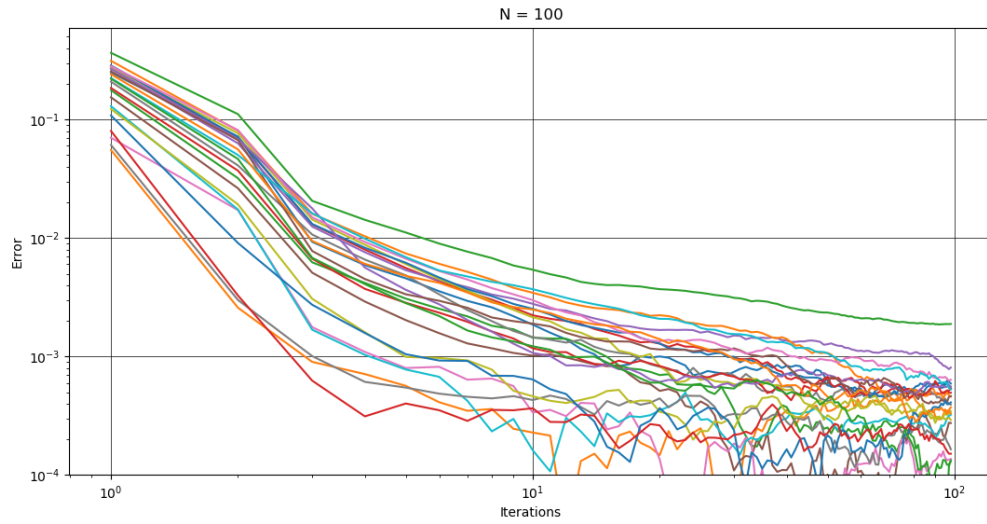


Figure C.20: The error evolution throughout the iterations for the ensemble size of $N = 100$.

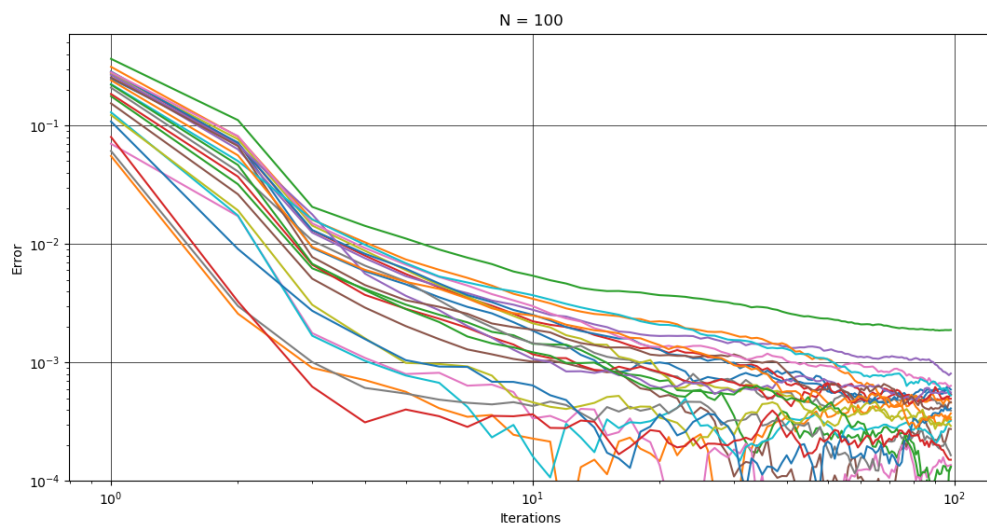


Figure C.21: The error evolution throughout the iterations for the ensemble size of $N = 100$.

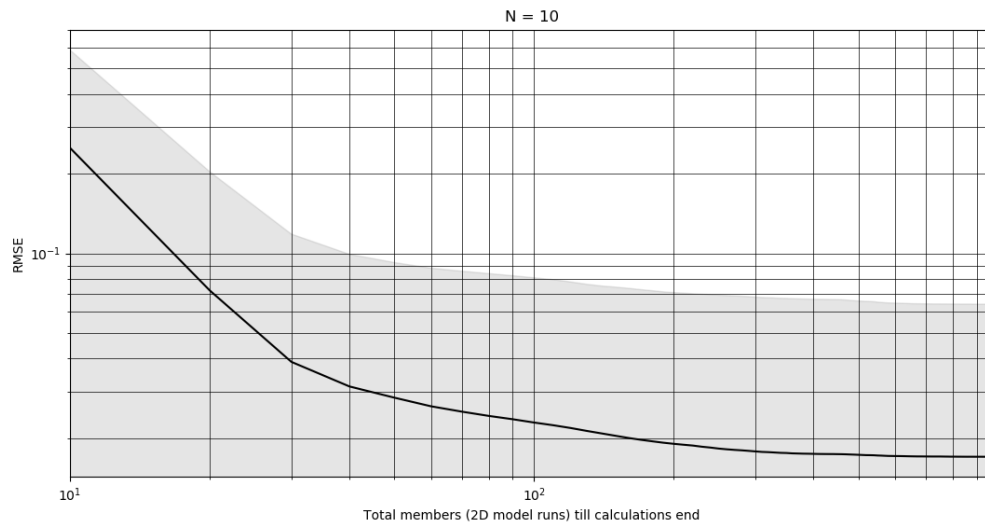


Figure C.22: The error evolution with a corresponding bandwidth of 2σ , averaged from 25 simulations, throughout the iterations for the ensemble size of $N = 10$.

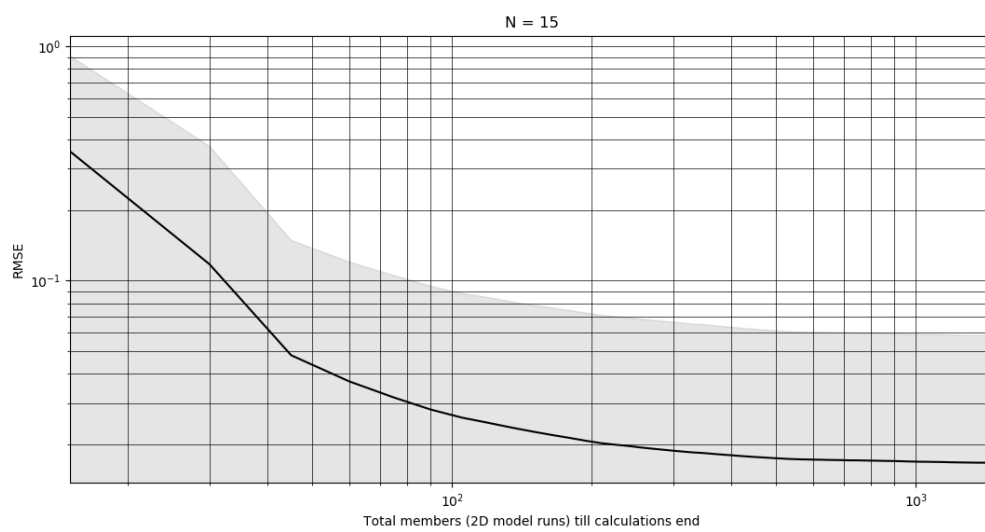


Figure C.23: The error evolution with a corresponding bandwidth of 2σ , averaged from 25 simulations, throughout the iterations for the ensemble size of $N = 15$.

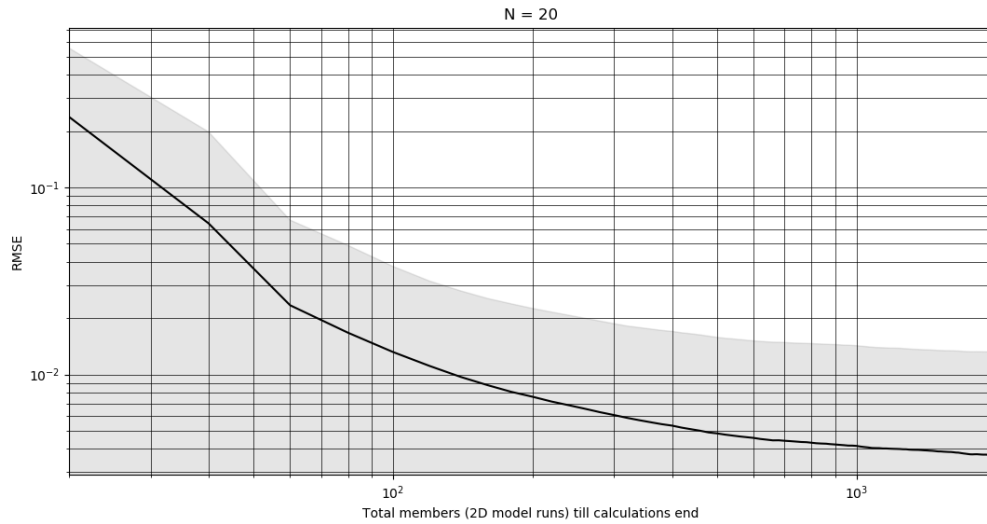


Figure C.24: The error evolution with a corresponding bandwidth of 2σ , averaged from 25 simulations, throughout the iterations for the ensemble size of $N = 20$.

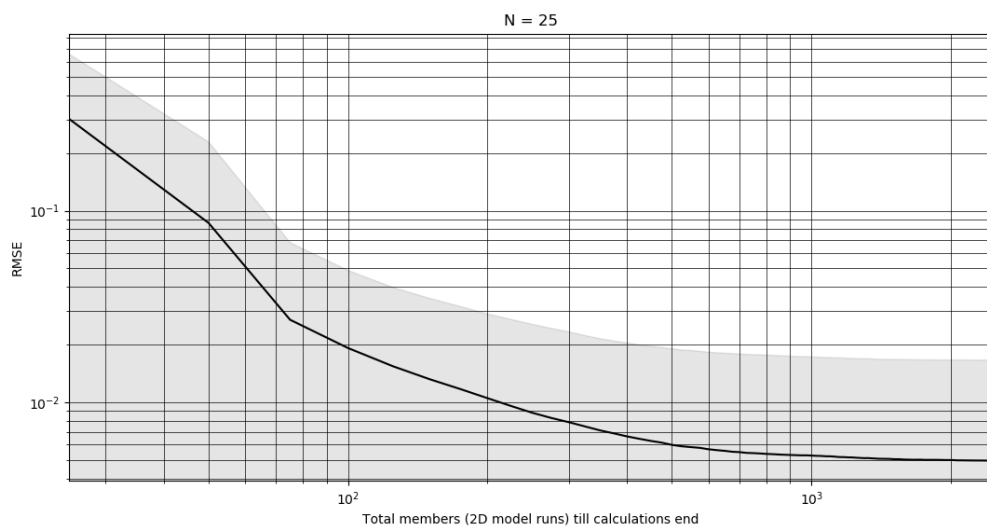


Figure C.25: The error evolution with a corresponding bandwidth of 2σ , averaged from 25 simulations, throughout the iterations for the ensemble size of $N = 25$.

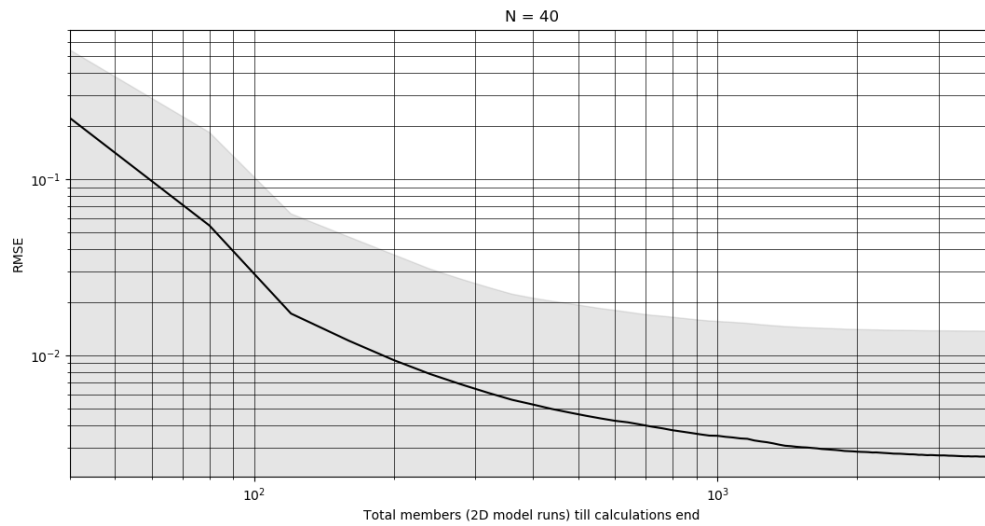


Figure C.26: The error evolution with a corresponding bandwidth of 2σ , averaged from 25 simulations, throughout the iterations for the ensemble size of $N = 40$.

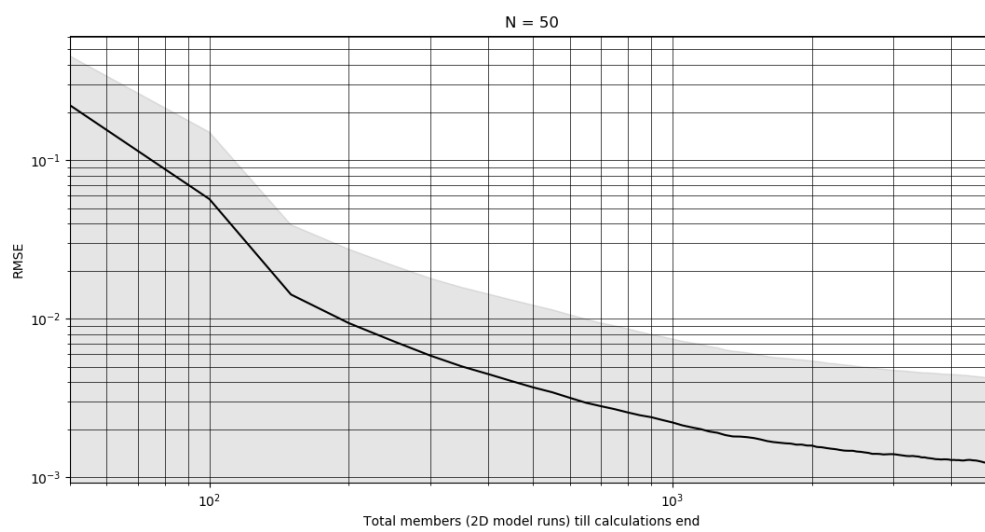


Figure C.27: The error evolution with a corresponding bandwidth of 2σ , averaged from 25 simulations, throughout the iterations for the ensemble size of $N = 50$.

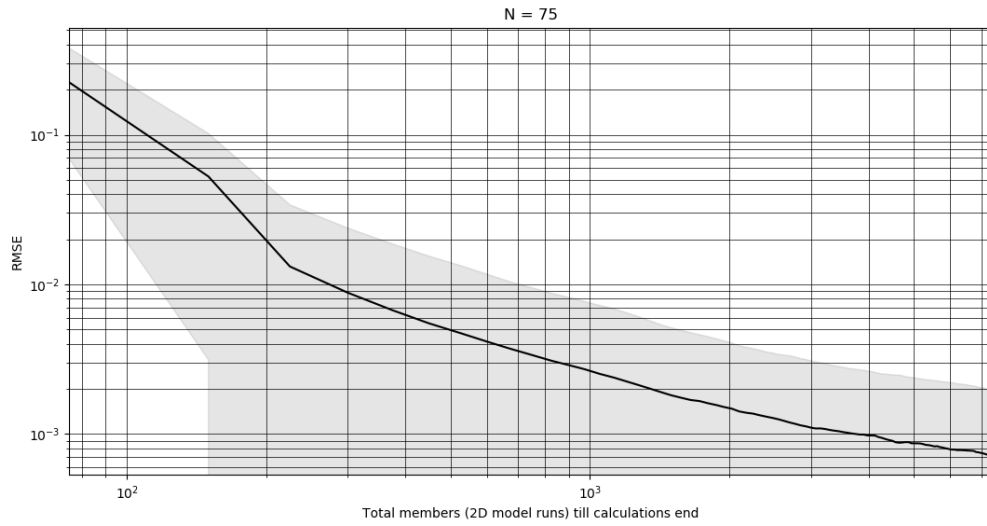


Figure C.28: The error evolution with a corresponding bandwidth of 2σ , averaged from 25 simulations, throughout the iterations for the ensemble size of $N = 75$.

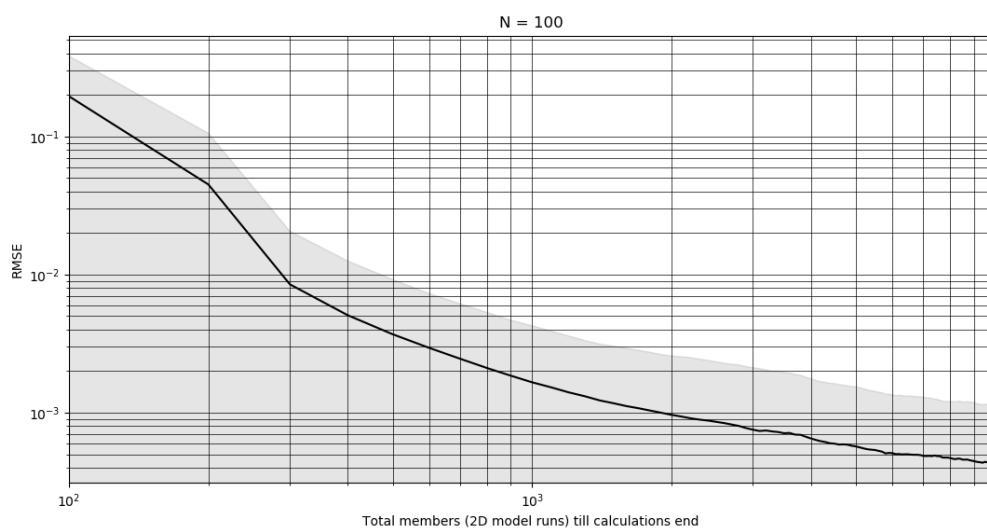


Figure C.29: The error evolution with a corresponding bandwidth of 2σ , averaged from 25 simulations, throughout the iterations for the ensemble size of $N = 100$.

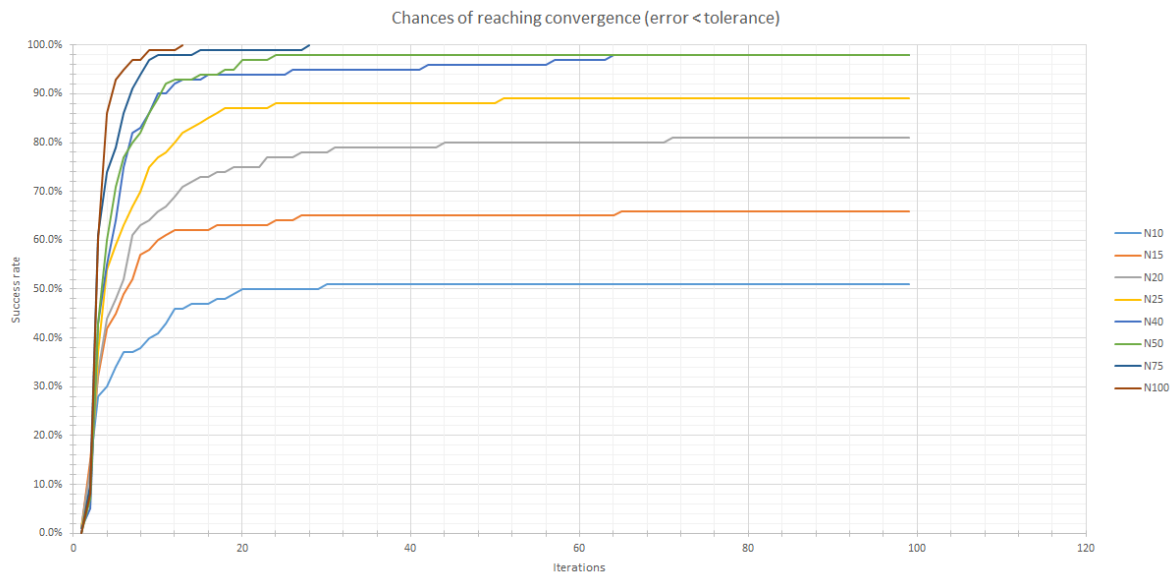


Figure C.30: The percentage value of script runs in which the computed error is below tolerance of 0.01 in a function of iterations for 8 ensemble sizes.

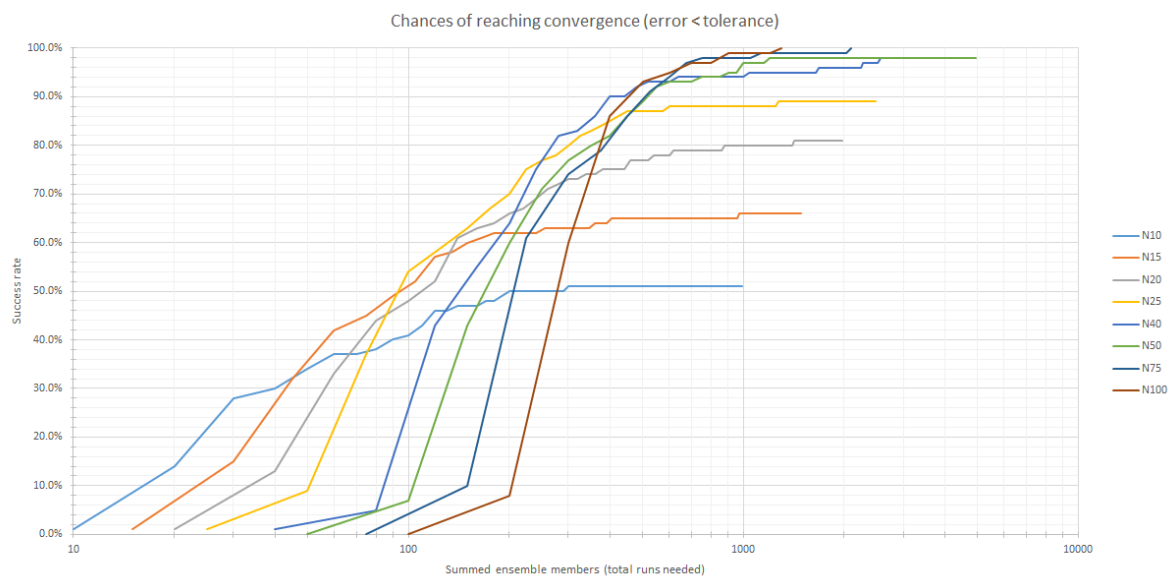


Figure C.31: The percentage value of script runs in which the computed error is below tolerance of 0.01 in a function of R value for 8 ensemble sizes.

D

Application of the inverse analysis in the FEM

D.1. Performance depending on the observation vector

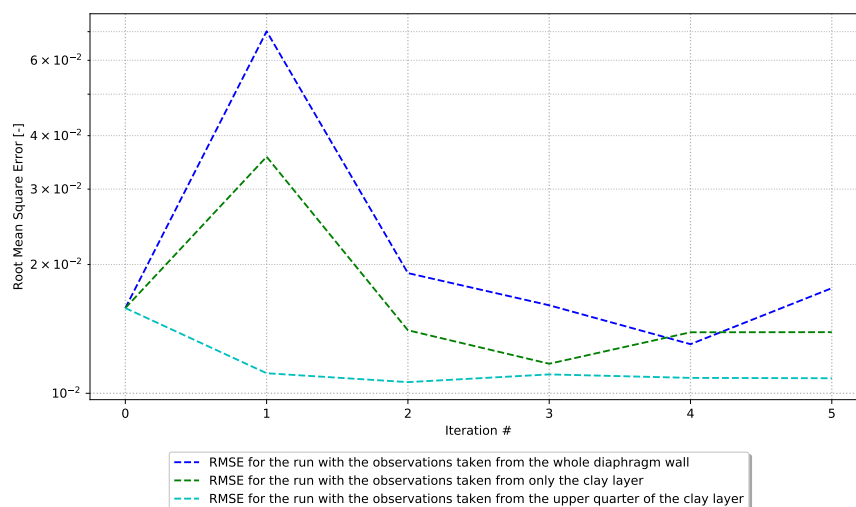


Figure D.1: The computed RMSE throughout the iterations for different observation types - manually created measurements case.

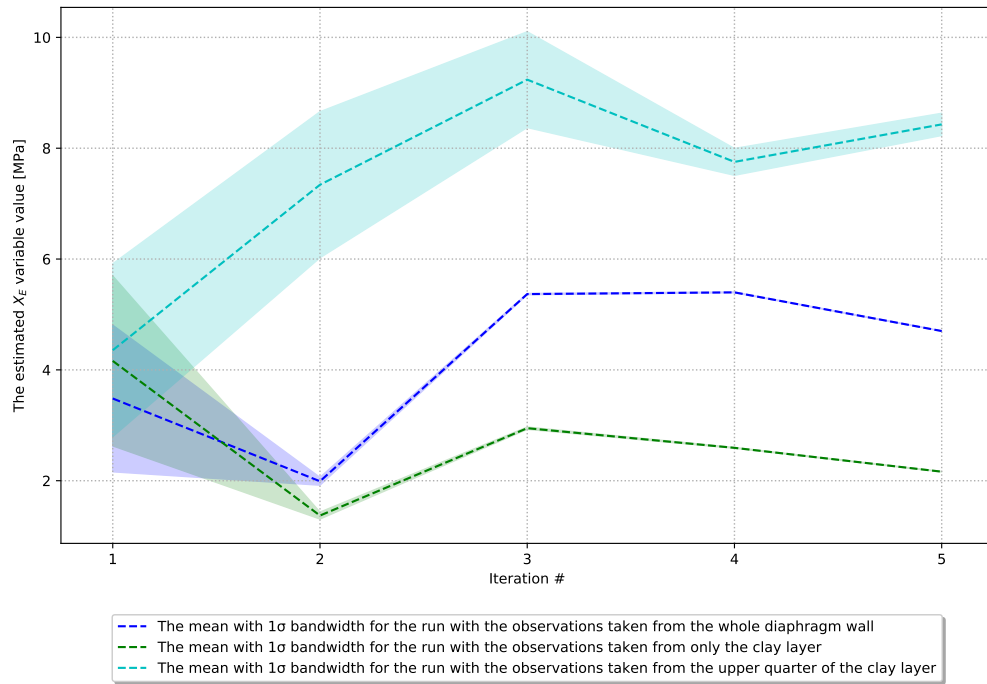


Figure D.2: The evolution of the estimated mean (the X_E variable) of the ensembles throughout the iterations for a different observation types - manually created measurements case with two variables.

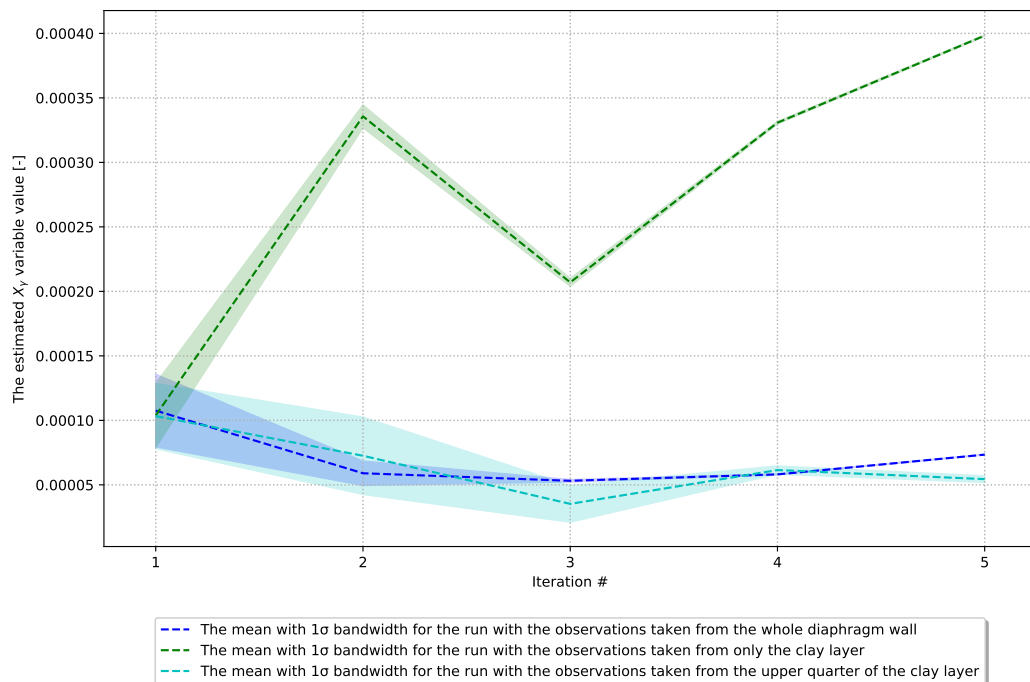


Figure D.3: The evolution of the estimated mean (the X_Y variable) of the ensembles throughout the iterations for a different observation types - manually created measurements case with two variables.